Space engineering

Space environment

This draft is distributed to the ECSS community for Public Review.
(Duration: 8 weeks)

Subject of the Public Review are only the modified parts of the document.
Note: The pdf-version identifies all deletions only with a revision bar. The MS Word file shows all changes w.r.t. to the previous version.

Start of Public Review: 14 March 2019
End of Public Review: 10 May 2019

DISCLAIMER (for drafts)
This document is an ECSS Draft Standard. It is subject to change without any notice and may not be referred to as an ECSS Standard until published as such.

ECSS Secretariat
ESA-ESTEC
Requirements & Standards Division
Noordwijk, The Netherlands

Foreword

This Standard is one of the series of ECSS Standards intended to be applied together for the management, engineering, product assurance and sustainability in space projects and applications. ECSS is a cooperative effort of the European Space Agency, national space agencies and European industry associations for the purpose of developing and maintaining common standards. Requirements in this Standard are defined in terms of what shall be accomplished, rather than in terms of how to organize and perform the necessary work. This allows existing organizational structures and methods to be applied where they are effective, and for the structures and methods to evolve as necessary without rewriting the standards.

This Standard has been prepared by the ECSS-E-ST-10-04C Rev.1 Working Group, reviewed by the ECSS Executive Secretariat and approved by the ECSS Technical Authority.

Disclaimer

Published by: ESA Requirements and Standards Division
ESTEC, P.O. Box 299,
2200 AG Noordwijk
The Netherlands

Change log

Change log for Draft development	
Next Steps	
14 December 2018	Draft for Review (DFR) submitted to ES
14 December 2018 – 30 January2019	DFR in preparation by ES for parallel Assessment
ECSS-E-ST-10-04C Rev.1 DFR1 30 January 2019	Parallel Assessment 31 January – 12 February 2019
Current Step	
ECSS-E-ST-10-04C Rev.1 DIR1 **30 January 2019**	**Public Review** **14 March – 10 May 2019**
Next Steps	
	Draft with implemented DRRs
	DRR Feedback
	TA Vote for publication
	Preparation of document for publication (including DOORS transfer for Standards)
	Publication
	Change log for published Standard (to be updated by ES before publication)
ECSS-E-ST-10-04A 21 January 2000	First issue
ECSS-E-ST-10-04B	Never issued
ECSS-E-ST-10-04C 15 November 2008	Second issue • General The whole document was re-written. The number of clauses and the space environment components addressed in the individual clauses were kept unchanged. The core of the document was newly structured into a main part, followed by normative and informative annexes. Descriptions, specifications of reference models and requirements, reference data and additional information are now clearly separated. Where possible, model uncertainties are given.

	• Main changes of standard models and requirements o Gravity The Joint Gravity Model 2 (JGM-2) for Earth was replaced by the EIGEN-GL04C gravity model. o Geomagnetic field The Internal Geomagnetic Field Model, IGRF-95, was replaced by IGRF-10. For the external field model no standard was defined previously. Now 2 options are given as standard: the model from Alexeev et al. from 2001 or the Tsyganenko model from 1996. o Natural electromagnetic radiation and indices The solar constant was updated to a value of 1 366,1 Wm^{-2} at 1 AU. New indices S10.7, M10.7 and IG12 were introduced. Reference values for the indices were changed or newly provided. Reference values for short term variations of a_p are newly provided. o Neutral atmosphere The standard model MSISE-90 was replaced by 2 different models: NRLMSISE-00 for temperatures and composition and JB-2006 for total atmospheric densities. A standard model for the Martian atmosphere was introduced. o Plasmas The International Reference Ionosphere model IRI 1995 was replaced by IRI 2007. For the plasma sphere of Earth the model from Carpenter and Anderson was replaced by the Global Core Plasma Model (GCPM). o Energetic particle radiation For trapped radiation the AE8 and AP8 models remain the standard with 2 newly introduced exceptions: new standards for electron fluxes near GEO and near GPS orbits are the IGE-2006 and the ONERA MEOv2 models, respectively. The new standard for solar event proton fluences is the ESP model (replacing JPL-91). CREME96, which was the standard model for solar particle event ions and Galactic Cosmic Rays (GCR), is now the standard for solar particle peak fluxes only. For GCR ISO 15390 is the new standard. The FLUMIC model is introduced as worst case for trapped electrons for internal charging analyses. A standard radiation model for Jupiter was introduced. o Space debris and meteoroids MASTER 2005 is the new standard model for Space Debris (previously no standard space debris model was defined). A new standard velocity distribution (HRMP) for the meteoroid model from Grün et al. was specified. The material density for meteoroids was changed from 2,0 g/cm^3 to 2,5 g/cm^3. For meteoroid stream fluxes the model from Cour-Palais was replaced by the model from Jenniskens and McBride. o Contamination Clear top level requirements for contamination assessments were introduced. The description of analysis methods and tools was

	streamlined and reduced.
ECSS-E-ST-10-04C Rev.1 DIR1 30 January 2019	Second issue Revision 1 Changes with respect to ECSS-E-ST-10-04C (15 November 2008) are identified with revision tracking. **Main changes are:** Implementation of Change requests: • Addition of definition for the term "flashover current" • xxx • yyy **Detailed changes** Added requirements: • xxx Modified requirements: • xxx Deleted requirements: • xxx Editorial corrections: • xxx …. NOTE: CHANGE LOG WILL BE COMPLETED BEFORE PUBLICATION.

Table of contents

Figures

Tables

Introduction

This standard forms part of the System Engineering branch (ECSS-E-10) of the Engineering area of the ECSS system. As such it is intended to assist in the consistent application of space environment engineering to space products through specification of required or recommended methods, data and models to the problem of ensuring best performance, problem avoidance or survivability of a product in the space environment.

The space environment can cause severe problems for space systems. Proper assessment of the potential effects is part of the system engineering process as defined in ECSS-E-ST-10. This is performed in the early phases of a mission when consideration is given to e.g. orbit selection, mass budget, thermal protection, and component selection policy. As the design of a space system is developed, further engineering iteration is normally necessary with more detailed analysis.

In this Standard, each component of the space environment is treated separately, although synergies and cross-linking of models are specified. Informative annexes are provided as explanatory background information associated with each clause.

1
Scope

This standard applies to all product types which exist or operate in space and defines the natural environment for all space regimes. It also defines general models and rules for determining the local induced environment.

Project-specific or project-class-specific acceptance criteria, analysis methods or procedures are not defined.

The natural space environment of a given item is that set of environmental conditions defined by the external physical world for the given mission (e.g. atmosphere, meteoroids and energetic particle radiation). The induced space environment is that set of environmental conditions created or modified by the presence or operation of the item and its mission (e.g. contamination, secondary radiations and spacecraft charging). The space environment also contains elements which are induced by the execution of other space activities (e.g. debris and contamination).

This standard may be tailored for the specific characteristic and constrains of a space project in conformance with ECSS-S-ST-00.

2
Normative references

The following normative documents contain provisions which, through reference in this text, constitute provisions of this ECSS Standard. For dated references, subsequent amendments to, or revision of any of these publications do not apply, However, parties to agreements based on this ECSS Standard are encouraged to investigate the possibility of applying the more recent editions of the normative documents indicated below. For undated references, the latest edition of the publication referred to applies.

ECSS-S-ST-00-01 ECSS system – Glossary of terms

[RN.1] C. Förste, F. Flechtner, R. Schmidt, R. König, U. Meyer, R. Stubenvoll, M. Rothacher, F. Barthelmes, H. Neumayer, R. Biancale, S. Bruinsma, J.-M. Lemoine, and S. Loyer, A Mean Global Gravity Field Model from the Combination of Satellite Mission and Altimetry/Gravimetry Surface Data – EIGEN-GL04C, Geophysical Research Abstracts, Vol.8, 03462, 2006

[RN.2] G. Petit, B. Luzum (eds.), in IERS Conventions (2010), IERS Technical Note No. 36, 2010, https://www.iers.org/SharedDocs/Publikationen/EN/IERS/Publications/tn/TechnNote36/tn36.html

[RN.3] W.M. Folkner et al, The Planetary and Lunar Ephemerides DE430 and DE431, IPN Progress Report 42-196, February 15, 2014

[RN.4] Picone, J. M., A. E. Hedin, D. P. Drob and Aikin, A. C., "NRLMSISE-00 Empirical Model of the Atmosphere: Statistical Comparisons and Scientific Issues", J. Geophys. Res., 107(A12), doi 10.1029/2002JA009430. 2002, p. 1468.

[RN.5] Bowman, B. R., Tobiska, W. K., Marcos, F. A., Valladares, "The JB2006 Empirical Thermospheric Density Model", Journal of Atmospheric and Solar-Terrestrial Physics, Vol. 70, Issue 5, pp. 774-793, 2008, doi:10.1016/j.jastp.2007.10.002.

[RN.6] Hedin, A.E., E.L. Fleming, A.H. Manson, F.J. Scmidlin, S.K. Avery, R.R. Clark, S.J. Franke, G.J. Fraser, T. Tsunda, F. Vial and R.A. Vincent, Empirical Wind Model for the Upper, Middle, and Lower Atmosphere, J. Atmos. Terr. Phys., 58, 1421-1447, 1996

[RN.7] E. Millour et al., "The Mars Climate Database (MCD version 5.3)", Vol. 19, EGU2017-12247, 2017

[RN.8] Gallagher D.L., P.D. Craven, and R.H. Comfort. Global Core Plasma model. J. Geophys. Res., 105, A8, 18819-18833, 2000.

[RN.9] D. Bilitza, D,., Altadill, V. D, Zhang Y, Mertens C, Truhlik, V. Shubin, I. Galkin, B. Reinisch, and X. Huang, V, et al.: The International Reference Ionosphere 2016: From ionospheric climate to real-time weather predictions, 2012 – a model of international collaboration. J. Space Weather, 15, 418-429, 2017 Space Clim., 2014,4, A07

[RN.10] Vette J.I., "The AE-8 Trapped Electron Model Environment", NSSDC/WDC-A-R&S Report 91-24, NASA-GSFC, 1991.

[RN.11] Sawyer D.M. and J.I. Vette, “AP8 Trapped Proton Environment For Solar Maximum and Solar Minimum”, NSSDC WDC-A-R&S 76-06, NASA-GSFC, 1976.

[RN.12] A Sicard-Piet, S. A.Bourdarie, D. M. Boscher, R. H. W. Friedel, M. Thomsen, T. Goka, H.Matsumoto, H. Koshiishi, “A new international geostationary electron model: IGE-2006, from 1 keV to 5.2 MeV”, Space Weather, 6, S07003, doi:10.1029/2007SW000368, 2008.

[RN.13] Sicard-Piet A., S. Bourdarie, D. Boscher, R. Friedel, T. Cayton, Solar Cycle Electron Radiation Environement at GNSS Like Altitude, session D5.5-04, Proceedings 57th International Astronautical Congress, Valencia, Sept 2006

[RN.14] Rodgers D.J, Hunter K.A and Wrenn G.L, The Flumic Electron Environment Model, Proceedings 8th Spacecraft Charging Technology Conference, Huntsville Alabama, 2003

[RN.15] Xapsos, M. A., G.P. Summers, J.L. Barth, E. G. Stassinopoulos and E.A. Burke, “Probability Model for Cumulative Solar Proton Event Fluences”, IEEE Trans. Nucl. Sci., vol. 47, no. 3, June 2000, pp 486-490

[RN.16] Lario et al., Radial and Longitudinal Dependence of solar 4-13 MeV and 27-37 MeV Proton Peak Intensities and Fluences: HELIOS and IMP8 Observations, Astrophys Journal, 653:1531-1544, Dec 20, 2006.

[RN.17] Bourdarie, S., A. Sicard-Piet, “Jupiter environment modelling”, ONERA Technical note 120 Issue 1.2, ESA contract 19735/NL/HB, FR 1/11189 DESP, October 2006

[RN.18] CREME96: https://creme96.nrl.navy.mil/

[RN.19] ISO Model 15390:2004, ISO/TC 20/SC 14 Space systems and operations, June 2004

[RN.20] Adams J.H., R. Silberberg and C.H. Tsao, “Cosmic Ray Effects on Microelectronics, Part I: The Near-Earth Particle Environment”, NRL Memorandum Report 4506, Naval Research Laboratory, Washington DC 20375-5000, USA, 1981.

[RN.21] Desorgher, L., MAGNETOCOSMICS User Manual 2003, http://reat.space.qinetiq.com/septimess/magcos/

[RN.22] Smart, D. F., Shea, M.A., Calculated cosmic ray cut-off rigidities at 450 km for epoch 1990, Proc. 25th ICRC, 2, 397-400, 1997.

[RN.23] Stassinopoulos E.G. and J.H. King, “Empirical Solar Proton Model For Orbiting Spacecraft Applications”, IEEE Trans. on Aerosp. and Elect. Systems AES-10, 442, 1973

[RN.24] D. C. Jensen and J. C. Cain, An Interim Geomagnetic Field, J. Geophys.Res. 67, 3568, 1962.

[RN.25] J. C. Cain, S. J. Hendricks, R. A. Langel, and W. V. Hudson, A Proposed Model for the International Geomagnetic Reference Field, 1965, J. Geomag. Geoelectr. 19, 335, 1967.

[RN.26] MASTER-8, https://sdup.esoc.esa.int, 2018

[RN.27] NOAA/SEC source of dates for solar maxima and minima: ftp://ftp.ngdc.noaa.gov/STP/SOLAR_DATA/SUNSPOT_NUMBERS/maxmin.new

[RN.28] Roberts C.S., “Co-ordinates for the Study of Particles Trapped in the Earth’s Magnetic Field: A Method of Converting from B,L to R,λ Co-ordinates”, J. Geophys. Res. 69, 5 089, 1964.

[RN.29] IGRF-10, the list of coefficients is given at the IGRF web page on the IAGA web site: http://www.ngdc.noaa.gov/IAGA/vmod/igrf.html

[RN.30] Alexeev I.I., Kalegaev V.V., Belenkaya E.S., Bobrovnikov S.Yu., Feldstein Ya.I., Gromova L.I. (2001), J. Geophys. Res., V.106, No A11, P. 25,683-25,694

[RN.31] Tsyganenko, N.A., and D.P. Stern, Modeling the global magnetic field of the large-scale Birkeland current sustems, J. Geophys. Res., V. 101, 27187-27198, 1996.

[RN.32] T.L. Gulyaeva et al., “Inter-hemispheric imaging of the ionosphere with the upgraded IRI-Plas model during the space weather storms”, Earth Planets Space, 63, 929-939, 2011

[RN.33] S. Bourdarie et al., “GEO-handbook V1.1”, TN 1/13377 DESP, April 2008, http://space-env.esa.int/Reports/ECSS/1-13377%20avril%202008%20GEO_handbook-V1.1.pdf

[RN.34] RadMod Research Ltd web-site for MAIRE: http://www.radmod.co.uk/maire, 2017

[RN.35] Fan Lei, Alex Hands, Simon Clucas, Clive Dyer, and Pete Truscott, “Improvement to and validations of the QinetiQ Atmospheric Radiation Model (QARM),” IEEE Trans Nucl Sci, Vol 53, No 4, pp1851-1858, 2006.

[RN.36] Paula H. Krisko. "The New NASA Orbital Debris Engineering Model ORDEM 3.0 (Invited)", AIAA/AAS Astrodynamics Specialist Conference, AIAA SPACE Forum, (AIAA 2014-4227) https://doi.org/10.2514/6.2014-4227, 2014

[RN.37] Moorhead, A. V., H. M. Koehler, and W. J. Cooke. "NASA Meteoroid Engineering Model Release 2.0." (2015)

[RN.38] Thebault et al, International Geomagnetic Reference Field 12th Generation, Earth, Planets and Space (2015) 67:79

[RN.39] Bowman, Bruce R., W. Kent Tobiska, Frank A. Marcos, Cheryl Y. Huang, Chin S. Lin, and William J. Burke (2008a), A new empirical thermosphericdensity model JB-2008 using new solar and geomagnetic indices, in AIAA/AAS Astrodynamics Specialist Conference and Exhibit, 18–21 August 2008, Honolulu, Hawaii, number AIAA 2008–6438

[RN.40] D.P. Drob et al., “An empirical model of the Earth’s horizontal wind fields: HWM-07”, J Geophys Res, Vol. 113, A12304, doi:10.1029/2008JA013668, 2008

3
Terms, definitions and abbreviated terms

3.1 Terms defined in other standards

a. For the purpose of this Standard, the terms and definitions from ECSS-S-ST-00-01 apply, in particular for the following terms:

1. contamination
2. environment
3. mission
4. space debris

3.2 Terms specific to the present standard

3.2.1 Ap, Kp indices

geomagnetic activity indices to describe fluctuations of the geomagnetic field

NOTE Values of *Ap* range from 0 to 400 and they are expressed in units of nT (nanotesla). *Kp* is essentially the logarithm of *Ap*.

3.2.2 absorbed dose

energy absorbed locally per unit mass as a result of radiation exposure which is transferred through ionization and excitation

NOTE A portion of the energy absorption can result in damage to the lattice structure of solids through displacement of atoms, and this is now commonly referred to as Non-Ionizing Energy Loss (NIEL).

3.2.3 albedo

fraction of sunlight which is reflected off a planet

3.2.4 atmospheric albedo neutrons

neutrons escaping from the earth's atmosphere following generation by the interaction of cosmic rays and solar particles

NOTE Albedo neutrons can also be produced by other planetary atmospheres and surfaces.

3.2.5 bremsstrahlung

high-energy electromagnetic radiation in the X-γ energy range emitted by charged particles slowing down by scattering of atomic nuclei

NOTE The primary particle is ultimately absorbed while the bremsstrahlung can be highly penetrating. In space, the most common source of bremsstrahlung is electron scattering.

3.2.6 confidence level

input which stipulates the level of risk one is willing to accept

NOTE 1 For example a 95% CL means that there is a 5% chance that the specified environment can be exceeded according to the model.

NOTE 2 Statistical environment models often provide outputs as a function of confidence level (CL).

NOTE 3 The CL does not account for systematic uncertainties associated with environment models.

3.2.7 current

the rate of transport of particles through a boundary

NOTE In contrast to flux, current is dependent on the direction in which the particle crosses the boundary (it is a vector integral). An isotropic omnidirectional flux, *f*, incident on a plane gives rise to a current of ¼ *f* normally in each direction across the plane. Current is often used in the discussion of radiation transport.

3.2.8 distribution function *f(x,v)*

function describing the particle density of a plasma in 6-D space made up of the three spatial vectors and the three velocity vectors, with units $s^3\ m^{-6}$

NOTE For distributions that are spatially uniform and isotropic, it is often quoted as *f(v)*, a function of scalar velocity, with units $s\ m^{-4}$, or *f(E)* a function of energy, with units $J^{-1}m^{-3}$. This can be converted to flux as follows:

$$Flux = \int Vf(v)dv \tag{3-1}$$

or

$$Flux = \int \frac{f(E)}{m} dE \tag{3-2}$$

where

v is the scalar velocity;

E is the energy;

m is the particle mass.

3.2.9 dose

quantity of radiation delivered at a position

NOTE In its broadest sense this can include the flux of particles, but in the context of space energetic particle radiation effects, it usually refers to the energy absorbed locally per unit mass as a result of radiation exposure.

3.2.10 dust

particulates which have a direct relation to a specific solar system body and which are usually found close to the surface of this body

NOTE For example Lunar, Marian or Cometary dust.

3.2.11 Earth infrared

thermal radiation emitted by the Earth

NOTE It is also called outgoing long wave radiation.

3.2.12 energetic particle

particles which, in the context of space systems radiation effects, can penetrate outer surfaces of spacecraft

NOTE For electrons, this is typically above 100 keV, while for protons and other ions this is above 1 MeV. Neutrons, gamma rays and X-rays are also considered energetic particles in this context.

3.2.13 equivalent fluence

quantity which attempts to represent the damage at different energies and from different species

NOTE 1 For example: For solar cell degradation it is often taken that one 10 MeV protons is “equivalent” to 3 000 electrons of 1 MeV. This concept also occurs in consideration of Non-ionizing Energy Loss effects (NIEL).

NOTE 2 Damage coefficients are used to scale the effect caused by particles to the damage caused by a standard particle and energy.

3.2.14 exosphere

part of the Earth’s atmosphere above the thermosphere for which the mean free path exceeds the scale height, and within which there are very few collisions between atoms and molecules

NOTE 1 Near the base of the exosphere atomic oxygen is normally the dominant constituent.

NOTE 2 With increasing altitude, the proportion of atomic hydrogen increases, and hydrogen normally becomes the dominant constituent

above about 1 000 km. Under rather special conditions (i.e. winter polar region) He atoms can become the major constituent over a limited altitude range.

NOTE 3 A small fraction of *H* and *He* atoms can attain escape velocities within the exosphere.

3.2.15 external field

part of the measured geomagnetic field produced by sources external to the solid Earth

NOTE the external sources are mainly: electrical currents in the ionosphere, the magnetosphere and coupling currents between these regions.

3.2.16 $F_{10.7}$ flux

solar flux at a wavelength of 10,7 cm in units of 10^4 Jansky (one Jansky equals 10^{-26} $Wm^{-2}Hz^{-1}$)

3.2.17 fluence

time-integration of the flux

3.2.18 flux

amount of radiation crossing a surface per unit of time

NOTE 1 The directional flux is the differential with respect to solid angle (e.g. particles cm^{-2} $steradian^{-1}s^{-1}$) while the "differential" flux is differential with respect to energy (e.g. particles cm^{-2} $MeV^{-1}s^{-1}$). In some cases fluxes are also treated as a differential with respect to Linear Energy Transfer (see 3.2.28).

NOTE 2 Flux is often expressed in "integral form" as particles per unit area per unit time (e.g. electrons $cm^{-2}s^{-1}$) above a certain threshold energy.

3.2.19 geocentric solar magnetospheric coordinates (GSM)

elements of a right-handed Cartesian coordinate system (X,Y,Z) with the origin at the centre of the Earth

NOTE *X* points towards the Sun; *Z* is perpendicular to *X*, lying in the plane containing the *X* and geomagnetic dipole axes; *Y* points perpendicular to *X* and *Z* and points approximately towards dusk magnetic local time (MLT).

3.2.20 GNSS orbits

orbits with altitudes between 20 500 km and 24 000 km within an inclination range of 55° ± 5°

3.2.21 heterosphere

Earth's atmosphere above 105 km altitude where the neutral concentration profiles are established due to diffusive equilibrium between the species

NOTE N_2 is normally dominant below approximately 200 km, *O* is normally dominant from approx 200 km to approx. 600 km, *He* is dominant above 600 km altitude, and H dominant at very high altitudes. These conditions depend on solar and geomagnetic activity, and the situation may be quite variable at high altitudes during major geomagnetic disturbances.

3.2.22 homosphere

Earth's atmosphere below 105 km altitude where complete vertical mixing yields a near-homogeneous composition of about 78,1% N_2, 20,9% O_2, 0,9% Ar, and 0,1% CO_2 and trace constituents

NOTE The homopause (or turbopause) marks the ceiling of the homosphere.

3.2.23 indirect flux

molecules impinging on a critical surface, after collision with, or collision and sojourn on other surfaces

3.2.24 internal field

part of the measured geomagnetic field produced by sources internal to the solid Earth, primarily due to the time-varying dynamo operating in the outer core of the Earth

3.2.25 interplanetary magnetic field

solar coronal magnetic field carried outward by the solar wind, pervading the solar system

3.2.26 isotropic

property of a distribution of particles where the flux is constant over all directions

3.2.27 *L* or *L* shell

parameter of the geomagnetic field, often used to describe positions in near-Earth space

NOTE *L* or *L* shell has a complicated derivation based on an invariant of the motion of charged particles in the terrestrial magnetic field (see Annex E). However, it is useful in defining plasma regimes within the magnetosphere because, for a dipole magnetic field, it is equal to the geocentric altitude in Earth-radii of the local magnetic field line where it crosses the equator.

3.2.28 linear energy transfer (LET)

rate of energy deposit from a slowing energetic particle with distance travelled in matter, the energy being imparted to the material

NOTE Normally used to describe the ionization track caused by passage of an ion. LET is material-dependent and is also a function of particle energy. For ions involved in space radiation effects, it increases with decreasing energy (it also increases at high energies, beyond the minimum ionizing energy). LET allows different ions to be considered together by simply representing the ion environment as the summation of the fluxes of all ions as functions of their LETs. This simplifies single-event upset calculation. The rate of energy loss of a particle, which also includes emitted secondary radiations, is the stopping power.

3.2.29 magnetic local time (MLT)

parameter analogous to longitude, often used to describe positions in near-Earth space

NOTE Pressure from the solar wind distorts the Earth magnetic field into a comet-like shape. This structure remains fixed with its nose towards the Sun and the tail away from it as the Earth spins within it. Hence longitude, which rotates with the Earth, is not a useful way of describing position in the magnetosphere. Instead, magnetic local time is used. This has value 0 (midnight) in the anti-sunward direction, 12 (noon) in the sunward direction and 6 (dawn) and 18 (dusk) perpendicular to the sunward/anti-sunward line. This is basically an extension of the local solar time on Earth, projected vertically upwards into space although allowance is made for the tilt of the dipole.

3.2.30 mass flow rate

mass (g) of molecular species crossing a specified plane per unit time and unit area (g $cm^{-2}s^{-1}$)

3.2.31 Maxwellian distribution

plasma distribution functions described in terms of scalar velocity, v, by the Maxwellian distribution below:

$$f(v) = 4\pi n \left(\frac{m}{2\pi kT} \right)^{\frac{3}{2}} v^2 \exp\left(-\frac{v^2 m}{2kT} \right) \quad (3\text{-}3)$$

where

n is the density;

k is the Boltzmann constant;

T is the temperature.

NOTE The complete distribution is therefore described by a pair of numbers for density and temperature. This distribution is valid in thermal equilibrium. Even non-equilibrium distributions can often be usefully described by a combination of two Maxwellians.

3.2.32 meteoroids

particles in space which are of natural origin

NOTE nearly all meteoroids originate from asteroids or comets.

3.2.33 meteoroid stream

meteoroids that retain the orbit of their parent body and that can create periods of high flux

3.2.34 nano-Tesla

standard unit of Geomagnetism

NOTE An older unit, not widely used now, is the Gauss, which is 10^5 nT.

3.2.35 omnidirectional flux

scalar integral of the flux over all directions

NOTE This implies that no consideration is taken of the directional distribution of the particles which can be non-isotropic. The flux at a point is the number of particles crossing a sphere of unit cross-sectional surface area (i.e. of radius $1/\sqrt{\pi}$). An omnidirectional flux is not to be confused with an isotropic flux.

3.2.36 plasma

partly or wholly ionized gas whose particles exhibit collective response to magnetic and electric fields

NOTE The collective motion is brought about by the electrostatic Coulomb force between charged particles. This causes the particles to rearrange themselves to counteract electric fields within a distance of the order of the Debye length. On spatial scales larger than the Debye length plasmas are electrically neutral.

3.2.37 radiation

transfer of energy by means of a particle (including photons)

3.2.38 single-event upset (SEU), single-event effect (SEE), single-event latch-up (SEL)

effects resulting from the highly localized deposition of energy by single particles or their reaction products and where the energy deposition is sufficient to cause observable effects

3.2.39 sporadic flux

random flux with no apparent pattern

3.2.40 total Solar irradiance (TSI)

NOTE mean level of solar radiation that falls on a unit area normal to the line from the Sun per unit time outside the Earth's atmosphere, at one AU from Sun-centre1 1 AU = 149 597 870 700 m.

NOTE 2 Total Solar Irradiance is historically known as "solar constant".

3.2.41 solar flare

emission of optical, UV and X-radiation from an energetic event on the Sun

NOTE There is some controversy about the causal relationship between solar flares and the arrival of large fluxes of energetic particles at Earth. Therefore, it is more consistent to refer to the latter as Solar Energetic Particle Events (SEPEs).

3.2.42 thermosphere

Earth's atmosphere between 120 km and 250 km to approximately 400 km (depending on the activity level), where temperature has an exponential increase up to a limiting value T_∞ at the thermopause (where T_∞ is the exospheric temperature)

3.2.43 trackable objects

objects regularly observed and catalogued by ground-based sensors of a space surveillance network

NOTE Trackable objects are typically objects larger than about 5 cm to 10 cm in LEO and larger than about 50 cm to 1 m in GEO.

3.2.44 world magnetic model

revised every five years by a US-UK geomagnetic consortium, primarily for military use

3.3 Abbreviated terms

For the purpose of this Standard, the abbreviated terms from ECSS-S-ST-00-01 and the following apply:

Abbreviation	Meaning
ASTM	American Society for Testing and Materials
AE	auroral electrojet
AO	atomic oxygen
BIRA	Belgisch Instituut voor Ruimte-Aeronomie
CIRA	COSPAR International Reference Atmosphere
COSPAR	Committee on Space Research
DISCOS	ESA's database and information system characterizing objects in space
DTM	density and temperature model
emf	electro-motive force
ESP Model	Emission of Solar Protons Model
GCR	galactic cosmic ray
GEO	geostationary Earth orbit
GNSS	global navigation satellite system
GRAM	global reference atmosphere model
GSM	geocentric solar magnetospheric co-ordinates
HEO	highly eccentric orbit
HWM	horizontal wind model
IAGA	International Association for Geomagnetism and Aeronomy
IASB	Institute d'Aeronomie Spatiale de Belgique
IERS	international earth rotation service
IGRF	international geomagnetic reference field
IMF	interplanetary magnetic field
JB-2006	Jacchia-Bowman semi-empirical model (2006)
JB-2008	Jacchia-Bowman semi-empirical model (2008)
LDEF	long duration exposure facility
LEO	low Earth orbit
LET	linear energy transfer
MAH	model of the high atmosphere
MASTER	meteoroid and space debris terrestrial environment reference model
MEO	medium (altitude) Earth orbit
MET	Marshall engineering thermosphere model

Abbreviation	Meaning
MLT	magnetic local time
MSIS	mass spectrometer and incoherent scatter
NIEL	non-ionizing energy loss
nT	nano-Tesla
R	sunspot number
R_C	rigidity Cut-off for geomagnetic shielding
R_E	Earth radius
RHU	radiosisotope heater unit
R_J	jovian radius
r.m.s.	root-mean-square
RTG	radioisotope thermo-electric generator
SEU	single-event upset
SEE	single-event effect
SEL	single-event latch-up
SEPs	solar energetic particles
SEPE	solar energetic particle events
sfu	solar flux unit
SPE	solar particle events
SRP	solar radiation pressure
SPIDR	Space Physics Interactive Data Resource
SW	solar wind
TD	total density model
URSI	Union Radio Science Internationale
USSA	US standard atmosphere
VUV	vacuum ultra violet
WMM	world magnetic model

4
Gravity

4.1 Introduction and description

4.1.1 Introduction

Any two bodies attract each other with a force that is proportional to the product of their masses, and inversely proportional to the square of the distance between them (Newton's law):

$$F = G\frac{m_1\, m_2}{r^2} \tag{4-1}$$

where

F is the gravitational force

G = (6,67408 ± 0,00031)×10^{-11}m^{3}kg^{-1}s^{-2} is the universal gravitational constant

m_1, m_2 are the two point masses

r is the distance between the masses

The simplest case of gravitational attraction occurs between bodies that can be considered as point masses. These are bodies at a relative distance r that is sufficiently large in comparison to the sizes of the bodies to ignore the *shape* of the bodies. For two spherical bodies with a homogeneous mass distribution Newton's law is correct also at all locations above their surface ("2-body problem").

Also third body perturbations and tidal effects are important for an accurate analysis of the gravitational interaction.

4.1.2 Gravity model formulation

Without compromising the general validity of underlying theories, all subsequent gravity model discussions are focused on the Earth. The gravity acceleration acting on a point mass, which is external to the central body, is the gradient of the potential function U of that body. The corresponding geopotential surface satisfies the so called Laplace equation:

$$\nabla^2 U = 0 \tag{4-2}$$

The corresponding perturbing acceleration can be determined from equation (4-3) by means of computationally efficient recursion algorithms (e.g. as in [RD.1]).

$$\ddot{\vec{r}} = \nabla U \tag{4-3}$$

where

$\ddot{\vec{r}}$ is the 2nd time derivative of the position vector.

The solution U of the partial differential equation (4-2) is typically written in the form of a series expansion, in terms of so-called surface spherical harmonic functions, for a location defined in spherical coordinates r, λ, φ.

$$U = \frac{GM}{r}\left\{1 + \sum_{l=2}^{N}\left(\frac{a_e}{r}\right)^l \sum_{m=0}^{l}\left[C_{lm}\cos(m\lambda) + S_{lm}\sin(m\lambda)\right] P_{lm}(\sin\varphi)\right\} \tag{4-4}$$

where

$GM = \mu$ is the gravity constant of the Earth (M being its mass);

$\mu = 3{,}986004415\times10^{14}$ m^{3}s^{-2} for the EIGEN-GL04C model

a_e is the mean equatorial radius of the Earth;

$a_e = 6\ 378\ 136{,}460$ m for the EIGEN-GL04C model

r is the radial distance from centre of the Earth to satellite

N is the maximum degree of the expansion

l is the degree of a certain harmonic function

m is the order of a certain harmonic function

C_{lm}, S_{lm} are coefficients that determine amplitude and phase of a certain harmonic function

λ is the geodetic longitude of the sub-satellite point

φ is the geodetic latitude of the sub-satellite point

P_{lm} are associated Legendre functions of the first kind, of degree l and order m; recurrance relations for these functions are available in the literature (e.g. [RD.1]).

A gravity model consists of adopted values for GM, a_e, and a set of model coefficients C_{lm}, S_{lm}. Practical implementations of gravity models, e.g. for numerical integration of a satellite orbit, are typically interested in the gravity acceleration resulting from the potential function U in (4-4). Corresponding partial derivatives of (4-4) in Cartesian coordinates of an Earth-fixed system x, y, z can be computed recursively (see [RD.1]).

The model coefficients C_{lm}, S_{lm} are typically provided in their normalized versions, according to (4-5) in order to limit their numerical range for higher degrees and orders.

$$\begin{Bmatrix} \overline{C}_{lm} \\ \overline{S}_{lm} \end{Bmatrix} = \sqrt{\frac{(l+m)!}{k\,(2l+1)\,(l-m)!}} \begin{Bmatrix} C_{lm} \\ S_{lm} \end{Bmatrix} \qquad k = \begin{cases} 1 & \text{for } m = 0 \\ 2 & \text{for } m \neq 0 \end{cases} \tag{4-5}$$

The Legendre functions $P_{lm}(\sin \varphi)$ in this case are normalized by the inverse of the square root in equation (4-5).

4.1.3 Third body gravitation

When acting as a third-body perturbation, the gravitational attraction by the Sun and its planets can be modelled by means of point mass attractions. This requires knowledge on the masses and positions of the bodies, as well as some guidelines on which effects are important. In general, for orbit computations of Earth-orbiting satellites it is sufficient to include the planetary gravity due to Venus, Mars, Jupiter and Saturn; the other planets are either too small, or too far away to have any significant impact on a satellite orbit around the Earth.

4.1.4 Tidal effects

The gravity potential of a central body only represents the static part of the gravitational acceleration acting on a satellite. There are, however, additional gravity-related effects due to tides that can be important for precise applications. Several tidal effects can be distinguished (see [RD.1]):

- Solid Earth tides associated with the deformations of the Earth's body under the gravitational effects of Sun and Moon and leading to complicated variations in the geopotential coefficients.
- Ocean tides, associated with the displacements of the ocean water masses under the effect of solar and lunar tides. The water displacements in turn modify the geopotential in complicated variational patterns.
- The permanent tide, which is a non-zero constant component of the above tides which nonetheless is not considered part of the static geopotential.
- Pole tides, which are due to the centrifugal effects of polar motion, which in turn is the movement of the Earth's body axis relative to the instantaneous axis of rotation.

4.2 Requirements for model selection and application

4.2.1 General requirements for gravity models

a. Gravity effects shall be included in all orbit determination and orbit prediction processes, and in attitude determination and prediction processes for Earth and planetary orbiters.

b. The inclusion of different gravity sources, their associated model details, and corresponding model truncation errors shall be compliant with the requirements on orbit and/or attitude determination accuracy, and they shall be at least of the same perturbation order as considered perturbing accelerations due to non-gravitational effects.

c. The retained accuracy level of a gravity model shall be compliant with the accuracy of the position and orientation of the central body.

NOTE Harmonic coefficients can lead to resonance effects, if they have a degree or order close to some integer multiple of the ground track repeat cycle. For orbits that are known to be repetitive, it is then recommendable to include discrete resonant harmonics of degrees that normally fall outside the truncated expansion series.

4.2.2 Selection and application of gravity models

a. For Earth orbits a gravity model shall be applied that fulfills the following:

1. The model is a global and static model
2. The model is based on Grace or GOCE data
3. The model is published at: http://icgem.gfz-potsdam.de/tom_longtime
4. The model is described by spherical harmonic coefficients up to at least degree and order of 70.

NOTE 1 For example the EIGEN-GLO4C model [RN.1] fulfills given requirements. It has a spatial resolution in latitude and longitude of 1° × 1° (corresponding to degree × order = 360 × 360).

NOTE 2 For other planetary environments no standard gravity model exists. Some information for Jupiter is provided in [RD.148].

b. Data on gravitational effects from tides and on Earth orientation parameters shall be obtained from the International Earth Rotation Service IERS given in [RN.2].

c. For third body gravitational perturbations the Development Ephemerides data on planets (DE-430) and the Lunar Ephemerides data (LE-430), both given in [RN.3], shall be used.

d. For planetary mass values the 2010 standards of the International Earth Rotation Services IERS, as described in IERS Technical Note 36 [RN.2], shall be used.

5
Geomagnetic fields

5.1 Introduction and description

5.1.1 The geomagnetic field and its sources

Within the magnetopause, the boundary between the influence of the solar wind and embedded IMF of solar origin, the near-Earth environment is strongly influenced by the geomagnetic field. The geomagnetic field is due to a variety of sources, those within the Earth, those within the ionosphere, and those within the magnetosphere.

The Earth's magnetic field is responsible for organizing the flow of ionized plasmas within most regions of the near-Earth environment. Hence, it determines the boundaries of distinct plasma regimes. The magnetic field is also used widely for attitude measurement and for important spacecraft sub-systems such as magneto-torquers.

5.1.2 The internal field

Under quiet solar and geomagnetic activity conditions, the magnetic field measured at the Earth's surface is primarily (>90%) due to a magneto-hydrodynamic dynamo, operating in the liquid outer core of the Earth. The secular (or time) variation of this field operates on a scale of months to centuries, or more, with position dependent amplitude of anywhere between zero and up to a few hundred nT $year^{-1}$. The core field morphology is closely dipolar, at least far from the Earth, and is inclined to the Earth's rotation axis by around 11 degrees at the present time (see Figure E-1).

Superimposed on this core field is the static magnetic field of geological sources in the lithosphere and upper mantle. Typically the field from these crustal rocks decays rapidly away from the source. For example, in low Earth orbit, the crustal signature is probably no more than about 20 nT, decaying rapidly with altitude.

Traditionally the combination of the core and crustal field is referred to as the 'main field'. The mean "main field" as measured at the Earth's surface is depicted in Figure E-1.

5.1.3 External field: ionospheric components

Currents flowing in the ionosphere induce an external magnetic field component. Sources of these currents include wind-driven motion of ionospheric plasma that produces a daily variation field known as *Sq* ('solar quiet'). This takes the form of two vortices, fixed north and south of the Sun-Earth line, on the dayside of the Earth, as the Earth rotates beneath. Along the geomagnetic equator an equatorial electrojet is formed, due to a high conductivity channel related to the near-horizontal field morphology. Below (or above) this electrojet the field amplitude can be enhanced by several hundred nT, within about five degrees i.e. a few hundred km of the magnetic equator.

At auroral latitudes (approximately 55-65 magnetic degrees), the auroral electrojet is formed at the open/closed field line boundary. This electrojet is fed by field-aligned currents that connect the ionosphere to the magnetospheric flanks and to the night-side tail and partial ring current sheet. The magnitude of the resulting induced fields is very dynamic and can be many hundreds of nT as observed at ground level or in low Earth orbit during periods of disturbed geomagnetic activity.

In the lower magnetosphere there are inter-hemispheric (field-aligned) currents of several nT at around 400 km altitude. Plasma 'bubbles' can also cause localised magnetic variations of a few nT to be measured by low-Earth orbit satellite altitudes. At high and polar latitudes the Earth's field is also open to the solar wind and cusp currents, also known as Region 0 currents flow.

5.1.4 External magnetic field: magnetospheric components

In the magnetosphere, there are several major current systems controlled by the interaction of the Earth's field with the solar wind. The strength of the total magnetospheric field is closely tied to solar and solar wind variations and to plasma outflow from the ionosphere. The major magnetospheric magnetic fields are a result of: magnetopause currents; cross-tail currents, and the symmetric and partial ring currents.

Magnetopause currents flow to shield the internal field from the IMF. And connect to a cross-tail current sheet that separates lobes of opposite magnetic polarity, extending hundreds of Earth radii down-wind from the Earth. An azimuthal drift of plasma (westward for ions, eastwards for electrons) around the Earth produces the symmetric ring current. The partial, or asymmetric, ring current is found on the dusk-side of the Earth and is closed via ionospheric currents. Figure E-2 provides the general morphology of model magnetospheric field lines, according to the Tsyganenko 1989 model [RD.111] showing the seasonal variation, dependent on rotation axis tilt. This figure shows a cut in the noon-midnight plane.

5.1.5 Models of the internal and external geomagnetic fields

The magnetic field is commonly modelled by expressing the field as a series of spherical harmonic terms. There has been much scientific activity in the field

modelling community and in source field reconstruction. This is due to several successful satellite magnetometer surveys, such as those of Ørsted, Champ and Swarm.

5.1.5.1 Models of the internal field

Scientific models of the internal field now extend to around spherical harmonic degree 100, equivalent to a minimum wavelength of 400 km at the Earth's surface. However the effective amplitudes of these high degree terms decrease rapidly with increasing altitude above the Earth's surface. The core field, which dominates for degrees less than about 14 at the Earth's surface, can be readily simplified to that of a simple inclined and offset dipole or a low-degree model for spacecraft operation above a few hundred km altitude.

Although they are by no means the only recognised high quality models, the IGRF models are products of the international community of geomagnetic scientists, updated on a five-year basis, assuming a linear secular variation between updates.

The descriptive annex to this Chapter (Annex E) describes in more detail the current revision of the IGRF, and further information on other internal field models.

5.1.5.2 Models of the external field

There are a number of dynamic models of the external field. These are typically either empirical (in the sense of a simplified mathematical model fit to measured data), analytic (based on physical models of the various external current systems), or magneto-hydrodynamic (or 'general circulation models'). Of the latter type, the science is rapidly evolving and whilst, in principle, they should fully capture the details of magnetospheric processes, such models are judged not yet mature enough to serve as a reliable standard.

Of those models that are currently maintained and updated in the light of new data and new field parameterisations, the model of Tsyganenko (revised repeatedly between 1987 and 2006 [RN.31] [RD.98] [RD.99] [RD.111] [RD.112]) is well used and is empirical in nature. The model of Alexeev *et al* (2001) [RN.30] is described as an analytic model. This model is at the core of an International Standards Organisation (ISO) standard external field model [RD.113].

The availability of suitable inputs to external models is a factor that affects whether they can be useful in common applications. *Alexeev et al (2001)* [RN.30] has inputs of date, time, solar wind density and velocity, and *Tsyganenko 1996* [RN.31]has inputs of solar wind pressure, Dst and IMF By and Bz components. *Tsyganenko 2002 to 2005* [RD.98] [RD.99] models require a more complex set of inputs.

Further discussion of these models and of their applications are dealt with in Annex E.

5.2 Requirements for model selection and application

5.2.1 The internal field

a. IGRF-12 [RN.29] [RN.38] shall be used as the Internal Geomagnetic Field Model.

NOTE As a stand-alone model, the inputs required of the IGRF-12 are either position in geodetic coordinates, according to the reference 'World Geodetic Service 84' standard ellipsoid, or position in a geocentric system, with respect to the centre of the Earth and for which the reference Earth radius is 6 371,2 km. The coordinates are therefore geodetic or geocentric latitude in decimal degrees, longitude (same in both coordinate systems), altitude in km above the reference ellipsoid, or distance in km from the centre of the Earth. Time is input in decimal years, e.g. 2 007,5. It is recommended that geocentric data are used, to avoid errors or confusion in respect of the reference ellipsoid.

b. If a different model is an inherent part of a specific space environment model, then that specific geomagnetic field model shall be used.

NOTE An example is the AE8 and AP8 radiation flux / belt models (see Clause 9)

5.2.1.2 Application

a. For times in the past and in the future, IGRF-12 shall be used, in association with its secular variations.

NOTE 1 IGRF-12 and future versions contain revisions of models of earlier epochs.

NOTE 2 Beyond 5 years from the assumed epoch (2015), the precision of the model is considerably reduced. IGRF-13 is expected to be issued for the epoch 2020, and can be used post 2019.

5.2.2 The external field

a. For modelling the average characteristics of the terrestrial magnetic field and its variation according to geomagnetic and solar activity, one of the following two external magnetic field models shall be used:

1. Alexeev et al 2001, [RN.30]
2. Tsyganenko 1996 [RN.31]

NOTE 1 These models are suitable for assessment of the mean and range of magnetic field strength; for estimation of B and L coordinates (but not for input to radiation belt models created with

different field models); and in calculation of geomagnetic shielding of cosmic rays and solar particles.

NOTE 2 Recently, external field models have been created (e.g. Tsyganenko 2001 [RD.98], 2004 [RD.99]) that are used in research environments for dynamic modelling of field variations, e.g. substorm development. These have the capacity to represent more accurately the instantaneous magnetic field, but are not given here as standards because the definition of inputs to the models is not reasonably achievable in an engineering environment.

5.3 Tailoring guidelines

a. <<deleted>>

b. <<deleted>>

Most engineering applications do not need the external-source model augmentation of these later Tsyganenko models. These are only useful for certain scientific magnetospheric missions, for instance if data on high latitude or high altitude variability of the fields with respect to local time and solar-geomagnetic activity was important.

6
Natural electromagnetic radiation and indices

6.1 Introduction and description

6.1.1 Introduction

A spacecraft in LEO receives electromagnetic radiation from three primary external sources. The largest source is the direct solar flux. The mean value of this solar flux at the mean Sun-Earth distance is called the "solar constant". It is not really a constant but varies by about 3,4 % during each year because of the slightly elliptical orbit of the Earth about the Sun. The two others radiation sources are the fraction of the incident sunlight reflected off the planet, termed albedo, and the Earth infrared radiation.

Solar and geomagnetic activities are often described by indices. The UV radiation of the Sun, which strongly affects the Earth atmosphere, cannot be directly measured from the ground. But it was found to be strongly correlated with e.g. the sunspot number and the cm wavelength Sun radiation. For example, the widely used 10,7 cm radio flux index (*F10.7*) gives an indication of the solar UV radiation output which is highly variable over a solar cycle.

Geomagnetic indices typically describe the variation of the geomagnetic field over a certain time period. They provide a measure of the disturbance of the magnetosphere which has direct consequences for the charged particle space environment, or the external component of the geomagnetic field.

Solar and geomagnetic indices are used as input for upper atmosphere and other models of the near Earth space environment. They are provided for short durations or as long time averages. Predictions for future index values are usually provided at different confidence levels and they are available for complete solar cycles. The given data are mainly average values. For detailed thermal analyses or certain special applications, more detailed data and models are required. These are outside the scope of this Standard.

6.1.2 Electromagnetic radiation and indices

6.1.2.1 Total Solar Irradiance (TSI)

The solar constant is defined as the radiation that falls on a unit area of surface normal to the line from the Sun, per unit time, outside the atmosphere, at one

astronomical unit (1 AU = average Earth-Sun distance). The currently measured 1-sigma standard deviation in the composite dataset is approximately 0,6 Wm-2 and there is a long-term (yearly) smoothed solar cycle minimum to maximum relative variation about the mean value of approximately 1,4 Wm-2 [RD.2] (largest during the period of maximum solar activity). The TSI value and one-sigma uncertainty are presently taken to be 1361 ± 0,5 W m^{-2} [RD.149]. In addition, the long-term (yearly) smoothed solar cycle minimum-to-maximum relative variation is approximately 1,3 W m^{-2}, with the (yearly) smoothed solar minimum value being approximately 1360,5 W m^{-2} and the smoothed solar maximum value being approximately 1362 W m^{-2} .

6.1.2.2 Solar spectrum

6.1.2.2.1 Soft X-rays or XUV (0,1 nm to 10 nm)

Usually associated with solar coronal phenomena, flares, million-degree temperatures, and atomic dissociation. The corona extends from about 21 000 km to 1 400 000 km above the photosphere. X-ray flares are responsible for enhancements in the D and E regions of the Earth's ionosphere.

6.1.2.2.2 Extreme ultraviolet or EUV (10 nm to 121 nm)

EUV has emission lines that come from the upper chromosphere (near-coronal temperatures), transition region, and lower corona. This spectral band is responsible for ionization and heating in the E and F regions of the ionosphere.

6.1.2.2.3 Ultraviolet or UV (100 nm to 400 nm)

UV solar flux is emitted primarily from the base of the sun's chromosphere layer, and has components due to active and quiet solar conditions. This band is responsible for only 1% of the total solar irradiance, but it is important because below 300 nm, it is completely absorbed by ozone and diatomic oxygen atoms in the earth's upper atmosphere.

6.1.2.2.4 Visible, optical or VIS (380 nm to 760 nm)

Visible light comes from the solar photosphere, which is only about 400 km thick, has a temperature of approximately 5 000 to 6 000 degrees Kelvin, and yet is responsible for the greatest percentage of the total solar radiation.

6.1.2.2.5 Infrared or IR (0,70 μm to 1 mm)

Solar infrared in this range is responsible for the direct heating of the Earth's lower atmosphere, through absorption by H_2O, and has an effect on minor species constituents in the Earth's mesosphere and thermosphere.

NOTE The ISO 21348 Standard on determining solar irradiances provides more details on the solar spectrum [RD.3].

6.1.2.3 Indices

6.1.2.3.1 General

Solar and geomagnetic indices are used to describe the activity levels of the Sun and the disturbance of the geomagnetic field. Most activity indices are given for

short periods and as long duration averages. They are also used for long range predictions of solar activities. Many space environment models require activity index values as input parameters.

6.1.2.3.2 Solar activity indices

- **Sunspot number (R)**

  The sunspot number (R, alternatively called Ri or Rz) is a daily index of sunspot activity, defined as

  $$R = k(10g + s)$$

  where

  s is the number of individual spots,

  g the number of sunspot groups, and

  k is an observatory factor.

  NOTE R12 (Rz12) is the 12-month running mean of the sunspot number R.

- **F10.7**

  F10.7 (abbreviated F10) is the traditional solar energy proxy that is used both for NRLMSISE-00 [RN.4] and JB-2006 [RN.5] atmosphere models. It corresponds to the solar radio flux emitted by the sun at 2 800 MHz (10,7 cm wavelength).

  NOTE The physical units of *F10.7* are 10^{-22} $Wm^{-2}Hz^{-1}$; the numerical value is used without the multiplier as is customarily done and expressed as solar flux units (sfu). In other words, a 10,7 cm radio emission of $150x10^{-22}$ W $m^{-2}Hz^{-1}$ is simply referred to as *F10.7* = 150 sfu.

  F10.7 and the sunspot number, *R*, are correlated. Averaged (over one month or longer) values can be converted by the following expression:

  $$F10.7 = 63{,}7 + 0{,}728R + 8{,}9 \times 10^{-4}R^2 \quad (6\text{-}2)$$

- **S10.7**

  S10.7 (abbreviated S10) [RD.122] is a solar energy proxy that is used for the JB-2006 and JB-2008 atmosphere model [RN.5] It is measured by SOHO with the Solar Extreme-ultraviolet Monitor (SEM) in the 26–34 nm solar EUV range, and normalized using a mean value of $1{,}9955x10^{10}$ photons $cm^{-2}s^{-1}$. It is expressed in sfu, as *F10.7*.

- **M10.7**

  M10.7 (abbreviated M10) [RD.122] is a solar energy proxy that is used for JB-2006 and JB-2008 atmosphere model. It is measured by NOAA 16 and NOAA 17 operational satellites with the Solar Backscatter Ultraviolet (SBUV) spectrometer. It is a measure of chromospheric and some photospheric solar active region activity and is expressed in sfu, as *F10.7* and *S10.7*.

- **IG12**

  IG12 [RD.147] is a solar activity index derived from the monthly mean noon f0F2 data available from thirteen ionospheric observations. The IG index has been confirmed as an alternative to sunspot number when predictions of f0F2 are being prepared with the aid of the CCIR atlas of ionospheric characteristics. IG12 is used for the IRI-2016 ionospheric model.

- **Solar wind speed**

  The solar wind speed is used in external magnetic field model computation. It is the outward flux of solar particles and magnetic fields from the sun. Typically, solar wind velocities are near 468 km s^{-1}.

6.1.2.3.3 Geomagnetic activity indices

Geomagnetic activity indices are used to describe fluctuations of the geomagnetic field.

- **Kp and a_p**

  Most widely used planetary indices are K_p and a_p. They are based on 3-hour measurements from 13 ground stations. Values of a_p range from 0 to 400 and are expressed in units of 2 nT. K_p is essentially the logarithm of a_p, its scale is 0 to 9 expressed in thirds of a unit, e.g. 5- is 4 2/3, 5o is 5 and 5+ is 5 1/3.The conversion from K_p to a_p is given in Table 6-1 (taken from [RD.100]. A daily index, A_p, is obtained by averaging the eight values of a_p for each day. The index A_p can have values intermediate to those of a_p.

- **Dst**

  Dst (Disturbance Storm Time) is a geomagnetic index used in external magnetic field model computation. It describes variations in the equatorial ring current and is derived from hourly scalings of low-latitude horizontal magnetic variation. It is expressed in nT.

- **IMF**

  IMF (Interplanetary Magnetic Field) is a geomagnetic index used in external magnetic field model computation. It corresponds to the part of the Sun's magnetic field that is carried into interplanetary space by the solar wind. The three orthogonal components of the IMF are *Bx*, *By* and *Bz*. *Bx and By* are oriented parallel to the ecliptic.

  The *IMF* is a weak field, varying in strength near the Earth from 1 to 37 nT, with an average value of about 6 nT.

6.2 Requirements

6.2.1 Electromagnetic radiation

a. <<deleted>>

b. The solar spectrum shall be approximated by a black body curve with a characteristic temperature of 5 778K.

c. A space sink temperature of 3 K shall be used.

6.2.2 Reference index values

a. For daily and 81-day averaged values of F10.7, S10.7 and M10.7 the values given in Table A-1 shall be used.

NOTE 1 A_p is only weakly correlated with the solar activity indices. It has a seasonal variation and is higher at the equinoxes.

NOTE 2 81 days corresponds to 3 solar rotations and 81 day averaged values are used as input for atmosphere models.

NOTE 3 Alternative daily and 81-day average values and forecast methods are available [ISO 27852:2016]. Their values can be more appropriate depending on the use-case.

b. For fixed index values, the numbers given in Table 6-3 for low, moderate and high solar and geomagnetic activities shall be used:

1. The long-term values are averaged values for periods longer than 27 days.
2. The long-term values apply as well for periods of 1 week or longer.
3. The short-term values are daily values.

c. The temporal evolution in a_p shown in Table 6-4 shall be used to describe the worst case fluctuations during successive three-hour intervals for a total duration of 24 hours.

d. The a_p values of Table 6-4 shall be used together with the relevant (low, moderate or high) long term averaged values of F10.7, S10.7 and M10.7 given in Table 6-3.

6.2.3 Tailoring guidelines

a. For design purposes the "worst-case" activity values given in Table 6-3 may be used.

NOTE These can be the high or low values, depending on the effect to be studied.

b. All worst-case values shall be used without any additional margin.

c. The values given in Table A-1 shall be used:

1. for applications that require a realistic sequence of index values for future predictions, for example orbital calculations using index-driven atmospheric models;
2. for a given specific phase of the respective solar activity cycle.

d. <<deleted>>

6.3 Tables

Table 6-1: Conversion from K_p to a_p

K_p	0	0+	1-	1o	1+	2-	2o	2+	3	3o	3+	4-	4o	4+
a_p	0	2	3	4	5	6	7	9	12	15	18	22	27	32
K_p	5-	5o	5+	6-	6o	6+	7-	7o	7+	8-	8o	8+	9-	9o
a_p	39	48	56	67	80	94	111	132	154	179	207	236	300	400

Table 6-2: Electromagnetic radiation values

Total Solar Irradiance (at 1 AU)	1 361 W m^{-2}
Solar energy flux at aphelion	1 316 W m^{-2}
Solar energy flux at perihelion	1 407 W m^{-2}
NOTE The solar constant, a historical term, is not constant. It varies geometrically with the Earth's distance from the Sun and physically with the Sun's magnetic field activity on short to long timescales. The value of 1 361±0,5 W m^{-2} is the current value agreed upon by the International Astronomical Union (IAU).	

Table 6-3: Reference fixed index values

	Long-term (27+ days)			Short-term (daily)		
	Low	**Moderate**	**High**	**Low**	**Moderate**	**High**
F10.7	65	140	250	65	140	300
S10.7	60	125	220	60	125	235
M10.7	60	125	220	60	125	240
A_p	0	15	45	0	15	240

NOTE 1 The reference index values are rounded numbers from the last solar cycle 23.
NOTE 2 Low, moderate or high values for A_p can occur at any time in the solar cycle.
NOTE 3 For short terms, higher values than those given in this table have been measured (e.g. F10.7 = 380 over a day and a_p= 400 for 3 hours). However, present atmosphere models are not developed for such high index values and its use leads to large and unknown errors.

Table 6-4: Reference index values for variations of ap

Time [hrs]	a_p
0	15
3	15
6	300
9	130
12	50
15	15
18	15
21	15
24	15

7
Neutral atmospheres

7.1 Introduction and description

7.1.1 Introduction

A good knowledge of temperature, total density, concentrations of gas constituents and pressure is important for many space missions exploiting the low-earth orbit regime (LEO), below approx. 1 000 km altitude. Aerodynamic forces on the spacecraft, due to the orbital motion of a satellite through a rarefied gas which itself can have variable high velocity winds, are important for the combination of planning satellite lifetime, for the maintenance of orbits, for sizing the necessary propulsion system, for the design of attitude control system, and for estimating the peak accelerations and torques imposed on sensitive payloads.

Surface corrosion effects due to the impact of large fluxes of atomic oxygen are assessed to predict the degradation of a wide range of sensitive coatings of spacecraft and instruments. The reactions of atomic oxygen around a spacecraft can also lead to intense “vehicle glow”.

7.1.2 Structure of the Earth’s atmosphere

The Earth atmosphere can be broadly divided into three distinct regimes:

- The homosphere which comprises the regions of the troposphere (surface up to ~ 10 - 12 km altitude), the stratosphere (~ 10 - 12 km up to 50 km), and the mesosphere (~50 km up to about 90 km);
- The thermosphere which extends from about 90 km altitude to approx. 400 km (depending on solar and geomagnetic activity levels);
- The exosphere which extends from the top of the thermosphere and extends into space.

More information on these three regions can be found in Annex G.

7.1.3 Models of the Earth’s atmosphere

7.1.3.1 NRLMSISE-00 model

The NRL Mass Spectrometer, Incoherent Scatter Radar Extended Model (NRLMSISE-00) model [RN.4] describes the neutral temperature and species densities in Earth's atmosphere.

It is based on a very large underlying set of supporting data from satellites, rockets and radars, with extensive temporal and spatial distribution. It has been extensively tested by the global scientific community against experimental data. The model has a flexible mathematical formulation.

It is valid for use from ground level to the exosphere.

Two indices are used in this model:

- *F10.7* (both the daily value of the previous day and the 81-day average centred on the input day),
- A_p (daily value).

7.1.3.2 JB-2006 model

The Jacchia-Bowman 2006 (JB-2006) model [RN.5] also describes the neutral temperature and the total density in Earth's thermosphere and exosphere. Its new features, described in Annex G, lead to a better and more accurate model representation of the mean total density, compared with previous models, including the NRLMSISE-00.

It is valid for use from an altitude of 120 km to the exosphere.

Four indices are used in this model:

- *F10.7* (both tabular value one day earlier and the 81-day average centred on the input time),
- *S10.7* (both tabular value one day earlier and the 81-day average centred on the input time),
- *M10.7* (both tabular value five days earlier and the 81-day average centred on the input time),
- A_p (tabular value 6,7 hours earlier).

7.1.4 Wind model of the Earth's homosphere and heterosphere

The Horizontal Wind Model (HWM) is a comprehensive empirical global model of horizontal winds in the mesosphere and thermosphere (middle and upper atmosphere). The HWM07 model [RN.40] is based on accumulated measurements made using a variety of observational techniques, including satellite, radar, and ground-based optical remote sensing. The model is used to provide the necessary winds, accounting for time, space and geophysical variations, for many ionospheric, dynamical, and aeronomical calculations It provides meridional (+ northward) and zonal (+ eastward) speed and covers all altitude regions.

Two indices are used in this model:

- *F10.7* (both the daily value of the previous day and the 81-day average centred on the input day),
- A_p (daily value).

7.2 Requirements for atmosphere and wind model selection

7.2.1 Earth atmosphere

7.2.1.1 General

a. The NRLMSISE-00 model [RN.4] shall be used for calculating the neutral temperature, the total density and the detailed composition of the atmosphere.

b. The JB-2006 model [RN.5] or JB-2008 model [RN.39]may be used for calculating the total atmospheric density above an altitude of 120 km.

c. <<deleted>>

7.2.1.2 Application guidelines

a. The NRLMSISE-00 model for species densities shall not be mixed with the JB-2006 model for total density.

b. For worst case high results and analysis periods not exceeding 1 week high daily short-term values given in Table 6-3 shall be used as input for daily activity together with the high long-term values for the 81-day average activity.

c. For analysis periods longer than 1 week the long term activities given in Table 6-3 shall be used as input for both, the daily and the 81-day averaged values.

d. For analysis periods longer than 1 week and conditions specified in 6.2.3c, the daily and 81-day averaged solar activities given in Table A-1 shall be used.

e. Short-term daily high solar activity values shall not be used together with low or moderate long-term solar activity values.

NOTE 1 Both models can only predict large scale and slow variations, on the order of 1 000 km (given by the highest harmonic component) and 3 hours. Spacecraft can encounter density variations with smaller temporal and spatial scales partly since they are in motion (for example, +100% or -50% in 30 s), and partly because smaller-scale disturbances certainly occur during periods of disturbed geomagnetic activity.

NOTE 2 Reference values for the key indices needed as inputs for the atmosphere models are given in Clause 6.

NOTE 3 The F10.7 81-day average activity can also be estimated by averaging three successive monthly predicted values.

NOTE 4 Information on density model uncertainties can be found in G.5 and in [RN.4] and [RN.5].

NOTE 5 For high activities the atmosphere models only give realistic results if high short term values are combined with high 81-day averaged values.

NOTE 6 High Ap values can be used with low, moderate or high solar activities.

7.2.2 Earth wind model

a. The HWM-07 model [RN.40] shall be used.

b. High daily short-term values shall be used as worst-case for the daily activity but the 81-day average activity shall not exceed the high long-term value.

NOTE 1 Reference values for the key Indices needed as inputs for the wind model are given in Clause 6.

NOTE 2 The F10.7 81-day average activity can also be estimated by averaging three successive monthly predicted values as given in Clause 6.

NOTE 3 The use of the HWM-93 model at high geomagnetic latitudes and for disturbed geomagnetic periods necessitates caution.

c. As an alternative to the model specified in 7.2.2a, the HWM-93 model [RN.6] may be used.

7.2.3 Models of the atmospheres of the planets and their satellites

a. For the Martian Atmosphere, the Martian Climate Database [RN.7] shall be used.

NOTE 1 No specific models are imposed for the other planets and their satellites.

NOTE 2 International Reference Atmospheres have been adopted for Mars (MIRA) and Venus (VIRA). There have also been major advances in the case of the atmospheres of Jupiter, Saturn, Neptune and Titan. This is a matter of ongoing work. Considerable work has also been performed for the atmosphere of Mercury.

NOTE 3 Additional information on Planetary Atmospheres is provided in Annex G.

8
Plasmas

8.1 Introduction and description

8.1.1 Introduction

All spacecraft, once they exceed about 60 km in altitude during the day or around 80 km at night, are exposed to the charged particles of the space plasma environment. These particles interact with and are collected by the surface materials of a spacecraft and change the electric fields on and around it. Of the continuum of charged particles of all energies, those below 50 keV are generally regarded as plasma and are covered in this clause. Higher energy particles are covered in the radiation environment clause (clause 9).

Within the magnetosphere, plasma flows almost freely up and down magnetic field lines but only slowly across it. Hence, two spacecraft observe similar plasmas if they are on the same field line, even if far apart. These spacecraft share the same *L*-shell and magnetic local time.

A brief overview of the effects of the plasma environment is given in Annex H.2. Requirements for design, analysis and testing of spacecraft, concerning the effects of plasma on spacecraft systems are described in a parallel standard ECSS-E-ST-20-06 (Spacecraft Charging).

8.1.2 Ionosphere

The ionosphere is the ionized plasma in the upper atmosphere, produced by the dissociation of atmospheric atoms. It is generally divided into layers D, E and F1 at low altitudes and F2 at higher altitude. The low altitude layers are significant only during daylight hours. F2 is permanent and the densest, peaking at around 300 km altitude. For most space applications, it is the electron density which is the most important characteristic. Immediately above the F2 peak, density falls off nearly exponentially with height. At mid to low latitudes, the density fall-off slows down at higher altitudes as the magnetic field traps plasma to form the plasmasphere.

Intense auroral charging environments are associated with discrete aurorae which are generally found between 60 and 77 degrees magnetic latitude. However, at times of enhanced geomagnetic activity, the auroral zone is moved southwards. In this region, ionospheric density can become irregular on the scale of metres to kilometres vertically and metres to hundreds of kilometres horizontally. The energetic electrons have energies of 10s of keV. Plasma

density in this region can suddenly increase by a factor of up to 100 during magnetically active periods.

In the Polar Cap, typically above 70° latitude, there is a strong winter-summer asymmetry because of the tilt of the Earth,. Strong drift motion occurs due to electric fields. In winter, density is maintained by this drift and by "polar rain", a weak electron flux from the solar wind with energy around 100eV. When both these processes are depressed, ionospheric density in this region can become very low.

Ionospheric plasma characteristics are expressed in the International Reference Ionosphere (IRI) [RN.9]. IRI is an empirical model based on a large volume of ground and space data. IRI describes monthly average conditions but can be updated to time-specific conditions using measured characteristic parameters, e.g., F-peak density and height, if these are available. This model calculates densities, temperatures and composition in the altitude range 60 to 2000 km. Auroral boundaries are part of the model but the auroral populations are currently not modelled in IRI-2016. The model describes the densities of O^+, H^+, He^+, NO^+, O_2^+, N^+, and Cluster ions. External drivers for the IRI model are the sunspot number and the ionospheric index IG; in both cases the 12-month running mean of the index is used.

8.1.3 Plasmasphere

The plasmasphere is a region of cold dense plasma originating in the ionosphere and trapped by the Earth's magnetic field. At low *L*-shells, the particles drift around the Earth on closed drift paths. This allows ions, escaping from the ionosphere, to accumulate to form this dense region. The boundary between closed and open drift paths is highly variable and the outer regions of the plasmasphere are continually being lost and refilled over a period of days. Typically, the plasmapause, the outer edge of the plasmasphere, lies at an *L*-shell (3.2.27) of 3 to 6, with a bulge in the dusk region of magnetic local time.

The Global Core Plasma Model (GCPM) [RN.8] is a widely used and well tested plasmasphere model and is recommended by the authors of IRI. It provides empirically derived plasma density as a function of geomagnetic conditions throughout the inner magnetosphere. Another plasmasphere model that it designed to complement the IRI model is IRI-PLAS [RD.167].

8.1.4 Outer magnetosphere

Beyond the plasmapause, the magnetospheric plasma environment is characterized by high temperatures and low densities. This region usually encompasses the geostationary orbit. The location of the outer boundary of this region, the magnetopause, is controlled by the balance between the ram pressure of the flowing solar wind and the magnetic pressure of the terrestrial magnetic field. See Annex H.3.4 for further discussion of the magnetopause position.

During active periods, large amounts of magnetic energy are injected into the plasma in this region. These are called magnetic storms and substorms and are detectable on the ground as magnetic disturbances at certain latitudes. Hence there is a strong link between hot plasma and high values of the magnetic index K_p.

8.1.5 Solar wind

The solar wind is part of the Sun's outer atmosphere, expanding outwards and carrying the solar magnetic field with it. Solar wind velocity near the Earth is commonly around 468 km s^{-1} but with frequent high-speed streams with velocities around 700 km s^{-1} and sometimes beyond 1 000 km s^{-1}. Earth-orbiting satellites and those in L1 and L2 see solar wind fluctuations at different times but otherwise do not observe noticeable differences in solar wind characteristics.

On average, the solar wind is made up mostly of protons (95%), with 4% alpha particles and around 1% minor ions, of which carbon, nitrogen, oxygen, neon, magnesium, silicon and iron are the most abundant [RD.5].

In interplanetary space, solar wind average density varies, to a good approximation with r^{-2} (where r is radial distance from the Sun) in the range ±40 degrees solar latitude. The average electron temperature has been seen to vary as $r^{-0,64}$ for r between 1,52 to 2,31 AU. Ion velocity does not show a significant radial variation.

8.1.6 Magnetosheath

Near the magnetopause the solar wind is slowed, compressed, heated and deflected by the 'bow shock'. This typically lies 3 R_E upstream of the magnetopause on the Earth-Sun line. The diameter of the bow shock perpendicular to the Earth-Sun axis increases in the anti-sunward direction so that around L2 (236 R_E downstream) it is around 100 R_E in radius. The region between the bow shock and the magnetopause is called the 'magnetosheath'.

8.1.7 Magnetotail and L2

Although the Earth's magnetosphere extends typically out to 10 R_E in the sunward direction, it extends to at least 500R_E in the anti-sunward direction. This downstream region of the magnetosphere is called the magnetotail.

Beyond about 30 R_E, the magnetotail becomes cylindrical with radius virtually independent of distance from the Earth (around 15 to 30 R_E in radius depending on solar wind pressure). It does not point directly anti-sunwards but swings according to solar wind velocity components up to about 10 degrees from the Earth-Sun line in both the ecliptic plane and perpendicular to it. The mean deflection with respect to the Earth-Sun line is about 4 degrees.

Within the magnetotail, there are somewhat different plasmas, with hotter plasma (the plasma sheet) around the ecliptic plane and the cooler plasma (the lobes/mantle) north and south of it [RD.117]. Although these are magnetically linked to regions near the Earth, populated with ions of ionospheric and solar wind origin respectively, in this region virtually all ions are of solar wind origin [RD.6] and the differences in density and temperature are not as strong as near the Earth.

The second Earth-Sun Lagrange point is in the anti sunward direction, some 1,5 million km from the Earth, in the deep magnetotail (the Moon's orbit has a semi-major axis of about 0,385 million km and also provides some ions to the deep tail environment).

8.1.8 Planetary environments

Whenever planets have strong magnetic fields that exclude the solar wind from around the planet, there is the possibility of plasma being trapped in a similar way to the plasma in the Earth's magnetosphere. Jupiter and Saturn, in particular, have large magnetic fields and larger magnetospheres than that of the Earth.

8.1.9 Induced environments

The natural plasma environment can be augmented by a number of sources inside or on the satellite surface, such as photo-emission, outgassing and electric propulsion systems.

8.2 Requirements for model selection and application

8.2.1 General

a. Applicable plasma regions that can be encountered shall be identified according to the spacecraft location or orbit as follows:

   1. The ionosphere for altitudes between 60 km and 2 000 km.
   2. The auroral charging environment for orbital inclinations above 50 degrees for altitudes above 80 km and below 2 000 km.
   3. The plasmasphere for altitudes above 2 000 km (approximately *L=1,3* at the equator) and below *L=7*.
   4. The outer magnetosphere for all *L* values above *L=3* and within the magnetopause as defined in clause 5, (including the geostationary regime).
   5. The magnetosheath for locations outside of the magnetopause as defined in clause 5 and within the bow shock.
   6. The solar wind for locations outside of the magnetopause and bow shock.
   7. The magnetotail and distant magnetosheath for locations within the bow shock but more than 30 R_E from the Earth in the anti-Sunward direction.
   8. Planetary plasma environments for regions within the planetary bow shock, or planetary magnetopause, or planetary ionopause, whichever of these are present.

      NOTE 1 See Annex E.5 for definition of *L* (L-shell).

      NOTE 2 Some typical orbits and regions encountered are described in Annex H

b. Applicable environments for each region shall be characterised according to the models specified in 8.2.2 to 8.2.6.

8.2.2 Ionosphere

a. For the ionospheric environment, the International Reference Ionosphere 2016 (IRI-2016) [RN.9], shall be used.

b. Inputs to the IRI-2016 model, shall be:

1. choice of geographic or geomagnetic coordinates;
2. latitude;
3. longitude;
4. date;
5. local or universal time;
6. altitude (start and end of range and step size).

c. Other inputs shall be the default solar and geomagnetic index values for dates up to 2018 or later periods if available from irimodel.org .

NOTE This means that Sunspot number Rz12, IG12 (see 6.1.2.3.2), F10.7 and a_p data are taken from default files.

d. For future dates not covered by the default files, for F10.7 and a_p the activity indices defined in clause 6 and corresponding values for IG12 and Rz12 shall be used.

NOTE Information on the accuracy of the IRI-2016 model and typical ionospheric density profiles are given in Annex H.3.1

8.2.3 Auroral charging environment

a. For auroral charging assessment, the following worst-case electron distribution function shall be used.

1. For E ≤17,44 keV:

$$f(v) = 3{,}9 \times 10^{-18} \quad s^3 m^{-6} \tag{8-1}$$

2. For E > 17,44:

$$f(v) = \frac{[N_0 (m_e)^{3/2} \exp\{-(E - E_0)/kT_0\}]}{(2\pi kT_0)^{3/2}} \tag{8-2}$$

where

$f(v)$ is the distribution function in $sec^3\ m^{-6}$

N_0 is the density in m^{-3}

m_e is the electron mass in kg

kT_0 is the thermal energy in J

E_0 is in J

E is energy in J

and parameters of the worst case environment are:

N_0 = 1,13E6 m^{-3}

kT_0 = 3,96 keV

E_0 = 17,44 keV

NOTE This comes from [RD.7] and is based on work described in [RD.8]. Unfortunately, it is printed in [RD.7] with a typographical error.

b. For worst case auroral charging assessments, a thermal ion density of 125 cm^{-3} and temperature 0,2 eV shall be used.

NOTE This low ion density comes from a severe charging case seen on the DMSP spacecraft by [RD.9]. Measuring ionospheric thermal ion density during a strong charging event is potentially prone to errors because of the way the charged satellite alters ion trajectories, so there is high a degree of uncertainty in this measurement but there is currently no better information..

c. A Maxwellian fit to the auroral electron distribution specified in 8.2.3a may be usedwith temperature 11keV and density 1.1e7m-3 [RD.168]

d. The worst case environments specified in 8.2.3a, 8.2.3b and 8.2.3c shall be applied for 10s.

8.2.4 Plasmasphere

a. The plasma parameters representing the terrestrial plasmasphere should be taken from the Global Core Plasma Model (GCPM) [RN.8].

NOTE 1 Profiles of typical plasmasphere densities versus altitude are given in Annex H.3.3.

NOTE 2 Outputs are densities of electrons, protons, helium ions and oxygen ions. Input parameters are: time, geocentric radial distance, solar magnetic local time, solar magnetic latitude and *Kp* index.

b. For spacecraft charging assessments, *Kp=9* shall be used to represent a worst case situation.

NOTE This is because the plasmasphere is a moderating influence on spacecraft charging, and so the worst case is considered to be when the plasmasphere is small which occurs when geomagnetic activity is high.

c. As an alternative to the model specified in 8.2.4a, the IRI-Plas model may be used [RD.167]

8.2.5 Outer magnetosphere

a. For assessment of surface charging, the worst-case environment listed in Table 8-1 shall be used as input to a spacecraft charging simulation or calculation, applicable to the outer magnetosphere environment.

NOTE 1 This is a dynamic region in terms of plasma density and temperature and for most engineering purposes, worst-case environments are the most important consideration. See Annex H.3.4 for typical plasma parameters in this region.

NOTE 2 See Annex H.3.4 for some other worst-case environments

8.2.6 The solar wind (interplanetary environment)

a. For calculation of engineering effects due to the solar wind, a flowing Maxwellian distribution shall be used, with density and temperature given in Table 8-2.

b. Spacecraft in L1 and L2 shall be considered to experience the same mean and range of plasma parameters in the solar wind as at the Earth.

NOTE Because the solar wind flows through the near-Earth interplanetary medium with negligible modification (unless it encounters the bow shock), the mean and range of plasma density and temperature can be considered spatially uniform in the vicinity of 1AU. However, variations in plasma at the Earth are seen at L1 and L2 between approximately 30 and 90 minutes earlier or later, respectively.

c. A r^{-2} variation shall be used to map the mean and range of solar wind density to other locations in the heliosphere in the ecliptic plane, where r is heliocentric distance.

d. A $r^{-0,64}$ variation shall be used to map the mean and range of the electron temperature to other locations in the heliosphere in the ecliptic plane.

e. The ion temperature and composition shall be assumed to be the same as near the Earth.

8.2.7 Other plasma environments

8.2.7.1 Magnetosheath

Magnetosheath plasma parameters differ according to the latitude and local time of the observation. No standard models for magnetosheath plasma characteristics are defined but typical values can be found in Annex H.3.5.

8.2.7.2 Magnetotail,distant magnetosheath and L2

No standard model for the magnetotail and distant magnetosheath are defined. Typical plasma parameters that can be encountered in the magnetotail and distant magnetosheath around the L2 point are given in Annex H.3.6.

8.2.7.3 Planetary environments

No standard models are defined for planetary environments because information in these regions is still quite limited. Information relevant to worst case charging environments around Jupiter and Saturn are described in Annex H.3.7.

8.2.7.4 Induced environments

There are no standard models related to plasma created by spacecraft surface interactions but information on the calculation of induced environment parameters is given in Annex H.3.8.

8.2.8 Tables

The values in Table 8-1 is a double-Maxwellian fit to an extremely severe event observed by the SCATHA spacecraft on 24 April 1979 [RD.114], when the spacecraft charged to -8 kV in sunlight. The values in Table 8-2 are taken from [RD.10]. Note that although the listed ion and electron densities are not equal, electrical neutrality is maintained by less energetic plasma which is not involved in the charging process and so not stated.

Table 8-1: Worst-case bi-Maxwellian environment

	Electron density (cm^{-3})	Electron temperature (keV)	Ion density (cm^{-3})	Ion temperature (keV)
Population 1	0,2	0,4	0,6	0,2
Population 2	1,2	27,5	1,3	28,0

Table 8-2: Solar wind parameters

Parameter	Mean	5-95 % Range
Speed ($km\ s^{-1}$)	468	320 - 710
Density (cm^{-3})	8,7	3,2 - 20
T_P (K)	$1{,}2 \times 10^5$	1×10^4 - 3×10^5
T_e (K)	$1{,}0 \times 10^5$	9×10^4 - 2×10^5
N_{alpha}/N_{proton}	0,047	0,017 - 0,078

9
Energetic particle radiation

9.1 Introduction and description

9.1.1 Introduction

Energetic charged particles with energies in the MeV range and above are encountered throughout the Earth magnetosphere, in interplanetary space, and in the magnetospheres of other planets [RD.12].

At pre-phase A, radiation environments are an element in trade-offs for orbit selection. Effects on both the payload and on the spacecraft carrier are considered.

A radiation environment specification for a mission is established wherein all types of radiation are considered, reflecting general and mission-specific radiation susceptibilities; this specification is then used for component selection, material effects and shielding optimisation.

For radiation analysis, there are general models and models more specific to particular orbits, such as geostationary orbits.

9.1.2 Overview of energetic particle radiation environment and effects

9.1.2.1 Radiation belts

Energetic electrons and ions are magnetically trapped around the Earth forming the radiation belts, also known as the Van Allen belts. The radiation belts extend from 100 km to 65 000 km and consist principally of electrons of up to a few MeV energy and protons of up to several hundred MeV energy. The high energy particle flux in the radiation belts is dependent on the solar activity. The so-called South Atlantic anomaly is the inner edge of the inner radiation belt encountered in low altitude orbits. The offset, tilted geomagnetic field brings the inner belt to its lowest altitudes in the South Atlantic region. More information can be found in references [RN.10] and [RN.11].

9.1.2.2 Solar energetic particles

Solar Energetic Particles (SEP) are high-energy particles that are encountered in interplanetary space and close to the Earth. These particles are seen in short duration bursts associated with other solar activity. Solar Energetic Particle

Events, as detected in Earth orbit, can last from a few hours to several days. The Earth's magnetic field provides a varying degree of geomagnetic shielding of near-Earth locations from these particles. They consist of protons, electrons and heavy ions with energies from a few tens of keV to GeV ranges ——and can originate from two processes: energisation in association with activity seen on the solar disk e.g. flaring, or by shock waves associated with Coronal Mass Ejection (CMEs) as they propagate through the heliosphere. They are of interest and importance because they can endanger life and electronics in outer space (especially particles exceeding some tens of MeV). Solar protons are the principle contributors to non-ionising dose effects in components at GEO and in interplanetary space, they are also the primary source of ionising dose for interplanetary missions and can cause sensor interference. Solar heavy ions are of particular interest and importance because they can endanger life and electronics in outer space (especially particles exceeding some tens of MeV). Solar electrons can be significant for certain applications and effects such as sensor interference and internal charging.

9.1.2.3 Galactic cosmic rays

Galactic cosmic rays (GCR) are high-energy charged particles that enter the solar system from the outside, the flux of which becomes modulated in anti-correlation with solar activity due to the solar wind. They are composed of protons, electrons, and fully ionized nuclei. There is a continuous and isotropic flux of Galactic Cosmic Ray (GCR) ions. Although the flux is low, a few particles $cm^{-2}s^{-1}$, GCRs include energetic heavy ions which can deposit significant amounts of energy in sensitive volumes and so cause problems to spacecrafts' electronics and humans in space. As for Solar particles, the Earth's magnetic field provides a varying degree of geomagnetic shielding of near-Earth locations from these particles.

9.1.2.4 Geomagnetic shielding

The Earth's magnetic field partially shields near-Earth space from solar energetic particles and cosmic rays, an effect known as geomagnetic shielding. However, these particles can easily reach polar regions and high altitudes such as the geostationary orbit. Geomagnetic shielding of ions at locations or on spacecraft trajectories is computed by considering locations or trajectories in geomagnetic *B*, *L* space.

9.1.2.5 Other planets

The above environments are common to planets other than the Earth. Jupiter, Saturn, Uranus and Neptune have strong magnetic fields inducing severe radiation environments in their radiation belts. Mercury has a small magnetosphere which may lead to transient radiation belts. The other planets (Mars, Venus) have no trapped radiation. Missions to them are only exposed to GCR and SEP.

No normative model is specified for the radiation environment at other planets. Some information on planetary radiation environments is provided in Annex I.7.

9.1.2.6 Neutrons

Neutrons are ejected by the Sun. They decay rapidly in the interplanetary medium, and only a few can reach the Earth. They are important for missions close to the Sun.

When highly energetic charged particles strike the earth's upper atmosphere they create secondary particles throughout the atmosphere including very significant fluxes of neutrons. Of these, some are emitted back into space as atmospheric albedo neutrons of between 0,1 and 2,2 $cm^{-2}s^{-1}$, depending on the geomagnetic latitude and the phase of the solar cycle, and these can be significant where there is a specific susceptibility, such as in human spaceflight or with sensitive detectors. Model results for albedo neutron spectra are given in Annex I.

For some planetary environments, such as Mars, the secondary neutrons from cosmic ray and solar proton interactions with the atmosphere and regolith become a relevant contributor, in particular for human missions.

9.1.2.7 Secondary radiation

Secondary radiation is generated by the interaction of the above environmental components with materials of the spacecraft. A wide variety of secondary radiations are possible, of varying importance. The ECSS-E-ST-10-12 standard deals with these sources of radiation. Secondary neutrons are important for human missions and also play a role in generating background in sensitive detector systems.

9.1.2.8 Other radiation sources

Other sources of radiation include emissions from on-board radioactive sources such as in instrument calibration units, Radioisotope Thermo-electric Generator (RTG) electrical power systems and Radioisotope Heating Units (RHU). Any use of reactor power sources provide intense fluxes of neutrons and gamma rays.

9.1.2.9 Effects survey

The above radiation environments represent important hazards to space missions. Energetic particles, particularly from the radiation belts and from solar particle events cause radiation damage to electronic components, solar cells and materials. They can easily penetrate typical spacecraft walls and deposit doses of hundreds of kilorads (1 rad = 1 cGy) during missions in certain orbits.

Radiation is a concern for manned missions. The limits of acceptable radiological dose for astronauts, determined to ensure as low as reasonably achievable long-term risk, is indicated in ECSS-E-ST-10-12. There are many possible radiation effects to humans, beyond the scope of this document. These are described in . Heavy ions and neutrons are known to cause severe biological damage, and therefore these contributions receive a heavier weighting than gamma radiation. The "quality factors", as they are called, are established by the International Commission on Radiological Protection [RD.13].

Energetic ions, primarily from cosmic rays and solar particle events, lose energy rapidly in materials, mainly through ionization. This energy transfer can disrupt or damage targets such as a living cell, or a memory element, leading to Single-event Effect (SEE) in a component, or an element of a detector (radiation background). These effects can also arise from nuclear interactions between very energetic trapped protons and materials (sensitive parts of components, biological experiments, detectors). Here, the proton breaks the nucleus apart and the fragments cause highly-localized ionization.

Energetic particles also interfere with payloads, most notably with detectors on astronomy and observation missions where they produce a "background" signal which is not distinguishable from the photon signal being counted, or which can overload the detector system.

Energetic electrons can penetrate thin shields and build up static charge in internal dielectric materials such as cable and other insulation, circuit boards, and on ungrounded metallic parts. These can subsequently discharge, generating electromagnetic interference.

Apart from ionizing dose, particles can lose energy through non-ionizing interactions with materials, particularly through "displacement damage", or "bulk damage", where atoms are displaced from their original sites. This can alter the electrical, mechanical or optical properties of materials and is an important damage mechanism for electro-optical components (e.g. solar cells and opto-couplers) and for detectors, such as CCDs.

For a more complete description of these effects refer to ECSS-E-ST-10-12.

9.2 Requirements for energetic particle radiation environments

9.2.1 Trapped radiation belt fluxes

9.2.1.1 Long term average fluxes for Earth orbits

a. For Earth orbits other than those addressed in 9.2.1.2, the standard models of the radiation belt energetic particle fluxes shall be the AE-8 and AP-8 models for electrons [RN.10] and protons [RN.11].

NOTE 1 These models are based on long term dataset averages and are most appropriate for long term cumulative effects on missions of more than 6 months duration. Statistical variation and uncertainties can be significant and are presented in Annex I.

b. They shall be used together with the geomagnetic field models shown in Table 9-1.

c. The version of the model, i.e. solar maximum/minimum that is commensurate with the solar activity levels (MIN or MAX), of the mission phase shall be used.

d. The dates of Minima and Maxima that shall be used for solar cycles 1 to 23 and the algorithm for forecasting future Minima and Maxima are presented in Annex B.1 and Table B-2.

NOTE 1 As it is difficult to define the % of solar MIN and MAX to apply for missions not scheduled in Max or Min periods, a more conservative analysis can be obtained for all periods using AE8MAX for electron fluxes and AP8MIN for proton fluxes.

e. For analysis of the South Atlantic Anomaly (SAA), the drift of the SAA due to geomagnetic field evolution shall be included.

NOTE The translation of the orbit locations eastward in longitude 0,3° per year since 1960 prior to accessing the models provides a first approximation to this drift. [RD.14].

9.2.1.2 Long term Flux models for specific orbits

9.2.1.2.1 Long term average fluxes in geostationary orbits

a. For electron fluxes at altitudes within 500 km of geostationary orbits (35 786 km) the standard model for Earth radiation belt energetic electrons shall be the IGE-2006 average model .

NOTE IGE-2006 model was previously called POLE [RN.12] and Annex B.2.

b. For conservative analysis, the IGE-2006 upper case model shall be used.

NOTE Information on model development and uncertainties can be found in [RN.33].

c. The mission duration parameter used with the IGE2006 model shall be rounded up to the nearest integral year.

d. For trapped proton fluxes in geostationary orbit, the trapped proton models (AP-8) specified in 9.2.1.1 shall be used.

9.2.1.2.2 Long term fluxes in GNSS/Navigation orbits

a. For electron fluxes in GPS orbits (circular, 20 200 km ± 500 km altitude; 55° Inclination) the standard model for Earth radiation belt energetic electrons shall be the ONERA MEOv2 average model (Annex B.3, [RN.13]).

b. For conservative analysis, the upper case MEOv2 model shall be used.

c. The mission duration parameter used with the MEOv2 model shall be rounded up to the nearest integral year.

d. Extrapolation of the flux spectrum from the MEOv2 model to higher energies shall use the orbit averaged spectral form provided by AE-8 MAX.

e. For trapped proton fluxes, the trapped proton models (AP-8) specified in 9.2.1.1 shall be used.

f. For trapped electron fluxes at altitudes between 20 500 km and 24 000 km and the Inclination range of 55° ± 5°, either the AE-8 or the MEOv2 model may be used.

NOTE If used above 20 500 km altitude the MEOv2 model can provide conservative results. More information on this model is given in Annex I.

9.2.1.2.3 Long term fluxes for other orbits

Models for other orbits are available; more information on these models is given in Annex I.

9.2.1.3 Worst case trapped electron fluxes for internal charging analyses

a. For Earth orbits, except the one in 9.2.1.3c, the FLUMIC V3 model (Annex B.4) [RN.14] shall be used.

NOTE 1 These electron belt models are also appropriate for short-term (from 1 day to 1 month) worst-case cumulative radiation effect analyses.

NOTE 2 For a conservative assessment with FLUMIC V3, 21 March 2005 corresponding to 0.219 'fraction of year' and 0.802 'fraction of solar cycle' can be assumed.

b. For geostationary orbits, the NASA worst case model (Annex B.5) may be used.

c. For GNSS orbits, the MOBE-DIC model (Annex B.9) shall be used.

d. The highest flux reported by the models during the mission shall be used.

9.2.1.4 Worst case trapped proton fluxes

There is no provision in this standard related to peak or worst case trapped proton fluxes. These particles can be significant for certain applications and effects, such as sensor interference.

9.2.2 Solar particle event models

Standard solar particle event models do not include electrons. These electrons can be significant for certain applications and effects like internal charging. Information on typical electron fluxes during solar particle events is given in [RD.15], [RD.16].

9.2.2.1 Directionality

a. Fluxes and fluences of solar energetic particles shall be assumed to be isotropic.

NOTE Anisotropic distributions do exist in near-Earth space due to geomagnetic shielding (see clause 9.2.4) and in the early stages of a SPE, where particles arrive along interplanetary field lines.

The direction of the interplanetary magnetic field can be variable and not along the Earth-Sun direction. An isotropic distribution is assumed due to a lack of knowledge for specific events.

9.2.2.2 Solar Particle Fluence Models

a. Proton fluence spectra from Solar Particle Events integrated over mission durations (of 1 year or more) shall be derived using the ESP model [RN.15] described in Annex B.6.

b. For mission durations shorter than 1 year, the fluences for one year shall be used [RN.15].

NOTE For mission durations shorter than 1 year, this results in a conservative fluence estimate.

c. When using the model to calculate fluences for mission durations longer than 1 solar cycle (11 years), the model shall be used with the total number of years of high solar activity during the mission.

d. For interplanetary missions, the results of the solar particle models shall be scaled by a factor calculated as the mean value over the mission of: r^{-2} for r<1AU [RN.16] and 1 for r>1AU, where r is in units of AU.

NOTE Beyond 1 AU using a factor of 1 corresponds to a conservative estimate of the maximum coefficient recommended in [RN.16].

e. For calculations of geomagnetic shielding all ions shall be treated based on CREME96 ionization states.

f. If CREME96 specified in 9.2.2.2e does not provide ionization states the ions shall be treated as half ionised.

g. Electron fluence from Solar Particle Events (SPEs) integrated over mission durations, of 6 months or more, may be derived using the IEM model [RD.150].

NOTE This is considered only relevant for applications such as sensitive instrument background on interplanetary missions. The fluxes and energies provide a negligible contribution to cumulative effects compared to solar protons or trapped particle fluxes.

9.2.2.3 Solar Particle Peak Flux Models

a. For solar particle fluxes (protons and other ions), either the CREME96 model [RN.18] (only available online) or Table B-10, Table B-11, and Table B-12 shall be used.

b. In Table B-10, Table B-11, and Table B-12 all ions shall be treated as fully ionised for geomagnetic shielding calculations.

NOTE In cases where the instantaneous solar proton flux is required or as a function of time during

an event, there are several large events that have been measured, their spectral fits are provided in Annex I.2.4.

c. For maximum SPE electron fluences, the IEM model [RD.150] may be used.

NOTE This is considered only relevant for applications such as sensitive instrument background on interplanetary missions. The fluxes and energies provide a negligible contribution to cumulative effects compared to solar protons or trapped particle fluxes.

9.2.3 Cosmic ray models

a. The ISO 15390:2004 Model [RN.19] of galactic cosmic rays shall be used for GCR flux calculations.

NOTE Although cosmic ray fluxes increase gradually with heliocentric distance, it is a reasonable engineering approximation for current missions to assume uniformity throughout the heliosphere.

9.2.4 Geomagnetic shielding

a. The minimum energies, i.e. cut-off energies, necessary for ions to penetrate to a geographic location shall be calculated with one of the following methods:

1. Størmer's theory [RN.20]
2. MAGNETOCOSMICS [RN.21]
3. The method given by Smart and Shea in [RN.22]
4. Stassinopoulos & King: no geomagnetic shielding for McIlwain L-shells greater than 5 R_E [RN.23]
5. No geomagnetic shielding for a conservative estimate.

9.2.5 Neutrons

a. To assess the atmospheric albedo neutron fluxes the models given in Annex I.7 may be used.

9.2.6 <<deleted>>

a. <<deleted>>

b. <<deleted>>

9.2.7 L2 and the Deep Magnetotail Environment

a. The interplanetary environment shall apply for the energetic particle environment at L2 and the deep tail.

b. For specific cases, as X-ray optics and detectors, the population of medium energy charged particles should be evaluated.

NOTE Further information is provided in Annex I.7.

9.3 Preparation of a radiation environment specification

a. A specification of the expected radiation environment of a space system shall be established.

b. The specification of a mission environment shall include:

1. Mission-average proton and electron energy spectra from trapped radiation issued from the chosen models (according to mission orbit and time).
2. The fluence spectrum of solar protons for the complete mission with geomagnetic shielding applied.
3. Maximum instantaneous energy spectra of trapped electrons, trapped protons and solar energetic protons (geomagnetically shielded) for the mission, for internal charging and sensor interference analysis.
4. The ion LET flux spectrum derived from the GCR flux spectra for the appropriate solar cycle phase, together with the worst 5 minute solar energetic particle LET spectrum, including:
   (a) Contributions from all ions from $Z = 1$ to $Z = 92$.
   (b) Geomagnetic shielding.
   (c) Material shielding. If no justification is available for another value, 1 g cm^{-2} of aluminium shielding is used.
5. The ion LET fluence spectrum derived from the GCR fluence spectra for the appropriate solar cycle phase, together with the fluence spectra from a number of events at worst day CREME96 solar energetic particle LET spectrum, including:
   (a) Contributions from all ions from $Z = 1$ to $Z = 92$.
   (b) Geomagnetic shielding.
   (c) Material shielding. If no justification is available for another value, 1 g cm^{-2} of aluminium shielding is used.
6. Orbital time-behaviour of radiation-belt (if any), cosmic ray and solar energetic particle fluxes if the mission has a susceptibility to radiation background in sensors.
7. Additional contributions from on-board nuclear/radioactive sources.

8. Uncertainties of the radiation models as applied for the given mission.

c. The uncertainties in results from the models shall be included in the risk assessment.

d. The specification shall include the evolution of the mission orbit whether caused naturally or by deliberate orbit manoeuvres.

NOTE This can have significant effects on radiation-belt exposure (e.g. due to natural perigee rise and apogee fall).

e. The effects of operations that result in geo-synchronization of the orbit shall be included in the assessment

NOTE 1 For example: geostationary, apogee longitude maintenance of near-synchronous HEO orbits.

NOTE 2 In such missions radiation belt exposures are not averaged out.

9.4 Tables

Table 9-1: Standard field models to be used with AE8 and AP8

Radiation-belt model	Geomagnetic field model
AE-8-MIN	Jensen-Cain 1960 [RN.24]
AE-8-MAX	Jensen-Cain 1960
AP-8-MIN	Jensen-Cain 1960
AP-8-MAX	GSFC 12/66 extrapolated to 1970 [RN.25]

10
Space debris and meteoroids

10.1 Introduction and description

10.1.1 The particulate environment in near Earth space

Every spacecraft in Earth orbit is exposed to a certain flux of natural micrometeoroids and man-made space debris. Collisions with these particles take place with hypervelocity speed.

The damage caused by collisions with meteoroids and space debris depends on the size, density, speed and direction of the impacting particle and on the characteristics of the impacted structure.

Impact analysis techniques fall naturally into two different categories: larger, trackable pieces and smaller, non-trackable particles.

Trackable orbiting objects, whose orbital elements are known, can be propagated along their orbit and their chance of a future collision with another spacecraft or fragment can be assessed. This deterministic approach provides at the same time all relevant parameters of such a potential collision, like impact velocity and direction.

For meteoroids and the abundant smaller space debris particles which cannot be tracked, the risk assessment is supported by statistical flux models as described in the subsequent chapters.

10.1.2 Space debris

Space debris are man-made objects that are remainders of human spaceflight activities. In early 2018 only 9% of the publically available catalogued orbit population are operational spacecraft, while 33% can be attributed to decommissioned satellites, spent upper stages, and mission related objects (launch adapters, lens covers, etc.). The remainder of 58% is mostly originating from more than 250 on-orbit fragmentations which have been recorded since 1961. These events are collisions (in at least seven cases) and explosions of spacecraft and upper stages. The total population of objects larger than 1 cm is on the order of 750 000 to 1 000 000.

One of the major sources of space debris, fragmentations of space objects, originates from spare fuel that mostly remains inside pressurized tanks once the rocket stage is discarded into Earth orbit. Over time, and in the harsh

environment of space, the mechanical integrity of the booster's internal components breaks down and tanks start to leak. The resulting sudden releases of pressure or even high energetic explosions expel numerous fragments into orbit. The most important non-fragmentation source is solid rocket motor firings during which aluminium oxide (Al_2O_3) in the form μm-sized dust and mm to cm-sized slag particles is exhausted. A second important source was the ejection of reactor cores during the end of operation of the Russian RORSATs (Radar Ocean Reconnaissance Satellites) in the 1980's, which released droplets of the reactor coolant (sodium potassium alloy (NaK)) into space. Another historic source was the release of thin copper wires as part of a radio communication experiment during the MIDAS missions in the 1960's. Finally, under the influence of the harsh space environment (extreme ultra violet radiation, impinging atomic oxygen and micro particle impacts), surfaces of space objects start to erode. This leads to mass losses of surface coatings and to the detachment of flakes of the surface paint, both with μm and mm sizes.

10.1.3 Meteoroids

Meteoroids are particles of natural origin. Nearly all meteoroids originate from asteroids or comets. The natural meteoroid flux represents, at any instant, a total of about 200 kg of mass within 2 000 km of the Earth surface [RD.21].

Meteoroid streams are accumulations of meteoroids with nearly identical heliocentric orbits. Relative to Earth all particles of a given meteoroid stream have nearly identical impact directions and velocities. Encounters with meteoroid streams typically last from a few hours to several days.

Meteoroids which do not form part of identified streams are called sporadics. Their flux is fairly constant over the year and they do not follow any apparent pattern with respect to incident direction or velocity. The annual integrated flux of meteoroid streams amounts to about 10% of the sporadic meteoroid flux.

10.2 Requirements for impact risk assessment and model selection

10.2.1 General requirements for meteoroids and space debris

a. Impact risk assessments shall be performed for space debris and meteoroid populations.

b. The statistical flux models as specified in 10.2.2 shall be used tailored for the specific mission parameters.

c. The directional and velocity distributions of the space debris and meteoroid fluxes shall be included in the impact risk assessment.

10.2.2 Model selection and application

10.2.2.1 Space debris

a. The space debris part of the MASTER-8 model [RN.26] shall be used for Earth orbits with perigee altitudes below 36 786 km.

b. The model shall be used for all mission durations.

c. The model shall be used for particle diameters from 1 micron to 100 m.

d. For conversion between mass and diameter the following shall be used:

1. An average density of 2,8 g cm^{-3}.

2. A spherical shape.

NOTE The density of 2,8 g cm^{-3} represents the average density of space debris objects > 1mm. Additional information is given in Annex J.2.2.1.4.

e. Densities and shapes different from ones specified in requirement 10.2.2.1d may be included in specific cases.

f. The MASTER-8 flux model [RN.26] shall be used together with the following input parameters:

1. Timeframes between 1957 and 2116.

2. The size interval given in terms of diameter.

3. Condensed population, with all sources included.

4. The Business-As-Usual case for future predicitions.

NOTE 1 Access points for the ESA MASTER-8 model and its patches are defined in Annex J.2.2.1, together with model characteristics, uncertainties, some general aspects and other space debris flux models.

NOTE 2 Tabulated reference values are provided in J.5.

NOTE 3 Due to the dynamic nature of the debris environment significant and abrupt increases of populations can occur.

g. Later versions of MASTER-8 or population files may be applied (see Annex J.2.2.1.2).

h. For specific missions, the debris flux implemented in ORDEM 3.0 [RN.36] may be used for Earth altitudes below 40 000 km.

i. For ORDEM 3.0 debris model the following shall be used:

1. Time range from 2010 to 2035

2. Nominal flux (zero sigma)

3. the density model implemented in ORDEM 3.0

4. particle diameters of 10 micron to over 1 m for altitudes below 34 000 km

5. particle diameters of 10 cm to over 1 m for altitudes from 34000 to 40000 km.

j. For Earth altitudes not covered by 10.2.2.1a or 10.2.2.1h space debris flux may be neglected.

10.2.2.2 Meteoroids

a. The Grün model [RD.22] shall be used to determine near-Earth meteoroid environments.

NOTE It gives the total average meteoroid flux (sporadic + stream average) in terms of the integral flux $F_{met,0}$ as:

$$F_{met,0}(m) = 3{,}15576 \times 10^7 \left(F_1(m) + F_2(m) + F_3(m)\right) \quad (10\text{-}1)$$

where

$F_{met,0}$ is the unshielded isotropic interplanetary flux at 1 AU distance from the Sun. It gives the number of particles with mass m or larger per m² per year impacting a single-sided randomly-tumbling flat plate.

and

$F_1(m) = (2{,}2 \times 10^3\, m^{0{,}306} + 15)^{-4{,}38}$

$F_2(m) = 1{,}3 \times 10^{-9}\, (m + 10^{11}\, m^2 + 10^{27} m^4)^{-0{,}36}$

$F_3(m) = 1{,}3 \times 10^{-16}\, (m + 10^6\, m^2)^{-0{,}85}$

with m in g

NOTE 1 The near-Earth environment includes Earth and Lunar orbits and the Lagrange points of the Sun-Earth and Earth-Moon systems.

NOTE 2 Tabulated reference values are provided in Table J-5

NOTE 3 .

b. The models specified in 10.2.2.2a and 10.2.2.2h shall be used for all mission durations.

c. For durations of less than three weeks the flux from the meteoroid stream model specified in 10.2.4.5 shall be added for the given mission period.

d. For conversion between mass and diameter and for impact damage assessments the following shall be used:

1. A density of 2,5 g cm^{-3} for the Grün model and 1,0 g cm^{-3} for the MEM model.

2. A spherical shape.

e. The meteoroid model given in 10.2.2.2a shall be used together with the normalised velocity distribution of meteoroids at 1 AU [RD.27] given in Table C-1.

f. The velocity distribution in Table C-1 shall be adjusted to reflect the altitude dependence of the meteoroid model given in Annex C according to one of the procedures specified in **Error! Reference source not found.**

NOTE The velocity correction which is used to increase the flux with decreasing distance from the Earth is used to adjust the velocity distribution which is then re-binned accordingly.

g. For Earth and Lunar orbits, the unshielded flux $F_{met,0}$ specified in 10.2.2.2a shall be modified to account for the gravitational attraction as specified in **Error! Reference source not found.**.

NOTE This enhances the meteoroid flux in the Earth proximity.

h. For specific missions, the MEM and LunarMEM models or the Divine-Staubach model may be used.

NOTE For interplanetary orbits no reference model is specified. Available interplanetary meteoroid flux models are given in Annex J.2.1.5

i. The MEM flux model [RN.27] shall be used with the following input parameters:

1. Mass range 10^{-6} - 10 g
2. Constant particle density of 1 g/cm^3

j. The LunarMEM flux model [RN.27] shall be used with the following input parameters:

1. Radius up to 66000 km from the Moon
2. Mass range 10^{-6} - 10 g
3. Constant particle density of 1 g/cm^3

k. The Divine-Staubach model [RD.108] shall be used with following input parameters:

1. Mass range 10^{-12} g to 1 g.
2. Inherent velocity distribution model.
3. Particle density equal to:
   (a) 2,0 g/cm^3 for m < 10^{-6} g
   (b) 1,0 g/cm^3 for 10^{-6} g < m < 10^{-2} g
   (c) 0,5 g/cm^3 for 10^{-2} g < m

10.2.3 <<deleted>> l

a. <<deleted>>

10.2.4 The meteoroid model

10.2.4.1 <<deleted>>

a. <<deleted>>

10.2.4.2 <<deleted>>

a. <<deleted>>

10.2.4.3 <<deleted>>

a. <<deleted>>

10.2.4.4 <<deleted>>

a. <<deleted>>

b. <<deleted>>

10.2.4.5 Meteoroid streams fluxes

a. For the calculation of meteoroid stream fluxes, the meteor stream parameters given in Table C-2 shall be used together with the flux calculation procedure given in Annex C.1.4.2 and C.1.4.3.

b. For each meteoroid stream the specific particle velocity shall be considered.

c. For meteoroid stream particles a mass density of 1,0 g cm^{-3} shall be used.

NOTE This meteoroid stream model is also implemented in MASTER-2005

10.2.5 Impact risk assessment

a. For the translation of flux F into number of impacts *N*, a linear increase of *N* with exposed area and with exposure time shall be used, as follows:

$$N = F \cdot A \cdot T \qquad (10\text{-}2)$$

Where:

N is the number of impacts ;

F is the particulate flux per unit time and unit area;

A is the total exposed area;

T is the exposure time.

b. Impact risk analyses based on the number of impacts *N* shall be conducted through the application of Poisson statistics.

c. The probability P_n of exactly n impacts occurring in the corresponding time interval shall be determined according to the expression:

$$P_n = \left(\frac{N^n}{n!} \right) e^{-N} \qquad (10\text{-}3)$$

NOTE Additional information on the conduct of impact risk assessments is provided in Annex [RD.91].

d. Simplified assessments may be performed with an average velocity and a constant impact angle of 45 degrees from the surface normal.

NOTE Typical average impact velocity for space debris in LEO is 10 km/s, 5 km/s for space debris in GEO and of 20 km/s for meteoroids.

10.2.6 Margins

a. For a nominal assessment of the space debris and meteoroid populations in the near-Earth environment the nominal flux models shall be applied without additional margin or uncertainty factors.

NOTE The flux models given in 10.2.2 10.2.3 were developed as best estimates rather than as conservative ones. Information on the model uncertainties is given in Annex J.2.3.

11 Contamination

11.1 Introduction and description

11.1.1 Introduction

This clause deals with the induced molecular and particulate environment in the vicinity of and created by the presence of a spacecraft in space. It is meant mainly to aid in the definition of the contamination environment of a satellite.

The quantitative modelling of this contamination environment is very complex. This is due to the high number of materials involved, with a variability of outgassing characteristics. Furthermore, there are interactions of the outgassing products with surfaces, residual gas and with other environmental parameters such as solar radiation and atomic oxygen.

The contamination analysis, which necessarily is very much dependent on a specific project/application, is not detailed in this standard. ECSS-Q-ST-70-01 defines amongst others the requirements to be followed and guidelines to be taken into account in order to control the particulate and molecular contamination within the specified limits during mission. It also includes a list of potential contamination effects on space hardware.

11.1.2 Description of molecular contamination

11.1.2.1 Primary sources of molecular contamination

11.1.2.1.1 Outgassing of organic materials

Outgassing of organic materials can be approached as a surface evaporation combined with diffusion for bulk contaminant species. These species can be either initially present components, or decomposition products.

Initially present outgassing species can be: water, solvents, additives, uncured monomeric material, lubricants, ground contamination species, due to e.g. processes, test, storage, handling, pre-launch and launch.

The decomposition products are due to exposure of molecular materials to other environments, such as: thermal, solar radiation, electromagnetic and charged particles, atomic oxygen, impacts by micrometeoroids or debris, electrical discharges and arcing

These products consist of lower molecular weight (higher volatility) species than the original species.

11.1.2.1.2 Plumes

Plume species can result from combustion, unburned propellant vapours, incomplete combustion products, sputtered material and other degradation products from a propulsion or attitude control system and its surroundings swept along with the jet.

Plumes can also be produced by dumps of gaseous and liquid waste materials of the environment control and life support systems in manned spacecraft or by leaks in systems or internal payloads. Return flux or back flow is possible due to ambient scattering, self scattering or diffusion processes.

11.1.2.1.3 Pyrotechnics and release mechanisms

During operation of pyrotechnics or other release mechanisms gases can evolve.

11.1.2.2 Secondary sources of molecular contamination

A surface can act as a secondary source if an incoming contaminant molecule reflects (i.e. does not accommodate, stick or condense on the surface) or if it has a limited residence time on that surface. Secondary sources can for example be solar panels having a higher temperature than the surrounding surfaces.

11.1.3 Transport mechanisms

Main transport mechanisms are: reflection on surfaces, re-evaporation from surfaces, migration on surfaces, collisions with the residual (natural) atmosphere, collisions with other outgassed molecules, ionization by other environmental parameters.

11.1.4 Description of particulate contamination

11.1.4.1 Sources of particulate contamination

Sources inherent to materials are: particles originating from manufacturing (machining, sawing), handling (e.g. for brittle materials such as certain paints) or wear (friction); degradation of binder under different environments (e.g. AO, UV) resulting in loose filler; crack formation and subsequent flaking as a result of thermal cycling; formation of particles due to oxidation in an atomic oxygen environment.

Sources external to materials are: Dust particles caused by atmospheric fall-out (dust) during assembly, integration and storage or by human sources during such activities (e.g. hair, skin flakes, lints or fibres from garments); particles produced during spacecraft propulsion or attitude control operations, the functioning of moving parts (such as shutters), and water dumps; particles resulting from micrometeoroid or debris impacts on materials.

11.1.5 Transport mechanisms

Particles can be transported by vibrations due to launch, on-orbit manoeuvring and docking. Pyrotechnic shocks can cause particles to migrate from one surface to another.

Particles can be charged due to their interaction with ambient plasma or photo emission, and subsequently attracted by electrically charged surfaces.

For specific missions other mechanisms can have an effect on the particles, such as: drag, due to the residual atmosphere in the lowest Earth orbits; radiation pressure due to solar radiation; gravitational tide, e.g. re-attraction to spacecraft.

11.2 Requirements for on-orbit contamination assessment

a. ; The evaluation of contamination levels on sensitive items should include the interaction with the following space environment components:

1. Atmospheric density at altitudes below 250 km
2. Atomic oxygen at altitudes below 400 km
3. UV radiation
4. EM and particle radiation.

NOTE Synergistic effects are indicated in Table 11-1.

b. <<deleted>>

c. <<deleted>>

d. <<deleted>>

Table 11-1: Contamination levels - interaction with the space environment components

Environment component	Clause	Effect
Atmosphere density level	7 - Neutral atmosphere	Collision scattering with atmosphere particles
Atomic Oxigen	7 - Neutral atmosphere	Erosion and modification of deposited contamination on sensitive items
UV	6 - Natural electromagnetic radiation and indeces	Deposition fixation on sensitive surfaces (sticking factors) and optical properies modification
EM and particle radiation	6 - Natural electromagnetic radiation and indeces 9 - Energetic particle radiation	Outgassing product ionization

Annex A (normative) Natural electromagnetic radiation and indices

A.1 Solar activity values for complete solar cycle

Table A-1 lists the minimum, mean and maximum daily and 81-day averaged values for *F10.7*, *S10.7* and *M10.7* for each month of solar cycle 23. The values are averaged over 30-day (1 month) intervals. This table is referred to in 6.2.2, 6.2.3 and 7.2.1.

A.2 Tables

Table A-1: Solar cycle 23 solar activity indices averaged over 30-day (1 month) intervals.

(Part 1 of 4)

Month	$F10_{min}$	$F10_{mean}$	$F10_{max}$	$F81_{min}$	$F81_{mean}$	$F81_{max}$	$S10_{min}$	$S10_{mean}$	$S10_{max}$	$S81_{min}$	$S81_{mean}$	$S81_{max}$	$M10_{min}$	$M10_{mean}$	$M10_{max}$	$M81_{min}$	$M81_{mean}$	$M81_{max}$
0	72	74	77	74	76	78	74	78	82	78	79	79	65	72	76	72	73	74
1	71	74	81	74	74	74	74	77	82	78	78	78	62	71	75	72	72	73
2	70	74	76	74	74	74	73	79	83	78	79	79	66	73	80	73	73	74
3	69	74	81	74	74	74	74	80	86	79	80	81	67	75	86	74	75	76
4	71	75	85	72	73	74	78	83	91	81	81	81	72	78	87	76	76	77
5	68	72	77	72	72	73	78	81	87	81	81	82	70	76	86	76	76	77
6	67	71	80	73	73	77	75	80	87	82	83	86	68	75	85	76	77	80
7	70	78	92	77	82	85	80	88	95	86	89	93	73	81	92	80	83	87
8	85	96	119	85	87	90	95	100	103	93	96	98	81	94	101	87	89	92
9	79	85	90	90	92	93	92	98	103	98	100	102	85	91	98	92	93	95
10	86	97	118	93	94	96	97	103	119	102	102	103	84	95	118	95	95	97
11	85	100	117	96	97	97	95	105	120	103	104	105	84	100	121	97	98	99
12	81	95	108	94	95	97	92	104	110	103	104	105	85	100	114	97	98	99
13	83	94	107	94	97	101	93	104	110	103	105	108	85	98	114	97	99	101
14	90	108	133	101	105	108	97	109	123	108	110	113	83	103	117	101	105	108
15	88	109	141	108	109	110	101	118	131	113	115	116	94	114	147	108	110	112
16	87	107	133	106	107	109	101	114	125	116	116	117	90	111	129	112	113	113
17	93	104	117	106	108	109	103	117	128	116	117	117	90	110	124	113	116	118
18	99	114	129	108	116	123	118	118	118	117	118	119	101	125	150	118	123	128
19	109	130	154	123	128	131	118	118	118	118	118	118	120	132	144	128	131	133
20	117	141	179	130	132	133	118	118	118	118	118	119	121	139	151	132	134	135
21	112	123	143	128	130	132	118	118	118	119	123	127	117	132	147	131	133	134
22	103	128	162	129	133	139	118	133	150	127	133	138	109	129	156	133	135	137
23	126	147	168	139	142	147	127	146	159	138	141	142	116	141	175	137	139	140
24	110	147	184	143	145	147	134	141	148	139	140	140	109	140	170	137	139	140
25	99	146	205	137	141	144	115	135	159	137	138	139	102	140	172	134	136	138
26	110	133	157	130	132	137	129	143	154	137	138	138	117	137	159	130	133	134
27	100	117	141	127	128	131	118	135	151	138	139	142	101	125	157	130	131	133
28	98	135	178	131	138	148	111	142	168	142	147	154	97	131	175	133	138	145
29	137	157	176	148	156	162	140	162	179	154	161	166	121	151	175	145	152	157
30	130	166	210	162	165	168	156	174	200	166	169	170	132	163	197	157	159	161
31	123	164	216	157	164	169	146	165	190	162	168	171	129	156	187	154	159	162
32	107	161	248	153	155	157	136	162	194	158	161	162	121	155	202	150	153	154
33	122	149	200	154	160	167	148	157	168	158	160	162	130	152	167	150	153	156

Table A-1: Solar cycle 23 solar activity indices averaged over 30-day (1 month) intervals.

(Part 2 of 4)

Month	$F10_{min}$	$F10_{mean}$	$F10_{max}$	$F81_{min}$	$F81_{mean}$	$F81_{max}$	$S10_{min}$	$S10_{mean}$	$S10_{max}$	$S81_{min}$	$S81_{mean}$	$S81_{max}$	$M10_{min}$	$M10_{mean}$	$M10_{max}$	$M81_{min}$	$M81_{mean}$	$M81_{max}$
34	143	184	249	167	172	181	151	166	187	162	166	170	134	161	195	156	159	164
35	143	175	221	175	177	181	153	176	193	168	171	173	139	165	186	161	164	167
36	130	172	217	163	167	177	143	170	200	170	171	173	125	165	209	163	164	167
37	126	159	208	165	172	181	142	173	196	171	174	179	129	166	209	163	166	171
38	141	193	233	181	186	191	157	182	201	179	184	189	131	171	196	171	175	181
39	164	199	234	189	192	195	173	198	214	187	189	191	156	189	213	178	180	183
40	127	174	244	182	187	194	165	181	206	186	188	191	146	171	199	177	179	182
41	146	193	262	181	185	194	165	185	212	184	186	192	141	175	210	173	176	183
42	156	188	245	186	190	196	176	193	222	192	194	197	152	183	224	181	184	187
43	148	191	262	178	181	186	185	208	234	193	195	197	162	196	236	182	184	187
44	131	159	194	170	177	184	162	184	212	184	189	193	131	175	220	174	179	183
45	133	184	232	171	172	174	166	179	197	181	182	184	150	173	196	173	174	174
46	150	172	204	171	175	179	171	185	197	181	182	183	137	177	211	173	174	176
47	135	168	205	171	174	176	156	178	224	183	184	184	126	165	211	174	175	176
48	144	180	201	166	171	174	158	186	209	179	182	183	139	177	203	170	174	176
49	148	163	184	155	161	166	174	179	185	171	176	179	154	176	188	159	166	170
50	130	145	177	155	163	168	158	164	179	171	174	176	127	147	179	158	162	164
51	134	193	274	165	169	170	155	185	218	173	174	174	141	170	216	157	158	159
52	123	163	196	166	170	172	152	170	186	173	174	174	116	157	188	158	161	163
53	130	147	180	155	161	166	151	163	173	168	170	173	125	153	173	161	161	163
54	116	165	221	150	151	155	151	174	190	165	166	168	142	170	194	159	160	161
55	115	137	167	151	156	163	142	156	168	166	167	168	133	149	172	159	160	162
56	143	177	226	163	180	193	167	175	195	168	177	185	145	166	188	162	169	177
57	173	230	285	193	209	222	189	204	230	185	195	203	173	197	223	177	189	197
58	171	215	248	216	219	222	192	208	232	203	205	206	176	201	234	197	199	201
59	170	215	271	214	221	226	182	201	232	204	206	209	168	197	225	200	203	206
60	206	234	275	223	224	226	197	213	232	207	210	213	196	214	233	203	209	212
61	189	229	261	213	221	227	197	218	235	210	212	213	195	220	243	210	213	214
62	172	197	235	200	204	213	191	202	213	200	205	210	192	203	228	200	204	210
63	166	184	217	185	190	200	181	189	195	190	194	200	176	186	202	189	193	200
64	147	185	226	179	182	185	171	189	203	181	185	190	167	188	212	183	186	189
65	157	178	191	159	169	179	161	179	194	168	176	181	157	185	210	171	178	183
66	131	146	170	159	163	165	150	161	174	163	166	168	143	164	188	165	168	171
67	129	177	242	163	169	177	144	162	181	163	165	168	139	165	201	165	167	170
68	135	183	241	177	182	183	149	172	202	168	171	172	134	173	214	170	173	176
69	136	173	221	174	177	182	150	173	198	169	172	173	144	175	207	173	175	176
70	136	168	183	164	170	174	150	165	180	163	166	169	146	169	190	165	169	173
71	137	168	199	162	165	169	149	161	176	160	163	166	140	162	185	161	165	169
72	114	157	213	148	157	162	135	164	177	154	158	161	130	164	193	153	159	163
73	115	144	189	137	143	148	133	149	172	144	150	154	128	149	182	143	149	154

Table A-1: Solar cycle 23 solar activity indices averaged over 30-day (1 month) intervals.

(Part 3 of 4)

Month	$F10_{min}$	$F10_{mean}$	$F10_{max}$	$F81_{min}$	$F81_{mean}$	$F81_{max}$	$S10_{min}$	$S10_{mean}$	$S10_{max}$	$S81_{min}$	$S81_{mean}$	$S81_{max}$	$M10_{min}$	$M10_{mean}$	$M10_{max}$	$M81_{min}$	$M81_{mean}$	$M81_{max}$
74	102	125	150	129	133	137	111	135	151	133	139	144	109	130	163	132	137	143
75	89	132	160	126	127	129	102	131	153	126	130	133	94	131	172	126	129	132
76	99	127	160	121	123	126	109	128	149	123	125	126	106	131	158	123	125	126
77	92	117	154	122	124	126	104	123	142	124	125	126	94	122	147	123	125	128
78	106	128	193	125	126	127	107	125	139	125	126	127	103	126	151	127	128	131
79	100	129	157	123	126	128	110	128	134	125	126	127	113	134	150	129	130	131
80	99	121	137	118	120	123	108	122	136	123	124	126	118	127	140	127	128	130
81	94	110	134	115	121	132	106	121	136	122	123	126	106	123	144	125	127	130
82	92	134	257	129	134	141	110	124	161	123	125	127	102	128	163	126	129	133
83	91	158	279	137	138	141	100	132	185	124	125	127	92	136	187	128	130	133
84	86	123	175	122	129	140	92	122	150	117	120	124	84	128	173	122	124	129
85	102	119	137	111	115	122	97	114	136	112	114	117	96	119	156	113	116	122
86	87	102	118	109	110	113	96	109	120	109	111	113	88	107	127	109	111	114
87	90	110	127	106	107	110	101	110	122	110	111	112	90	107	123	108	109	112
88	88	108	129	104	105	106	101	113	125	109	110	110	99	112	126	107	108	109
89	85	99	118	99	101	104	99	105	111	104	106	109	95	104	115	103	105	108
90	83	99	119	97	102	108	97	101	107	102	103	104	87	102	116	101	103	105
91	78	114	175	106	109	112	89	106	125	103	104	105	81	108	142	102	104	106
92	83	117	165	111	113	115	88	105	118	105	105	106	79	107	135	105	107	108
93	86	105	131	102	107	114	97	105	112	102	104	106	85	108	131	103	106	108
94	87	92	112	106	107	108	92	97	111	104	104	105	86	98	109	106	107	109
95	95	122	141	106	106	107	103	111	122	104	104	105	99	113	131	107	107	109
96	85	99	113	101	105	107	92	101	113	101	102	104	87	105	129	103	106	108
97	83	103	145	98	100	101	89	99	119	96	98	101	83	101	117	98	101	103
98	82	101	133	97	98	99	85	99	119	93	95	96	79	102	121	95	97	98
99	74	92	114	91	93	97	76	89	101	89	91	93	72	92	113	92	93	95
100	77	84	90	90	91	93	81	87	92	88	89	90	75	89	101	91	92	94
101	77	99	126	92	93	95	81	90	100	89	89	90	75	93	109	93	93	94
102	82	96	116	94	97	99	84	90	98	89	91	92	79	96	107	94	95	97
103	72	95	130	93	94	95	77	91	107	89	90	91	72	94	123	92	94	95
104	71	87	111	91	92	95	72	85	103	89	89	90	71	89	118	92	93	94
105	74	95	119	85	89	91	74	90	101	84	86	89	72	93	110	88	90	92
106	72	82	112	84	85	85	73	83	98	82	83	84	71	88	105	85	87	88
107	72	78	100	83	84	85	70	78	83	80	81	82	71	81	91	84	85	86
108	80	92	106	85	86	88	78	83	89	81	82	83	79	88	102	85	86	87
109	77	85	93	83	86	88	76	84	93	82	83	83	75	88	107	85	86	87
110	74	81	94	78	81	83	72	79	88	77	80	82	72	81	96	80	83	85
111	72	76	79	78	79	80	71	75	79	77	77	77	70	78	86	79	80	80
112	72	83	100	79	81	82	71	79	88	77	79	80	72	82	91	80	82	83
113	72	85	101	82	83	83	74	84	89	80	81	82	77	90	108	83	85	86

Table A-1: Solar cycle 23 solar activity indices averaged over 30-day (1 month) intervals.

(Part 4 of 4)

Month	$F10_{min}$	$F10_{mean}$	$F10_{max}$	$F81_{min}$	$F81_{mean}$	$F81_{max}$	$S10_{min}$	$S10_{mean}$	$S10_{max}$	$S81_{min}$	$S81_{mean}$	$S81_{max}$	$M10_{min}$	$M10_{mean}$	$M10_{max}$	$M81_{min}$	$M81_{mean}$	$M81_{max}$
114	72	78	85	78	80	82	72	79	88	78	80	81	69	83	97	81	84	85
115	70	77	87	76	77	78	70	76	82	75	76	78	70	79	91	78	80	81
116	70	73	85	77	78	79	69	72	76	74	74	75	67	75	82	78	78	79
117	73	82	89	77	78	78	70	75	82	74	74	74	67	80	92	76	77	78
118	70	76	85	78	78	79	67	75	81	74	74	75	66	77	92	75	76	76
119	70	78	91	79	80	83	66	72	81	74	74	75	63	71	81	74	75	76
120	77	89	103	82	83	85	73	78	90	74	74	75	63	78	86	74	76	77
121	72	83	94	83	84	85	68	74	80	74	75	75	62	77	89	76	77	77
122	76	83	92	79	80	83	72	74	77	72	73	74	67	76	84	73	75	76
123	71	74	78	74	76	79	67	70	75	70	71	72	65	70	74	70	72	73
124	69	72	75	73	73	74	64	68	73	68	69	70	64	68	74	69	69	70
125	68	75	87	73	74	75	63	67	71	68	68	69	62	69	80	69	70	71
126	67	75	87	74	74	75	66	70	79	68	68	69	64	72	89	70	71	72
127	65	71	84	72	73	74	61	68	79	67	68	69	62	72	89	70	71	72
128	66	71	79	70	70	72	62	66	70	65	66	67	61	69	76	68	69	70
129	67	69	72	68	69	70	61	64	66	63	64	65	60	65	69	66	66	68
130	65	67	69	68	68	68	60	61	62	61	62	63	61	64	67	65	65	66
131	67	68	69	68	69	71	59	61	66	61	61	62	61	64	67	65	66	69
132	67	70	75	71	73	74	59	61	64	62	62	64	62	68	80	69	71	72
133	71	79	94	74	75	75	60	65	71	64	64	65	62	79	94	72	72	72
134	70	74	80	72	74	75	61	67	76	64	64	65	61	67	77	67	70	72
135	68	71	73	72	72	72	59	62	66	63	63	64	64	67	74	67	67	67
136	68	74	89	71	71	72	60	64	70	63	63	64	64	67	71	66	67	67
137	67	70	76	70	71	71	60	64	70	63	64	64	62	65	70	66	66	66
138	66	68	72	67	68	70	58	63	68	60	61	63	62	65	70	65	65	66
139	65	66	67	66	67	67	57	58	60	58	59	60	62	63	65	63	64	65

NOTE 1 F10 (F10.7), S10 (S10.7) and M10 (M10.7) are the daily activity indices, F81, S81 and M81 are the corresponding 81-day averaged values.

NOTE 2 The subscripts min, mean and max, denote the minimum, mean and maximum values for the given month of the solar cycle.

Annex B (normative)
Energetic particle radiation

B.1 Historical dates of solar maximum and minimum

The dates of the commencement of solar minimum and solar maximum are provided in Table B-2 based on data from NOAA/SEC [RN.27].

For use with the trapped radiation belt models specified in 9.2.1.1 and for solar particle models, a period of solar maximum activity is considered to be starting 2,5 years before the year of maximum sunspot number and ending 4,5 years after the period of solar maximum. For solar cycles beyond cycle 23, the year of solar maximum for cycle i is estimated by the following formula:

$$Year\ of\ Solar\ Max_i = 2013{,}5 + 11(i - 24) \quad \text{(B-1)}$$

B.2 GEO model (IGE-2006)

IGE-2006 (International GEO electrons) (referred to in 9.2.1.2.1) is an international model based on two and a half solar cycles of in-orbit data coming from different space environment monitors which have been inter-calibrated. It provides the average and upper case electron flux at geostationary orbit for different energies (from 0,9 keV to 5,2 MeV) and for the eleven years around Solar Min (see Table B-3 and Table B-4). The upper case model includes uncertainties in the models and underlying data.

B.3 ONERA MEOv2 model

The ONERA MEOv2 (referred to in 9.2.1.2.2) model is based on data from intercalibrated space environment monitors on board LANL-GPS satellites in the period 1990 to 2006. It provides the average and upper case electron flux at GNSS orbits for different energies (from 280 keV to 2,24 MeV) and for the eleven years around Solar Min (see Table B-5 and Table B-6). The upper case model includes uncertainties in the models and underlying data.

B.4 FLUMIC model

B.4.1 Overview

FLUMIC (Flux Model for Internal Charging) model (referred to in 9.2.1.3) is for evaluating severe internal charging environment in the Earth's magnetosphere. The model is a fit to the upper boundary envelope of daily-averaged fluxes. The algorithms used by FLUMIC version 3 [RN.14] are shown below.

B.4.2 Outer belt (L>2,5 Re)

B.4.2.1. >2MeV flux at L=6,6 Re

The peak integral flux above 2 MeV at L= 6,6 is taken to be 8×10^8 $m^{-2}s^{-1}sr^{-1}$.

B.4.2.2. Solar cycle

$$F(fsc) = 8 \times 10^8 \{0{,}625 + 0{,}375 \sin[2\pi \times (fsc - 0{,}7)] + 0{,}125 \sin[4\pi \times (fsc - 0{,}15)]\} \quad \text{(B-2)}$$

where

fsc is the solar cycle phase starting at solar minimum

B.4.2.3. Season

$$f(foy, fsc) = F(fsc)\{0{,}625 - 0{,}375 \cos[4\pi(foy + 0{,}03)] - 0{,}125 \cos[2\pi(foy + 0{,}03)]\} \quad \text{(B-3)}$$

where

foy is the fraction of year starting from 1st January.

B.4.2.4. Spectrum

$$F(> E, 6.6) = F(> 2MeV) \times \exp\left[\frac{2-E}{E_0}\right] \quad \text{(B-4)}$$

where

$$E_0 = 0{,}25 \text{ for } F(> 2MeV) \leq 10^7 \text{ m}^{-2}\text{s}^{-1}\text{sr}^{-1}$$

$$E_0 = 0{,}25 + 0{,}11(\log_{10}[F(> 2MeV)] - 7)^{1.3} \text{ for } F(>2MeV) > 10^7 \text{ m}^{-2}\text{s}^{-1}\text{sr}^{-1}$$

B.4.2.5. Flux versus L profile

$$F(>E, L) = F(>E, 6{,}6) \times 16 \tanh[0{,}6(L - 2{,}5)] / \cosh[1{,}5(L - 4{,}3)] \text{ m}^{-2}\text{s}^{-1}\text{sr}^{-1} \quad \text{(B-5)}$$

where

$$F(E, L = 6{,}6) = F(foy, fsc)\ x\ \exp(\frac{2 - E}{E_0})$$

B.4.3 Inner belt (L<2,5 Re)

B.4.3.1. >1MeV flux versus L profile

$$F(>1MeV, L) = 4{,}0 \times 10^{\{2{,}12+45{,}4/(L+0{,}05)^2 - 45{,}6/(L+0{,}05)^3\}} \text{ m}^{-2}\text{s}^{-1}\text{sr}^{-1} \quad \text{(B-6)}$$

B.4.3.2. Spectrum

$$F(>E) = F(>1MeV) \times \exp\left(\frac{1-E}{E_0}\right) \quad \text{(B-7)}$$

where

$E_0 = 0{,}14\,MeV$

B.4.3.3. B/B_0

B.4.3.3.1 For L < 3

$$Flux = Flux(equatorial) \times 10^{\left(-a\left(\left(\frac{B}{B_0}\right)-1\right)\right)} \quad \text{(B-8)}$$

where

$$a = -0{,}4559L + 1{,}4385 \quad \text{for } L \geq 1{,}75$$

$$a = 36{,}0\left[\frac{1}{\sinh((L-1)\times 10)}\right] + 0{,}7 \quad \text{for } L < 1{,}75$$

B.4.3.3.2 For L ≥ 3

The formula of Vette [RN.10] is used, as in AE8, i.e.

$$Flux = Flux(equatorial) \times \left(\frac{B}{B_0}\right)^{-m} \times \left(1 - \frac{\left(0{,}52 \times \left(\frac{B}{B_0}\right)\right)}{L^3}\right)^{m+0{,}5} \quad \text{(B-9)}$$

where

$$m = 0{,}6 \text{ for } L \geq 4$$

$$m = 0{,}6 + 0{,}06 \times (4 - L) + 0{,}06 \times (4 - L)^6 \quad \text{for } 3 \leq L < 4$$

B.5 NASA worst case GEO spectrum

The model given in Table B-7 (referred to in 9.2.1.3) is a worst case spectrum for geostationary orbits.

This model is provided by NASA-HDBK-4002 and is based on data from the LANL SOPA and ESP instruments for an approximately 99,9 % worst day for GOES >2MeV fluxes.

B.6 ESP solar proton model specification

The ESP model [RN.15], (first published in [RD.146]; referred to in 9.2.2.2) provides a technique to compute the percentile of the distribution of cumulated solar proton fluence. It is based on an explicit formula for the probability of exceeding a given fluence φ of protons with energy above E, over a duration T:

$$F(\varphi, T \mid \Phi_{RV}(E), \Phi_{mean}(E)) = \frac{1}{\sigma\sqrt{2\pi}} \int_0^{\varphi} \frac{1}{x} \exp\left(-\frac{1}{2\sigma^2} [\ln(x) - \mu]^2 \right) dx \quad \text{(B-10)}$$

with

$$\sigma^2 = \ln(1 + \Phi_{RV} / T) \quad \text{(B-11)}$$

and

$$\mu = \ln(T \cdot \Phi_{mean}) - \frac{\sigma^2}{2} \quad \text{(B-12)}$$

where

Φ_{RV} and Φ_{mean} are respectively the relative variance and the mean of 1 year averaged proton fluence at 1 AU from the sun in the corresponding energy range.

The values for Φ_{RV} and Φ_{mean} for different energy ranges during solar maximum are given in Table B-8 and Table B-9.

The parameter values given in Table B-8 and Table B-9 have been calculated at NASA for periods during solar active years. The latest update of these parameters, which are used for these tables, dates from 14 Nov. 2002.

The extension to higher energy (up to > 300 MeV) is done through using the probability parameters for the > 100 MeV fluence, φ (>100 MeV), and scaling the fluence according to Table B-9.

Tabulated values of the proton fluence as obtained from the ESP model for different confidence levels are given in Table I-4.

B.7 Solar ions model

Table B-10, Table B-11, and Table B-12 are derived from the CREME-96 solar proton worst 5-minute, worst day and worst week fluxes in an interplanetary environment. These tables are referred to in 9.2.2.

B.8 Geomagnetic shielding (Størmer theory)

At a given location in the field there are minimum cut-off energies necessary for ions to penetrate to that point. Størmer's theory gives a cut-off rigidity, P_c, for particle arrival at a point, depending on the point's geomagnetic R, λ coordinates and the angle of ion arrival from east, γ [RN.20].

$$P_c = \frac{\left\{M \cos^4 \lambda\right\}}{\left\{R^2\left[1+\left(1-\cos^3(\lambda)\cos(\gamma)\right)^{1/2}\right]^2\right\}} \quad \text{(B-13)}$$

M is the normalized dipole moment of the Earth. From this equation, it can be seen that cosmic rays penetrate the geomagnetic field more easily from the west (γ = 180°) than from the east (γ = 0). The R, λ coordinates can be computed from B and L according to the method of Roberts [RN.28]. For vertical arrival, the expression simplifies to:

$$P_c \cong \frac{16\cos^4(\lambda)}{R^2} = \frac{16}{L^2} GV \quad \text{(B-14)}$$

since γ =90° and $R = L \cos^2(\lambda)$

An approximate value of 16 for the constant M/4 is used to fit with observed effective cut-offs. Magnetospheric disturbances, which often follow solar-flares or CMEs, can result in a lowering of cut-off; this has been described by Adams et al. [RN.20] as:

$$\frac{AP_c}{P_c} = 0{,}54 \exp\left(-\frac{P_c}{2{,}9}\right) \quad \text{(B-15)}$$

with P_c in units of GV.

B.9 MOBE-DIC

B.9.1 Overview

MOBE-DIC (Model for Outer Belt Electrons for Dielectric Internal Charging) [RD.166], is based on Giove-A/Merlin-SURF data at MEO and from GOES data at GEO. The model provides electron fluxes during enhanced periods as a function of confidence level and location within the magnetosphere.

B.9.2 Spectral form

Differential flux (units: e/cm2/s/sr/MeV)

$f(E) = A \times e^{-\frac{E}{E_0}}$	(B-16)

Integral flux (units: e/cm2/s/sr)

$f(>E) = A \times \mathrm{E}_0 \times e^{-\frac{E}{E_0}}$	(B-17)

Where:

Values for A and E_0 are given Table B-1 for three confidence levels.

Table B-1: A and E_0 for three confidence levels

Fit Parameter	100 % (Worst Case)	99 %	90 %
Normalisation, A (e/cm²/s/sr/MeV)	2,76 x 10^7	1,19 x 10^7	6,94 x 10^6
Folding energy, E_0 (MeV)	0,836	0,696	0,552

B.9.3 L-shell profile

$F(L,E) = f(E) \times g(L,E)$	(B-18)

Where

$g(L,E) = 16 \times \frac{\tanh(0.6*(L-2.5))}{\cosh(1.5*(L-4.3))} \times \frac{g(4.5,E)}{12.76}$ 3<L<4.5

$g(L,E) = \frac{\max(g_1(L,E),g_2(L,E))}{g_1(4.7,E)}$ 4.5≤L<8

and

$g_1(L,E) = A_1 \times e^{\frac{-(L-4.5)^2}{2*\sigma^2}}$

$g_2(L,E) = A_2 \times e^{-0.6*(L-4.5)}$

The parameters, A1, A2 & σ are defined as follows (energy in MeV):

$$A_1(E) = 1.1 \times (1 - e^{-2.5\times(E-0.05)})$$

$$A_2(E) = 0.0871 \times E^3 - 0.585 \times E^2 + 1.005 \times E + 0.1436$$

$$\sigma(E) = 0.75 - 0.0878 \times E$$

The L-shell profile for integral flux is almost identical to the differential profile. However, an additional factor is applied to allow for the influence of changing L shell profile at higher energies.

$$F_{int}(L, > E) = f(> E) \times g(L, E) \times g_{cor}(L, E)$$

$$g_{cor}(L, E) = \frac{\int f(E) \times g(L, E)\, dE}{\int f(E)\, dE}$$

B.9.4 Magnetic latitude profile

This is taken from the FLUMIC3 model, which itself is based on Vette et al. [RN.10].

$$F(B/B_0, L, E) = F(L, E) \times h(B/B_0, L)$$

$$h(B/B_0, L) = \left(1 - \frac{0.52 \times \left(\frac{B}{B_0}\right)}{L^3}\right) \times \left(\frac{B}{B_0}\right)^{-m(L)}$$

$$m(L) = \max(9.767 - 2.87 \times L, 1.17 - 0.15 \times L, 0.6)$$

B.10 Tables

Table B-2: Minima and maxima of sunspot number cycles

Sunspot cycle cumber	Year of min	Smallest smoothed monthly mean	Year of max	Largest smoothed monthly mean	Rise to max (years)	Fall to min (years)	Cycle length (years)
1	1755,2	8,4	1761,5	86,5	6,3	5	11,3
2	1766,5	11,2	1769,7	115,8	3,2	5,8	9
3	1775,5	7,2	1778,4	158,5	2,9	6,3	9,2
4	1784,7	9,5	1788,1	141,2	3,4	10,2	13,6
5	1798,3	3,2	1805,2	49,2	6,9	5,4	12,3
6	1810,6	0	1816,4	48,7	5,8	6,9	12,7
7	1823,3	0,1	1829,9	71,7	6,6	4	10,6
8	1833,9	7,3	1837,2	146,9	3,3	6,3	9,6
9	1843,5	10,5	1848,1	131,6	4,6	7,9	12,5
10	1856	3,2	1860,1	97,9	4,1	7,1	11,2
11	1867,2	5,2	1870,6	140,5	3,4	8,3	11,7
12	1878,9	2,2	1883,9	74,6	5	5,7	10,7
13	1889,6	5	1894,1	87,9	4,5	7,6	12,1
14	1901,7	2,6	1907	64,2	5,3	6,6	11,9
15	1913,6	1,5	1917,6	105,4	4	6	10
16	1923,6	5,6	1928,4	78,1	4,8	5,4	10,2
17	1933,8	3,4	1937,4	119,2	3,6	6,8	10,4
18	1944,2	7,7	1947,5	151,8	3,3	6,8	10,1
19	1954,3	3,4	1957,9	201,3	3,6	7	10,6
20	1964,9	9,6	1968,9	110,6	4	7,6	11,6
21	1976,5	12,2	1979,9	164,5	3,4	6,9	10,3
22	1986,8	12,3	1989,6	158,5	2,8	6,8	9,7
23	1996,4 [a]	8,0	2001,9 [a]	120,8	5,5	7,0	12,5
24	2008,9	2,2	2014,3	116,4	5,4		

a. May 1996 marks the mathematical minimum of cycle 23. October 1996 marks the consensus minimum determined by an international group of solar physicists. April 2000 marks the mathematical maximum of cycle 23. However, several other solar indices recorded a higher secondary maximum in late 2001.

b. Similar to cycle 23 the solar cycle 24 also displayed a double peak in the sunspot number although the peak was observed in 2014,3 there was an earlier peak in 2011. Thus, the maximum date used to estimate future solar maxima Annex B.1 is selected to be 2013,5.

Table B-3: IGE-2006 GEO average model – electron flux ($kev^{-1}cm^{-2}s^{-1}sr^{-1}$) according to year in the solar cycle (referred to solar min: 0) and for different energies for a mission duration of 1 year.

(Part 1 of 2)

Energy (keV)	-6	-5	-4	-3	-2	-1	0 (solar min)	1	2	3	4
9,17E-01	1,35E+07	1,43E+07	1,25E+07	9,80E+06	8,57E+06	6,93E+06	7,13E+06	7,87E+06	8,99E+06	9,98E+06	1,39E+07
1,20E+00	1,15E+07	1,21E+07	1,06E+07	8,41E+06	7,29E+06	6,01E+06	6,22E+06	6,86E+06	7,80E+06	8,58E+06	1,19E+07
1,57E+00	9,85E+06	1,04E+07	9,13E+06	7,32E+06	6,34E+06	5,28E+06	5,47E+06	6,02E+06	6,85E+06	7,47E+06	1,02E+07
2,05E+00	8,39E+06	8,84E+06	7,80E+06	6,32E+06	5,52E+06	4,63E+06	4,53E+06	4,71E+06	5,70E+06	6,27E+06	8,53E+06
2,67E+00	7,07E+06	7,42E+06	6,62E+06	5,42E+06	4,78E+06	4,01E+06	3,91E+06	4,02E+06	4,93E+06	5,36E+06	7,21E+06
3,47E+00	5,85E+06	6,06E+06	5,52E+06	4,59E+06	4,08E+06	3,40E+06	3,54E+06	3,85E+06	4,45E+06	4,70E+06	6,15E+06
4,53E+00	4,67E+06	4,76E+06	4,45E+06	3,77E+06	3,38E+06	2,79E+06	2,96E+06	3,21E+06	3,69E+06	3,85E+06	4,94E+06
5,90E+00	3,57E+06	3,58E+06	3,47E+06	2,99E+06	2,70E+06	2,19E+06	2,35E+06	2,52E+06	2,88E+06	3,00E+06	3,80E+06
7,73E+00	2,57E+06	2,54E+06	2,56E+06	2,24E+06	2,04E+06	1,61E+06	1,75E+06	1,84E+06	2,10E+06	2,20E+06	2,76E+06
1,02E+01	1,73E+06	1,68E+06	1,77E+06	1,57E+06	1,45E+06	1,10E+06	1,19E+06	1,24E+06	1,41E+06	1,51E+06	1,87E+06
1,33E+01	1,08E+06	1,05E+06	1,15E+06	1,01E+06	9,56E+05	7,09E+05	7,50E+05	7,72E+05	8,79E+05	9,68E+05	1,18E+06
1,74E+01	6,28E+05	6,10E+05	6,99E+05	6,06E+05	5,85E+05	4,28E+05	4,35E+05	4,39E+05	5,09E+05	6,17E+05	7,05E+05
3,00E+01	1,92E+05	1,89E+05	2,39E+05	2,13E+05	2,42E+05	2,14E+05	1,74E+05	1,61E+05	1,92E+05	2,14E+05	1,59E+05
6,12E+01	6,66E+04	6,42E+04	8,20E+04	7,54E+04	8,92E+04	7,76E+04	6,39E+04	5,87E+04	6,82E+04	7,30E+04	5,52E+04
8,87E+01	2,62E+04	2,48E+04	3,19E+04	3,02E+04	3,70E+04	3,18E+04	2,64E+04	2,41E+04	2,74E+04	2,83E+04	2,18E+04
1,26E+02	9,18E+03	8,52E+03	1,11E+04	1,08E+04	1,35E+04	1,17E+04	9,86E+03	9,02E+03	1,00E+04	9,90E+03	7,83E+03
1,84E+02	3,45E+03	3,15E+03	4,13E+03	4,22E+03	5,37E+03	4,71E+03	4,02E+03	3,66E+03	3,91E+03	3,65E+03	2,99E+03
2,66E+02	1,23E+03	1,10E+03	1,48E+03	1,58E+03	2,07E+03	1,79E+03	1,53E+03	1,36E+03	1,43E+03	1,27E+03	1,07E+03
3,97E+02	3,83E+02	3,23E+02	4,77E+02	5,41E+02	7,31E+02	6,22E+02	5,24E+02	4,53E+02	4,64E+02	3,87E+02	3,33E+02
6,12E+02	7,56E+01	6,33E+01	9,96E+01	1,22E+02	1,71E+02	1,45E+02	1,17E+02	9,93E+01	9,87E+01	7,70E+01	6,57E+01
9,08E+02	1,81E+01	1,57E+01	2,80E+01	3,51E+01	5,39E+01	4,28E+01	3,26E+01	2,73E+01	2,66E+01	1,97E+01	1,60E+01

Table B-3: IGE-2006 GEO average model – electron flux ($kev^{-1}cm^{-2}s^{-1}sr^{-1}$) according to year in the solar cycle (referred to solar min: 0) and for different energies for a mission duration of 1 year.

(Part 2 of 2)

1,29E+03	4,63E+00	4,56E+00	8,68E+00	1,11E+01	1,86E+01	1,37E+01	9,84E+00	8,07E+00	7,78E+00	5,52E+00	4,25E+00
1,99E+03	5,79E-01	6,73E-01	1,39E+00	1,81E+00	3,41E+00	2,28E+00	1,52E+00	1,22E+00	1,15E+00	7,74E-01	5,56E-01
2,44E+03	1,96E-01	2,45E-01	5,26E-01	6,92E-01	1,37E+00	8,79E-01	5,65E-01	4,48E-01	4,21E-01	2,76E-01	1,92E-01
3,07E+03	5,29E-02	7,23E-02	1,62E-01	2,15E-01	4,54E-01	2,76E-01	1,71E-01	1,34E-01	1,24E-01	7,93E-02	5,30E-02
3,97E+03	9,09E-03	1,37E-02	3,21E-02	4,32E-02	9,74E-02	5,60E-02	3,31E-02	2,56E-02	2,36E-02	1,46E-02	9,36E-03
5,20E+03	1,27E-03	2,12E-03	5,23E-03	7,12E-03	1,72E-02	9,33E-03	5,27E-03	4,01E-03	3,67E-03	2,19E-03	1,35E-03

:

Table B-4: IGE 2006 GEO upper case model - maximum electron flux ($kev^{-1}cm^{-2}s^{-1}sr^{-1}$) according to year in the solar cycle (referred to solar min: 0) and for different energies for a mission duration of 1 year.

(Part 1 of 2)

Energy (keV)	-6	-5	-4	-3	-2	-1	0 (solar min)	1	2	3	4
9,17E-01	1,89E+07	2,00E+07	1,75E+07	1,37E+07	1,20E+07	9,71E+06	9,99E+06	1,10E+07	1,26E+07	1,40E+07	1,95E+07
1,20E+00	1,61E+07	1,69E+07	1,48E+07	1,18E+07	1,02E+07	8,42E+06	8,71E+06	9,61E+06	1,09E+07	1,20E+07	1,67E+07
1,57E+00	1,38E+07	1,46E+07	1,28E+07	1,03E+07	8,88E+06	7,40E+06	7,66E+06	8,43E+06	9,60E+06	1,05E+07	1,43E+07
2,05E+00	1,18E+07	1,24E+07	1,09E+07	8,86E+06	7,73E+06	6,49E+06	6,35E+06	6,60E+06	7,99E+06	8,79E+06	1,20E+07
2,67E+00	9,91E+06	1,04E+07	9,28E+06	7,60E+06	6,70E+06	5,62E+06	5,48E+06	5,63E+06	6,91E+06	7,51E+06	1,01E+07
3,47E+00	8,20E+06	8,50E+06	7,74E+06	6,44E+06	5,72E+06	4,77E+06	4,96E+06	5,40E+06	6,24E+06	6,59E+06	8,62E+06
4,53E+00	6,55E+06	6,68E+06	6,24E+06	5,29E+06	4,74E+06	3,91E+06	4,15E+06	4,50E+06	5,18E+06	5,40E+06	6,93E+06
5,90E+00	5,01E+06	5,02E+06	4,87E+06	4,20E+06	3,79E+06	3,07E+06	3,30E+06	3,54E+06	4,04E+06	4,21E+06	5,33E+06
7,73E+00	3,61E+06	3,57E+06	3,60E+06	3,15E+06	2,87E+06	2,26E+06	2,46E+06	2,58E+06	2,95E+06	3,09E+06	3,88E+06

Table B-4: IGE 2006 GEO upper case model - maximum electron flux (kev-1cm-2s-1sr-1) according to year in the solar cycle (referred to solar min: 0) and for different energies for a mission duration of 1 year.

(Part 2 of 2)

1,02E+01	2,43E+06	2,36E+06	2,49E+06	2,21E+06	2,04E+06	1,55E+06	1,67E+06	1,74E+06	1,98E+06	2,12E+06	2,63E+06
1,33E+01	1,52E+06	1,48E+06	1,62E+06	1,42E+06	1,35E+06	9,98E+05	1,06E+06	1,09E+06	1,24E+06	1,36E+06	1,66E+06
1,74E+01	8,86E+05	8,60E+05	9,86E+05	8,55E+05	8,25E+05	6,04E+05	6,14E+05	6,19E+05	7,18E+05	8,70E+05	9,94E+05
3,00E+01	2,72E+05	2,68E+05	3,39E+05	3,02E+05	3,43E+05	3,03E+05	2,47E+05	2,28E+05	2,72E+05	3,03E+05	2,25E+05
6,12E+01	9,57E+04	9,22E+04	1,18E+05	1,08E+05	1,28E+05	1,11E+05	9,18E+04	8,43E+04	9,80E+04	1,05E+05	7,93E+04
8,87E+01	3,81E+04	3,60E+04	4,64E+04	4,39E+04	5,38E+04	4,62E+04	3,84E+04	3,50E+04	3,98E+04	4,11E+04	3,17E+04
1,26E+02	1,35E+04	1,26E+04	1,64E+04	1,59E+04	1,99E+04	1,73E+04	1,45E+04	1,33E+04	1,48E+04	1,46E+04	1,16E+04
1,84E+02	5,21E+03	4,76E+03	6,24E+03	6,37E+03	8,11E+03	7,11E+03	6,07E+03	5,53E+03	5,91E+03	5,51E+03	4,52E+03
2,66E+02	1,92E+03	1,72E+03	2,31E+03	2,46E+03	3,23E+03	2,79E+03	2,39E+03	2,12E+03	2,23E+03	1,98E+03	1,67E+03
3,97E+02	6,27E+02	5,29E+02	7,81E+02	8,86E+02	1,20E+03	1,02E+03	8,58E+02	7,42E+02	7,60E+02	6,34E+02	5,46E+02
6,12E+02	1,34E+02	1,12E+02	1,76E+02	2,16E+02	3,02E+02	2,56E+02	2,07E+02	1,75E+02	1,74E+02	1,36E+02	1,16E+02
9,08E+02	3,52E+01	3,05E+01	5,45E+01	6,83E+01	1,05E+02	8,32E+01	6,34E+01	5,31E+01	5,17E+01	3,83E+01	3,11E+01
1,29E+03	1,01E+01	9,91E+00	1,89E+01	2,41E+01	4,04E+01	2,98E+01	2,14E+01	1,75E+01	1,69E+01	1,20E+01	9,24E+00
1,99E+03	1,50E+00	1,75E+00	3,61E+00	4,70E+00	8,85E+00	5,91E+00	3,94E+00	3,16E+00	2,98E+00	2,01E+00	1,44E+00
2,44E+03	5,61E-01	7,02E-01	1,51E+00	1,98E+00	3,92E+00	2,52E+00	1,62E+00	1,28E+00	1,21E+00	7,90E-01	5,50E-01
3,07E+03	1,72E-01	2,34E-01	5,25E-01	6,97E-01	1,47E+00	8,95E-01	5,54E-01	4,34E-01	4,02E-01	2,57E-01	1,72E-01
3,97E+03	3,44E-02	5,18E-02	1,21E-01	1,63E-01	3,68E-01	2,12E-01	1,25E-01	9,68E-02	8,93E-02	5,52E-02	3,54E-02
5,20E+03	5,74E-03	9,58E-03	2,36E-02	3,22E-02	7,77E-02	4,22E-02	2,38E-02	1,81E-02	1,66E-02	9,90E-03	6,10E-03

Table B-5: MEOv2 average case model - average electron flux ($Mev^{-1}cm^{-2}s^{-1}sr^{-1}$) according to year in the solar cycle (referred to solar min: 0) and for different energies for a mission duration of 1 year.

Energy (MeV)	-6	-5	-4	-3	-2	-1	0 (solar min)	1	2	3	4
0,28	2,90E+06	2,89E+06	3,79E+06	3,95E+06	4,93E+06	4,31E+06	3,88E+06	3,46E+06	3,69E+06	3,36E+06	2,90E+06
0,4	1,61E+06	1,57E+06	2,25E+06	2,53E+06	3,35E+06	2,89E+06	2,47E+06	2,15E+06	2,22E+06	1,87E+06	1,61E+06
0,56	6,75E+05	6,48E+05	1,01E+06	1,22E+06	1,70E+06	1,44E+06	1,17E+06	1,00E+06	9,98E+05	7,91E+05	6,75E+05
0,8	2,00E+05	1,94E+05	3,33E+05	4,14E+05	6,19E+05	5,03E+05	3,89E+05	3,28E+05	3,21E+05	2,42E+05	2,00E+05
1,12	5,80E+04	5,99E+04	1,11E+05	1,40E+05	2,27E+05	1,72E+05	1,27E+05	1,05E+05	1,02E+05	7,35E+04	5,80E+04
1,6	1,21E+04	1,37E+04	2,70E+04	3,48E+04	6,14E+04	4,34E+04	3,01E+04	2,44E+04	2,33E+04	1,61E+04	1,21E+04
2,24	2,15E+03	2,62E+03	5,45E+03	7,12E+03	1,35E+04	8,98E+03	5,94E+03	4,75E+03	4,49E+03	3,01E+03	2,15E+03

Table B-6: MEOv2 upper case model - maximum electron flux ($Mev^{-1}cm^{-2}s^{-1}sr^{-1}$) according to year in the solar cycle (referred to solar min: 0) and for different energies for a mission duration of 1 year.

Energy (MeV)	-6	-5	-4	-3	-2	-1	0 (solar min)	1	2	3	4
0,28	7,39E+06	7,40E+06	9,54E+06	9,79E+06	1,20E+07	1,06E+07	9,65E+06	8,65E+06	9,27E+06	8,55E+06	7,39E+06
0,4	4,38E+06	4,27E+06	6,03E+06	6,73E+06	8,78E+06	7,61E+06	6,58E+06	5,74E+06	5,94E+06	5,05E+06	4,38E+06
0,56	1,99E+06	1,91E+06	2,95E+06	3,53E+06	4,86E+06	4,16E+06	3,41E+06	2,92E+06	2,92E+06	2,32E+06	1,99E+06
0,8	6,48E+05	6,24E+05	1,06E+06	1,32E+06	1,94E+06	1,60E+06	1,25E+06	1,05E+06	1,03E+06	7,82E+05	6,48E+05
1,12	2,13E+05	2,18E+05	4,01E+05	5,06E+05	8,09E+05	6,22E+05	4,61E+05	3,82E+05	3,71E+05	2,69E+05	2,13E+05
1,6	5,24E+04	5,88E+04	1,15E+05	1,48E+05	2,60E+05	1,85E+05	1,29E+05	1,05E+05	1,00E+05	6,96E+04	5,24E+04
2,24	1,11E+04	1,34E+04	2,77E+04	3,61E+04	6,78E+04	4,55E+04	3,03E+04	2,43E+04	2,30E+04	1,54E+04	1,11E+04

Table B-7: Worst case spectrum for geostationary orbits

Electron Energy, MeV	Flux, $cm^{-2}s^{-1}sr^{-1}$
0,225	6,5E6
0,315	4,2E6
0,5	2,2E6
0,75	1,0E6
1,1	4,4E5
1,5	2,0E5
1,8	1,05E5
3,5	6,4E3

Table B-8: Values of the parameters for the ESP model

Energy range	Φ_{mean} (cm^{-2})	Φ_{RV}
> 1 MeV	8,877E+10	0,940
> 3 MeV	3,297E+10	3,038
> 5 MeV	1,973E+10	5,250
> 7 MeV	1,371E+10	7,575
> 10 MeV	9,089E+09	11,239
> 15 MeV	5,476E+09	17,675
> 20 MeV	3,707E+09	24,351
> 25 MeV	2,687E+09	31,126
> 30 MeV	2,034E+09	37,889
> 35 MeV	1,589E+09	44,572
> 40 MeV	1,273E+09	51,130
> 45 MeV	1,038E+09	57,504
> 50 MeV	8,602E+08	63,674
> 55 MeV	7,215E+08	69,642
> 60 MeV	6,117E+08	75,368
> 70 MeV	4,518E+08	86,122
> 80 MeV	3,431E+08	95,852
> 90 MeV	2,665E+08	104,635
> 100 MeV	2,109E+08	112,465

Table B-9: Values to scale fluence from >100 MeV to >300 MeV

Energy Range:	Fluence (p cm^{-2}):
> 125 MeV	0,603 x φ(>100 MeV)
> 150 MeV	0,390 x φ(>100 MeV)
> 175 MeV	0,267 x φ(>100 MeV)
> 200 MeV	0,191 x φ(>100 MeV)
> 225 MeV	0,141 x φ(>100 MeV)
> 250 MeV	0,107 x φ(>100 MeV)
> 275 MeV	0,0823 x φ(>100 MeV)
> 300 MeV	0,0647 x φ(>100 MeV)

Table B-10: CREME-96 solar ion worst 5-minute fluxes in an interplanetary environment (Part 1 of 2)

	Ion Flux [# $m^{-2}s^{-1}sr^{-1}(MeV/nucl)^{-1}$]					
Energy [MeV/nucl]	H	He	C	N	O	Fe
1,0E+00	1,36E+09	5,25E+07	5,05E+05	1,29E+05	1,07E+06	4,11E+05
2,0E+00	6,36E+08	2,09E+07	2,01E+05	5,15E+04	4,27E+05	1,64E+05
3,0E+00	3,81E+08	1,11E+07	1,07E+05	2,74E+04	2,27E+05	8,70E+04
4,0E+00	2,56E+08	6,76E+06	6,50E+04	1,66E+04	1,38E+05	5,30E+04
5,0E+00	1,83E+08	4,47E+06	4,29E+04	1,10E+04	9,12E+04	3,50E+04
6,0E+00	1,37E+08	3,12E+06	3,00E+04	7,69E+03	6,38E+04	2,45E+04
7,0E+00	1,06E+08	2,27E+06	2,18E+04	5,59E+03	4,64E+04	1,78E+04
8,0E+00	8,44E+07	1,71E+06	1,64E+04	4,20E+03	3,48E+04	1,34E+04
9,0E+00	6,83E+07	1,31E+06	1,26E+04	3,23E+03	2,68E+04	1,03E+04
1,0E+01	5,61E+07	1,03E+06	9,91E+03	2,54E+03	2,11E+04	8,08E+03
2,0E+01	1,32E+07	1,25E+05	1,20E+03	3,09E+02	2,56E+03	1,37E+03
3,0E+01	4,89E+06	2,30E+04	2,21E+02	5,66E+01	4,69E+02	2,96E+02
4,0E+01	2,26E+06	6,90E+03	6,62E+01	1,70E+01	1,41E+02	7,94E+01
5,0E+01	1,20E+06	2,71E+03	2,61E+01	6,68E+00	5,54E+01	2,87E+01
6,0E+01	6,95E+05	1,27E+03	1,22E+01	3,12E+00	2,59E+01	1,25E+01
7,0E+01	4,31E+05	6,67E+02	6,40E+00	1,64E+00	1,36E+01	6,18E+00
8,0E+01	2,81E+05	3,83E+02	3,67E+00	9,42E-01	7,81E+00	3,37E+00
9,0E+01	1,91E+05	2,35E+02	2,25E+00	5,77E-01	4,79E+00	1,97E+00
1,0E+02	1,35E+05	1,52E+02	1,46E+00	3,73E-01	3,09E+00	1,22E+00
2,0E+02	1,18E+04	8,78E+00	8,43E-02	2,16E-02	1,79E-01	5,41E-02
3,0E+02	2,70E+03	1,72E+00	1,65E-02	4,23E-03	3,50E-02	9,03E-03
4,0E+02	9,45E+02	5,53E-01	5,31E-03	1,36E-03	1,13E-02	2,60E-03

Table B-10: CREME-96 solar ion worst 5-minute fluxes in an interplanetary environment

(Part 2 of 2)

	Ion Flux [# $m^{-2}s^{-1}sr^{-1}(MeV/nucl)^{-1}$]					
Energy [MeV/nucl]	**H**	**He**	**C**	**N**	**O**	**Fe**
5,0E+02	4,00E+02	2,20E-01	2,11E-03	5,40E-04	4,48E-03	9,47E-04
6,0E+02	1,74E+02	1,03E-01	9,91E-04	2,54E-04	2,11E-03	4,14E-04
7,0E+02	9,16E+01	5,45E-02	5,24E-04	1,34E-04	1,11E-03	2,06E-04
8,0E+02	5,27E+01	3,14E-02	3,01E-04	7,72E-05	6,40E-04	1,13E-04
9,0E+02	3,24E+01	1,93E-02	1,85E-04	4,74E-05	3,93E-04	6,60E-05
1,0E+03	2,09E+01	1,24E-02	1,20E-04	3,06E-05	2,54E-04	4,10E-05
2,0E+03	1,19E+00	7,06E-04	6,78E-06	1,74E-06	1,44E-05	1,77E-06
3,0E+03	2,21E-01	1,32E-04	1,26E-06	3,24E-07	2,69E-06	2,83E-07
4,0E+03	6,72E-02	4,00E-05	3,84E-07	9,85E-08	8,17E-07	7,68E-08
5,0E+03	2,67E-02	1,59E-05	1,53E-07	3,91E-08	3,24E-07	2,80E-08
6,0E+03	1,25E-02	7,47E-06	7,17E-08	1,84E-08	1,52E-07	1,22E-08
7,0E+03	6,63E-03	3,94E-06	3,79E-08	9,71E-09	8,05E-08	6,09E-09
8,0E+03	3,81E-03	2,27E-06	2,18E-08	5,58E-09	4,63E-08	3,33E-09
9,0E+03	2,34E-03	1,39E-06	1,34E-08	3,43E-09	2,84E-08	1,95E-09
1,0E+04	1,51E-03	9,01E-07	8,65E-09	2,22E-09	1,84E-08	1,21E-09
2,0E+04	8,58E-05	5,11E-08	4,90E-10	1,26E-10	1,04E-09	5,24E-11
3,0E+04	1,60E-05	9,53E-09	9,15E-11	2,34E-11	1,94E-10	8,35E-12
4,0E+04	4,86E-06	2,89E-09	2,78E-11	7,13E-12	5,91E-11	2,27E-12
5,0E+04	1,93E-06	1,15E-09	1,10E-11	2,83E-12	2,35E-11	8,25E-13
6,0E+04	9,08E-07	5,40E-10	5,19E-12	1,33E-12	1,10E-11	3,61E-13
7,0E+04	4,79E-07	2,85E-10	2,74E-12	7,02E-13	5,82E-12	1,80E-13
8,0E+04	2,76E-07	1,64E-10	1,58E-12	4,04E-13	3,35E-12	9,82E-14
9,0E+04	1,69E-07	1,01E-10	9,68E-13	2,48E-13	2,06E-12	5,76E-14
1,0E+05	1,09E-07	6,52E-11	6,26E-13	1,60E-13	1,33E-12	3,57E-14

Table B-11: CREME-96 solar ion worst day fluxes in an interplanetary environment (Part 1 of 2)

	Ion Flux [# $m^{-2}s^{-1}sr^{-1}(MeV/nucl)^{-1}$]					
Energy [MeV/nucl]	**H**	**He**	**C**	**N**	**O**	**Fe**
1,0E+00	3,24E+08	1,25E+07	1,20E+05	3,08E+04	2,56E+05	9,81E+04
2,0E+00	1,54E+08	5,07E+06	4,87E+04	1,25E+04	1,03E+05	3,97E+04
3,0E+00	9,34E+07	2,72E+06	2,61E+04	6,70E+03	5,55E+04	2,13E+04
4,0E+00	6,32E+07	1,67E+06	1,60E+04	4,11E+03	3,41E+04	1,31E+04
5,0E+00	4,57E+07	1,11E+06	1,07E+04	2,74E+03	2,27E+04	8,71E+03
6,0E+00	3,44E+07	7,82E+05	7,51E+03	1,93E+03	1,60E+04	6,13E+03
7,0E+00	2,68E+07	5,73E+05	5,50E+03	1,41E+03	1,17E+04	4,48E+03
8,0E+00	2,14E+07	4,32E+05	4,15E+03	1,06E+03	8,82E+03	3,38E+03
9,0E+00	1,74E+07	3,34E+05	3,21E+03	8,23E+02	6,82E+03	2,62E+03
1,0E+01	1,44E+07	2,64E+05	2,53E+03	6,49E+02	5,38E+03	2,06E+03
2,0E+01	3,47E+06	3,31E+04	3,18E+02	8,14E+01	6,75E+02	3,61E+02
3,0E+01	1,31E+06	6,17E+03	5,93E+01	1,52E+01	1,26E+02	7,95E+01
4,0E+01	6,16E+05	1,88E+03	1,80E+01	4,62E+00	3,83E+01	2,16E+01
5,0E+01	3,29E+05	7,45E+02	7,15E+00	1,83E+00	1,52E+01	7,86E+00
6,0E+01	1,92E+05	3,50E+02	3,36E+00	8,62E-01	7,14E+00	3,44E+00
7,0E+01	1,19E+05	1,85E+02	1,78E+00	4,55E-01	3,77E+00	1,71E+00
8,0E+01	7,82E+04	1,06E+02	1,02E+00	2,62E-01	2,17E+00	9,35E-01
9,0E+01	5,33E+04	6,53E+01	6,27E-01	1,61E-01	1,33E+00	5,49E-01
1,0E+02	3,75E+04	4,22E+01	4,05E-01	1,04E-01	8,62E-01	3,40E-01
2,0E+02	3,22E+03	2,39E+00	2,30E-02	5,89E-03	4,89E-02	1,47E-02
3,0E+02	7,02E+02	4,47E-01	4,29E-03	1,10E-03	9,12E-03	2,35E-03
4,0E+02	2,32E+02	1,36E-01	1,30E-03	3,34E-04	2,77E-03	6,38E-04
5,0E+02	9,29E+01	5,39E-02	5,17E-04	1,33E-04	1,10E-03	2,32E-04
6,0E+02	3,91E+01	2,53E-02	2,43E-04	6,23E-05	5,17E-04	1,02E-04
7,0E+02	2,06E+01	1,34E-02	1,28E-04	3,29E-05	2,73E-04	5,06E-05
8,0E+02	1,18E+01	7,69E-03	7,39E-05	1,89E-05	1,57E-04	2,76E-05
9,0E+02	7,27E+00	4,72E-03	4,54E-05	1,16E-05	9,64E-05	1,62E-05
1,0E+03	4,70E+00	3,05E-03	2,93E-05	7,52E-06	6,23E-05	1,01E-05
2,0E+03	2,66E-01	1,73E-04	1,66E-06	4,26E-07	3,53E-06	4,35E-07
3,0E+03	4,97E-02	3,23E-05	3,10E-07	7,95E-08	6,59E-07	6,94E-08
4,0E+03	1,51E-02	9,82E-06	9,43E-08	2,42E-08	2,00E-07	1,88E-08
5,0E+03	6,00E-03	3,90E-06	3,74E-08	9,59E-09	7,95E-08	6,86E-09
6,0E+03	2,82E-03	1,83E-06	1,76E-08	4,51E-09	3,74E-08	3,00E-09

Table B-11: CREME-96 solar ion worst day fluxes in an interplanetary environment

(Part 2 of 2)

	Ion Flux [# $m^{-2}s^{-1}sr^{-1}(MeV/nucl)^{-1}$]					
Energy [MeV/nucl]	**H**	**He**	**C**	**N**	**O**	**Fe**
7,0E+03	1,49E-03	9,68E-07	9,29E-09	2,38E-09	1,97E-08	1,49E-09
8,0E+03	8,57E-04	5,57E-07	5,35E-09	1,37E-09	1,14E-08	8,16E-10
9,0E+03	5,26E-04	3,42E-07	3,28E-09	8,41E-10	6,98E-09	4,79E-10
1,0E+04	3,40E-04	2,21E-07	2,12E-09	5,44E-10	4,51E-09	2,97E-10
2,0E+04	1,93E-05	1,25E-08	1,20E-10	3,08E-11	2,56E-10	1,29E-11
3,0E+04	3,60E-06	2,34E-09	2,24E-11	5,75E-12	4,77E-11	2,05E-12
4,0E+04	1,09E-06	7,10E-10	6,82E-12	1,75E-12	1,45E-11	5,56E-13
5,0E+04	4,34E-07	2,82E-10	2,71E-12	6,94E-13	5,75E-12	2,03E-13
6,0E+04	2,04E-07	1,33E-10	1,27E-12	3,26E-13	2,70E-12	8,87E-14
7,0E+04	1,08E-07	7,00E-11	6,72E-13	1,72E-13	1,43E-12	4,41E-14
8,0E+04	6,20E-08	4,03E-11	3,87E-13	9,91E-14	8,22E-13	2,41E-14
9,0E+04	3,81E-08	2,47E-11	2,37E-13	6,09E-14	5,05E-13	1,41E-14
1,0E+05	2,46E-08	1,60E-11	1,54E-13	3,93E-14	3,26E-13	8,77E-15

Table B-12: CREME-96 solar ion worst week fluxes in an interplanetary environment (Part 1 of 2)

	Ion Flux [# $m^{-2}s^{-1}sr^{-1}(MeV/nucl)^{-1}$]					
Energy [MeV/nucl]	**H**	**He**	**C**	**N**	**O**	**Fe**
1,0E+00	4,64E+07	2,36E+06	2,75E+04	7,04E+03	5,84E+04	1,57E+04
2,0E+00	2,28E+07	9,53E+05	1,11E+04	2,85E+03	2,36E+04	6,34E+03
3,0E+00	1,41E+07	5,12E+05	5,97E+03	1,53E+03	1,27E+04	3,41E+03
4,0E+00	9,77E+06	3,14E+05	3,66E+03	9,39E+02	7,79E+03	2,09E+03
5,0E+00	7,19E+06	2,09E+05	2,44E+03	6,25E+02	5,19E+03	1,39E+03
6,0E+00	5,51E+06	1,47E+05	1,72E+03	4,40E+02	3,65E+03	9,80E+02
7,0E+00	4,36E+06	1,08E+05	1,26E+03	3,22E+02	2,67E+03	7,17E+02
8,0E+00	3,53E+06	8,13E+04	9,48E+02	2,43E+02	2,02E+03	5,41E+02
9,0E+00	2,91E+06	6,29E+04	7,33E+02	1,88E+02	1,56E+03	4,19E+02
1,0E+01	2,44E+06	4,96E+04	5,78E+02	1,48E+02	1,23E+03	3,30E+02
2,0E+01	6,61E+05	5,20E+03	6,06E+01	1,55E+01	1,29E+02	4,93E+01
3,0E+01	2,74E+05	1,13E+03	1,32E+01	3,37E+00	2,80E+01	1,07E+01
4,0E+01	1,38E+05	3,81E+02	4,45E+00	1,14E+00	9,45E+00	3,63E+00
5,0E+01	7,90E+04	1,64E+02	1,92E+00	4,92E-01	4,08E+00	1,57E+00
6,0E+01	4,88E+04	8,27E+01	9,65E-01	2,47E-01	2,05E+00	7,91E-01
7,0E+01	3,20E+04	4,63E+01	5,40E-01	1,38E-01	1,15E+00	4,43E-01
8,0E+01	2,20E+04	2,80E+01	3,26E-01	8,36E-02	6,94E-01	2,68E-01
9,0E+01	1,56E+04	1,80E+01	2,09E-01	5,37E-02	4,45E-01	1,72E-01
1,0E+02	1,14E+04	1,21E+01	1,41E-01	3,61E-02	2,99E-01	1,16E-01
2,0E+02	1,27E+03	8,86E-01	1,03E-02	2,65E-03	2,20E-02	1,28E-02
3,0E+02	3,16E+02	1,92E-01	2,24E-03	5,74E-04	4,76E-03	4,00E-03
4,0E+02	1,13E+02	6,50E-02	7,58E-04	1,94E-04	1,61E-03	1,76E-03
5,0E+02	4,79E+01	2,80E-02	3,27E-04	8,38E-05	6,95E-04	9,28E-04
6,0E+02	2,13E+01	1,41E-02	1,64E-04	4,21E-05	3,50E-04	5,51E-04
7,0E+02	1,19E+01	7,89E-03	9,20E-05	2,36E-05	1,96E-04	3,54E-04
8,0E+02	7,20E+00	4,77E-03	5,56E-05	1,43E-05	1,18E-04	2,42E-04
9,0E+02	4,62E+00	3,06E-03	3,57E-05	9,14E-06	7,58E-05	1,73E-04
1,0E+03	3,11E+00	2,06E-03	2,40E-05	6,15E-06	5,10E-05	1,28E-04
2,0E+03	2,30E-01	1,51E-04	1,76E-06	4,51E-07	3,74E-06	1,76E-05
3,0E+03	5,00E-02	3,27E-05	3,82E-07	9,79E-08	8,12E-07	5,51E-06
4,0E+03	1,69E-02	1,11E-05	1,29E-07	3,31E-08	2,75E-07	2,42E-06
5,0E+03	7,31E-03	4,78E-06	5,57E-08	1,43E-08	1,18E-07	1,28E-06
6,0E+03	3,68E-03	2,40E-06	2,80E-08	7,18E-09	5,96E-08	7,58E-07

Table B-12: CREME-96 solar ion worst week fluxes in an interplanetary environment

(Part 2 of 2)

	Ion Flux [# $m^{-2}s^{-1}sr^{-1}(MeV/nucl)^{-1}$]					
Energy [MeV/nucl]	**H**	**He**	**C**	**N**	**O**	**Fe**
7,0E+03	2,06E-03	1,34E-06	1,57E-08	4,02E-09	3,33E-08	4,88E-07
8,0E+03	1,25E-03	8,13E-07	9,48E-09	2,43E-09	2,01E-08	3,33E-07
9,0E+03	8,02E-04	5,21E-07	6,08E-09	1,56E-09	1,29E-08	2,38E-07
1,0E+04	5,40E-04	3,51E-07	4,09E-09	1,05E-09	8,69E-09	1,76E-07
2,0E+04	3,98E-05	2,57E-08	3,00E-10	7,69E-11	6,38E-10	2,42E-08
3,0E+04	8,66E-06	5,58E-09	6,51E-11	1,67E-11	1,38E-10	7,59E-09
4,0E+04	2,94E-06	1,89E-09	2,20E-11	5,64E-12	4,68E-11	3,33E-09
5,0E+04	1,27E-06	8,14E-10	9,49E-12	2,43E-12	2,02E-11	1,76E-09
6,0E+04	6,39E-07	4,09E-10	4,78E-12	1,22E-12	1,02E-11	1,04E-09
7,0E+04	3,58E-07	2,29E-10	2,67E-12	6,85E-13	5,68E-12	6,72E-10
8,0E+04	2,17E-07	1,38E-10	1,62E-12	4,14E-13	3,43E-12	4,59E-10
9,0E+04	1,39E-07	8,88E-11	1,04E-12	2,66E-13	2,20E-12	3,27E-10
1,0E+05	9,35E-08	5,97E-11	6,97E-13	1,79E-13	1,48E-12	2,42E-10

Annex C (normative)
Space debris and meteoroids

C.1 Flux models

C.1.1 <<deleted>>

NOTE .

C.1.2 <<deleted>>

C.1.3 <<deleted>>

.

C.1.4 Meteoroid streams

C.1.4.1. Introduction and description

Table C-2 gives the parameters for the main annual meteor streams. From these stream parameters fluxes are derived according to the method given in C.1.4.2.

The meteoroid streams model is based on a method by N. McBride [RD.28] to derive meteoroid fluxes from meteor data. The present reference model uses data for 50 annual meteor streams as given by P. Jenniskens [RD.29]. These data were collected by a large number of observers over a 10 year period from observation sites in both the northern and southern hemispheres.

The meteoroid streams model below is implemented in MASTER-8 [RN.26] and in ESABASE2/DEBRIS [RD.30].

C.1.4.2. Meteor stream fluxes

The meteoroid streams model is based on a method by N. McBride [RD.28] to derive meteoroid fluxes from meteor data. The present reference model uses data for 50 annual meteor streams as given by P. Jenniskens [RD.29]. These data were collected by a large number of observers over a 10 year period from observation sites in both the northern and southern hemispheres.

The meteor stream geometry and activity at shower maximum is defined by:

- The solar longitude λ at shower maximum λ_{max}.
- The maximum zenithal hourly rate ZHR_{max} , which is the number of 'visible' meteors seen after various observer and location related corrections have been applied.
- Apparent radiant position in RA (right ascension of the radiant) and Dec (declination of the radiant). These values are tabulated in Table C-2 at an epoch defined by the solar longitude λ^0.
- The geocentric meteoroid speeds, defined as the final geocentric velocity V_∞ (in km s^{-1}) as the meteoroids reach the top of the atmosphere.

The right ascension of the radiant and for the declination for an instantaneous value of the solar longitude λ are obtained by

$$RA(\lambda) = RA(\lambda^\circ) + \Delta RA(\lambda - \lambda^\circ) \quad \text{(C-19)}$$

$$Dec(\lambda) = Dec(\lambda^\circ) + \Delta Dec(\lambda - \lambda^\circ) \quad \text{(C-20)}$$

The shower activity as a function of time around its maximum is described by

$$ZHR(\lambda) = ZHR_{\max} 10^{-B|\lambda - \lambda_{\max}|} \quad \text{(C-21)}$$

where B is given in Table C-2 and describes the slopes of the activity profiles. Since most streams are found to have symmetrical profiles a single value of B is sufficient. The Geminids are the exception; this stream needs a different value of B for the inward and outward slope. Six of the streams do not have a strong enough ZHR to produce a slope, here a 'typical' value of B = 0,2 is used. Six other streams are best

represented by the sum of 2 activity profiles, defined by a peak profile ZHR^{p}_{max} and B^{p} and a background profile ZHR^{b}_{max} with separate inward and outward slope values B^{b+} and B^{b-} respectively. This results in the following expression:

$$ZHR(\lambda) = ZHR^{p}_{\max} 10^{-B^{p}|\lambda-\lambda_{\max}|} + ZHR^{b}_{\max}\left(10^{-B^{b-}(\lambda_{\max}-\lambda)} + 10^{-B^{b+}(\lambda-\lambda_{\max})}\right) \quad \text{(C-22)}$$

The cumulative flux at solar longitude λ can now be expressed as:

$$F(m,\lambda) = F(m)_{\max}\frac{ZHR(\lambda)}{ZHR_{\max}} \quad \text{(C-23)}$$

with

$$F(m)_{\max} = k\, m^{-\alpha} \quad \text{(C-24)}$$

The total particle flux F_{TOT} is obtained by summation over all streams

$$F_{TOT} = F_{SPORADIC} + \sum F_{ST} \quad \text{(C-25)}$$

NOTE If the stream model is used in combination with the reference model of. 10.2.2.2 it is considered that the model in 10.2.2.2 already includes the average yearly stream contribution.

C.1.4.3. Calculation of meteoroid stream fluxes

The following algorithm applies to determine the individual streams' fluxes:

a. Given λ, choose the closest value of λ_{max} in Table C-2 and determine the stream number.

b. From $\Delta\lambda = 2/B$ determine if λ is within the range $(\lambda_{max} - \Delta\lambda) < \lambda < (\lambda_{max} + \Delta\lambda)$ ($\Delta\lambda$ determined by 1% of ZHR_{max}), if not, skip this stream (λ_{max} to be taken from Table C-2).

c. Calculate ZHR within the profile

$$ZHR(\lambda) = ZHR^{p}_{\max} 10^{-B|\lambda-\lambda_{\max}|} \quad \text{(C-26)}$$

d. For the six streams in Table C-2 which have two activity profiles (non vanishing B^{b+} / B^{b-} values), calculate ZHR(λ) according to equation (C-22).

e. Form the ratio

$$Q = \frac{ZHR(\lambda)}{ZHR_{\max}} \quad \text{(C-27)}$$

f. The cumulative flux is now given by

$$F(m) = F(m)_{\max}\cdot Q \quad \text{(C-28)}$$

with

$$F(m)_{\max} = km^{-\alpha} \tag{C-29}$$

or

$$dF = -\alpha\, k\, m^{-(\alpha+1)}\, dm \tag{C-30}$$

k and α are obtained from Table C-2 according to the relevant stream number.
The *arrival velocity* V_∞ includes the gravitational corrections due to the Earth gravity.

C.1.5 Grün meteoroid model

C.1.5.1. Altitude dependent scaling method

The velocity distribution given in Table C-1 is modified by the gravitational attraction of the central body.

In case of a single velocity value the flux increase due to gravity at a given distance r of the centre of the central body is described by the factor G which is given by

$$G = 1 + \frac{v_{esc}^2}{v_\infty^2} \tag{C-1}$$

or

$$G = \frac{v^2}{v^2 - v_{esc}^2} \tag{C-2}$$

with

$$v^2 = v_{esc}^2 + v_\infty^2 \tag{C-3}$$

G describes the factor by which a particle flux a large distance from the central body, is enhanced when measured near to it, due to the gravitational bending of trajectories (causing an increase in particle spatial density) and increase of particle velocity [RD.121].

Using the product μ of the constant of gravitation with the mass of the central body (for Earth $\mu = 3{,}986\ 10^5\ km^3/s^2$; for the Moon $\mu = 4{,}900\ 10^3\ km^3/s^2$), the escape velocity at distance r can be written as

$$v_{esc} = \sqrt{\frac{2\,\mu}{r}} \tag{C-4}$$

and v_∞ is the velocity in free space, i.e. in the absence of the gravity potential which is tabulated in Table C-1, and v is the 'enhanced' meteoroid velocity at distance r. To obtain the correct flux enhancement in case a velocity distribution is given we realise that G is a function of v_∞. Thus the enhanced flux F_E is obtained from the flux $F_{met,0}$ by

$$F_E = \overline{G} \cdot F_{met,0} \tag{C-5}$$

with

$$\overline{G} = \int_0^\infty n(v_\infty)G(v_\infty)dv_\infty \tag{C-6}$$

$\overline{G}$ is the weighted mean G factor for a given velocity distribution. This assumes that the velocity distribution $n(v_\infty)$ has been normalised:

$$\int_0^\infty n(v_\infty)dv_\infty = 1 \tag{C-7}$$

The above formulas contain the necessary information to calculate the altitude dependence of the velocity distribution, since we can write

$$\overline{G} = \int_0^\infty n(v_\infty)G(v_\infty)dv_\infty \approx \sum_{k=1}^{N} n_k G_k = \sum_{k=1}^{N} n_k' \tag{C-8}$$

With $n_k = n(v_\infty,k)$ and $n'_k = n'(v,k)$ representing the tabulated values for the original distribution function and for the distribution function at distance r respectively. N gives the number of bins used for the velocity distribution. Given the escape velocity at distance r, v_{esc} and the tabulated values of $n(v_\infty)$ in 1 km/s bins n_k, we calculate the values n'_k for the distribution $n'(v)$ at distance r by

$$n_k' = G_k\, n_k \tag{C-9}$$

with

$$G_k = \frac{v_k^2}{v_k^2 - v_{esc}^2} \tag{C-10}$$

and

$$v_k = \sqrt{v_{esc}^2 + v_{\infty,k}^2} \tag{C-11}$$

If we now tabulate the values of n'_k we need to change the bin limits by inserting the values of v at the places of the given values of v_∞ which is done by using again the formula

$$v = \sqrt{v_{esc}^2 + v_\infty^2} \tag{C-12}$$

As a result the bin widths are now no longer equidistant in v, which is the independent variable of the new distribution function $n'(v)$. The new distribution function is re-normalized and re-binning is required by interpolating the values of n'(v) to obtain equidistant bins in v. This completes the calculation procedure of the new table for the velocity distribution $n'(v)$ at the given distance r.

The gravitational enhancement, expressed by the factor $\overline{G}$, increases the flux due to a real increase in spatial density of meteoroids due to gravitational attraction and also due to the increase in the meteoroids' velocity. Expression) accounts for both effects.

C.1.5.2. Flux enhancement

C.1.5.2.1 Overview

The meteoroid flux to an orbiting spacecraft is given by:

$$F_{met} = F_{met,0} \cdot \overline{G} \cdot s_f \cdot K \qquad \text{(C-13)}$$

With gravitational enhancement factor $\overline{G}$, central body shielding factor s_f and spacecraft motion factor K. Values of $\overline{G}$, s_f and K for typical Earth orbits are given in Table J-6.

C.1.5.2.2 Geometric shielding

The shielding factor, s_f, for a given surface depends on the spacecraft altitude above the surface of the central body and on the relative orientation of the surface normal with respect to the direction of the central body.

The average shielding factor is given by:

$$s_f = \frac{(1+\cos\eta)}{2} \qquad \text{(C-14)}$$

with:

$$\sin\eta = \frac{(R+R_A)}{(R+h)} \qquad \text{(C-15)}$$

where

R is the radius of the central body (for Earth R = 6 378 km);

R_A is the altitude of the atmosphere (for Earth R_A = 100 km);

h is the spacecraft altitude above surface;

The shielding factors are derived from [RD.21].

C.1.5.2.3 Spacecraft motion

In addition to the attraction and shielding by the central body, the spacecraft velocity causes the encountered flux to increase. The flux increase is given by v_{rel}/v where v is the (gravitational enhanced) meteoroid velocity and v_{rel} is the relative velocity of the meteoroid with respect to the spacecraft. When calculating fluxes using numerical codes one generally considers each meteoroid velocity v_k bin separately. However, the outcome, which depends on the velocity distribution, is a single enhancement factor K.

C.2 Tables

Table C-1: Normalized meteoroid velocity distribution

v [km/s]	$n(v_{1AU})$	$n(v_{400\ km})$	v [km/s]	$n(v_{1AU})$	$n(v_{400\ km})$	v [km/s]	$n(v_{1AU})$	$n(v_{400\ km})$
0.5	7.2E-04	0.0E+00	24.5	2.0E-02	3.2E-02	48.5	4.2E-02	3.7E-04
1.0	5.7E-04	0.0E+00	25.0	2.0E-02	3.0E-02	49.0	4.3E-02	3.5E-04
1.5	1.0E-03	0.0E+00	25.5	2.1E-02	2.8E-02	49.5	4.3E-02	3.4E-04
2.0	1.2E-03	0.0E+00	26.0	2.1E-02	2.6E-02	50.0	4.3E-02	3.3E-04
2.5	1.3E-03	0.0E+00	26.5	2.2E-02	2.4E-02	50.5	4.3E-02	3.2E-04
3.0	1.5E-03	0.0E+00	27.0	2.3E-02	2.3E-02	51.0	4.4E-02	3.2E-04
3.5	1.7E-03	0.0E+00	27.5	2.3E-02	2.1E-02	51.5	4.4E-02	3.1E-04
4.0	1.8E-03	0.0E+00	28.0	2.4E-02	2.0E-02	52.0	4.4E-02	3.1E-04
4.5	2.0E-03	0.0E+00	28.5	2.4E-02	1.9E-02	52.5	4.4E-02	3.0E-04
5.0	2.1E-03	0.0E+00	29.0	2.5E-02	1.8E-02	53.0	4.5E-02	2.9E-04
5.5	2.3E-03	0.0E+00	29.5	2.6E-02	1.7E-02	53.5	4.5E-02	2.8E-04
6.0	2.6E-03	0.0E+00	30.0	2.6E-02	1.6E-02	54.0	4.5E-02	2.8E-04
6.5	2.8E-03	0.0E+00	30.5	2.7E-02	1.5E-02	54.5	4.5E-02	2.7E-04
7.0	3.1E-03	0.0E+00	31.0	2.7E-02	1.4E-02	55.0	4.5E-02	2.7E-04

7.5	3.4E-03	0.0E+00	31.5	2.8E-02	1.3E-02	55.5	4.6E-02	2.6E-04
8.0	3.7E-03	0.0E+00	32.0	2.8E-02	1.2E-02	56.0	4.6E-02	2.6E-04
8.5	4.0E-03	0.0E+00	32.5	2.9E-02	1.1E-02	56.5	4.6E-02	2.5E-04
9.0	4.3E-03	0.0E+00	33.0	3.0E-02	1.0E-02	57.0	4.6E-02	2.4E-04
9.5	4.6E-03	0.0E+00	33.5	3.0E-02	9.2E-03	57.5	4.6E-02	2.3E-04
10.0	4.9E-03	0.0E+00	34.0	3.1E-02	8.4E-03	58.0	4.6E-02	2.1E-04
10.5	5.2E-03	0.0E+00	34.5	3.1E-02	7.7E-03	58.5	4.7E-02	2.0E-04
11.0	5.6E-03	4.3E-02	35.0	3.2E-02	7.1E-03	59.0	4.7E-02	1.9E-04
11.5	6.0E-03	7.4E-02	35.5	3.2E-02	6.5E-03	59.5	4.7E-02	1.8E-04
12.0	6.4E-03	7.5E-02	36.0	3.3E-02	5.9E-03	60.0	4.7E-02	1.7E-04
12.5	6.9E-03	7.5E-02	36.5	3.3E-02	5.4E-03	60.5	4.7E-02	1.6E-04
13.0	7.3E-03	7.3E-02	37.0	3.4E-02	4.9E-03	61.0	4.7E-02	1.5E-04
13.5	7.7E-03	7.2E-02	37.5	3.4E-02	4.4E-03	61.5	4.7E-02	1.5E-04
14.0	8.2E-03	7.0E-02	38.0	3.5E-02	4.0E-03	62.0	4.8E-02	1.4E-04
14.5	8.6E-03	6.8E-02	38.5	3.5E-02	3.6E-03	62.5	4.8E-02	1.3E-04
15.0	9.0E-03	6.6E-02	39.0	3.5E-02	3.2E-03	63.0	4.8E-02	1.2E-04
15.5	9.4E-03	6.4E-02	39.5	3.6E-02	2.9E-03	63.5	4.8E-02	1.1E-04
16.0	1.0E-02	6.2E-02	40.0	3.6E-02	2.6E-03	64.0	4.8E-02	9.7E-05
16.5	1.1E-02	6.1E-02	40.5	3.7E-02	2.3E-03	64.5	4.8E-02	8.8E-05
17.0	1.1E-02	5.9E-02	41.0	3.7E-02	2.1E-03	65.0	4.8E-02	7.9E-05
17.5	1.2E-02	5.8E-02	41.5	3.8E-02	1.9E-03	65.5	4.8E-02	7.0E-05
18.0	1.2E-02	5.6E-02	42.0	3.8E-02	1.7E-03	66.0	4.8E-02	6.3E-05
18.5	1.3E-02	5.4E-02	42.5	3.8E-02	1.5E-03	66.5	4.8E-02	5.5E-05
19.0	1.3E-02	5.3E-02	43.0	3.9E-02	1.3E-03	67.0	4.8E-02	4.7E-05
19.5	1.4E-02	5.1E-02	43.5	3.9E-02	1.1E-03	67.5	4.9E-02	4.0E-05
20.0	1.4E-02	4.9E-02	44.0	3.9E-02	9.9E-04	68.0	4.9E-02	3.4E-05
20.5	1.5E-02	4.8E-02	44.5	4.0E-02	8.8E-04	68.5	4.9E-02	2.9E-05
21.0	1.6E-02	4.6E-02	45.0	4.0E-02	7.7E-04	69.0	4.9E-02	2.4E-05
21.5	1.6E-02	4.4E-02	45.5	4.1E-02	6.9E-04	69.5	4.9E-02	2.0E-05
22.0	1.7E-02	4.2E-02	46.0	4.1E-02	6.1E-04	70.0	4.9E-02	1.7E-05
22.5	1.7E-02	4.0E-02	46.5	4.1E-02	5.4E-04	70.5	4.9E-02	1.4E-05
23.0	1.8E-02	3.8E-02	47.0	4.1E-02	4.8E-04	71.0	4.9E-02	1.1E-05
23.5	1.9E-02	3.6E-02	47.5	4.2E-02	4.4E-04	71.5	4.9E-02	8.0E-06
24.0	1.9E-02	3.4E-02	48.0	4.2E-02	4.0E-04			

Table C-2: The annual meteor streams

(Part 1 of 2)

	λ_{max}	RA_{max}	ΔRA	Dec_{max}	ΔDec	$ZRHP_{max}$	B^{P+}	B^{P-}	ZHR^{b}_{max}	B^{b+}	B^{b-}	α	k	v$_\infty$
Bootids	283,3	232	0,6	45	-0,31	10	2,5	2,5	20	0,37	0,45	0,92	8,4E-17	43
γVelids	285,7	124	0,5	-47	-0,2	2,4	0,12	0,12	0	0	0	1,1	5,8E-19	35
αCrucids	294,5	193	1,1	-63	-0,4	3	0,11	0,11	0	0	0	1,06	1,9E-19	50
αHydrusids	300	138	0,7	-13	-0,3	2	0,2	0,2	0	0	0	1,03	3,4E-19	44
αCarinids	311,2	99	0,4	-54	0	2,3	0,16	0,16	0	0	0	0,92	1,3E-17	25
δVelids	318	127	0,5	-50	-0,3	1,3	0,2	0,2	0	0	0	1,1	3,1E-19	35
αCentaurids	319,4	210	1,3	-58	-0,3	7,3	0,18	0,18	0	0	0	0,83	3,7E-18	57
ocentaurids	323,4	176	0,9	-55	-0,4	2,2	0,15	0,15	0	0	0	1,03	1,9E-19	51
θCentaurids	334	220	1,1	-44	-0,4	4,5	0,2	0,2	0	0	0	0,95	4,4E-19	60
δLeonids	335	169	1	17	-0,3	1,1	0,049	0,049	0	0	0	1,1	1,9E-18	23
Virginids	340	165	0,9	9	-0,2	1,5	0,2	0,2	0	0	0	1,1	1,5E-18	26
γNormids	353	285	1,3	-56	-0,2	5,8	0,19	0,19	0	0	0	0,87	1,9E-18	56
δPavonids	11,1	311	1,6	-63	-0,2	5,3	0,075	0,075	0	0	0	0,95	5,1E-19	60
Lyrids	32,4	274	1,2	33	0,2	12,8	0,22	0,22	0	0	0	0,99	2E-18	49
μVirginids	40	230	0,5	-8	-0,3	2,2	0,045	0,045	0	0	0	1,1	1,1E-18	30
ηAquarids	46,5	340	0,9	-1	0,3	36,7	0,08	0,08	0	0	0	0,99	1,5E-18	66
βCorona Aust.	56	284	1,3	-40	0,1	3	0,2	0,2	0	0	0	1,13	1,5E-19	45
αScorpiids	55,9	252	1,1	-27	-0,2	3,2	0,13	0,13	0	0	0	0,92	4,7E-17	21
Da.Arietids	77	47	0,7	24	0,6	54	0,1	0,1	0	0	0	0,99	2,6E-17	38
γSagitarids	89,2	286	1,1	-25	0,1	2,4	0,037	0,037	0	0	0	1,06	1,9E-18	29
τCetids	95,7	24	0,9	-12	0,4	3,6	0,18	0,18	0	0	0	0,92	3,7E-19	66
θOphiuchids	98	292	1,1	-11	0,1	2,3	0,037	0,037	0	0	0	1,03	3,5E-18	27
τAquarids	98	342	1	-12	0,4	7,1	0,24	0,24	0	0	0	0,92	8,9E-19	63
νPhoenicids	111,2	28	1	-40	0,5	5	0,25	0,25	0	0	0	1,1	2,6E-19	48
oCygnids	116,7	305	0,6	47	0,2	2,5	0,13	0,13	0	0	0	0,99	1,4E-18	37
Capricornid	122,4	302	0,9	-10	0,3	2,2	0,041	0,041	0	0	0	0,69	8,3E-17	25
τAquarids N	124,1	324	1	-8	0,2	1	0,063	0,063	0	0	0	1,19	3,6E-20	42
Pisces Aust.	124,4	339	1	-33	0,4	2	0,4	0,4	0,9	0,03	0,1	1,16	1,5E-19	42
δAquarids S.	125,6	340	0,8	-17	0,2	11,4	0,091	0,091	0	0	0	1,19	3,6E-19	43

	λ_{max}	RA_{max}	ΔRA	Dec_{max}	ΔDec	$ZRHP_{max}$	B^{P+}	B^{P-}	ZHR^{b}_{max}	B^{b+}	B^{b-}	α	k	v_∞
τAquarids S.	131,7	335	1	-15	0,3	1,5	0,07	0,07	0	0	0	1,19	1,2E-19	36
Perseids	140,2	47	1,3	58	0,1	70	0,35	0,35	23	0,05	0,092	0,92	1,2E-17	61
κCygnids	146,7	290	0,6	52	0,3	2,3	0,069	0,069	0	0	0	0,79	3E-17	27
πEridanids	153	51	0,8	-16	0,3	40	0,2	0,2	0	0	0	1,03	1,7E-18	59
γDoradids	155,7	60	0,5	-50	0,2	4,8	0,18	0,18	0	0	0	1,03	1,1E-18	41
Aurigids	158,2	73	1	43	0,2	9	0,19	0,19	0	0	0	0,99	2,9E-19	69
κAquarids	177,2	339	0,9	-5	0,4	2,7	0,11	0,11	0	0	0	1,03	1,9E-17	19
εGeminids	206,7	104	0,7	28	0,1	2,9	0,082	0,082	0	0	0	1,1	2,1E-20	71
Orionids	208,6	96	0,7	16	0,1	25	0,12	0,12	0	0	0	1,13	1,6E-19	67
Leo Minorids	209,7	161	1	38	-0,4	1,9	0,14	0,14	0	0	0	0,99	1,1E-19	61
Taurids	223,6	50	0,3	18	0,1	7,3	0,026	0,026	0	0	0	0,83	4,3E-17	30
δEridanids	229	54	0,9	-2	0,2	0,9	0,2	0,2	0	0	0	1,03	7,5E-19	31

Table C-2: The annual meteor streams

(Part 2 of 2)

	λ_{max}	RA_{max}	ΔRA	Dec_{max}	ΔDec	$ZRHP_{max}$	B^{P+}	B^{P-}	ZHR^{b}_{max}	B^{b+}	B^{b-}	α	k	v_∞
ζPuppids	232,2	117	0,7	-42	-0,2	3,2	0,13	0,13	0	0	0	1,22	9,5E-20	41
Leonids	235,1	154	1	22	0,4	19	0,55	0,55	4	0,025	0,15	1,22	3,4E-20	71
Puppids/Vel	252	128	0,8	-42	-0,4	4,5	0,034	0,034	0	0	0	1,06	8,2E-19	40
Phoenicids	252,4	19	0,8	-58	0,4	2,8	0,3	0,3	0	0	0	1,03	2,5E-17	18
Monoceroti.	260,9	100	1	14	-0,1	2	0,25	0,25	0	0	0	1,25	3,3E-20	43
Geminids	262,1	113	1	32	0,1	74	0,59	0,81	18	0,09	0,31	0,95	7,8E-17	36
σHydrusids	265,5	133	0,9	0	-0,3	2,5	0,1	0,1	0	0	0	1,1	4,7E-20	59
Ursids	271	224	-0,2	78	-0,3	10	0,9	0,9	2	0,08	0,2	1,22	8,1E-19	35

Annex D (informative) Gravitation

D.1 Gravity models: background

Equation (4-4) can be rewritten in terms of amplitude J_{lm} and phase angle λ_{lm} of individual contributions of the spherical harmonic functions to the geopotential.

$$U = \frac{GM}{r}\left\{1 - \sum_{l=2}^{N}\left(\frac{a_e}{r}\right)^l \sum_{m=0}^{l} J_{lm}\cos\left(m[\lambda - \lambda_{lm}]\right) P_{lm}(\sin\phi)\right\} \quad \text{(D-1)}$$

The equivalence of J_{lm}, λ_{lm} and C_{lm}, S_{lm} is governed by the following equations.

$$C_{lm} = -J_{lm}\cos(m\,\lambda_{lm}) \quad \text{(D-2)}$$

$$S_{lm} = -J_{lm}\sin(m\,\lambda_{lm}) \quad \text{(D-3)}$$

$$J_{lm} = \sqrt{C_{lm}^2 + S_{lm}^2} \quad \text{(D-4)}$$

$$\lambda_{lm} = \frac{2}{m}\arctan\left(\frac{S_{lm}}{J_{lm} + C_{lm}}\right) \quad \text{(D-5)}$$

For m $\neq$ l, the terms C_{lm}, S_{lm} are called tesseral harmonics. These components divide the Earth's surface in a checkerboard pattern of hills and valleys, the amplitude and phase of which are determined by the associated coefficients J_{lm}, λ_{lm}.

For l = m, the functions P_{lm} = 1,0. These terms are called sectorial harmonics. They divide the spherical surface into longitude-dependent sectors, similar to the segments of a basket ball.

For m = 0, the only remaining terms $C_{l0} = -J_{l0}$ (where J_{l0} is mostly abbreviated as J_l) are called zonal harmonics. They divide the spherical surface into purely latitude-dependent bands of toroidal hills and valleys, with Earth oblateness (J_2) as the dominating contribution. J_2 reflects the equilibrium response of a rotating, elastic Earth under the influence of centrifugal and gravitational forces. For the model EIGEN-GL04C the resulting Earth ellipsoid has an equatorial radius of $a_e = 6378136$ m (can slightly vary with the selected geopotential model), a polar

radius of $b_e = 6356752\ \mathrm{m}$ (can slightly vary with the selected geopotential model), and an oblateness of $f_e = (a_e - b_e)/a_e = 1/298{,}257$.

By convention, the central attraction term of a spherical body of uniform mass distribution is $C_{00} = -J_{00} = 1$. If the centre of mass coincides with the origin of the body-centred coordinate system, then $C_{10} = C_{11} = S_{11} = 0$. If the body-fixed coordinate axes furthermore coincide with the axes of the main moments of inertia, then $C_{21} = S_{21} = S_{22} = 0$.

In order to develop a geopotential model it is necessary to measure the gravitational acceleration directly or indirectly, and estimate the set of model coefficients (*GM*, a_e, C_{lm}, S_{lm}) in a least squares sense on the basis of an adequately large number of such measurements. Direct measurements of the gravity potential are difficult, and typically involve highly sensitive gradiometers that measure the acceleration gradient. Indirect measurements of the gravity potential are obtained from precise tracking data for Earth orbiting satellites. Because of the difficulties of collecting global gravity measurements on land or sea, relevant global geopotential models did not exist before the days of artificial Earth orbiting satellites, and only the first few degree and order terms were known with some accuracy.

However, a revolution in gravity model development has occurred after the year 2000, in the form of the three dedicated gravity field missions: CHAMP, GRACE and GOCE. All three satellites employ precise global tracking via GPS, allowing continuous high quality orbit determination, and measure the gravity acceleration *directly*. The arrival of these dedicated gravity missions has essentially rendered any earlier gravity model obsolete. GRACE-only models of 360×360 resolution in degree and order (about 1°×1° patches, with ~100 km resolution on the Earth's surface) have demonstrated to be superior to any of the earlier combined models, even if these were based on the accumulated satellite data sets from three preceding decades. The GRACE models are accurate enough to investigate the temporal variability of the gravity field, for instance due to seasonal displacements of water masses. The EIGEN-6C4 model [RD.170] based on GOCE mission data with a resolution up to 2190 in degree and order (sub-degree, ~10km resolution) is one of the latest state of the art models to consider for gravity model applications.

D.2 Guidelines for use

The evaluation of a complete 360 × 360 geopotential model at every satellite location of interest represents a substantial computational effort that is usually both undesirable and unnecessary. This section explains how an adequate truncation level of the expansion series can be selected for a satellite orbit of interest, based on two elementary observations.

The first observation is that the term $(a_e/r)^l$ in equations (D-1) and (4-4) leads to a rapid attenuation of the gravity potential with orbit radius *r*, so that the details of the geopotential become less and less notable at increasing height (in other words, the Earth rapidly turns into a point mass with increasing distance).

The second observation is that the expansion series can always be safely truncated at a degree l that provides contributions of lower order of magnitude than the inherent noise level of the model itself.

Considering these observations, an adequate truncation degree can be determined on the basis of Kaula's rule ([RD.31] and equation D.6). This is briefly illustrated via an example that selects a suitable truncation degree l for the orbit height of GNSS constellations, which have a radius r of about 4 times the equatorial radius a_e (i.e. an altitude of H≈25 000 km).

In theory, the degree N of the expansion should be infinite to model the exact variability of the geopotential surface. In practice the maximum degree remains finite. This leads to truncation errors in the expansion series, and thus in a quantification error of the gravity acceleration. In order to get an impression of the truncation effect, Kaula (see [RD.31]) formulated a rule-of-thumb that provides the order of magnitude of normalized expansion coefficients as a function of the degree l:

$$\overline{C}_{lm}, \overline{S}_{lm} = \frac{10^{-5}}{l^2} \qquad \text{(D-6)}$$

This estimate has turned out to be remarkably accurate, even for modern day models that expand up to degree and order 360 or higher.

Table D-1 shows for increasing degree l the signal power in the harmonic components for that degree according to the Kaula rule, the attenuation factor $(a_e / r)^l$ for that degree, and the product of these two, which represents the remaining signal power at the orbit height of interest.

The inherent noise level of a 360 × 360 degree model can be approximated by the signal power for l = 360, which is $7{,}7 \times 10^{-11}$.

Looking in the last column of Table D-1, it appears that the attenuating effect of the 25 000 km orbit height already reduces the degree 8 terms of the model to an order of magnitude that is below the noise level of the model.

In practice, one should account for the fact that Kaula's rule is just an approximation, albeit an accurate one. Instead of applying the estimated 8 × 8 resolution, one can choose to apply e.g. a 12 × 12 resolution for GPS orbits, especially because the effort of evaluating a 12 × 12 field is still trivial in comparison to the evaluation of the full 360 × 360 model.

The above selection process for a suitable truncation degree does not account for cases where the orbital motion of the satellite, in combination with the rotation of the Earth, leads to a resonance situation where certain harmonic components are continuously sensed by the satellite in exactly the same way. This is particularly likely to happen for so called repeat orbits, where the ground track of the spacecraft returns to the same point on the Earth surface after M orbital revolutions, which take exactly the same amount of time as N revolutions of the Earth (= days). This is, for instance, the case for geosynchronous, GNSS, and Earth observation satellites. Even very small harmonic components that are in exact phase with orbital motion can then result in significant orbital perturbations after sufficient propagation time intervals.

For Earth-orbiting satellites, the only tide generating bodies of interest are the Sun and the Moon. This leads to the following main conclusions:

- The tidal effects of the Moon are more pronounced than those due to the Sun, because the effect of distance is stronger than that of mass.
- The main gravity harmonic perturbation is the zonal harmonic J_2 which is of order 10^{-3}, while further gravity harmonics are of order 10^{-6} or smaller. Consequently, tidal effects can only be ignored in cases where the gravity field is truncated at degree 2 (Earth oblateness only) or 1 (central body gravity only).

Hence, luni-solar tide effects become non negligible when modelling harmonic perturbations of the gravity field for degrees 3 or higher.

Table D-2 gives the coefficients of the EIGEN-GLO4C model up to degree and order 8x8.

Figure D-1 shows a graphical representation of the EIGEN-GLO4C Geoid (greatly exaggerated).

D.3 Availability of models

- The EIGEN-GLO4C and other EIGEN model data and implementation details can be downloaded from the International Centre for Global Earth Models http://icgem.gfz-potsdam.de/ICGEM/ICGEM.html
- The IERS report 36 can be downloaded from http://www.iers.org/
-
- The DE430 directory is available at ftp://ssd.jpl.nasa.gov/pub/eph/planets/ascii/de430
- A modified version including additional perturbing asteroids can be found at ftp://ssd.jpl.nasa.gov/pub/eph/planets/
- The SPICE kernal version of DE430 is located at ftp://ssd.jpl.nasa.gov/pub/eph/planets/bsp/de430.bsp

D.4 Tables

Table D-1: Degree power attenuation for an orbit at 25 000 km altitude

degree l	Kaula signal power for this degree	attenuation factor at H=25 000 km	remaining signal power at H=25 000 km
2	2,500E-06	6,250E-02	1,563E-07
3	1,111E-06	1,563E-02	1,736E-08
4	6,250E-07	3,906E-03	2,441E-09
5	4,000E-07	9,766E-04	3,906E-10
6	2,778E-07	2,441E-04	6,782E-11
7	2,041E-07	6,104E-05	1,246E-11
8	1,563E-07	1,526E-05	2,384E-12
9	1,235E-07	3,815E-06	4,710E-13
10	1,000E-07	9,537E-07	9,537E-14

degree l	Kaula signal power for this degree	attenuation factor at H=25 000 km	remaining signal power at H=25 000 km
12	6,944E-08	5,960E-08	4,139E-15
15	4,444E-08	9,313E-10	4,139E-17
20	2,500E-08	9,095E-13	2,274E-20
50	4,000E-09	7,889E-31	3,155E-39
100	1,000E-09	6,223E-61	6,223E-70
360	7,716E-11	1,813E-217	1,399E-227

Table D-2: Coefficients of the EIGEN-GL04C model up to degree and order 8 × 8

	m = 0	1	2	3	4	5	6	7	8
l = 0	1,00E+00 0,00E+00								
1	0,00E+00 0,00E+00	0,00E+00 0,00E+00							
2	-4,84E-04 0,00E+00	-2,55E-10 1,44E-09	2,44E-06 -1,40E-06				C-coefficient S-coefficient		
3	9,57E-07 0,00E+00	2,03E-06 2,48E-07	9,05E-07 -6,19E-07	7,21E-07 1,41E-06					
4	5,40E-07 0,00E+00	-5,36E-07 -4,74E-07	3,51E-07 6,62E-07	9,91E-07 -2,01E-07	-1,88E-07 3,09E-07				
5	6,87E-08 0,00E+00	-6,29E-08 -9,44E-08	6,52E-07 -3,23E-07	-4,52E-07 -2,15E-07	-2,95E-07 4,98E-08	1,75E-07 -6,69E-07			
6	-1,50E-07 0,00E+00	-7,59E-08 2,65E-08	4,87E-08 -3,74E-07	5,72E-08 8,94E-09	-8,60E-08 -4,71E-07	-2,67E-07 -5,37E-07	9,46E-09 -2,37E-07		
7	9,05E-08 0,00E+00	2,81E-07 9,51E-08	3,30E-07 9,30E-08	2,50E-07 -2,17E-07	-2,75E-07 -1,24E-07	1,65E-09 1,79E-08	-3,59E-07 1,52E-07	1,52E-09 2,41E-08	
8	4,95E-08 0,00E+00	2,32E-08 5,89E-08	8,00E-08 6,53E-08	-1,94E-08 -8,60E-08	-2,44E-07 6,98E-08	-2,57E-08 8,92E-08	-6,60E-08 3,09E-07	6,73E-08 7,49E-08	-1,24E-07 1,21E-07

D.5 Figures

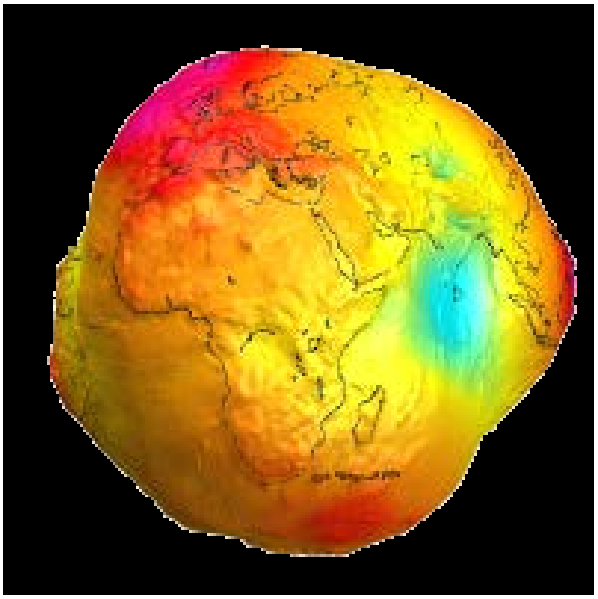

Figure D-1: Graphical representation of the EIGEN-GLO4C geoid (note: geoid heights are exaggerated by a factor 10 000).

Annex E (informative) Geomagnetic fields

E.1 Overview of the effects of the geomagnetic field

Spacecraft motion across the geomagnetic field results in a motionally-induced e.m.f. given by E=v×B in the spacecraft. If a current path can be completed, a current flows through the spacecraft and the surrounding plasma. These phenomena can lead to generation of a few volts potential differences on large spacecraft in LEO. The effect is also used or studied in tethered satellite missions where the length of the tether perpendicular to $\underline{B}$ can lead to large currents and potentials.

Interaction between the magnetic field and an on-board magnetic moment $\underline{m}$ gives rise to a force:

$$\underline{F} = (\underline{m}.\underline{\nabla})\underline{B} \qquad \text{(E-1)}$$

which can be used for attitude control where an on-board magnetic torquer provides $\underline{m}$.

Dynamic fluctuations in plasma populations, electric fields and geomagnetic fields are intimately connected and plasma disturbances can be monitored via observations of the geomagnetic field. These are quantified by the familiar K_p, A_p, D_{st} and other geomagnetic indices (see clause 6 for more detail on geomagnetic activity indices.

E.2 Models of the internal geomagnetic field

Examples of recognised, high-degree, models of the internal field are those due to Olsen *et al*. [RD.138] and Maus *et al*. [RD.139]. These models currently cover the period (approximately) of 2000 to 2005. Another is the 'Comprehensive Model' of Sabaka *et al* (2004) [RD.140]. This model seeks to represent all field sources under magnetically quiet conditions and models the time variation of sources by cubic splines. The Comprehensive Model is widely used in the scientific community: it has a long history and is regarded as being amongst the most accurate and flexible for scientific purposes. It can be expected that this model, now at revision four (CM4), continues to be occasionally updated, in the light of new scientific advances. However the set of input parameters is relatively complex and it is not applicable under all solar and geomagnetic activity conditions. Moreover the external field component is not as flexible as the purely internal field models such as the IGRF even though it does include a representation of the dayside *Sq* ionospheric magnetic field.

Models such as the International Geomagnetic Reference Field (IGRF) and World Magnetic Model (WMM) represent the internal fields of the Earth only.

See Figure E-1 for more information on the current revision of the IGRF. These models are updated on a five-year basis, assuming a linear secular variation between updates. The IGRF currently extends to spherical harmonic degree 13 (equivalent to a wavelength of 3 077 km on the ground) and is produced by a collaboration of IAGA scientists. IAGA also define a definitive reference field (DGRF) for a given epoch (most recently DGRF2010), where it is agreed that no new data is likely to be forthcoming to revise and improve the existing IGRF for that epoch or earlier. Prior to 2000, the IGRF is truncated at degree 10, the increased resolution after that date being due to the improved quality of recent global satellite surveys of the main field.

The World Magnetic Model (WMM), produced jointly with the US National Geophysical Data Centre (NGDC), is the standard model in UK Ministry of Defence and US Department of Defence navigation and attitude reference systems. It is also used widely in civilian navigation systems. The model is used on marine charts. Like the IGRF the WMM is revised according to fixed procedures every five years. The current model, WMM2015, extends to spherical harmonic degree 12 and is valid till 2020.

E.3 Models of the external geomagnetic field

Spherical harmonic models of external fields, e.g. CM4, are typically no higher than degree two (i.e. quadrupolar) and capture only the quasi-static elements of the external field. There is usually some dependence on the *Dst* (or similar) geomagnetic index, which parameterises variations in the symmetric ring current intensity. Neither the IGRF nor WMM have an external field component.

For satellite operations closer to the Earth, the spherical harmonic models of Olsen *et al* [RD.138] or Sabaka *et al* [RD.140] can be useful. However, these models are inaccurate on the dayside of the Earth (approximately 0700-1700 local solar time), at geomagnetic latitudes above about 55 degrees, or during more active geomagnetic conditions (approximately $Kp>3$). They are also likely to be degraded in accuracy beyond low-Earth orbit (>800km altitude), where the magnetic survey satellites that measure the base data for these models are flown.

Non-spherical harmonic models use a variety of geomagnetic and solar wind data to parameterise the various external current systems. Dynamic models are widely used and combined with internal models such as IGRF. The models of Tsyganenko and of Alexeev and co-workers both use the IGRF as the core field. They therefore both provide a consistent model of the total field measured by any *in-situ* spacecraft, from approximately 2-70 Earth radii.

Older dynamic models also exist, dating back to the 1960s, and these are occasionally used in the space science and engineering community, e.g. when using radiation belt models of that era. These include models due to Mead and Fairfield (1975) [RD.141], Olsen and Pfitzer (1977) [RD.142], Hilmer (1989) [RD.143] and Voight (1981) [RD.144]. For further information on these older models see the review of Jordan (1994) [RD.145].

E.4 Magnetopause boundary

The location and field strength of the magnetopause is integral to most external field models. However, it is sometimes useful to be able to estimate the magnetopause

location explicitly. Some simple expressions can be used to estimate basic locations of magnetospheric boundaries for mission planning. The stand-off radial distance of the magnetopause in the sunward direction is given approximately by:

$$L_{mp} = 107{,}4(n_{sw}u_{sw}^2)^{-1/6} \quad \text{(E-2)}$$

where

L_{mp} is in units of Earth-radii,

n_{sw} the solar wind proton number density is in units of cm^{-3} and

u_{sw} the solar wind bulk velocity is in units of km s^{-1}.

Typical values for n_{sw} and u_{sw} are 8 cm^{-3} and 450 km s^{-1} respectively, leading to a stand-off distance of about 10 R_E.

The model of Sibeck et al. [RD.32] represents the complete magnetopause position, not just at the sub-solar point, as the function:

$$R^2 + Ax^2 + Bx + C = 0 \quad \text{(E-3)}$$

where

$R^2 = y^2 + z^2$;

x, y, and z are GSM coordinates, in Earth-radii;

A, B and C are fit parameters dependent on the solar wind pressure as given in Table E-1.

E.5 Geomagnetic coordinate system – *B* and *L*

Geomagnetic coordinates are useful or necessary for a number of applications where charged particle morphology or behaviour needs to be described in the magnetosphere. The most important application is in models of the Earth's radiation-belt environment (see clause 9). These particle models give fluxes of trapped energetic particles as functions of particle energy and of McIlwain's geomagnetic co-ordinates L and B/B_0 [RD.102].

The kinetic energy of a charged particle trapped in a geomagnetic field model is conserved (a constant of motion) provided the B-field is stationary (independent of time), and provided that the acceleration by magnetospheric electric fields can be neglected. This is a satisfactory approximation for particles whose kinetic energy is larger than 500 keV.

When the kinetic energy of the particles is smaller than 500 MeV their motion can be described as the superposition of a gyration about the magnetic field lines, a latitudinal oscillation between two conjugate mirror points and an azimuthal drift around the Earth. Three adiabatic invariants (μ, I and Φ) can be associated respectively with these three periodic motions provided certain conditions are satisfied. The approximate conservation of the adiabatic invariants, contributes to the definition of invariant coordinates for mapping directional and omni-directional fluxes of particles trapped in the Earth's Radiation Belts.

Two invariant coordinates, e.g. mirror point magnetic field (B_m) and I (E-4), are required to define a drift shell, i.e. the surface formed by the segments of geomagnetic field lines between conjugate mirror points of particles.

$$I = \int_{l_1}^{l_2} \left(1 - \frac{B}{B_m}\right)^{1/2} dl \qquad \text{(E-4)}$$

B_m is the magnetic field strength at the mirror points (the low altitude edge of a drift shell); since the magnetic moment μ of trapped particles is the first adiabatic invariant of motion of trapped particles, B_m is also an invariant coordinate characterizing a drift shell;

I is the second invariant coordinate required to identify uniquely the drift shell. The integral in (E-4) is evaluated along the field line between both conjugate mirror points l_1 and l_2 .

Since I is not a visually suggestive coordinate, McIwain [RD.101], [RD.102], [RD.118] introduced his L parameter which is approximately (but not exactly) equal to the equatorial distance of the magnetic field line passing across the point of an observational measurement.

When B_m is determined by using a geomagnetic field model (e.g. IGRF) the value of L is uniquely determined by the mathematical transformation (E-5):

$$L^3\left(\frac{B_m}{M_d}\right) = f\left(\frac{I^3 B_m}{M_d}\right) \qquad \text{(E-5)}$$

In this equation I is computed by numerical integration of (E-4) using the same magnetic field model (IGRF).

M_d = 31 165,3 nT R_E^3 is the fixed value of the magnetic moment of the reference dipole adopted in 1961 by McIwain to map the measured fluxes of trapped of radiation belt particles [RD.102], [RD.118].

L is the second invariant coordinate used (instead of I) to label drift shells.

The pair of invariant coordinates (B_m, L) uniquely defines a drift shell. It should be emphasized that different points along the same geomagnetic field lines can be characterized by different values L and by different drift shells.

The function *f* (E-5) was calculated by McIlwain [RD.102] and a simple approximation for *f* was found by Hilton [RD.103].

Note that a drift shell can also be characterized by Φ the third invariant of motion (the flux invariant), and an associated L* parameter. In general L and L* are not equal, except for a dipole geomagnetic field. However, the invariance of Φ or L* requires that the geomagnetic field distribution does not change significantly over a time period longer than the azimuthal drift period (> 10 minutes), while the adiabatic invariance of I or L requires that the B-field distribution is independent of time over only several bounce periods (> 1 second).

Other pairs of invariant coordinates derived from B_m and L have been proposed and happen to be more appropriate in certain cases: e.g. the invariant latitude (Λ), the invariant radius (R), or the invariant altitude (*h_inv*) [RD.120] which is quite convenient to bin/map fluxes measurements at low-altitudes in the Radiations Belts.

E.6 Tables

Table E-1: Magnetic pole positions since 1900 as determined from IGRF-12 in WGS84 geodetic latitude (taken from [RN.38])

	North dip pole		South dip pole		North geomagnetic pole		South geomagnetic pole	
Epoch	Latitude	Longitude	Latitude	Longitude	Latitude	Longitude	Latitude	Longitude
1900	70.46	-96.19	-71.72	148.32	78.68	-68.79	-78.68	111.21
1905	70.66	-96.48	-71.46	148.55	78.68	-68.75	-78.68	111.25
1910	70.79	-96.72	-71.15	148.64	78.66	-68.72	-78.66	111.28
1915	71.03	-97.03	-70.8	148.54	78.64	-68.57	-78.64	111.43
1920	71.34	-97.39	-70.41	148.2	78.63	-68.38	-78.63	111.62
1925	71.79	-98	-69.99	147.63	78.62	-68.27	-78.62	111.73
1930	72.27	-98.69	-69.52	146.79	78.6	-68.26	-78.6	111.74
1935	72.8	-99.34	-69.06	145.77	78.57	-68.36	-78.57	111.64
1940	73.3	-99.87	-68.57	144.6	78.55	-68.51	-78.55	111.49
1945	73.93	-100.24	-68.15	144.44	78.55	-68.53	-78.55	111.47
1950	74.64	-100.86	-67.89	143.55	78.55	-68.85	-78.55	111.15
1955	75.18	-101.41	-67.19	141.5	78.54	-69.16	-78.54	110.84
1960	75.3	-101.03	-66.7	140.23	78.58	-69.47	-78.58	110.53
1965	75.63	-101.34	-66.33	139.53	78.6	-69.85	-78.6	110.15
1970	75.88	-100.98	-66.02	139.4	78.66	-70.18	-78.66	109.82
1975	76.15	-100.64	-65.74	139.52	78.76	-70.47	-78.76	109.53
1980	76.91	-101.68	-65.42	139.34	78.88	-70.76	-78.88	109.24
1985	77.4	-102.61	-65.13	139.18	79.04	-70.9	-79.04	109.1

1990	78.09	-103.68	-64.91	138.9	79.21	-71.13	-79.21	108.87
1995	79.09	-105.42	-64.79	138.76	79.39	-71.42	-79.39	108.58
2000	80.97	-109.64	-64.66	138.3	79.61	-71.57	-79.61	108.43
2005	83.19	-118.24	-64.55	137.85	79.82	-71.81	-79.82	108.19
2010	85.02	-132.84	-64.43	137.32	80.09	-72.21	-80.09	107.78
2015	86.29	-160.06	-64.28	136.59	80.37	-72.63	-80.37	107.37
2020	86.39	169.8	-64.11	135.76	80.65	-73.17	-80.65	106.83

Table E-2 Sibeck et al. Magnetopause model

Solar wind pressure range (nPa)	A	B	C	Sub-solar point (R_E)	Dawn meridian (R_E)
0,54-0,87	0,19	19,3	-272,4	12,6	16,5
0,87-1,47	0,19	19,7	-243,9	11,7	15,6
1,47-2,60	0,14	18,2	-217,2	11,0	14,7
2,60-4,90	0,15	17,3	-187,4	10,0	13,7
4,90-9,90	0,18	14,2	-139,2	8,8	11,8
Sibeck et al. [RD.32]					

E.7 Figures

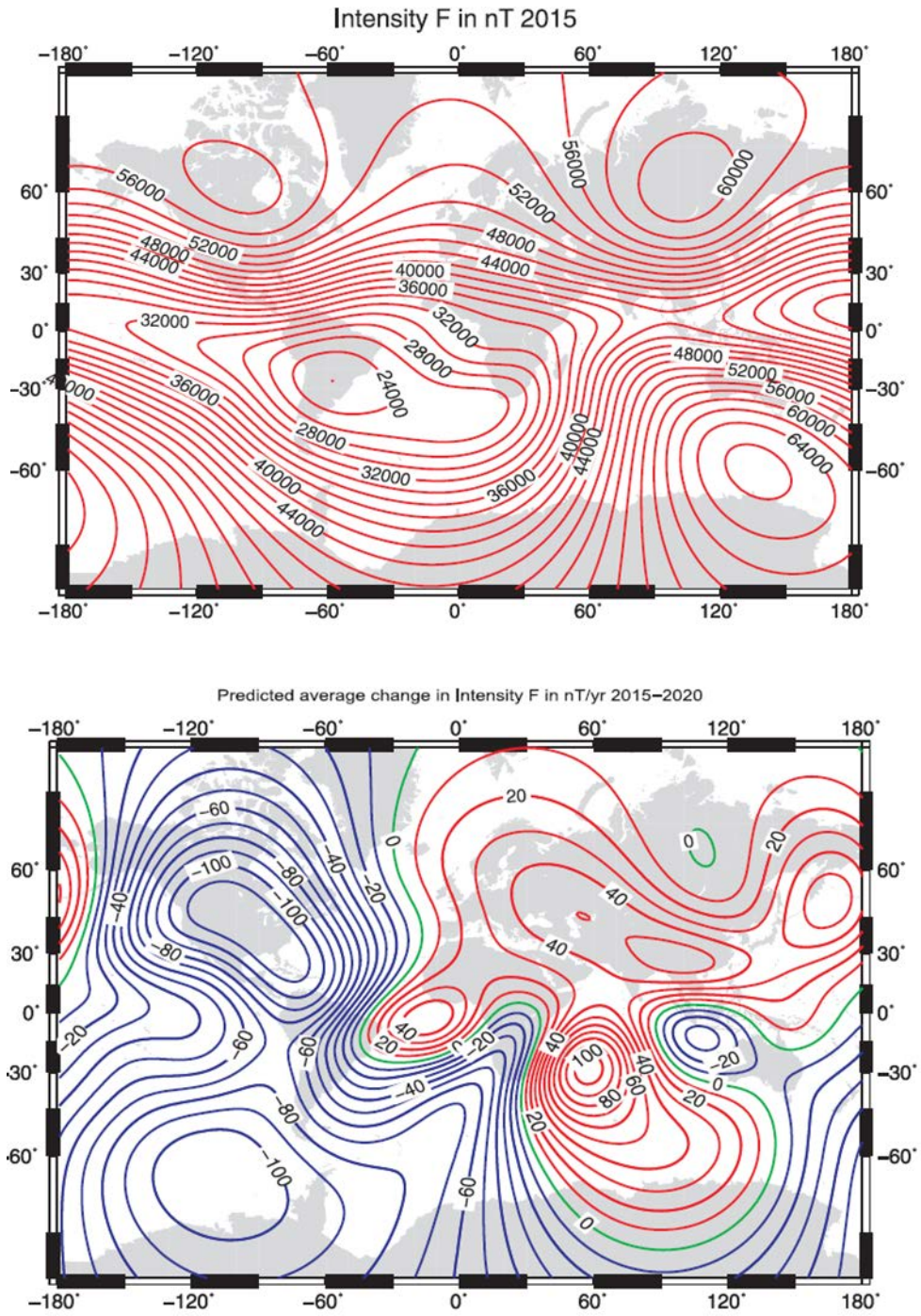

Figure E-1: The IGRF-12 field strength (nT, at 2015) and predicted change in intensity between 2015 and 2020 at the mean Earth radius. (Mercator projection, from [RN.38])

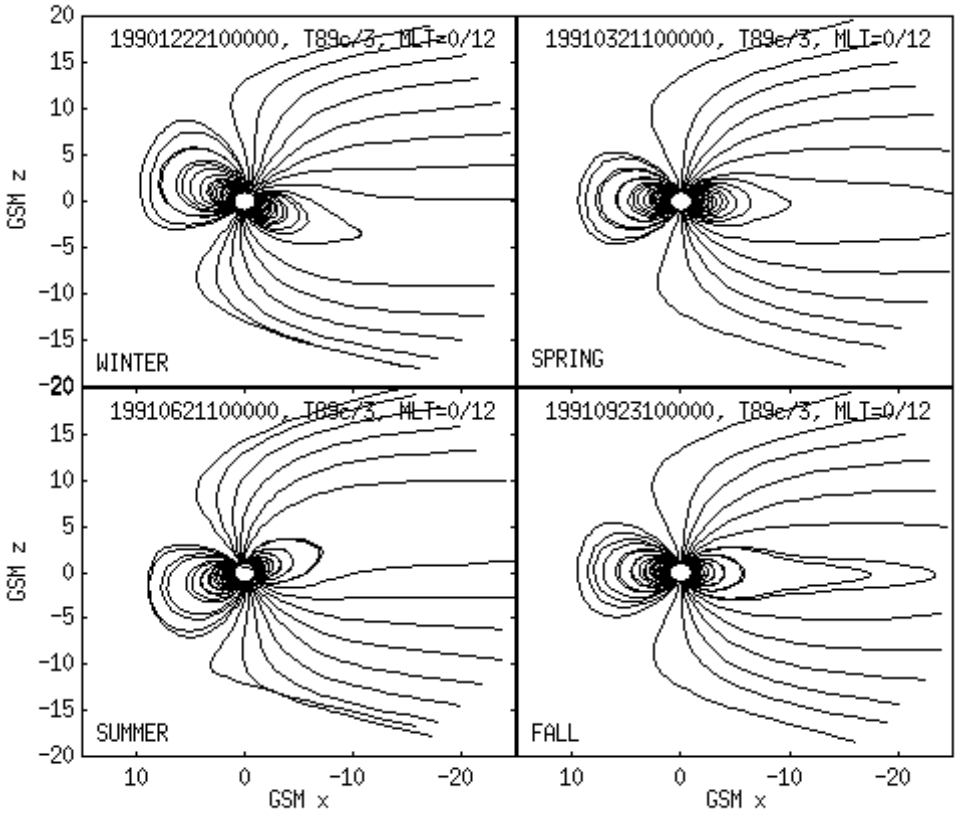

The Figure shows a cut in the noon-midnight plane, with the Sun to the left and with distance Re in GSM coordinates.

Figure E-2: The general morphology of model magnetospheric field lines, according to the Tsyganenko 1989 model, showing the seasonal variation, dependent on rotation axis tilt

Annex F (informative)
Natural electromagnetic radiation and indices

F.1 Solar spectrum

In 2000, the American Society for Testing and Materials developed an AM0 reference spectrum (ASTM E-490) for use by the aerospace community [RD.33]. That ASTM E490 Air Mass Zero solar spectral irradiance is based on data from satellites, space shuttle missions, high-altitude aircraft, rocket soundings, ground-based solar telescopes, and modelled spectral irradiance. The integrated spectral irradiance has been made to conform to the value of the solar constant accepted by the space community; which is 1 362W m^{-2}. Figure F-1 shows the solar irradiation spectrum at AM0 and AM1.5.

F.2 Solar and geomagnetic indices – additional information

F.2.1 E10.7

Although not used in atmosphere models described in clause 7, *E10.7* is the integration in the range from 1 to 105 nm of the energy flux of solar irradiance, reported in solar flux units (sfu) or $x10^{-22}$ Watts per meter squared per Hertz.

F.2.2 F10.7

The sun emits radio energy with a slowly varying intensity. This radio flux, which originates from atmospheric layers high in the sun's chromosphere and low in its corona, changes gradually from day-to-day in response to the number of spot groups on the disk. Solar flux density at 10,7 cm wavelength has been recorded routinely by radio telescope near Ottawa since February 14, 1947.

Each day, levels are determined at local noon (1700 GMT). Beginning in June 1991, the solar flux density measurement source is Penticton, B.C., Canada. Its observations are available through the DRAO website and all values are also archived at the Space Physics Interactive Data Resource (SPIDR).

Three sets of fluxes - the observed, the adjusted, and the absolute - are summarized. Of the three, the observed numbers are the least refined, since they contain fluctuations as large as 7% that arise from the changing sun-earth distance. In contrast, adjusted fluxes have this variation removed; the numbers in these tables equal the energy flux received by a detector located at the mean distance between sun and earth. Finally, the absolute levels carry the error reduction one step further; here each adjusted value is multiplied by 0,90 to compensate for uncertainties in antenna gain and in waves reflected from the ground.

F.2.3 S10.7

The NASA/ESA Solar and Heliospheric Observatory (SOHO) research satellite operates in a halo orbit at the Lagrange Point 1 (L1) on the Earth-Sun line and has an uninterrupted view of the Sun. One of the instruments on SOHO is the Solar Extreme-ultraviolet Monitor (SEM) that measures the 26–34 nm solar EUV emission with 15-second time resolution in its first order broadband wavelength range. The integrated 26–34 nm emission is normalized. The normalized value is converted to sfu through linear regression with *F10.7* (for historical data) over the common time frame and the resulting index is called *S10.7*.

The broadband (wavelength integrated) SEM 26-34 nm irradiances, represented by the *S10.7* index, are EUV line emissions dominated by the chromospheric He II line at 30,4 nm with contributions from other chromospheric and coronal lines. This energy principally comes from solar active regions, plage, and network. Once the photons reach the Earth, they are deposited (absorbed) in the terrestrial thermosphere mostly by atomic oxygen above 200 km.

F.2.4 M10.7

NOAA 16 and NOAA 17 operational satellites host the Solar Backscatter Ultraviolet (SBUV) spectrometer that has the objective of monitoring ozone in the Earth's lower atmosphere. In its discrete operating mode, a diffuser screen is placed in front of the instrument's aperture in order to scatter solar MUV radiation near 280 nm into the instrument. This solar spectral region contains both photospheric continuum and chromospheric line emissions. The chromospheric Mg II h and k lines at 279,56 and 280,27 nm, respectively, and the weakly varying photospheric wings or continuum longward and shortward of the core line emission, are operationally observed by the instrument.

On the ground, the Mg II core-to-wing ratio is calculated between the variable lines and nearly non-varying wings. The result is a measure of chromospheric and some photospheric solar active region activity is referred to as the Mg II core-to-wing ratio (cwr), and is provided daily by NOAA Space Environment Center (SEC). The ratio is an especially good proxy for some solar FUV and EUV emissions and it can represent very well the photospheric and lower chromospheric solar FUV Schumann-Runge Continuum emission. The daily Mg II cwr is used in a linear regression with *F10.7* to derive the *M10.7* index for reporting in *F10.7* units and with a 5-day lag.

F.3 Additional information on short-term variation

The profile given in Table 6-4 starts from medium activity levels. Then an x-ray / gamma-ray flare occurs. On the sun-surface this goes together with the ejection of highly energetic charged particles. The flare can push up the *F10.7* index near Earth almost instantaneously. The a_p is still at its normal value for medium activity between 7 and 15. The *F10.7* then fades within about 9 hours to pre-flare values. After a little less than a day the fastest solar wind particles arrive at Earth, disturb the magnetic field, and thus the a_p index increases. The disturbance lasts only about 6 hours. Thereafter it settles at its pre-event levels between 7-15 hours. The *F10.7* stays at its average value.

The profile covers 1 day. It can be recurring as a disturbance event can easily last about a week. During such an event, flares occur repeatedly within the same active region on the

sun. Extreme values of *F10.7* and a_p do not usually occur simultaneously. Such a situation only occurs at the Earth if a second flare, essentially unrelated to the first, occurred on the sun at the same time that the charged particles from the first flare arrived at Earth. That situation is possible but happens rarely and seems not to have occurred within the historical data set.

The activity profile given in Table 6-4 describes a "worst case" event but is neither unrealistic nor overly conservative. The x-rays (high *F10.7*) can lead to enhanced intensities and heating at equatorial and low latitude regions where the solar radiation intensity is highest. The high a_p values lead mainly to an increase of atmospheric density in the high latitude and polar regions where the effect of dissipation of energy and momentum from the magnetosphere is largest.

The short term variation profile in Table 6-4 addresses a_p only. Short term variations of the geomagnetic field have larger effects on the atmosphere than short term variations of the solar activity. The atmospheric effects of solar activity variations on time scales of hours are still uncertain. Large short term variations of a_p can occur during all phases of a solar cycle.

F.4 Useful internet references for indices

- Indices glossary: https://www.swpc.noaa.gov/content/space-weather-glossary
- F10.7, Kp, Ap, Dst, Solar Wind Speed, IMF archive values at ESA Space Weather User Portal http://swe.ssa.esa.int/
- S10.7 and M10.7 at JB-2006 website:
  http://sol.spacenvironment.net/~JB2006/indices.html
- F10.7 predictions at Marshall Space Flight Center's: *http://sail.msfc.nasa.gov/*

F.5 Earth electromagnetic radiation

F.5.1 Earth albedo

The fraction of incident sunlight that is reflected off a planet is termed albedo. For an orbiting spacecraft the albedo value depends mainly on the sunlit part of the Earth which it can see. Albedo radiation has approximately the same spectral distribution as the Sun and in this Standard albedo refers to the total solar spectrum albedo. Albedo is highly variable across the globe and depends on surface properties and cloud cover. It also depends on the solar zenith angle. Average albedo values have sometimes to be used with care, e.g. for short duration analyses or for Sun-synchronous orbits where albedo is from specific local times.

The average albedo of the Earth is 0,3. For an orbiting spacecraft, the albedo can vary between 0,05 (open ocean) and 0,6 (high cloud/icecap).

A model has been constructed for estimating the influence of latitude and longitude on albedo variability (seasonal effect) [RD.34]. The albedo, a, is given by:

$$a = a_0 + a_1 P_1(\sin\varphi) + a_2 P_2(\sin\varphi) \quad \text{(F-1)}$$

where

$$a_1 = c_0 + c_1 \cos(\omega(JD - t_0)) + c_2 \sin(\omega(JD - t_0))$$

t_0 is the date

ω is the orbital pulsation (=2π/365,25)

φ is the equatorial latitude

JD is the Julian date of interest

P_n is the nth degree Legendre polynomial

and

a_0=0,34

a_1 [c_0=0, c_1=0,10, c_2=0]

a_2=0,29

F.5.2 Earth infrared

The Earth-emitted thermal radiation has a spectrum of a black body with a characteristic average temperature of 288 K. The Earth infrared radiation also varies across the globe but less than the albedo. It also shows a diurnal variation which is small over the ocean but can amount to 20 % for desert areas.

The average infrared radiation emitted by Earth is 230 W m^{-2}. For an orbiting spacecraft, it can vary from 150 W m^{-2} to 350 W m^{-2}. The diurnal variations can amount to about 20 % over desert areas while being smaller over the oceans.

A model has been constructed for estimating the influence of latitude and longitude on Earth infrared variability (seasonal effect) [RD.34], given by:

$$e = e_0 + e_1 P_1(\sin\varphi) + e_2 P_2(\sin\varphi) \quad \text{(F-2)}$$

where

$$e_1 = k_0 + k_1 \cos(\omega(JD - t_0)) + k_2 \sin(\omega(JD - t_0))$$

t_0 is the date

ω is the orbital pulsation (=2π/365,25)

φ is the equatorial latitude

JD is the Julian date of interest

P_n is the nth degree Legendre polynomial

and the following values are proposed:

e_0= 0,68

e_1 [k_0=0, k_1=-0,07, k_2=0]

e_2= -0,18

F.6 Electromagnetic radiation from other planets

F.6.1 Planetary albedo

Albedo is the fraction of sunlight, which is reflected off a planet. The reflection is assumed to be diffuse. For the albedo the same spectral shape as for sunlight is assumed. The actual albedo spectrum can change, depending on properties of the surface (different materials can lead to absorption in certain wavelength bands and result in a highly variable spectrum). Albedo values are only applicable when the portion of the planet that is seen by the spacecraft is sunlit.

F.6.2 Planetary infrared

A large portion of the incident solar radiation being absorbed as heat by the planet is re-emitted in the infrared range of the spectrum. Reference values for average planetary albedo and infra-red radiation are given in Table F-1.

F.7 Activity indices information

Figure F-2 and Figure F-3 show the F10.7, Sunspot Number R and A_p indices over the last two solar cycles. Figure F-2 gives the daily and Figure F-3 the monthly mean values. The large fluctuations in the daily values are averaged out in the monthly mean values (please note the different scale of the figures). The short term A_p spikes are important for density variations and this is not well reflected in the long term high values.

F.8 Tables

Table F-1: Reference values for average planetary albedo and infra-red radiation

Planet	Average Albedo	Albedo Range	Average IR [K]	IR Range [K]
Mercury	0,106	0,09 – 0,45	442	100 – 725
Venus	0,65		231,7	737 (surface)
Mars	0,15		210,1	184 - 242
Jupiter	0,52		110,0	112 @ 100 hPa
Saturn	0,47		81,1	1 – 143 @ 1000 hPa
Uranus	0,51		58,2	76 @ 1000 hPa 53@ 100 hPa
Neptune	0,41		46,6	72@1000 hPa, 44 @ 100 hPa
Titan	0,22			

F.9 Figures

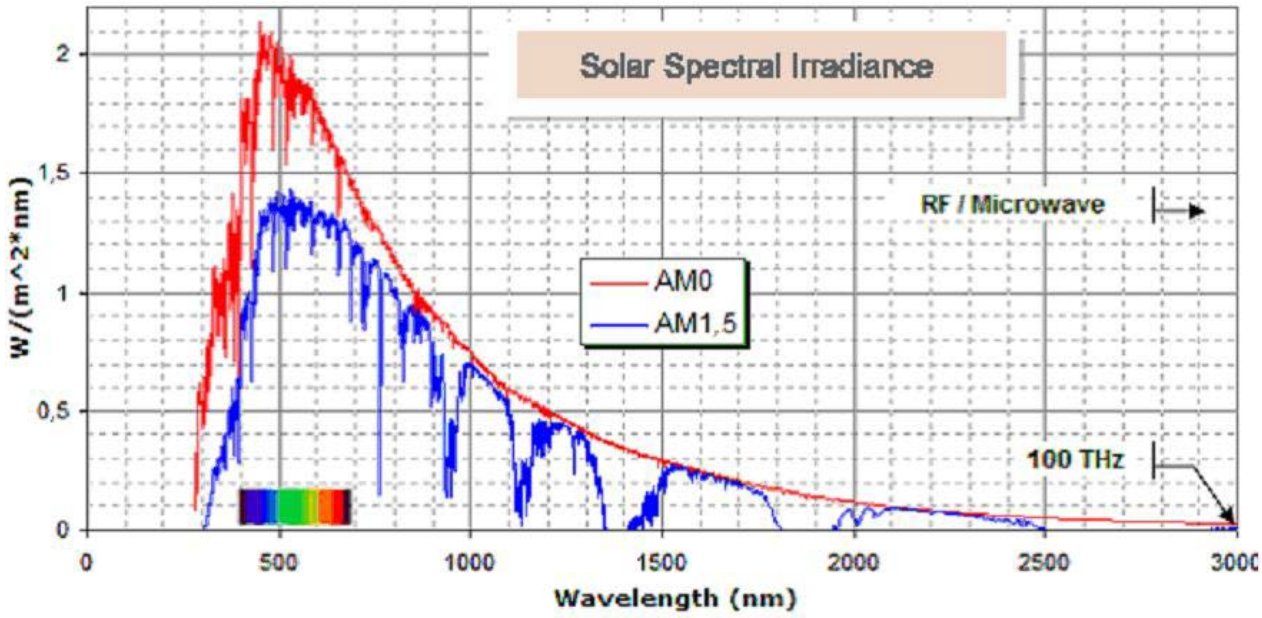

Figure F-1: Solar spectral irradiance (in red, AM0 (Air Mass 0) is the radiation level outside of the Earth's atmosphere (extraterrestrial), in blue, AM1,5 is the radiation level after passing through the atmosphere 1,5 times, which is about the level at solar zenith angle 48,19°s, an average level at the Earth's surface (terrestrial)).

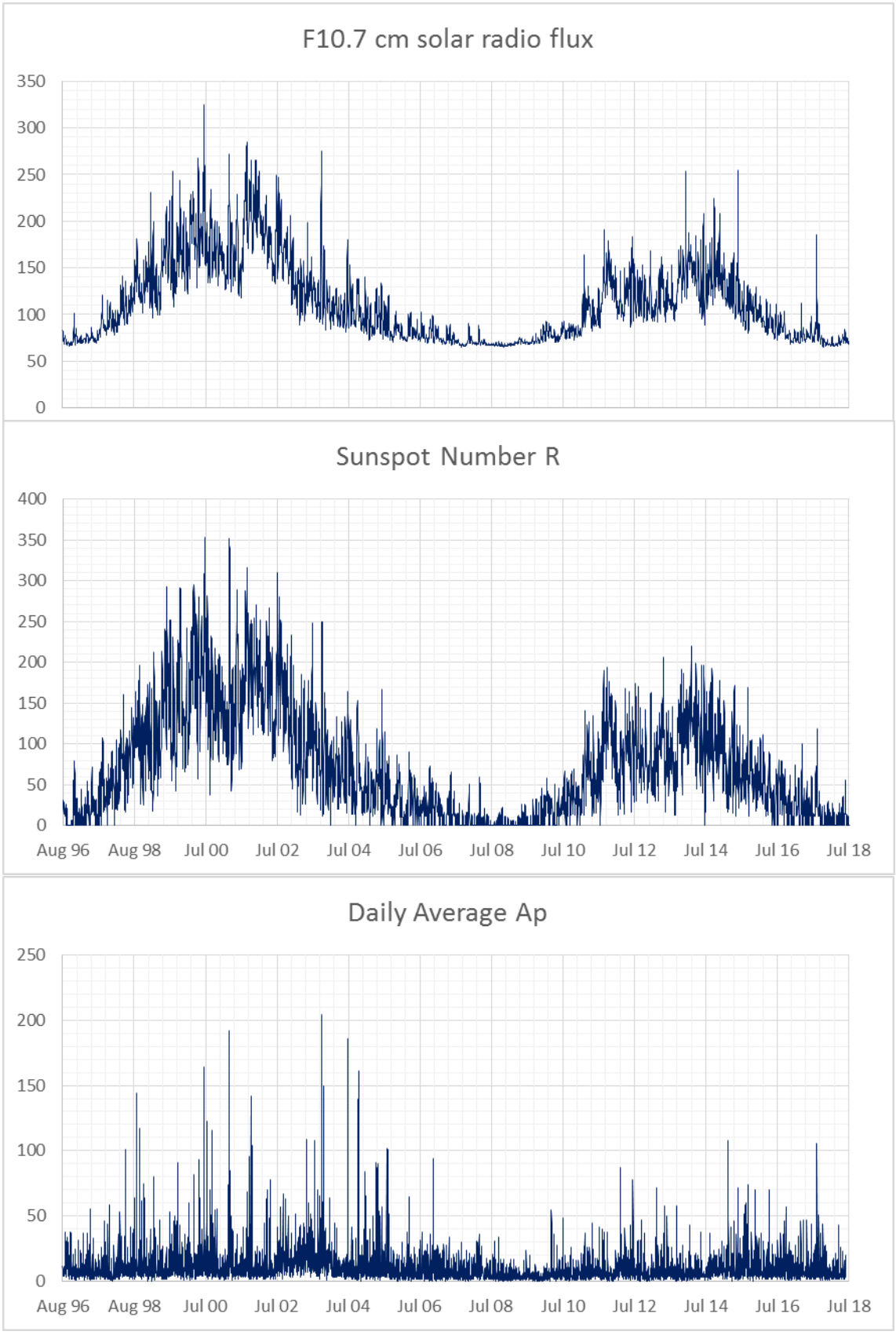

Figure F-2: Daily solar and geomagnetic activity indices over the last two solar cycles

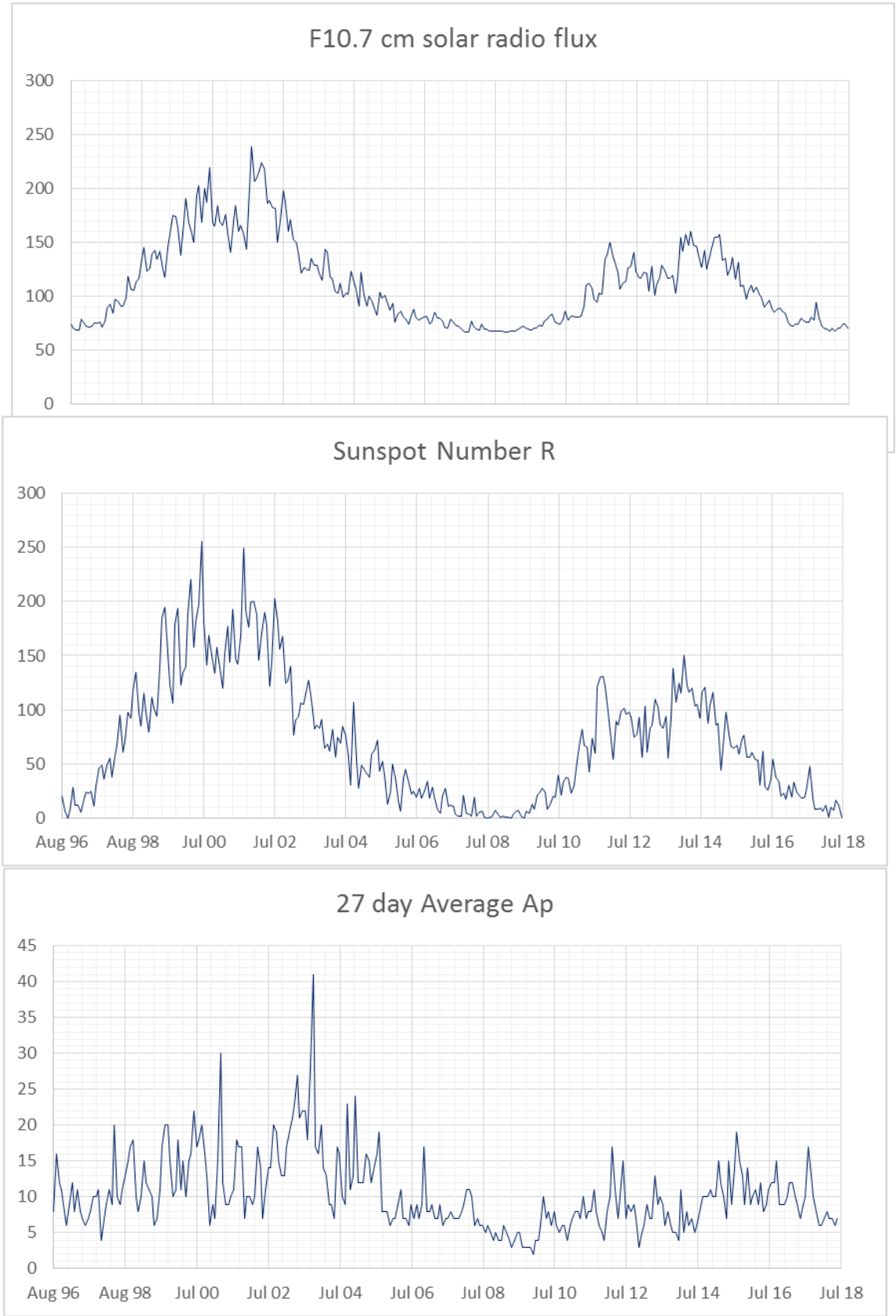

Figure F-3: Monthly (27 day) mean solar and geomagnetic activity indices over the last two solar cycles

Annex G (informative) Neutral atmospheres

G.1 Structure of the Earth's atmosphere

The Earth atmosphere can be broadly divided into three distinct regimes, as shown in Figure G-1:

- the homosphere comprises the regions of the troposphere (surface up to ~ 10 - 12 km altitude), the stratosphere (~ 10 - 12 km up to 50 km), and the mesosphere (~50 km up to 90 km),
- the thermosphere extends from about 90 km altitude to approx 400 km, depending on solar and geomagnetic activity,
- the exosphere extends from the top of the thermosphere and extends into space.

The boundaries between these regions are classically defined by relatively sharp and consistent changes in the temperature profile as a function of altitude, with the exception of the base of the exosphere. The exosphere base is defined by that altitude where the mean free path equals the scale height. In practice, all of these boundaries, whether determined in altitude or in a pressure co-ordinate system, vary with solar, seasonal, latitudinal and other conditions.

Due to vertical winds and turbulent mixing the homosphere has a nearly uniform composition of about 78,1% N_2, 20,9% O_2, and 0,9% Ar. The temperature profile of the heterosphere shows alternating gradients with (normally) the maximum temperature at the surface (global average ~288K), a local minimum at the tropopause (global average ~218K), a local maximum at the stratopause (global average ~280K), and another local minimum at the mesopause (≈150K – 250K).

G.2 Development of models of the Earth's atmosphere

A "Standard Atmosphere" is defined as a vertical distribution of atmospheric temperature, pressure, and density, which by international agreement is taken to be representative of the Earth's atmosphere. The first "Standard Atmospheres" established by international agreement were developed in the 1920's primarily for purposes of pressure altimeter calibrations, aircraft performance calculations, aircraft and rocket design, ballistic tables, etc. Later some countries, notably the United States, also developed and published "Standard Atmospheres". The term "Reference Atmosphere" is used to identify vertical descriptions of the atmosphere for specific geographical locations or globally. These were developed by organizations for specific applications, especially as the aerospace industry began to mature after World War II. The term "Standard Atmosphere" has in recent years also been used by national and international

organizations to describe vertical descriptions of atmospheric trace constituents, the ionosphere, atomic oxygen, aerosols, ozone, winds, water vapour, planetary atmospheres, etc.

Currently some of the most commonly used Standard and Reference Atmospheres include the ISO Standard Atmosphere, 1975 [RD.126], 1982 [RD.127] the U. S. Standard Atmosphere Supplements, 1962 [RD.123], 1966 [RD.124]] 1976 [RD.125], the COSPAR International Reference Atmosphere (CIRA), 1986 [RD.128] (previously issued as CIRA 1961 [RD.129], CIRA 1965 [RD.130] and CIRA 1972 [RD.131]), the NASA/MSFC Global Reference Atmosphere Model (GRAM), 1999 [RD.136] (previously issued as GRAM-86 [RD.132]], GRAM-88 [RD.133], GRAM-90 [RD.134] and GRAM-95 [RD.135]), the NRLMSISE-00 Thermospheric Model, 2000 [RN.4] (previously issued as MSIS-77 [RD.35], -83 [RD.37], -86 [RD.38]] and MSISE-90 [RD.137]) and most recently the JB-2006 density Model [RN.5].

G.3 NRLMSISE-00 and JB-2006 - additional information

The Mass Spectrometer and Incoherent Scatter (MSIS) series of models developed between 1977 and 1990 are used extensively by the scientific community for their superior description of neutral composition. The models utilized atmospheric composition data from instrumented satellites and temperatures from ground-based radars. The initial MSIS 1977 model [RD.35] was based on the Jacchia temperature profile framework, but the density at 120 km varied with local time and other geophysical parameters to fit the measurements. Exospheric temperature and density variations were represented by spherical harmonics resulting in requiring fewer parameters for a given level of accuracy. Subsequent versions of the model include the longitude variations [RD.36], a refined geomagnetic storm effect [RD.37], improved high latitude, high solar flux data [RD.38] and a boundary lowered to sea level [RD.39].

The NRLMSISE-00 model [RN.4] of atmospheric composition, temperature, and total mass density from ground to exobase includes the following:

- drag data based on orbit determination,
- more recent accelerometer data sets,
- new temperature data derived from Millstone Hill and Arecibo incoherent scatter radar observations,
- observations of O_2 by the Solar Maximum Mission (SMM), based on solar ultraviolet occultation.

A new species, “anomalous oxygen,” primarily for drag estimation, allows for appreciable O+ and hot atomic oxygen contributions to the total mass density at high altitudes.

The new Jacchia-Bowman density (JB-2006) model [RN.5] is based on the Jacchia model heritage. It includes two key novel features. Firstly, there is a new formulation concerning the semi-annual density variation observed in the thermosphere, but not previously included in any of the semi-empirical atmospheric models. Secondly, there is a new formulation of solar indices, relating more realistically to the dependence of heat and energy inputs from the solar radiation to specific altitude regions and heating processes within the upper atmosphere. JB-2006 inserts the improved J70 temperature formulations into the CIRA 1972 model to permit integrating the diffusion equation at every point rather than relying on look-up tables.

G.4 The GRAM series of atmosphere models.

The GLOBAL Reference Atmosphere Models have been produced on behalf of NASA to describe the terrestrial atmosphere from ground level upward for operational purposes. These models are available via license to qualified users, and provide usability and information quality similar to that of the NRLMSISE-00 Model [RD.40].

G.5 Atmosphere model uncertainties and limitations

For mean activity conditions, the estimated uncertainty of the NRLMSISE-00 species density is 15%. For short term and local-scale variations, the estimated uncertainty of the NRLMSISE-00 species density is 100%. Within the homosphere (below 90 km), the uncertainty is below 5% [RD.40].

For mean activity conditions, the estimated uncertainty of the JB-2006 total density within the thermosphere is 10-15% (depending on altitude). For extreme conditions (very high solar or geomagnetic activities), this uncertainty can considerably increase due to the lack of corresponding measurement data. The total density can have +/- 100% variation at 400-500 km for some activities and locations.

It should be noted that the NRLMSISE-00 model's accuracy of prediction of atmospheric density and other parameters is limited by the complex behaviour of the atmosphere, and the causes of variability. While certain aspects of atmospheric variability are more or less deterministic, meteorological variations of the homosphere are difficult to predict more than 3 – 5 days in advance, and yet have effects on higher regions of the atmosphere (thermosphere). In the thermosphere, the response to varying solar and geomagnetic activity is complex, particularly in respect of the latter. Upper atmosphere density models can be used for prediction of future orbital lifetime, either to determine the orbital altitude insertions to ensure a given lifetime, or to estimate energy requirements for maintaining a particular orbit, for a particular spacecraft/satellite. The primary influence on accuracy of the model's density output is the accuracy of the future predictions of solar and geomagnetic activity used as inputs, rather than the accuracy of the specific model in representing the density as a function of solar and geomagnetic activity.

G.6 HWM07 additional information

The HWM is an empirical model of the horizontal neutral wind in the upper thermosphere. It is based on an extensive data set gathering 60x106 observations from 35 different instruments spanning 50 years (see Table 1 of [RN.40]. A limited set of vector spherical harmonics is used to describe the zonal and meridional wind components. The first edition of the model released in 1987 (HWM87) [RD.42] was intended for winds above 220 km. With the inclusion of wind data from ground-based incoherent scatter radar and Fabry-Perot optical interferometers, HWM90 was extended down to 100 km and using MF/Meteor data HWM93 was extended down to the ground [RN.6]. Solar cycle variations are included (since HWM90), but they are found to be small and not always very clearly delineated be the current data. Variations with magnetic activity (A_p) are included. Mid- and low-latitude data are reproduced quite well by the model. The polar vortices are present, but not in full detail. The model describes the transition from predominately diurnal variations in the upper thermosphere to semidiurnal variations in the lower thermosphere and a transition from summer to winter flow above 140 km to winter to summer flow below. Significant altitude gradients in the wind extend up to 300

km at some local times. The model software provides zonal and meridional winds for specified latitude, longitude, time, and A_p index. A comparison of the HWM values with winds derived from IRI parameters and from ionosonde measurements have shown in general good agreement. The HMW07 model provides a better agreement with obervational data. Its ability to represent the observed variations of the atmosphere is significantly improved compared to that of HWM93. While HWM07 represents geomagnetically quiet conditions the DWM07 component (see **Error! Reference source not found.**) represents storm-induced thermospheric disturbance winds in the altitude range from 200 km to 600 km, based on the 3h Kp geomagnetic activity index.

G.7 Planetary atmospheres models

G.7.1 Jupiter

Because Jupiter is a large planet that rotates fast, the equatorial tangential velocity of the atmosphere is 12,7 km s^{-1}, and decreases like the cosine of latitude. In the reference frame rotating with the planet the acceleration of gravity is 22,88 m s^{-2} at the equator and 25 N kg^{-1} at the poles.

The structure of the upper atmosphere of Jupiter is reasonably well-known between 60 degrees north and south down to a pressure of 1 hPa, thanks to the measurements of the Composite Infrared Spectrometer, during the swing-by of the Cassini spacecraft past Jupiter in late 2000 and early 2001 [RD.43]. In addition the equatorial atmosphere has been explored down to a pressure of 2,1E+06 hPa during the entry and descent of the Galileo probe [RD.44].

These measurements reveal that the structure of the atmosphere of Jupiter is relatively simple: a troposphere in convective equilibrium with a constant adiabatic lapse rate, topped by a well-defined tropopause at a minimum temperature of about 100 K above which the temperature increases to a temperature of 160 K and remains practically constant in the region of maximum deceleration and heat fluxes during entry. Above that constant temperature region, roughly above 300 km the temperature increases again.

The composition of the atmosphere of Jupiter has been measured by the Galileo probe between pressure levels of 5,1E+04 hPa and 2,11E+06 hPa[RD.44]. This composition is as follows (volume mixing ratio): H_2 (86%), He (13,6%), CH_4 (0,18%), N_2 (0,07%). The above composition is valid for the troposphere and most of the stratosphere. The corresponding molar mass is 2,31x10^{-3} kg mol^{-1}.

The atmosphere of Jupiter is subject to a small seasonal cycle and the equatorial stratosphere experiences cyclic temperature variations of about 10 K with a quasi-quadrennial cycle. This cycle seems to be related to wave activity [RD.45], and large-scale gravity waves have been observed by the Galileo Atmosphere Structure Instrument (ASI) during the Galileo entry [RD.46].

G.7.2 Venus

A Venus International Reference Atmosphere (VIRA), from 0 to 100 km, has been compiled by COSPAR [RD.47], with follow-up work ongoing to update the original model [RD.153]. It consists of a deep atmosphere, extending from 0 to 32 km (altitudes are referenced to a planetary radius of 6 052 km) whose vertical structure is independent

of latitude and characterized by a surface pressure of 9,21E+06 hPa, surface temperature of 753,3 K and surface density of 64,8 kg m^{-3} and a lapse rate increasing from 8 to 9 K km^{-1}. Above 32 km, the atmosphere shows some latitude dependence, and is tabulated by bands of latitude.

G.7.3 Mars

Basic knowledge of the Martian atmospheric environment can be found in [RD.48].

For Mars two reference models exist: the MarsGRAM-2010 [RD.49], [RD.50] developed by NASA MSFC and the Martian Climate Database (EMCD) developed jointly by Laboratoire de Météorologie Dynamique (France), Oxford University (UK) and the Institute of Astrophysics of Andalusia (Spain) [RN.7].

These models, which cover the altitude range 0–250 km, have been derived with the help of a combination of geophysical measurements and simulations using general circulation models of the Martian atmosphere [RD.41], [RD.51].

The models agree broadly with each other but differ in many details. Ultimately the use of one or the other model for mission design gives equivalent results if appropriate margins have been taken into account.

G.7.4 Saturn

There is currently no adopted Reference Atmosphere Model for Saturn, however global circulation models are being developed ([RD.154] and [RD.155]) and form the most accurate source of information to date. Saturn's atmosphere is about 96 percent hydrogen and 3 percent helium by volume, a proportion similar to that found in the sun and Jupiter. Small amounts of methane, ammonia, and water also are present. A layer of clouds composed of ammonia ice compose what is seen in photographs and through the telescope. Deeper in the atmosphere, the clouds can be formed of water ice.

G.7.5 Titan

An engineering-level atmospheric model for Titan (Titan-GRAM) has been developed [RD.52] for use in NASA's systems analysis studies of aerocapture applications in missions to outer planets. A Titan atmosphere database has been gathered in Europe [RD.156] including Cassini/Huygens data, but is not tailored for engineering purposes..

G.7.6 Neptune

An engineering-level atmospheric models for Neptune (Neptune-GRAM) has been developed [RD.52] for use in NASA's systems analysis studies of aerocapture applications in missions to outer planets.

G.7.7 Mercury

There is currently no adopted Reference Atmosphere Model for Mercury. The atmosphere is more accurately described as an exosphere, where individual atoms and molecules reside mainly on the surface, until released into ballistic orbits by a combination of excitation by solar photons and energetic particles (again, primarily of solar origin). The composition is

not precisely known, but O, H, He, Na, Ca and K have been detected. The temperature reflects the Mercury surface temperature, the surface pressure is of order 10^{-7} hPa, with a number density of order 10^{11} m^{-3}

G.8 Reference data

NRLMSISE-00 altitude profiles at equatorial latitude of temperature, and number densities (concentrations) are listed in Table G-1, Table G-2, and Table G-3 for low solar and geomagnetic activities ($F10.7 = F10.7_{avg} = 65$, $A_p = 0$), moderate solar and geomagnetic activities ($F10.7 = F10.7_{avg} = 140$, $A_p = 15$), and high long term solar and geomagnetic activities ($F10.7 = F10.7_{avg} = 250$, $A_p = 45$), respectively. The tables cover both homospheric and heterospheric altitudes from ground level up to 900 km, averaged over diurnal and seasonal variations. Figure G-1, illustrates the altitude profile of the temperature. Figure G-3 shows the atomic oxygen number densities at low, moderate and high long term activity conditions. For moderate activity levels, Figure G-4 shows the logarithmic number concentration profiles of the main atmospheric constituents.

A JB-2006 altitude profile of total density at equatorial latitude is listed in Table G-4 and plotted again in Figure G-2 for

- low solar and geomagnetic activities
  ($F10.7 = F10.7_{avg} = 65$, $S10.7 = S10.7_{avg} = 60$, $M10.7 = M10.7_{avg} = 60$, $A_p = 0$)
- moderate solar and geomagnetic activities
  ($F10.7 = F10.7_{avg} = 140$, $S10.7 = S10.7_{avg} = 125$, $M10.7 = M10.7_{avg} = 125$, $A_p = 15$)
- high long term (27 days or longer) solar and geomagnetic activities
  ($F10.7 = F10.7_{avg} = 250$, $S10.7 = S10.7_{avg} = 220$, $M10.7 = M10.7_{avg} = 220$, $A_p = 45$)
- and high short term (daily) solar and geomagnetic activities
  ($F10.7 = 300$, $F10.7_{avg} = 250$, $S10.7 = 235$, $S10.7_{avg} = 220$, $M10.7 = 240$, $M10.7_{avg} = 220$, $A_p = 240$)
- The subscript ‘avg’denotes the 81-day average.

These values have been averaged over diurnal and seasonal variations.

G.9 Tables

Table G-1: Altitude profiles of the atmosphere constituents N_2, O, O_2, He, Ar, H, N and anomalous O for low solar and geomagnetic activities (NRLMSISE-00 model - *F10.7* = $F10.7_{avg}$ = 65, A_p = 0)

H (km)	n_{HE} (m^{-3})	n_O (m^{-3})	n_{N2} (m^{-3})	n_{O2} (m^{-3})	n_{AR} (m^{-3})	n_H (m^{-3})	n_N (m^{-3})	$n_{Anomal\ O}$ (m^{-3})	T(K)	ϱ ($kg.m^{-3}$)
0	1,17E+20	0,00E+00	1,74E+25	4,67E+24	2,08E+23	0,00E+00	0,00E+00	0,00E+00	3,00E+02	1,07E+00
20	9,46E+18	0,00E+00	1,41E+24	3,78E+23	1,69E+22	0,00E+00	0,00E+00	0,00E+00	2,06E+02	8,68E-02
40	4,05E+17	0,00E+00	6,04E+22	1,62E+22	7,23E+20	0,00E+00	0,00E+00	0,00E+00	2,57E+02	3,72E-03
60	3,29E+16	0,00E+00	4,90E+21	1,31E+21	5,86E+19	0,00E+00	0,00E+00	0,00E+00	2,45E+02	3,01E-04
80	1,89E+15	3,01E+15	2,73E+20	7,27E+19	3,25E+18	2,65E+13	6,64E+10	2,28E-51	2,06E+02	1,68E-05
100	1,17E+14	4,78E+17	1,02E+19	2,38E+18	1,04E+17	2,70E+13	3,10E+11	2,24E-37	1,71E+02	6,18E-07
120	2,50E+13	7,23E+16	3,11E+17	4,36E+16	1,36E+15	6,07E+12	1,19E+12	1,41E-27	3,53E+02	1,88E-08
140	1,50E+13	2,12E+16	4,89E+16	4,45E+15	1,09E+14	2,17E+12	6,16E+12	2,44E-19	5,21E+02	3,08E-09
160	1,16E+13	9,37E+15	1,38E+16	1,06E+15	1,88E+13	1,09E+12	1,61E+13	1,12E-12	6,05E+02	9,49E-10
180	9,61E+12	4,88E+15	4,76E+15	3,34E+14	4,23E+12	7,31E+11	2,20E+13	1,45E-07	6,48E+02	3,70E-10
200	8,21E+12	2,73E+15	1,80E+15	1,15E+14	1,08E+12	5,94E+11	2,02E+13	1,20E-03	6,70E+02	1,63E-10
220	7,12E+12	1,59E+15	7,14E+14	4,11E+13	2,98E+11	5,32E+11	1,51E+13	1,22E+00	6,82E+02	7,80E-11
240	6,21E+12	9,42E+14	2,93E+14	1,51E+13	8,62E+10	4,98E+11	1,04E+13	2,43E+02	6,88E+02	3,97E-11
260	5,45E+12	5,66E+14	1,23E+14	5,66E+12	2,59E+10	4,75E+11	6,85E+12	1,40E+04	6,92E+02	2,13E-11
280	4,78E+12	3,44E+14	5,27E+13	2,16E+12	8,02E+09	4,57E+11	4,50E+12	3,08E+05	6,94E+02	1,18E-11
300	4,21E+12	2,10E+14	2,30E+13	8,42E+11	2,54E+09	4,41E+11	2,96E+12	3,26E+06	6,95E+02	6,80E-12
320	3,71E+12	1,30E+14	1,01E+13	3,33E+11	8,22E+08	4,27E+11	1,96E+12	1,96E+07	6,96E+02	4,01E-12
340	3,28E+12	8,05E+13	4,54E+12	1,33E+11	2,71E+08	4,13E+11	1,30E+12	7,64E+07	6,96E+02	2,41E-12
360	2,90E+12	5,02E+13	2,06E+12	5,42E+10	9,06E+07	4,00E+11	8,74E+11	2,13E+08	6,96E+02	1,47E-12
380	2,56E+12	3,15E+13	9,43E+11	2,23E+10	3,07E+07	3,87E+11	5,88E+11	4,60E+08	6,96E+02	9,14E-13
400	2,27E+12	1,99E+13	4,37E+11	9,29E+09	1,06E+07	3,75E+11	3,98E+11	8,15E+08	6,96E+02	5,75E-13
420	2,01E+12	1,26E+13	2,04E+11	3,91E+09	3,66E+06	3,64E+11	2,70E+11	1,24E+09	6,96E+02	3,66E-13
440	1,78E+12	8,06E+12	9,61E+10	1,66E+09	1,29E+06	3,53E+11	1,85E+11	1,69E+09	6,96E+02	2,35E-13
460	1,58E+12	5,17E+12	4,56E+10	7,13E+08	4,55E+05	3,42E+11	1,26E+11	2,09E+09	6,96E+02	1,53E-13
480	1,41E+12	3,33E+12	2,18E+10	3,09E+08	1,63E+05	3,32E+11	8,68E+10	2,42E+09	6,96E+02	1,01E-13
500	1,25E+12	2,15E+12	1,05E+10	1,35E+08	5,87E+04	3,22E+11	5,99E+10	2,66E+09	6,96E+02	6,79E-14
520	1,11E+12	1,40E+12	5,11E+09	5,92E+07	2,13E+04	3,12E+11	4,15E+10	2,81E+09	6,96E+02	4,63E-14
540	9,91E+11	9,14E+11	2,50E+09	2,62E+07	7,81E+03	3,03E+11	2,88E+10	2,88E+09	6,96E+02	3,21E-14
560	8,83E+11	5,99E+11	1,23E+09	1,17E+07	2,88E+03	2,94E+11	2,00E+10	2,88E+09	6,96E+02	2,28E-14
580	7,88E+11	3,94E+11	6,07E+08	5,24E+06	1,07E+03	2,85E+11	1,40E+10	2,83E+09	6,96E+02	1,65E-14
600	7,04E+11	2,60E+11	3,02E+08	2,36E+06	4,01E+02	2,77E+11	9,79E+09	2,74E+09	6,96E+02	1,23E-14
620	6,29E+11	1,73E+11	1,51E+08	1,07E+06	1,51E+02	2,69E+11	6,88E+09	2,63E+09	6,96E+02	9,37E-15
640	5,63E+11	1,15E+11	7,59E+07	4,90E+05	5,74E+01	2,61E+11	4,84E+09	2,50E+09	6,96E+02	7,33E-15
660	5,04E+11	7,67E+10	3,84E+07	2,25E+05	2,19E+01	2,54E+11	3,42E+09	2,37E+09	6,96E+02	5,88E-15
680	4,51E+11	5,14E+10	1,95E+07	1,04E+05	8,42E+00	2,46E+11	2,42E+09	2,23E+09	6,96E+02	4,83E-15
700	4,04E+11	3,45E+10	9,94E+06	4,84E+04	3,26E+00	2,39E+11	1,72E+09	2,09E+09	6,96E+02	4,04E-15
720	3,63E+11	2,33E+10	5,10E+06	2,26E+04	1,27E+00	2,33E+11	1,22E+09	1,96E+09	6,96E+02	3,44E-15
740	3,26E+11	1,58E+10	2,63E+06	1,06E+04	4,97E-01	2,26E+11	8,70E+08	1,83E+09	6,96E+02	2,98E-15
760	2,93E+11	1,07E+10	1,36E+06	5,00E+03	1,96E-01	2,20E+11	6,21E+08	1,70E+09	6,96E+02	2,61E-15
780	2,63E+11	7,28E+09	7,06E+05	2,37E+03	7,75E-02	2,14E+11	4,45E+08	1,59E+09	6,96E+02	2,31E-15
800	2,37E+11	4,97E+09	3,68E+05	1,13E+03	3,09E-02	2,08E+11	3,20E+08	1,48E+09	6,96E+02	2,06E-15
820	2,13E+11	3,40E+09	1,93E+05	5,41E+02	1,24E-02	2,02E+11	2,30E+08	1,38E+09	6,96E+02	1,85E-15
840	1,92E+11	2,33E+09	1,02E+05	2,60E+02	4,99E-03	1,97E+11	1,66E+08	1,28E+09	6,96E+02	1,67E-15
860	1,73E+11	1,61E+09	5,36E+04	1,26E+02	2,02E-03	1,91E+11	1,20E+08	1,19E+09	6,96E+02	1,51E-15
880	1,57E+11	1,11E+09	2,85E+04	6,09E+01	8,25E-04	1,86E+11	8,68E+07	1,11E+09	6,96E+02	1,38E-15
900	1,41E+11	7,67E+08	1,52E+04	2,97E+01	3,38E-04	1,81E+11	6,30E+07	1,03E+09	6,96E+02	1,26E-15

Table G-2: Altitude profiles of the atmosphere constituents N_2, O, O_2, He, Ar, H, N and anomalous O for mean solar and geomagnetic activities (NRLMSISE-00 model - *F10.7* = $F10.7_{avg}$ = 140, A_p = 15)

H (km)	n_{HE} (m^{-3})	n_O (m^{-3})	n_{N2} (m^{-3})	n_{O2} (m^{-3})	n_{AR} (m^{-3})	n_H (m^{-3})	n_N (m^{-3})	$n_{Anomal\ O}$ (m^{-3})	T(K)	ϱ ($kg.m^{-3}$)
0	1,26E+20	0,00E+00	1,88E+25	5,04E+24	2,25E+23	0,00E+00	0,00E+00	0,00E+00	3,00E+02	1,16E+00
20	1,02E+19	0,00E+00	1,52E+24	4,09E+23	1,82E+22	0,00E+00	0,00E+00	0,00E+00	2,06E+02	9,37E-02
40	4,38E+17	0,00E+00	6,53E+22	1,75E+22	7,81E+20	0,00E+00	0,00E+00	0,00E+00	2,57E+02	4,02E-03
60	3,55E+16	0,00E+00	5,29E+21	1,42E+21	6,33E+19	0,00E+00	0,00E+00	0,00E+00	2,45E+02	3,26E-04
80	2,07E+15	3,71E+15	3,00E+20	7,66E+19	3,56E+18	2,53E+13	8,61E+10	8,53E-51	1,98E+02	1,83E-05
100	1,16E+14	5,22E+17	9,60E+18	2,00E+18	9,71E+16	1,89E+13	3,76E+11	7,28E-37	1,88E+02	5,73E-07
120	3,08E+13	9,27E+16	3,36E+17	3,95E+16	1,49E+15	3,47E+12	1,77E+12	5,52E-27	3,65E+02	2,03E-08
140	1,83E+13	2,73E+16	5,38E+16	3,84E+15	1,26E+14	8,82E+11	9,45E+12	8,98E-19	6,10E+02	3,44E-09
160	1,39E+13	1,31E+16	1,72E+16	9,29E+14	2,64E+13	3,46E+11	2,73E+13	4,12E-12	7,59E+02	1,20E-09
180	1,16E+13	7,47E+15	7,08E+15	3,22E+14	7,67E+12	2,01E+11	4,18E+13	5,33E-07	8,53E+02	5,46E-10
200	1,00E+13	4,67E+15	3,27E+15	1,31E+14	2,61E+12	1,53E+11	4,31E+13	4,43E-03	9,11E+02	2,84E-10
220	8,91E+12	3,06E+15	1,62E+15	5,81E+13	9,73E+11	1,33E+11	3,64E+13	4,48E+00	9,49E+02	1,61E-10
240	8,00E+12	2,07E+15	8,36E+14	2,71E+13	3,84E+11	1,23E+11	2,82E+13	8,94E+02	9,73E+02	9,60E-11
260	7,24E+12	1,43E+15	4,44E+14	1,31E+13	1,58E+11	1,17E+11	2,10E+13	5,14E+04	9,88E+02	5,97E-11
280	6,59E+12	9,94E+14	2,40E+14	6,48E+12	6,69E+10	1,13E+11	1,56E+13	1,14E+06	9,98E+02	3,83E-11
300	6,01E+12	7,00E+14	1,32E+14	3,27E+12	2,90E+10	1,10E+11	1,15E+13	1,20E+07	1,00E+03	2,52E-11
320	5,50E+12	4,96E+14	7,35E+13	1,67E+12	1,28E+10	1,07E+11	8,60E+12	7,22E+07	1,01E+03	1,69E-11
340	5,04E+12	3,54E+14	4,13E+13	8,66E+11	5,75E+09	1,05E+11	6,45E+12	2,81E+08	1,01E+03	1,16E-11
360	4,62E+12	2,54E+14	2,35E+13	4,54E+11	2,61E+09	1,02E+11	4,86E+12	7,85E+08	1,01E+03	7,99E-12
380	4,24E+12	1,83E+14	1,34E+13	2,40E+11	1,20E+09	1,00E+11	3,68E+12	1,69E+09	1,01E+03	5,60E-12
400	3,90E+12	1,32E+14	7,74E+12	1,28E+11	5,61E+08	9,79E+10	2,79E+12	3,00E+09	1,02E+03	3,96E-12
420	3,59E+12	9,56E+13	4,50E+12	6,90E+10	2,64E+08	9,59E+10	2,13E+12	4,57E+09	1,02E+03	2,83E-12
440	3,30E+12	6,96E+13	2,63E+12	3,74E+10	1,25E+08	9,38E+10	1,63E+12	6,21E+09	1,02E+03	2,03E-12
460	3,04E+12	5,08E+13	1,55E+12	2,05E+10	6,00E+07	9,19E+10	1,25E+12	7,70E+09	1,02E+03	1,47E-12
480	2,80E+12	3,72E+13	9,15E+11	1,13E+10	2,90E+07	9,00E+10	9,59E+11	8,92E+09	1,02E+03	1,07E-12
500	2,58E+12	2,73E+13	5,44E+11	6,24E+09	1,41E+07	8,81E+10	7,39E+11	9,81E+09	1,02E+03	7,85E-13
520	2,38E+12	2,01E+13	3,26E+11	3,48E+09	6,90E+06	8,64E+10	5,71E+11	1,04E+10	1,02E+03	5,78E-13
540	2,20E+12	1,48E+13	1,96E+11	1,95E+09	3,40E+06	8,46E+10	4,42E+11	1,06E+10	1,02E+03	4,29E-13
560	2,03E+12	1,10E+13	1,18E+11	1,10E+09	1,69E+06	8,29E+10	3,43E+11	1,06E+10	1,02E+03	3,19E-13
580	1,88E+12	8,17E+12	7,19E+10	6,24E+08	8,42E+05	8,12E+10	2,67E+11	1,04E+10	1,02E+03	2,39E-13
600	1,74E+12	6,08E+12	4,38E+10	3,55E+08	4,23E+05	7,96E+10	2,08E+11	1,01E+10	1,02E+03	1,80E-13
620	1,61E+12	4,54E+12	2,68E+10	2,04E+08	2,13E+05	7,81E+10	1,62E+11	9,69E+09	1,02E+03	1,36E-13
640	1,49E+12	3,40E+12	1,65E+10	1,17E+08	1,08E+05	7,65E+10	1,27E+11	9,22E+09	1,02E+03	1,04E-13
660	1,38E+12	2,55E+12	1,02E+10	6,78E+07	5,52E+04	7,50E+10	9,91E+10	8,72E+09	1,02E+03	7,98E-14
680	1,28E+12	1,92E+12	6,33E+09	3,94E+07	2,83E+04	7,36E+10	7,78E+10	8,20E+09	1,02E+03	6,16E-14
700	1,18E+12	1,45E+12	3,94E+09	2,30E+07	1,46E+04	7,22E+10	6,11E+10	7,70E+09	1,02E+03	4,80E-14
720	1,10E+12	1,09E+12	2,46E+09	1,34E+07	7,54E+03	7,08E+10	4,81E+10	7,20E+09	1,02E+03	3,76E-14
740	1,02E+12	8,27E+11	1,54E+09	7,91E+06	3,92E+03	6,94E+10	3,80E+10	6,73E+09	1,02E+03	2,98E-14
760	9,45E+11	6,28E+11	9,72E+08	4,67E+06	2,05E+03	6,81E+10	3,00E+10	6,28E+09	1,02E+03	2,38E-14
780	8,78E+11	4,78E+11	6,14E+08	2,77E+06	1,07E+03	6,68E+10	2,37E+10	5,85E+09	1,02E+03	1,92E-14
800	8,16E+11	3,64E+11	3,89E+08	1,65E+06	5,65E+02	6,56E+10	1,88E+10	5,45E+09	1,02E+03	1,57E-14
820	7,58E+11	2,78E+11	2,47E+08	9,83E+05	2,99E+02	6,44E+10	1,49E+10	5,07E+09	1,02E+03	1,29E-14
840	7,05E+11	2,13E+11	1,58E+08	5,89E+05	1,59E+02	6,32E+10	1,19E+10	4,72E+09	1,02E+03	1,07E-14
860	6,56E+11	1,63E+11	1,01E+08	3,54E+05	8,47E+01	6,20E+10	9,45E+09	4,40E+09	1,02E+03	9,03E-15
880	6,11E+11	1,26E+11	6,47E+07	2,14E+05	4,53E+01	6,09E+10	7,54E+09	4,09E+09	1,02E+03	7,67E-15
900	5,69E+11	9,68E+10	4,16E+07	1,29E+05	2,44E+01	5,98E+10	6,02E+09	3,81E+09	1,02E+03	6,59E-15

Table G-3: Altitude profiles of the atmosphere constituents N_2, O, O_2, He, Ar, H, N and anomalous O for high long term solar and geomagnetic activities (NRLMSISE-00 model - *F10.7* = $F10.7_{avg}$ = 250, A_p = 45)

H (km)	n_{HE} (m^{-3})	n_O (m^{-3})	n_{N2} (m^{-3})	n_{O2} (m^{-3})	n_{AR} (m^{-3})	n_H (m^{-3})	n_N (m^{-3})	$n_{Anomal\ O}$ (m^{-3})	T(K)	ϱ ($kg.m^{-3}$)
0	1,41E+20	0,00E+00	2,10E+25	5,65E+24	2,52E+23	0,00E+00	0,00E+00	0,00E+00	3,00E+02	1,29E+00
20	1,14E+19	0,00E+00	1,71E+24	4,57E+23	2,04E+22	0,00E+00	0,00E+00	0,00E+00	2,06E+02	1,05E-01
40	4,90E+17	0,00E+00	7,31E+22	1,96E+22	8,74E+20	0,00E+00	0,00E+00	0,00E+00	2,57E+02	4,49E-03
60	3,98E+16	0,00E+00	5,92E+21	1,59E+21	7,09E+19	0,00E+00	0,00E+00	0,00E+00	2,45E+02	3,64E-04
80	2,34E+15	4,36E+15	3,39E+20	8,15E+19	4,02E+18	2,51E+13	1,23E+11	2,04E-50	1,93E+02	2,03E-05
100	1,21E+14	5,70E+17	9,71E+18	1,72E+18	9,73E+16	1,43E+13	5,38E+11	1,57E-36	2,02E+02	5,64E-07
120	3,61E+13	1,15E+17	3,72E+17	3,37E+16	1,62E+15	2,13E+12	3,08E+12	1,36E-26	3,80E+02	2,22E-08
140	2,09E+13	3,51E+16	6,07E+16	3,02E+15	1,43E+14	3,93E+11	1,76E+13	2,12E-18	7,10E+02	3,93E-09
160	1,59E+13	1,86E+16	2,17E+16	6,80E+14	3,51E+13	1,24E+11	5,84E+13	9,74E-12	9,16E+02	1,54E-09
180	1,34E+13	1,15E+16	1,00E+16	2,29E+14	1,21E+13	6,34E+10	1,02E+14	1,26E-06	1,05E+03	7,87E-10
200	1,17E+13	7,72E+15	5,24E+15	9,68E+13	4,91E+12	4,52E+10	1,18E+14	1,05E-02	1,14E+03	4,57E-10
220	1,05E+13	5,42E+15	2,93E+15	4,65E+13	2,18E+12	3,83E+10	1,09E+14	1,06E+01	1,19E+03	2,86E-10
240	9,62E+12	3,93E+15	1,71E+15	2,42E+13	1,03E+12	3,51E+10	9,18E+13	2,11E+03	1,23E+03	1,87E-10
260	8,85E+12	2,90E+15	1,03E+15	1,32E+13	5,02E+11	3,34E+10	7,39E+13	1,22E+05	1,25E+03	1,27E-10
280	8,19E+12	2,17E+15	6,30E+14	7,43E+12	2,52E+11	3,23E+10	5,87E+13	2,68E+06	1,27E+03	8,87E-11
300	7,60E+12	1,64E+15	3,91E+14	4,28E+12	1,30E+11	3,15E+10	4,65E+13	2,84E+07	1,28E+03	6,31E-11
320	7,07E+12	1,25E+15	2,46E+14	2,51E+12	6,77E+10	3,08E+10	3,70E+13	1,71E+08	1,29E+03	4,56E-11
340	6,59E+12	9,53E+14	1,56E+14	1,49E+12	3,59E+10	3,02E+10	2,95E+13	6,65E+08	1,30E+03	3,34E-11
360	6,16E+12	7,32E+14	1,00E+14	8,94E+11	1,93E+10	2,97E+10	2,36E+13	1,85E+09	1,30E+03	2,47E-11
380	5,75E+12	5,65E+14	6,44E+13	5,41E+11	1,05E+10	2,91E+10	1,90E+13	4,00E+09	1,30E+03	1,85E-11
400	5,38E+12	4,37E+14	4,18E+13	3,30E+11	5,75E+09	2,86E+10	1,54E+13	7,10E+09	1,30E+03	1,40E-11
420	5,04E+12	3,39E+14	2,73E+13	2,03E+11	3,18E+09	2,82E+10	1,24E+13	1,08E+10	1,30E+03	1,06E-11
440	4,72E+12	2,64E+14	1,79E+13	1,26E+11	1,78E+09	2,77E+10	1,01E+13	1,47E+10	1,31E+03	8,13E-12
460	4,42E+12	2,06E+14	1,18E+13	7,84E+10	1,00E+09	2,72E+10	8,21E+12	1,82E+10	1,31E+03	6,26E-12
480	4,14E+12	1,62E+14	7,85E+12	4,91E+10	5,66E+08	2,68E+10	6,69E+12	2,11E+10	1,31E+03	4,84E-12
500	3,89E+12	1,27E+14	5,23E+12	3,10E+10	3,23E+08	2,64E+10	5,47E+12	2,32E+10	1,31E+03	3,76E-12
520	3,65E+12	9,97E+13	3,50E+12	1,96E+10	1,85E+08	2,60E+10	4,48E+12	2,45E+10	1,31E+03	2,94E-12
540	3,43E+12	7,86E+13	2,36E+12	1,25E+10	1,07E+08	2,55E+10	3,67E+12	2,51E+10	1,31E+03	2,31E-12
560	3,22E+12	6,21E+13	1,59E+12	8,01E+09	6,21E+07	2,51E+10	3,02E+12	2,51E+10	1,31E+03	1,82E-12
580	3,02E+12	4,92E+13	1,08E+12	5,15E+09	3,62E+07	2,48E+10	2,48E+12	2,47E+10	1,31E+03	1,43E-12
600	2,84E+12	3,91E+13	7,34E+11	3,33E+09	2,13E+07	2,44E+10	2,04E+12	2,39E+10	1,31E+03	1,14E-12
620	2,67E+12	3,11E+13	5,02E+11	2,16E+09	1,25E+07	2,40E+10	1,69E+12	2,29E+10	1,31E+03	9,06E-13
640	2,52E+12	2,48E+13	3,44E+11	1,41E+09	7,41E+06	2,36E+10	1,39E+12	2,18E+10	1,31E+03	7,23E-13
660	2,37E+12	1,98E+13	2,37E+11	9,19E+08	4,41E+06	2,33E+10	1,15E+12	2,06E+10	1,31E+03	5,79E-13
680	2,23E+12	1,58E+13	1,63E+11	6,03E+08	2,63E+06	2,29E+10	9,57E+11	1,94E+10	1,31E+03	4,65E-13
700	2,10E+12	1,27E+13	1,13E+11	3,97E+08	1,58E+06	2,26E+10	7,94E+11	1,82E+10	1,31E+03	3,75E-13
720	1,98E+12	1,02E+13	7,86E+10	2,63E+08	9,50E+05	2,22E+10	6,60E+11	1,70E+10	1,31E+03	3,03E-13
740	1,87E+12	8,21E+12	5,48E+10	1,74E+08	5,74E+05	2,19E+10	5,50E+11	1,59E+10	1,31E+03	2,46E-13
760	1,76E+12	6,62E+12	3,83E+10	1,16E+08	3,48E+05	2,16E+10	4,58E+11	1,48E+10	1,31E+03	2,00E-13
780	1,66E+12	5,35E+12	2,68E+10	7,74E+07	2,12E+05	2,13E+10	3,82E+11	1,38E+10	1,31E+03	1,63E-13
800	1,57E+12	4,33E+12	1,88E+10	5,19E+07	1,29E+05	2,10E+10	3,20E+11	1,29E+10	1,31E+03	1,34E-13
820	1,48E+12	3,51E+12	1,33E+10	3,48E+07	7,93E+04	2,07E+10	2,67E+11	1,20E+10	1,31E+03	1,10E-13
840	1,40E+12	2,85E+12	9,39E+09	2,35E+07	4,87E+04	2,04E+10	2,24E+11	1,12E+10	1,31E+03	9,06E-14
860	1,32E+12	2,32E+12	6,65E+09	1,59E+07	3,01E+04	2,01E+10	1,88E+11	1,04E+10	1,31E+03	7,50E-14
880	1,25E+12	1,89E+12	4,72E+09	1,07E+07	1,86E+04	1,98E+10	1,58E+11	9,67E+09	1,31E+03	6,23E-14
900	1,18E+12	1,54E+12	3,36E+09	7,30E+06	1,16E+04	1,95E+10	1,33E+11	9,01E+09	1,31E+03	6,00E-14

Table G-4: Altitude profiles of total density ρ [kg m^{-3}] for low, moderate, high long and high short term solar and geomagnetic activities (JB-2006 model)

(Part 1 of 2)

H (km)	Low activity	Moderate activity	High activity (long term)	High activity (short term)
100	5,31E-07	5,47E-07	5,44E-07	5,43E-07
120	2,18E-08	2,40E-08	2,45E-08	2,46E-08
140	3,12E-09	3,98E-09	4,32E-09	4,45E-09
160	9,17E-10	1,36E-09	1,54E-09	1,60E-09
180	3,45E-10	6,15E-10	7,40E-10	7,77E-10
200	1,47E-10	3,17E-10	4,10E-10	4,38E-10
220	6,96E-11	1,77E-10	2,46E-10	2,70E-10
240	3,54E-11	1,05E-10	1,56E-10	1,77E-10
260	1,88E-11	6,47E-11	1,04E-10	1,21E-10
280	1,03E-11	4,12E-11	7,12E-11	8,57E-11
300	5,86E-12	2,69E-11	5,00E-11	6,22E-11
320	3,40E-12	1,80E-11	3,59E-11	4,60E-11
340	2,02E-12	1,23E-11	2,61E-11	3,45E-11
360	1,22E-12	8,48E-12	1,93E-11	2,63E-11
380	7,46E-13	5,95E-12	1,44E-11	2,02E-11
400	4,63E-13	4,22E-12	1,09E-11	1,57E-11
420	2,92E-13	3,02E-12	8,32E-12	1,23E-11
440	1,87E-13	2,18E-12	6,40E-12	9,69E-12
460	1,21E-13	1,59E-12	4,96E-12	7,70E-12
480	8,04E-14	1,17E-12	3,87E-12	6,16E-12
500	5,44E-14	8,60E-13	3,04E-12	4,95E-12
520	3,77E-14	6,39E-13	2,40E-12	4,01E-12
540	2,68E-14	4,77E-13	1,91E-12	3,25E-12
560	1,96E-14	3,58E-13	1,52E-12	2,66E-12
580	1,47E-14	2,71E-13	1,22E-12	2,18E-12
600	1,14E-14	2,06E-13	9,82E-13	1,79E-12
620	9,10E-15	1,57E-13	7,93E-13	1,48E-12
640	7,41E-15	1,20E-13	6,43E-13	1,23E-12
660	6,16E-15	9,28E-14	5,22E-13	1,02E-12
680	5,22E-15	7,19E-14	4,25E-13	8,49E-13
700	4,50E-15	5,60E-14	3,47E-13	7,09E-13
720	3,93E-15	4,40E-14	2,84E-13	5,94E-13

Table G-4: Altitude profiles of total density ρ [kg m^{-3}] for low, moderate, high long and high short term solar and geomagnetic activities (JB-2006 model)

(Part 2 of 2)

740	3,48E-15	3,48E-14	2,34E-13	4,98E-13
760	3,10E-15	2,79E-14	1,92E-13	4,19E-13
780	2,79E-15	2,26E-14	1,59E-13	3,54E-13
800	2,53E-15	1,85E-14	1,32E-13	2,99E-13
820	2,30E-15	1,53E-14	1,10E-13	2,54E-13
840	2,11E-15	1,28E-14	9,21E-14	2,16E-13
860	1,94E-15	1,08E-14	7,72E-14	1,84E-13
880	1,78E-15	9,27E-15	6,50E-14	1,57E-13
900	1,65E-15	8,01E-15	5,49E-14	1,35E-13

NOTE: Low, moderate, high long term and high short term solar and geomagenetic activities have the following meanings:
low ($F10.7 = F10.7_{avg} = 65$, $S10.7 = S10.7_{avg} = 60$, $M10.7 = M10.7_{avg} = 60$, $A_p = 0$)
moderate ($F10.7 = F10.7_{avg} = 140$, $S10.7 = S10.7_{avg} = 125$, $M10.7 = M10.7_{avg} = 125$, $A_p = 15$),
high long term ($F10.7 = F10.7_{avg} = 250$, $S10.7 = S10.7_{avg} = 220$, $M10.7 = M10.7_{avg} = 220$, $A_p = 45$)
high short term ($F10.7 = 300$, $F10.7_{avg} = 250$, $S10.7 = 235$, $S10.7_{avg} = 220$, $M10.7 = 240$, $M10.7_{avg} = 220$, $A_p = 240$)

G.10 Figures

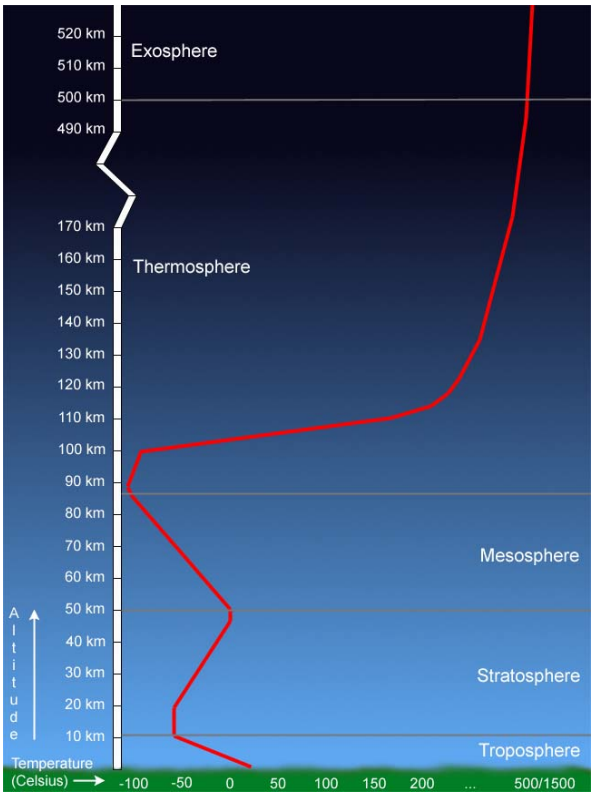

Figure G-1: Temperature profile of the Earth's atmosphere

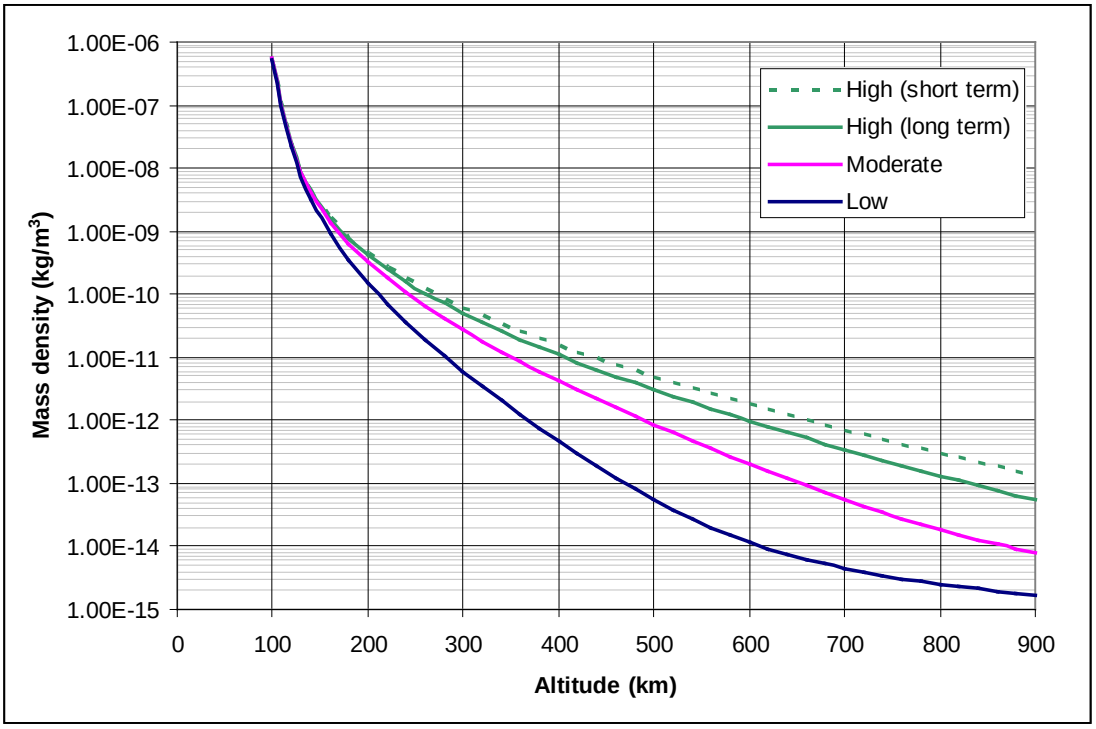

Low, moderate, high long term and high short term solar and geomagenetic activities have the following meanings:
low ($F10.7 = F10.7_{avg} = 65$, $S10.7 = S10.7_{avg} = 60$, $M10.7 = M10.7_{avg} = 60$, $A_p = 0$)
moderate ($F10.7 = F10.7_{avg} = 140$, $S10.7 = S10.7_{avg} = 125$, $M10.7 = M10.7_{avg} = 125$, $A_p = 15$)
high long term ($F10.7 = F10.7_{avg} = 250$, $S10.7 = S10.7_{avg} = 220$, $M10.7 = M10.7_{avg} = 220$, $A_p = 45$)
high short term ($F10.7 = 300$, $F10.7_{avg} = 250$, $S10.7 = 235$, $S10.7_{avg} = 220$, $M10.7 = 240$, $M10.7_{avg} = 220$, $A_p = 240$)

Figure G-2: Variation of the JB-2006 mean air density with altitude for low, moderate, high long and high short term solar and geomagnetic activities

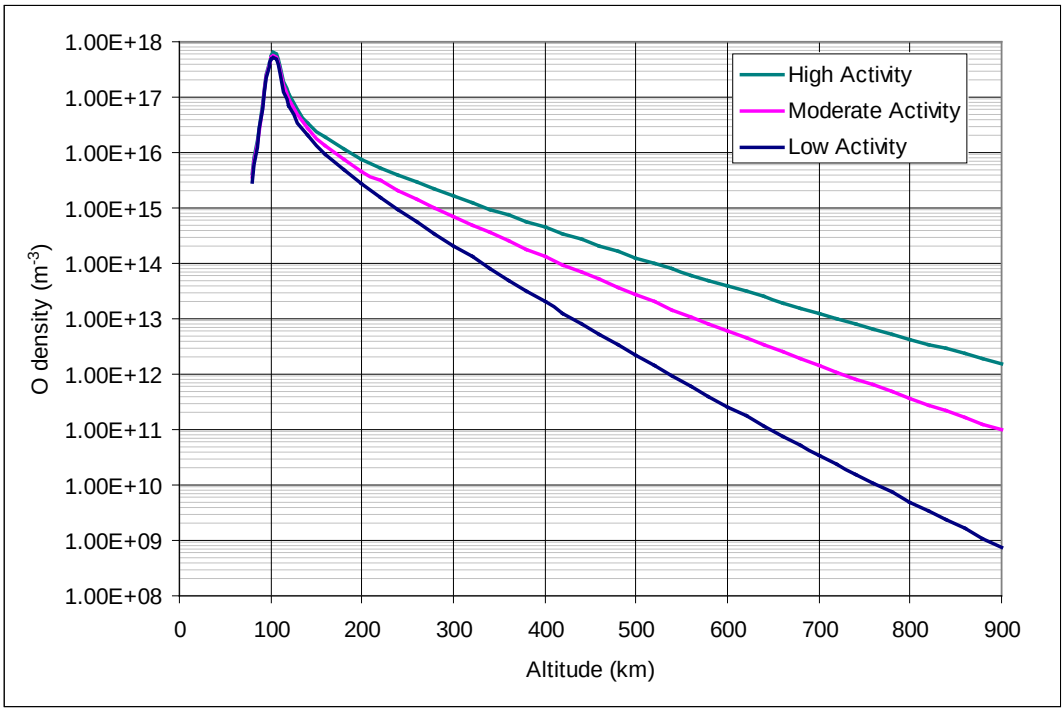

Low, moderate, and high long term solar and geomagenetic activities have the following meanings:
low ($F10.7 = F10.7_{avg} = 65$, $A_p = 0$)
moderate ($F10.7 = F10.7_{avg} = 140$, $A_p = 15$)
high long term ($F10.7 = F10.7_{avg} = 250$, $A_p = 45$)

Figure G-3: Variation of the NRLMSISE-00 mean atomic oxygen with altitude for low, moderate and high long solar and geomagnetic activities

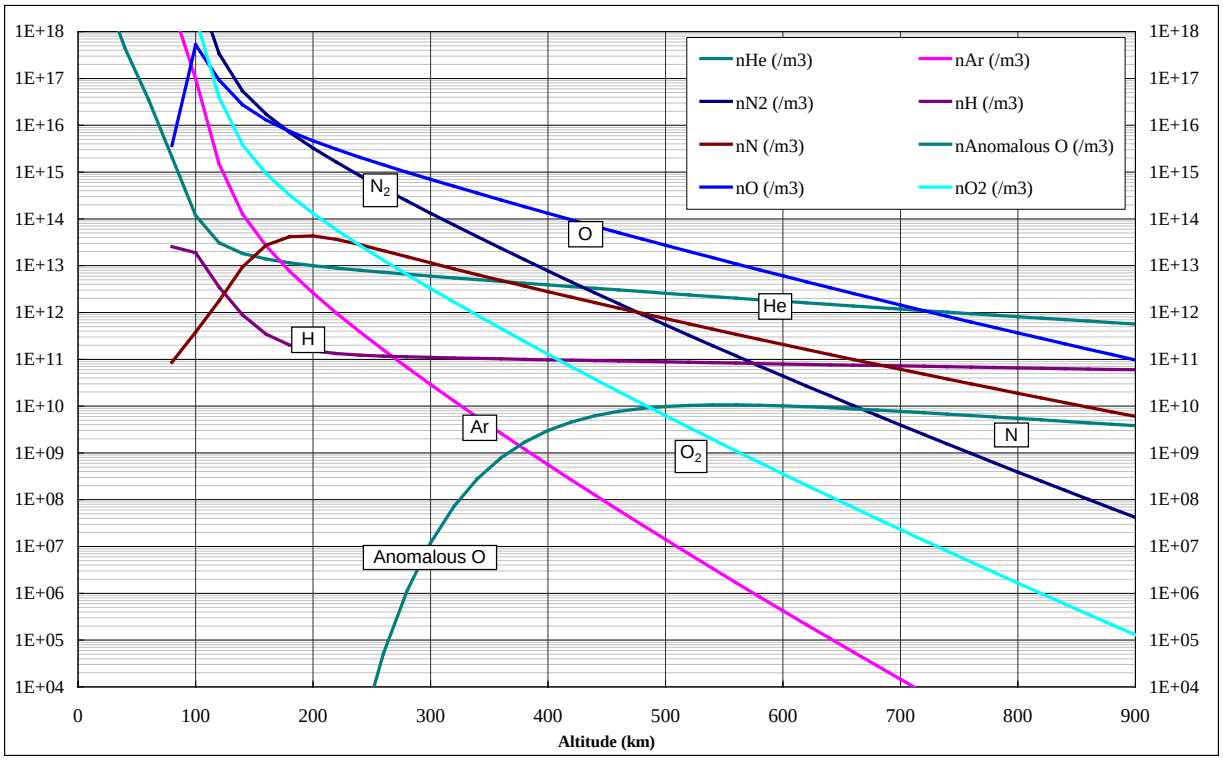

Figure G-4: Variation of the NRLMSISE-00 mean concentration profile of the atmosphere constituents N_2, O, O_2, He, Ar, H, N and anomalous O with altitude for moderate solar and geomagnetic activities ($F10.7 = F10.7_{avg} = 140$, $A_p = 15$)

Annex H (informative) Plasmas

H.1 Identification of plasma regions

Some typical examples of plasma regimes to be considered are given in Table H-2.

H.2 Plasma effects on spacecraft

The principal spacecraft engineering concerns caused by space plasmas in different regions are outlined in Table H-3. Some of the most significant effects are listed below.

Because of their higher mobility, electrons preferentially accumulate on exposed spacecraft surfaces, causing them to charge negatively. In hot plasmas in the 10 keV range charging can reach hundreds or thousands of volt. Charging is however greatly mitigated by secondary electron emission and photoemission. In cold plasma (e.g. ionosphere) charging levels are generally very low, however, the high velocity of an orbiting spacecraft relative to ion velocity in this region leads to a plasma void in its wake. This can permit high-voltage surface charging to occur on wake surfaces during auroral crossings.

High plasma densities (such as found in the ionosphere) cause reflection of radio beams below a critical frequency, as well as refraction and scintillation. Hence this acts as a barrier to satellite-ground communications and complicates satellite radar altimetry, satellite navigation systems and the radio tracking of satellites.

For high potential surfaces, in dense plasmas, ions and electrons are drawn to negative and positive regions respectively, allowing a current to flow through the plasma. This acts as a current drain on high voltage systems, such as solar arrays and can affects the spacecraft floating potential.

Ion impacts due to flowing plasma (such as the solar wind) can result in sputtering from surface materials. Although solar wind plasma is cold, the ions carry considerable kinetic energy, typically ~1 keV for protons and ~4 keV for He^{++}.

Neutral spacecraft-generated atoms can be ionized by sunlight or charge-exchange with other ions, to create a low-energy (<10 eV) ion population. These ions can be drawn to negatively charged surfaces and can cause surface contamination.

Further details on spacecraft-plasma interactions can be found in the ECSS-E-ST-20-06 (Spacecraft Charging) standard.

H.3 Reference data

H.3.1 Introduction

This section provides further information about the different space plasma regimes. This does not form part of the requirements but can help the user by describing typical data derived from the standard models or models that have not yet been defined as standards.

H.3.2 Ionosphere

H.3.2.1. IRI 2016

IRI-2016 contains a number of options suitable for different applications. Recommended choices are indicated when the code is run. The accuracy of the IRI electron density model is typically

- 50-80% at heights from 65 km to 95 km
- 5-15% at heights from 100 km to 200 km during daytime
- 15-30% at heights from 100 km to 200 km during night-time
- 15-25% at heights from 200 km to 1 000 km at low and middle dip latitudes (< 60°)
- 50-80% at heights from 200 km to 1 000 km at high dip latitudes (> 60°)

Table H-4 shows a typical altitude profile of electron density. This has been calculated from IRI-2016, at 0° longitude and latitude, on 1st January 2016, for a real-time smoothed sunspot number Rz12 of 39,2, at 0 h and 12 h local time, using otherwise default options.

The IRI model homepage at *http://irimodel.org/* provides information and references about the IRI project, lets users download the IRI Fortran source code, and lets them also compute and plot IRI parameters.

H.3.2.2. Auroral charging environment

The auroral charging environment in section 8.2.3 is expressed in terms of distribution function but charging simulations often require input spectra in terms of flux.

Flux in $cm^{-2}s^{-1}sr^{-1}keV^{-1}$ can be found from the distribution function as follows:

$$Flux(E_{keV}) = 2000 \times E_{keV} e^2 f(v) / m_e^2 \qquad \text{(H-1)}$$

where

E_{keV} is energy in keV

H.3.3 Plasmasphere

Typical ion and electron temperatures, throughout the plasmasphere are of the order of 0,5 eV. The electron temperature is thus far too low to produce hazardous charging effects.

The CGPM code [RN.8] has been widely distributed by the Marshall Space Flight Center and can generally be obtained directly from them.

A representative profile though the ionosphere and plasmasphere is shown in Table A-1. The density profile is dependent on geomagnetic activity as indicated in Figure H-1.

There are various other plasma sphere models which can also be useful and which are generally available directly from the authors. A selection is mentioned below:

- IMAGE/RPI model [RD.157]. There is also new function in IRI that makes a smooth transition between IRI and the RPI model [RD.158]. This is one of 4 models named in ISO TS 16457.
- IZMIRAN/IRI-Plas [RN.32]. This is also one of 4 ISO TS 16457 models.
- Global Plasma Ionosphere Density Model (GPID), [RD.159]. This is also an ISO TS 16457 model.
- IPM Ionosphere - Plasmasphere Model [RD.160]. This can be run in ESWP (www.spaceweather.eu) and on NASA: ccmc.gsfc.nasa.gov

H.3.4 Outer magnetosphere

NASA has defined a severe charging environment [RD.53] based on the 90th percentile of severe environments. However, this is not the one adopted as the ECSS Standard.

The requirement 9.2.1.3a is based on a 2-Maxwellian fit to a severe charging event when the Scatha spacecraft charged in sunlight. An improved fit using 3 Maxwellians has been made to the same event [RD.168]. It is given below.

Table H-1: Worst-case 3-Maxwellian environment

	Electron density (cm^{-3})	Electron temperature (keV)	Ion density (cm^{-3})	Ion temperature (keV)
Population 1	0,2	0,1	1	3
Population 2	2	10	1	20
Population 3	0,01	50	0,05	40

This study also investigated alternative definitions of a 'worst-case' event using data from LANL spacecraft – highest flux above 10 keV, highest flux at all energies, lowest flux at high energy and mean spectrum producing charging over 5 kV. These are all severe spectra that can be used in further analysis of possible charging levels.

Table H-6 gives typical plasma parameters for the geostationary environment for quiet and substorm periods.

The outer boundary of the magnetosphere, the magnetopause, is controlled by the balance between the pressure of the magnetic field and that of the solar wind. Along the Earth-Sun line, the magnetopause is closest to the Earth and its position can be expressed approximately [RD.54] as:

$$L_m = \left(\frac{B_0^2}{\mu_0 nmV^2} \right)^{1/6} \qquad \text{(H-2)}$$

where

L_m is the distance from the centre of the Earth to the magnetopause, at the subsolar point, in Earth-radii;

B_0 is the strength of the terrestrial internal magnetic field, at surface of the Earth, on the equator = 3×10^4 nT;

μ_0 is the permeability of free space;

n is the density of the solar wind;

m is the mass of the proton;

V is the velocity of the solar wind.

L_m is typically 10 Earth-radii away from the subsolar point. The magnetopause flares out on the flanks and is effectively infinite in length in the anti-solar direction. This boundary is described in more detail in clause 5.

H.3.5 Magnetosheath

Magnetosheath plasma parameters differ according to the latitude and local time of the observation. The highest density and temperature and the steepest velocity drop are observed at the subsolar point i.e. zero degrees latitude at local noon. Typical values for this region are given in Table H-7.

H.3.6 Magnetotail and distant magnetosheath

Typical plasma parameters that can be encountered in the magnetotail and distant magnetosheath around the L2 point are given in Table H-8.

H.3.7 Planetary environments

For charging investigations around Jupiter and Saturn, a description of the plasma environment has been described by Garrett and Hoffman [RD.11]. This describes the environments as either a Maxwellian distribution or a Kappa distribution or a sum of the two, as follows

Maxwellian:

$$f(v) = \frac{\left[N_0 (m_e)^{3/2} \exp\{-(E - E_0)/kT_0\}\right]}{(2\pi kT_0)^{3/2}} \quad \text{m}^{-6}\text{s}^3 \qquad \text{(H-3)}$$

Kappa:

$$f(v) = \frac{\left[N_0 (m_e)^{3/2}\right]}{(2\pi\kappa kT_0)^{3/2}} \frac{\Gamma(\kappa+1)}{\Gamma(\kappa-1/2)(1+E/\kappa kT_0)^{\kappa+1}} \quad \text{m}^{-6}\text{s}^3 \qquad \text{(H-4)}$$

where

Γ is the Gamma Function.

[RD.11] lists appropriate parameters for various regions in the magnetospheres of Jupiter and Saturn.

Worst-case plasma parameters, i.e. corresponding to the highest calculated charging level in eclipse in [RD.11], are given in Table H-9.

H.3.8 Induced environments

H.3.8.1. Photo- and secondary electrons

The electron flux at the spacecraft surface can be determined from the incident UV and primary electron fluxes, multiplied by the yield for the surface in question. Away from the emitting surface the density can be calculated from the following [RD.115]:

$$\frac{N}{N_0} = \left(1 + \frac{z}{\sqrt{2}\lambda_0}\right)^{-2} \qquad \text{(H-5)}$$

where

N is the density (cm^{-3});

N_0 is the density at emitter (cm^{-3});

z is the distance from surface;

λ_0 is the shielding distance, calculated as the Debye length due to the emitted electrons.

Table H-10 gives typical photoelectron sheath parameters [RD.55].

H.3.8.2. Ionization of contaminant gasses

Once neutral gas is released into space by whatever mechanism, it becomes subject to photoionization and dissociation by solar UV and ionization by charge exchange with solar wind ions. Production of new ions can be calculated from the appropriate photoionization rates and charge exchange cross-sections (from [RD.57]).

$$Q = N_i(\nu + \sigma n_{SW} v_{SW}) \qquad \text{(H-6)}$$

where

Q is the production rate, ions s^{-1};

N_i is the ion density;

ν is the photoionization rate coefficient;

n_{sw} is the solar wind density;

v_{sw} is the solar wind velocity;

σ is the charge exchange coefficient.

Photoionization rates depend on the atom or molecule concerned, and UV intensity and spectrum. Huebner and Giguere [RD.56] have tabulated a number of rate coefficients for different species, for sunlight at 1 AU. As an example, some photoionization rates for common gasses are listed in Table H-11.

For H_2O, where the charge exchange coefficient is around $2{,}1 \times 10^{-19}$ m^{-2} [RD.57], photoionization and charge exchange are comparable processes. However, all species and

dissociation products need to be considered to calculate the total production of emitted ions.

H.4 Tables

Table H-2: Regions encountered by different mission types

Orbit	Regions encountered
Low inclination LEO (<50°)	Ionosphere
High-inclination LEO e.g. Polar orbit	Ionosphere, Auroral zone
Geostationary orbit	Outer magnetosphere, Plasmasphere, Magnetosheath (occasionally)
MEO circular orbit e.g. Galileo	Outer magnetosphere, Plasmasphere, Magnetosheath (possibly at high latitude)
Geostationary transfer orbit	Ionosphere, Plasmasphere, Outer magnetosphere, Magnetosheath (occasionally)
High apogee elliptical orbit	All regions can be encountered, depending on orbit.
L1, L4, L5 Lagrangian points	Solar wind
L2	Solar wind, magnetotail and distant magnetosheath
Interplanetary cruise	Solar wind
Planetary orbit / encounter	Planetary environment

Table H-3: Main engineering concerns due to space plasmas

Scenario	Problem
Outer magnetosphere	Surface charging - possibly harmful electrostatic discharges.
High-voltage systems in the ionosphere	Power leakage, possible discharges, high spacecraft ground potential, sputtering.
Large spacecraft in the ionosphere	Spacecraft wake creation.
Auroral zone crossings	Surface charging - sputtering and possible electrostatic discharges.
All spacecraft	Ionospheric barrier to ground-space communications below a threshold frequency. Perturbation of signals at higher frequencies.
Radar/navigation	Ionospheric propagation delays to beams.
Electric propulsion	Interactions between generated plasma, ambient plasma, and the spacecraft.
Scientific spacecraft	Low level charging and photoelectrons which interfere with plasma measurements. Plasma entry into sensitive detectors.

Table H-4: Ionospheric electron density profiles derived from IRI-2016 for date **01/01/2016, lat=0, long=0.**

Height (km)	Midnight electron density (cm^{-3})	Noon electron density (cm^{-3})
100	2158	129695
200	5391	311762
300	401021	849210
400	353819	1032826
500	171281	510255
600	86533	236362
700	49193	125124
800	31014	75084
900	21192	49611
1000	15404	35235
1100	11744	26433
1200	9296	20684
1300	7581	16730
1400	6334	13894
1500	5398	11788
1600	4676	10179
1700	4107	8918
1800	3649	7909
1900	3275	7087
2000	2964	6408
NOTE: Sunspot number Rz12=112,1 for this date		

Table H-5: Profile of densities for solar magnetic local time = 18hr, solar magnetic latitude=0, Kp = 5,0 from the GCPM for 1/1/1999

R_E	Electron Density (cm^{-3})	Proton Density (cm^{-3})	Helium Ion Density (cm^{-3})	Oxygen Ion Density (cm^{-3})
1,3	5,31E+03	4,73E+03	5,46E+02	3,24E+01
1,35	4,98E+03	4,44E+03	5,22E+02	2,69E+01
1,4	4,68E+03	4,16E+03	4,91E+02	2,42E+01
1,5	4,12E+03	3,68E+03	4,25E+02	2,08E+01
1,75	3,00E+03	2,70E+03	2,85E+02	1,50E+01
2,0	2,19E+03	1,99E+03	1,90E+02	1,09E+01
2,5	1,16E+03	1,07E+03	8,35E+01	5,81E+00
3,0	6,17E+02	5,77E+02	3,67E+01	3,08E+00
3,5	3,27E+02	3,10E+02	1,61E+01	1,64E+00

4,0	1,74E+02	1,66E+02	7,04E+00	8,69E-01
NOTE: Distance in Earth radii (R_E) is measured from the centre of the Earth.				

Table H-6: Typical plasma parameters at geostationary orbit

	Density (cm^{-3})	Ion temperature	Electron temperature	λD(m)
Quiet	10	1 eV-1 keV	1 eV-1 keV	50
Substorm	1	10 keV	10 keV	500

Table H-7: Typical magnetosheath plasma parameters

Local time	Speed ($km\ s^{-1}$)	Tp (K)	Te (K)	Density (cm^{-3})
12 noon	50	2×10^6	2×10^6	35
06 hours	350	1×10^6	1×10^6	20
NOTE From [RD.116]				

Table H-8: Typical plasma parameters around L2

	n cm^{-3}	Ti eV	Te eV	V $km\ s^{-1}$
Magnetosheath	1,0	80	26	312
Lobe	0,1	540	180	60
Plasma sheet	0,15	610	145	72
NOTE: Ttaken from 50% cumulative probability measurement from Geotail [RD.6])				

Table H-9: Worst-case environments for eclipse charging near Jupiter and Saturn

	Jupiter		Saturn	
	Electrons	Protons	Electrons	Protons
-	10^4	$7{,}2 \times 10^5$		$7{,}4 \times 10^5$
-	1,0	0,028		0,026
10^4	-	$1{,}11 \times 10^5$		$3{,}0 \times 10^3$
1,0	-	0,458		30,8
2,0	-	1,7		8,5
Co-rotation velocity $km\ s^{-1}$	-	250	-	80

Table H-10: Photoelectron sheath parameters

Temperature (eV)	Photoelectron current ($A\ m^{-2}$)	Surface electron density (m^{-3})
3	1×10^{-5}	1×10^8

Table H-11: Some solar UV photoionization rates at 1 AU

Species	Photoionization rate (s^{-1})
H_2O	$3{,}34 \times 10^{-7}$
O_2	$5{,}13 \times 10^{-7}$
N_2	$3{,}52 \times 10^{-7}$
NOTE: From [RD.56]	

H.5 Figures

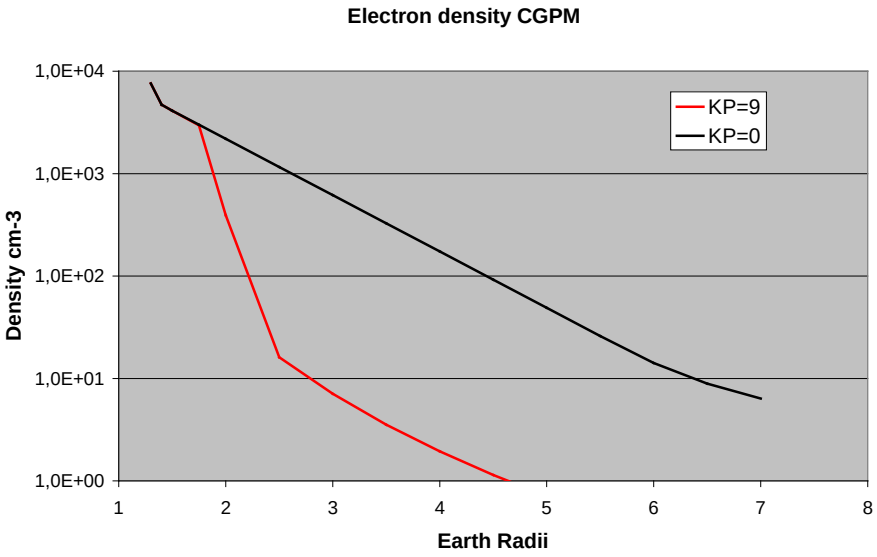

Figure H-1: Profile of electron density for solar magnetic local time = 18hr, solar magnetic latitude=0, Kp =0 and 9 from the GCPM for 1/1/1999.

Annex I (informative) Energetic particle radiation

I.1 Trapped radiation belts

I.1.1 Basic data

Trapped radiation belt charged energetic particles gyrate in the geomagnetic field with a gyration period:

$$t_c = \frac{2\pi m}{eB} \quad \text{(I-1)}$$

and a radius of gyration of :

$$R_c = \frac{mv}{eB} \quad \text{(I-2)}$$

Table I-2 gives typical characteristics of energetic particles.

I.1.2 Tailoring guidelines: orbital and mission regimes

In the following sections, attention is drawn to special considerations for various orbit types.

I.1.2.1. Geostationary orbit

Geostationary orbit is a circular orbit usually encountering an environment dominated by energetic electrons. This environment is characterized by strong time variations with many extended quiet periods of low radiation levels and many episodes of intense injections of energetic electrons which increase e.g. dose, sensor interference and electrostatic charging. Solar protons and cosmic rays have unrestricted access to this orbit. Solar particles make short-lived but important contributions to the total dose, interference and single event effects. They do not directly participate in charging processes. Cosmic rays provide a continuous source of single-event effects and sensor interference.

I.1.2.2. Between LEO and GEO

Orbits between LEO and GEO encounter the electron-dominated environment mentioned above, but in addition can encounter the inner, proton radiation belt. In these orbits, single-event effects from protons and proton non-ionizing damage need to be considered.

These orbits often encounter more severe electron environments, near the peak of the electron belt (the location of which is also variable) than geostationary orbit and so electrostatic charging can be a more serious threat.

I.1.2.3. LEO

Currently manned activities are limited to low (< 550 km) and medium-inclination (<57.1°) orbits, however, this is going to change in the future. We refer to these orbital regimes as LEO. Missions in these orbits encounter the inner edge of the radiation belt. This region is dominated by the South Atlantic anomaly. Also important is the asymmetry in energetic proton fluxes from East and West. The low-altitude environment is characterized by high-energy radiation-belt trapped protons. The deflection of charged particles from outside the magnetosphere by the Earth magnetic field (geomagnetic shielding) reduces the fluxes of cosmic rays and solar energetic particles, but the shielding is not total. Like polar orbits, LEO orbits also encounter outer-belt trapped electrons at high-latitudes.

There is a low-flux population of low energy protons near the geomagnetic equator at low altitude, created by double charge-exchange: energetic neutral atoms from the ring current subsequently charge exchange in the upper atmosphere [RD.163]. This population is important to consider in cases of specific sensitivity such as on low altitude low inclination astrophysics missions.

I.1.2.4. Polar

Polar orbits are generally of less than 1 500 km altitude with inclinations above 80°. They encounter the inner proton and electron belts in the form of the South Atlantic anomaly and also the outer electron belt where the geomagnetic field lines bring it to low altitudes at "auroral" latitudes above about 50°. On the high-latitude parts of the orbit a spacecraft is exposed to almost unattenuated fluxes of cosmic rays and solar energetic particles. At low latitudes, geomagnetic shielding considerably reduces these fluxes.

I.1.3 Existing trapped radiation models

I.1.3.1. Overview

For trapped radiation and all earth orbits, the best known and most widely used models of radiation belt energetic particles are the AE-8 and AP-8 models for electrons [RN.10] and protons [RN.11], respectively. They were developed at Aerospace Corporation for the NSSDC at NASA/GSFC based on data from satellites flown in the 1960s and early 1970s. The models give omni-directional fluxes as functions of idealized geomagnetic dipole coordinates B/B_0 and L. The user defines an orbit, generates a trajectory, transforms it to geomagnetic coordinates and access the radiation belt models to compute flux spectra, using the same geomagnetic field as used to develop the model. Apart from separate versions for solar maximum and solar minimum, there is no description of the temporal behaviour of fluxes. At high altitudes in particular (e.g. around geostationary orbit) fluxes vary by orders of magnitude over short times and exhibit significant diurnal variations; the models do not describe these. In addition, the models do not contain any explicit flux directionality.

At low altitudes, on the inner edge of the radiation belts, particle fluxes rise very steeply with altitude and small errors in computing locations can give rise to large errors in

particle fluxes. This is a problem since the geomagnetic field is shifting and decaying so that the situation is no longer the same as when the model data were acquired. Use of a geomagnetic field model other than the one used in generating the model can result in large flux errors at low altitude.

Although use of an old field model and epoch can reduce errors in the magnitudes of fluxes, it does not model the spatial locations of radiation-belt features (e.g. the position of the South Atlantic anomaly), or particle fluxes, as they are today.

The AP-8 model for protons gives proton fluxes from 0,1 to 400 MeV while the AE-8 model for electrons covers electrons from 0,04 to 7 MeV. Figure I-1 shows contour plots of AE-8 and AP-8 model omnidirectional, integral fluxes for energies above 1 MeV and 10 MeV, respectively, in idealized dipole space.

Figure I-2 shows values of energetic electron and proton particle fluxes as stored in these models, for positions on the geomagnetic equator ($B=B_0$), as functions of L for both solar maximum and solar minimum. This shows that as far as the models are concerned, the solar activity only affects electron fluxes in the mid-L range and protons at low altitude where the higher neutral atmospheric density at solar maximum leads to reduced proton fluxes because of enhanced loss. Solar cycle effects on electrons appear to differ from this behaviour in reality [RD.58].

I.1.3.2. Uncertainties in trapped particle models

The accuracy of the predicted fluxes is within a factor of 2 for AP8 and within a factor depending on the location and incident electron energy for AE8. In [RN.10], a reasonable limit of the error on AE8 is a factor of 2, however, in some regions (L=3) this can increase to a factor of 4.5 and is energy dependent, the error is higher for the higher energies. In other regions, such as geostationary orbits, the AE8 models are pessimistic.

For short term estimates the models can underpredict by a considerable amount – instantaneous fluxes measured at specific locations in the electron belts have been measured to be several orders of magnitude higher than the long term model fluxes.

I.1.3.3. Specific orbits

For electron fluxes in geostationary orbit a great number of measurements exist. The standard model IGE-2006 (International GEO Electron model version 2006) developed by ONERA & LANL [RN.12], is a statistical model based on more than 2 solar cycles of electron flux data from radiation monitors on-board different international GEO satellites (mainly US and Japan) see Figure I-4. This model is available in the SPENVIS [RD.59] or OMERE [RD.60] space environment tools.

The accuracy of IGE-2006 is included in the model as the upper case takes into account uncertainties in the measurements, in the duration and strength of the solar cycle.

For MEO altitude, the electron environment is very hard, intense and dynamic. The model developed at ONERA [RN.13] and given in Table B-5 and Table B-6, is based on GPS data acquired from Los Alamos, covering from the early nineties to 2007. Data have been analysed in terms of saturation, contamination and global coherence to ensure high fidelity. This MEO model provides energetic electrons fluxes in the energy spectral range 0,28 MeV–2,24 MeV and gives three spectra: an average case, a lower case and an upper case. The accuracy of MEO-V2 is included in the model as the upper case takes into account uncertainties in the measurements, in the duration and the strength of the solar cycle.

The electron fluxes obtained in the mean case of MEO model are very close to electron fluxes deduced from NASA/AE8 model over a full solar cycle (7 years MAX and 4 years MIN for AE8), see Figure I-5. Similarly, the electron fluxes from the MEO mean model propagated to near geostationary orbit are in agreement with electron fluxes deduced from IGE-2006 model.

I.1.3.4. Other trapped radiation models

Other trapped radiation models exist. Amongst them, the main known are:

Those based on CRRES data:

CRRESELE: The Combined Radiation and Release Effects Satellite (CRRES) electron flux model specifies the location and intensity of electron omni-directional flux over the energy range 0,5-6,6 MeV for a range of geomagnetic activity levels [RD.61].

CRRESPRO: The Combined Radiation and Release Effects Satellite (CRRES) proton flux model specifies the location and intensity of proton omni-directional flux over the energy range 1-100 MeV for quiet, average, or active geophysical conditions [RD.62].

TPM1 (Trapped Proton model) [RD.25] which provides a solar-cycle dependent low-altitude extension to the CRRESPRO trapped energetic proton model based on NOAA/TIROS data from 1,5 to 81 MeV (but it is ITAR restricted).

These models are available in the AF-GEOSPACE tool, see: *http://www.kirtland.af.mil/library/factsheets/factsheet.asp?id=7899*

Other models are also listed and available in *http://modelweb.gsfc.nasa.gov/*

I.1.4 The South Atlantic Anomaly

I.1.4.1. Overview

The South Atlantic Anomaly (see clause 9.2.1) produces an “island” of radiation and provides the only significant radiation encountered on low Earth orbits with altitudes below about 800 km and inclinations below about 40°. Figure I-3 shows the South Atlantic Anomaly at 400 km.

I.1.4.2. Anisotropy

I.1.4.2.1 The "East-West effect"

Because of the inclination of geomagnetic field-lines with respect to the atmosphere here, particles reaching a point from the West have gyrated from higher altitude while those arriving from the East have gyrated from lower altitude. There are fewer coming from below because of atmospheric absorption and an asymmetry in the fluxes results. This can be important in certain cases, including the International Space Station. The current standard AP-8 model does not treat this effect but models have been developed by NASA [RD.63] and BIRA [RD.64]. The ratio of the East and West peak fluxes is about 4,6 for 100 MeV protons in an ISS type orbit. Measurements from MIR are also available which are consistent with this ratio [RD.65].

I.1.4.2.2 Pitch-angle distribution

The directional distribution of trapped particles at low altitude is peaked perpendicular to the magnetic field direction. This is due to atmospheric absorption of particles with a significant parallel component that gyrate to lower altitiudes. Radiation belt models where particle fluxes are described according to geomagnetic coordinates can be readily used to derive the directional distribution ("pitch angle distribution") through transformations [RD.162].

I.1.4.3. Location of the South Atlantic Anomaly

The slow movement of the South Atlantic Anomaly as a result of shifts in the geomagnetic field has been clearly observed. This shift is essentially westward at a rate of $0{,}3°yr^{-1}$ (~10° since the models were created) and account is taken of this figure for low Earth orbits when planning operations which involve a sensitivity to radiation (payload radiation background, astronaut EVA). Models including this shift capability are available [RD.14].

I.1.4.4. Equatorial soft protons

As mentioned in clause I.1.2.3, there is a low-flux population of low energy protons near the geomagnetic equator. A model for this population was created by Petrov et al. [RD.163].

I.1.5 Dynamics of the outer radiation belt

The dynamic nature of the outer electron radiation belt, together with its diurnal variations mean that unless one is interested in long-term averages (such as provided by AE-8), some statistical description is desirable. This is especially true when deep dielectric charging and radiation background are of concern. No standard models for the variability are yet available, but for engineering purposes the CRRESELE model has been developed [RD.61]. An older version of the AE-8 electron model, AE-4 [RD.26], included a statistical model giving standard deviations of the logarithm of electron fluxes (assumed to be normally-distributed). It also included a model for local time flux modulation. This was a sinusoidal model providing amplitudes of the variation, with a fixed maximum at 11:00 hours local time. These have been extended and applied to the AE-8 model [RD.66], although this extension is unvalidated.

I.1.6 Internal charging

The FLUMIC (Flux Model for Internal Charging) model used for internal charging assessments is integral to the DICTAT internal charging tool but can be applied separately. FLUMIC describes the electron flux, which has an exponential dependence on energy E and varies with L, time of year and phase of the solar cycle. FLUMIC version 1 and 2 covered L-shells above 2,8, i.e. the outer belt only. The exponential spectrum can a priori be extrapolated down to lower energy (say a few 100 keV), although for more dynamics in the lower energy environment more sophisticated models are available. Version 3 of FLUMIC is broadly similar to FLUMIC version 2 in the outer belt because here it is based on the same data. However, it also models electron fluxes in the inner belt (see Annex B.4).

The FLUMIC v3 model, presented in Annex B.4, has been evaluated with in-flight data and shown to provide electron fluxes between 0,8 MeV and 2,8 MeV that exceed 95-98% of the data for L-Shells above 4 Earth Radii. For the Geostationary orbit, the models provided electron fluences that exceeded 95% of the data points [RD.67].

The MOBE-DIC (Model for Outer Belt Electrons for Dielectric Internal Charging), as presented in Annex B.9, is based on Giove-A/Merlin-SURF data at MEO and on GOES data at GEO. The model provides electron fluxes during enhanced periods as a function of confidence level and location within the magnetosphere.

I.2 Solar particle event models

I.2.1 Overview

During energetic events on the Sun, large fluxes of energetic protons are produced which can reach the Earth. Solar particle events, because of their unpredictability and large variability in magnitude, duration and spectral characteristics, are treated statistically. Current models make the assumption that large events are confined to a 7-year period defined as solar maximum. Although large events are absent during the remaining 4 solar minimum years of the 11-year solar cycle (see clause 6) the occasional small event can still occur.

An inherent input to probablistic models is the use of a "confidence level". As a result:

- the risks of encountering environments can be more severe than the one predicted, and
- margins are implicitly assumed by applying high confidence levels.

Two main approaches are currently described in the literature to specify the mission integrated fluence: the ESP model approach and the JPL model approach.

I.2.2 ESP model

The ESP model approach is based on the observation that a good fit to the distribution of the yearly accumulated fluence from the solar maximum periods of the solar cycles 20, 21 and 22 is obtained with a log-normal distribution. It is deduced from this observation that the distribution of the logarithm of the n-year accumulated fluence should also have a gaussian distribution with a mean and a relative variance that can be expressed as a function of the 1-year distribution mean and variance as follows:

$$\Phi_{RV}(n \cdot years) = \Phi_{RV}(1year)/n \qquad \text{(I-3)}$$

and

$$\Phi_{mean}(n \cdot years) = n \cdot \Phi_{mean}(1year) \qquad \text{(I-4)}$$

I.2.3 JPL models

The approach used in JPL models, JPL85 and JPL91 [RD.68] [RD.69], is based on a combined consideration of:

- the distribution of fluences seen in SEP events and

- the probability of occurrence of an event (irrespective of magnitude) over a given period.

A normal probability distribution function, *f*, is employed to describe the $\log_{10}$ of individual event fluences, *F*,

$$f(F) = (1/\sqrt{2\pi}\sigma)\exp -\frac{1}{2}[(F-\mu)/\sigma]^2 \quad \text{(I-5)}$$

where

μ is the mean of the distribution of the log_{10} of fluence values

σ is the standard deviation

The probability *p* of *n* events occurring in time τ is given by a Poisson distribution such that

$$p(n, w\tau) = e^{-w\tau}(w\tau)^n / n! \quad \text{(I-6)}$$

where

w is the average number of events occurring per active year

The probability, *P*, of exceeding a selected fluence level, *F*, during a mission lifetime, τ can be expressed analytically as,

$$P(>F,\tau) = \sum_{n=1}^{\infty} p(n, w\tau)Q(F,n) \quad \text{(I-7)}$$

where

Q(F, n) is the probability that the sum of all fluences due to n ($n = [1, \infty]$) events will exceed 10^F

The derivation of *P* requires an estimate of the parameters *w*, μ and σ to perform computer based Monte Carlo simulations to derive *Q(F, n)*.

JPL-91 has been a de-facto standard for many years. However, it was recently shown that the values of the parameters μ, σ and *w* derived from the data for JPL-91 lead to an underestimation of the fluence [RD.70]. Updated values of these parameters have been proposed for the fluence specification in the energy ranges >10 MeV and >30 MeV [RD.70], [RD.71]. The values of the parameters μ, σ and *w* of the model that are recommended to be used are given in Table I-3.

The complete calculation of $P(>F,\tau)$ has been coded in IDL™ and the source code can be found in [RD.70].

I.2.4 Spectrum of individual events

I.2.4.1. Overview

Solar proton event spectra are variable, the worst-case event at one energy is not necessarily worst-case at another. The August 1972 event yield worst-case doses at most typical spacecraft shielding (1-10 mm) where particles of energy 10-70 MeV are most important. The October 1989 flare is apparently more severe at lower and higher

energies. Lower energies are important for surface material and solar cell effects and the higher energies more important for deep shielding (e.g. for heavy spacecraft, manned missions and planetary atmospheres) and for nuclear interactions giving rise to certain types of background and SEUs. Hence the term "worst-case" is application dependent.

I.2.4.2. August 1972 event

The August 1972 event produced a peak flux near the Earth in excess of 10^6 protons $cm^{-2}s^{-1}$ above 10 MeV energy. A fluence spectrum which is often used to represent a worst case flare, classified as "anomalously large" is based on the very large August 1972 event [RD.72]:

$$J(E) = 7{,}9 \times 10^9 \exp\left\{\frac{30 - E}{26{,}5}\right\} \qquad \text{(I-8)}$$

with energy E in MeV and fluence J in protons cm^{-2}.

I.2.4.3. October 1989 event

The October 1989 event was the largest seen since August 1972 but had lower fluences at the medium energies. The events of 19, 22 and 24 October 1989 have been fitted to Weibull spectral forms as suggested by Xapsos et al [RD.73]. Account has been taken of ground level neutron monitors in addition to spacecraft data as suggested by Dyer et al [RD.74] in order to get the correct spectra at higher energies. The differential flux spectrum is given by the form:

$$J(E) = A\,\kappa\,\alpha\,E^{(\alpha-1)} \exp\left(-\kappa E^{\alpha}\right) \qquad \text{(I-9)}$$

With energy E in MeV and the flux J in protons $cm^{-2}\ s^{-1}\ sr^{-1}\ MeV^{-1}$. The parameters for the peak fluxes during these events are given in Table I-5.

I.2.4.4. Worst case

It has been proposed that a truncated power law can provide a good fit to the distribution of the log of the intensity of the solar proton events [RD.12]. Such a model predicts therefore a worst case event which is found to be 1,3E+10 cm^{-2} for proton with energy above 30 MeV. Consideration on the statistical uncertainty leads to estimate that an actual worst case is about 3E+10 cm^{-2}.

The JPL approach is based on a good fit of the distribution of the log of the intensity of events through a Gaussian function. With the parameters given in Table I-3 above for the range > 30 MeV, a fluence of 3E+10 cm^{-2} is likely to not be exceeded by 99,5% of the events.

I.2.5 Event probabilities

The probability p of n events occurring in time τ is given by a Poisson distribution such that

$$p(n, w\tau) = e^{-w\tau}(w\tau)^n / n! \qquad \text{(I-10)}$$

where

w is the average number of events occurring per active year

The value of w depends of the definition of an event. Values of w given in Table I-3 can be used for the relevant energy range.

I.2.6 Other SEP models

Other model are under development. These developments relate to alternative statistical approaches and models for peak fluxes.

The Nymmik proton model ([RD.75] and [RD.76]) is in the process to be considered as an ISO standard (ISO TS 15391).

The PSYCHIC solar particle model [RD.105] includes heavy ions and extends the energy range of solar protons to 300 MeV.

I.3 Cosmic ray environment and effects models

Cosmic ray environment and effects models were originally created by Adams and co-workers at the U.S. Naval Research Laboratory [RD.77], under the name CREME. They provided a comprehensive set of cosmic ray and flare ion LET and energy spectra, including treatment of geomagnetic shielding and material shielding. CREME has been superseded by CREME96 [RD.78]. The major differences to the environment specification are in the inclusion of a model of the cosmic ray environment and its solar-cycle modulation due to Nymmik et al. [RD.79], improved geomagnetic shielding calculation, and more realistic Solar Energetic Particle event (SEP) ion environments (see clause 9.2.3).

The cosmic ray fluxes are anti-correlated with solar activity so the highest cosmic ray fluxes occur at solar minimum.

I.4 Geomagnetic shielding

The Earth's magnetic field partially shields near-Earth space from solar energetic particles and cosmic rays, an effect known as geomagnetic shielding. However, these particles can easily reach polar regions and high altitudes such as the geostationary orbit. Geomagnetic shielding of protons is computed on the basis of the trajectory in geomagnetic B, L space (see Clause 5).

Stassinopoulos and King [RD.80] developed a model which has total cut-off at L = 5. It assumes that no protons can penetrate to lower values. It can be shown that this model corresponds to a quiet magnetosphere vertical cut-off model excluding protons of E < 200 MeV from L < 5 Earth-radii. This model is adequate for most cases. However, in reality protons of lower energy can penetrate below L = 5 with non-vertical arrival directions, especially in a disturbed magnetosphere where the geomagnetic shielding is weakened. For westward arrival at the L = 5 geomagnetic equator in a disturbed magnetosphere, the energy cut-off can be as low 30 MeV.

For engineering purposes, geomagnetic cut-off is usually not applied to orbits spending more than 50 % of the orbit period above L = 5. Geomagnetic cut-off is usually applied to orbits spending more than 75 % of their time below L = 5.

I.5 <<deleted>>

I.6 Planetary environments

I.6.1 Overview

As giant planets (Neptune, Jupiter, Saturn) have large magnetospheres, spacecrafts orbiting close to them encounter intense trapped radiation environments inducing direct radiation effects and internal charging. As information is very limited, no models are defined as normative in this standard but an environment needs to be specified for each mission on a case-by-case basis, along with appropriate margins.

Note that operating close to moons or rings of large planets induces important changes to the radiation environment that are important to consider.

I.6.2 Existing models

I.6.2.1. Jupiter

Three models are currently available, see Figure I-8:

- The Divine and Garett model which is constructed using data from Pioneer 10 and 11 and which extends to 10 jovian radii R_J for protons and more than 100 R_J for electrons [RD.20].
- GIRE (Galileo Interim Electron Environment) based on Galileo and Pioneer electron data between 8 to 16 R_J [RD.83] and developed at ONERA [RN.17] using a physical model. This model has been validated by comparing calculated synchroton radiation with that measured from the ground by the VLA telescope and extends to 10 R_J.
- JOSE (Jovian Specification Environment) developed at ONERA based on Galileo data and validated with all relevant data measured by spacecraft having flown by or orbited Jupiter, in order to obtain an easy-to-use engineering model for Jupiter's environment. This model has been developed for protons and electrons from several tens of keV to several hundreds of MeV [RD.164].

However, the main data used for modelling are from a NASA Galileo Energetic Particle Detector instrument that had broad energy channels, was not tailored for provision of high energy data, and was not calibrated. As a consequence, the reliability of the data and therefore models are uncertain and careful consideration has to be given to margins.

During the development of the JUICE mission, shortcomings of the models were identified that necessitated custom adaptations of the models. The JUICE Environment

Specfication [RD.165] reflects these changes, including improved data interpretation, improved magnetic coordinate system and the effects of the presence of Ganymede and its magnetic field.

I.6.2.2. Internal charging

For internal charging see [RD.19].

I.6.2.3. Mars

For Mars the orbital environment is very similar to an interplanetary environment – as the planet has no significant magnetic field that can neither support trapped radiation, nor provide adequate geomagnetic shielding. The only significant deviation from the interplanetary environment is the solid angle subtended by the planet that can provide some shielding - particularly for low altitude orbits. The radiation environment on the surface of Mars largely derives from the secondary particles produced by cosmic rays and solar protons in the atmosphere and regolith. For manned missions to the planet the dominant particle species of concern is the neutron. Several software packages have been developed to calculate the ambient environment at Mars due to atmospheric interactions [RD.84],[RD.85],[RD.86]. Residual crustal magnetic fields do exists that can provide some form of magnetic shielding, the effectiveness of which can be evaluated using the PLANETOCOSMICS software [RD.86].

I.7 Atmospheric albedo neutron models

MAIRE (Models for Atmospheric Ionising Radiation Effects) [RN.34] is a successor to the QARM [RN.35] , and uses a combination of the Geant4-based MAGNETOCOSMICS code to calculate particle rigidities, and tables of FLUKA-based response functions for particle fluxes as a function of depth from monoenergetic ions incident upon the atmosphere. The key features of the model are:

- The GCR environment can be based on either the ISO-15390 or Badhwar O'Neill (2011) models at the used-defined epoch
- The user can select from a list of example SEP events, or define own SEP spectra
- The outputs include the effective dose and H*(10) dose based on ICRP74 and Pelliccioni (2000) coefficients
- Instead of just calculating fluence or flux or radiological dose, MAIRE can be used to calculate SEE rates based on user-supplied device cross-section parameters
- MAIRE is web-based, allowing user-friendly operation of the model.

It can be applied to give the upward (albedo) neutron flux at 100 km altitude and this can then be scaled to any spacecraft altitude using the inverse square law:

$$\varphi(h) = \varphi(100) \times \frac{(R_e + 100)^2}{(R_e + h)^2} \qquad \text{(I-11)}$$

where

φ is the particle flux,

h is the altitude in km and

R_e is the earth's radius in km

Results for three cut-off rigidities are given for solar minimum and maximum respectively in Figure I-6 and Figure I-7.

Claret et al. **Error! Reference source not found.** and Combier et al. **Error! Reference source not found.** have recently modelled production of neutrons from particles up to 1 TeV with the FLUKA code, and provided the following table as example of the outputs, for 450km altitude.

Table I-1: Example albedo neutron environment at 450 km altitude Error! Reference source not found.

	Mean	**Max**	**Min**
GCR solar min n flux	0,42 /cm²/s	1,25 /cm²/s	0,07 /cm²/s
GCR solar max n flux	0,23 /cm²/s	0,54 /cm²/s	0,06 /cm²/s
SEP Jan 2005 event n fluence	1,53E+07 /cm²	5,22E+07 /cm²	4,25E+06 /cm²
SEP Oct 2003 event n fluence	1,32E+08 /cm²	2,78E+08 /cm²	6,28E+07 /cm²

I.8 Interplanetary environments

The interplanetary environment is characterized by cosmic rays and occasional solar energetic particle events. For mission analysis, it is important to take into account the variations in particle intensities with heliocentric radius and solar cycle modulation as specified in 9.2.2.

Science missions also take place at the Lagrangian points of the Sun-Earth system or Earth-Moon system, locations which are usually considered interplanetary from the point of view of the radiation environment.

The interplanetary charged particle environment also contains penetrating electrons (roughly >200 keV) which are accelerated in solar flares and CMEs and in the radiation belts of Jupiter. To assess the interplanetary electron environment the Interplanetary Electron Model (IEM) [RD.150] can be used. This gives solar electron cumulative fluence and peak spectra in the range 0,31 MeV to 4,13 MeV and Jovian electron fluxes for positions as a function of their magnetic connection to Jupiter.

I.9 Tables

Table I-2: Characteristics of typical radiation belt particles

	Particle	
	1 MeV Electron	**10 MeV Proton**
Range in aluminium (mm)	2	0,4
Peak equatorial omni-directional flux ($cm^{-2}s^{-1}$)*	4×10^{6}	$3,4 \times 10^{5}$
Radial location (L) of peak flux (Earth-radii)*	4,4	1,7
Radius of gyration (km)		
@ 500 km	0,6	50
@ 20 000 km	10	880
Gyration period (s)		
@ 500 km	10^{-5}	7×10^{-3}
@ 20 000 km	2×10^{-4}	0,13
Bounce period (s)		
@ 500 km	0,1	0,65
@ 20 000 km	0,3	1,7
Longitudinal drift period (min)		
@ 500 km	10	3
@ 20 000 km	3,5	1,1
* derived from the models of clause 9.3.1		

Table I-3: Recommended updated values of the parameters of the JPL model

Parameter	>10MeV	>30MeV
μ	8,07	7,42
Σ	1,10	1,2
W	6,15	5,40
NOTE: Taken from [RD.70] (>10MeV) and [RD.71] (>30MeV)		

Table I-4: Proton fluence levels for energy, mission duration and confidence levels from the ESP model with the NASA parameters from Table B-8.

Energy (MeV)	Probability (confidence) level (%)	1 year (cm^2)	2 years (cm^2)	3 years (cm^2)	5 years (cm^2)	7 years (cm^2)
>1	50	6,37E+10	1,46E+11	2,32E+11	4,07E+11	5,83E+11
>1	75	1,10E+11	2,23E+11	3,30E+11	5,39E+11	7,41E+11
>1	90	1,81E+11	3,24E+11	4,54E+11	6,93E+11	9,20E+11
>1	95	2,43E+11	4,06E+11	5,48E+11	8,06E+11	1,05E+12

Energy (MeV)	Probability (confidence) level (%)	1 year (cm^2)	2 years (cm^2)	3 years (cm^2)	5 years (cm^2)	7 years (cm^2)
>1	99	4,23E+11	6,20E+11	7,83E+11	1,07E+12	1,33E+12
>10	50	2,60E+09	7,07E+09	1,25E+10	2,52E+10	3,94E+10
>10	75	7,55E+09	1,79E+10	2,90E+10	5,24E+10	7,63E+10
>10	90	1,97E+10	4,11E+10	6,19E+10	1,01E+11	1,38E+11
>10	95	3,51E+10	6,78E+10	9,75E+10	1,50E+11	1,97E+11
>10	99	1,03E+11	1,73E+11	2,28E+11	3,15E+11	3,84E+11
>30	50	3,26E+08	9,11E+08	1,65E+09	3,47E+09	5,62E+09
>30	75	1,19E+09	2,93E+09	4,92E+09	9,33E+09	1,41E+10
>30	90	3,79E+09	8,36E+09	1,31E+10	2,27E+10	3,23E+10
>30	95	7,59E+09	1,57E+10	2,36E+10	3,87E+10	5,29E+10
>30	99	2,80E+10	5,10E+10	7,10E+10	1,05E+11	1,34E+11
>100	50	1,98E+07	5,58E+07	1,02E+08	2,18E+08	3,57E+08
>100	75	8,59E+07	2,17E+08	3,70E+08	7,21E+08	1,11E+09
>100	90	3,22E+08	7,34E+08	1,18E+09	2,12E+09	3,09E+09
>100	95	7,09E+08	1,53E+09	2,36E+09	4,04E+09	5,71E+09
>100	99	3,12E+09	6,01E+09	8,69E+09	1,36E+10	1,80E+10

Table I-5: Parameters for the fit to the peak fluxes from the October 1989 events.

Event	A $[cm^{-2}s^{-1}sr^{-1}MeV^{-1}]$	K	α
19 Oct. 1989	214	0,526	0,366
22 Oct 1989	429	0,458	0,3908
24 Oct 1989	54 900	2,38	0,23
NOTE Some of the parameters in the reference [RD.74] Table I are incorrect and the verified values are presented in Table I-5.			

I.10 Figures

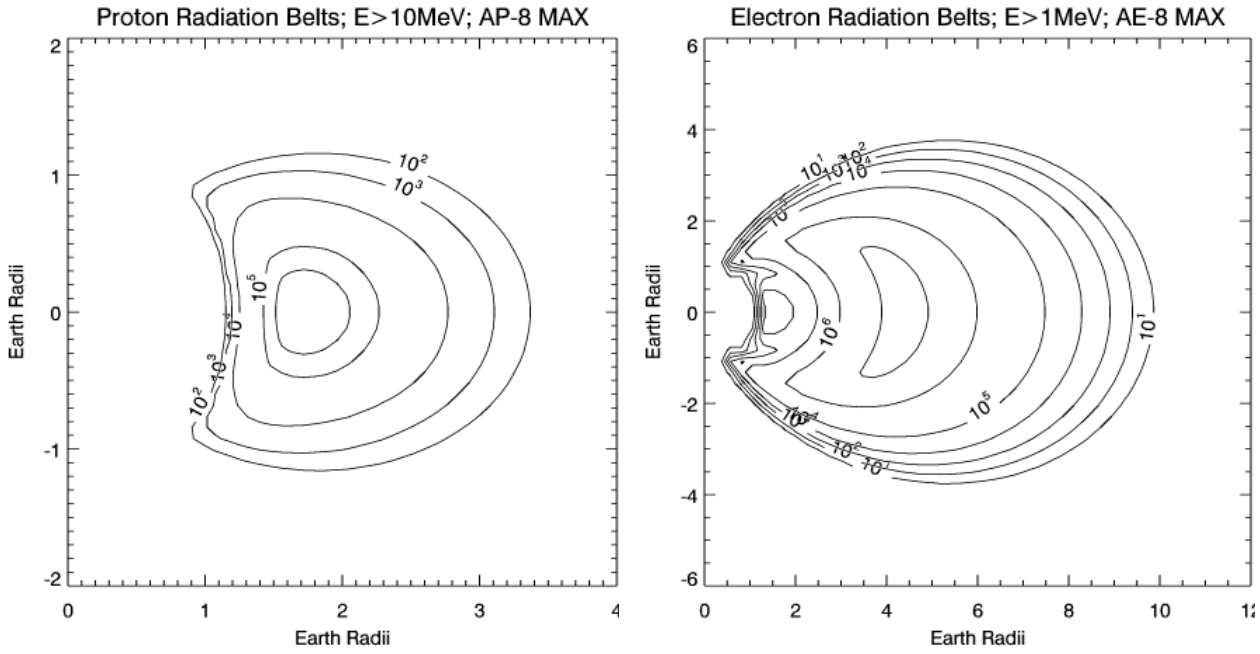

NOTE: Omnidirectional fluxes are for particles >10 MeV and >1 MeV respectively for protons and electrons. The data are derived from the AP-8 and AE-8 models, respectively, and are shown in an idealised dipole representation of the Earth's magnetic field.

Figure I-1: Contour plots of the proton and electron radiation belts

(a) Electron

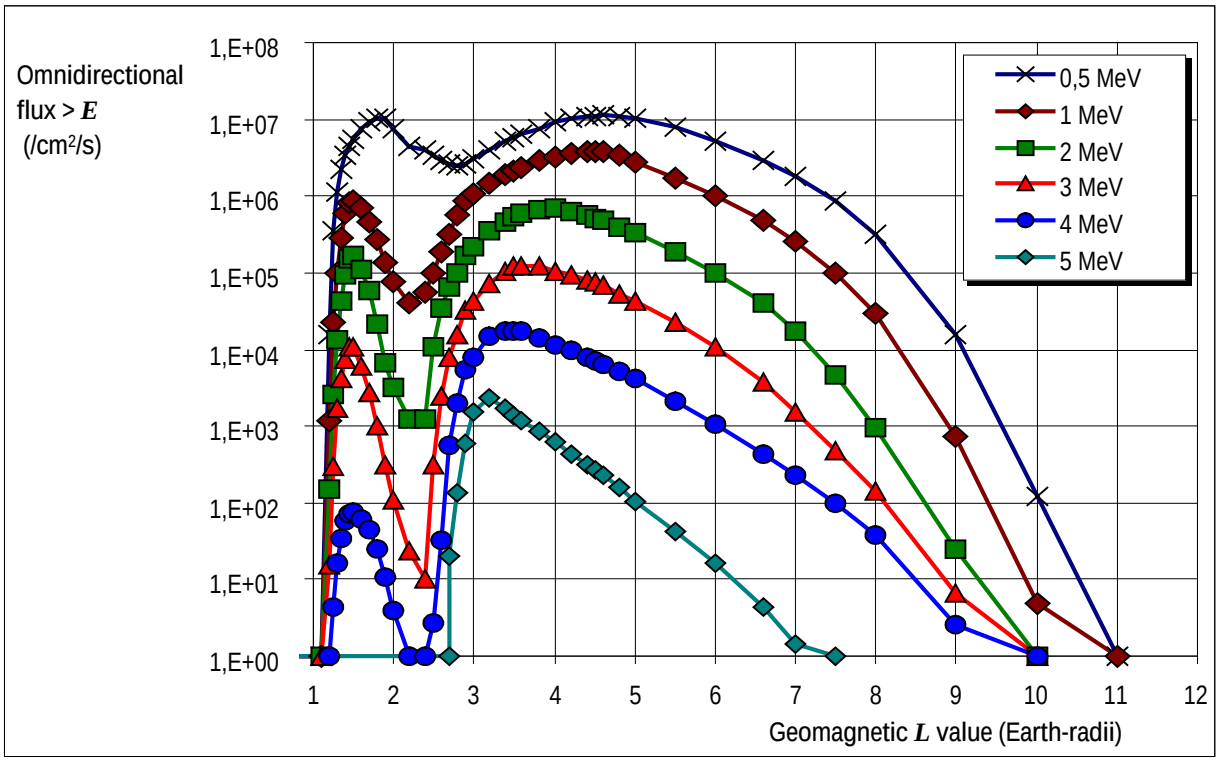

(b) Proton

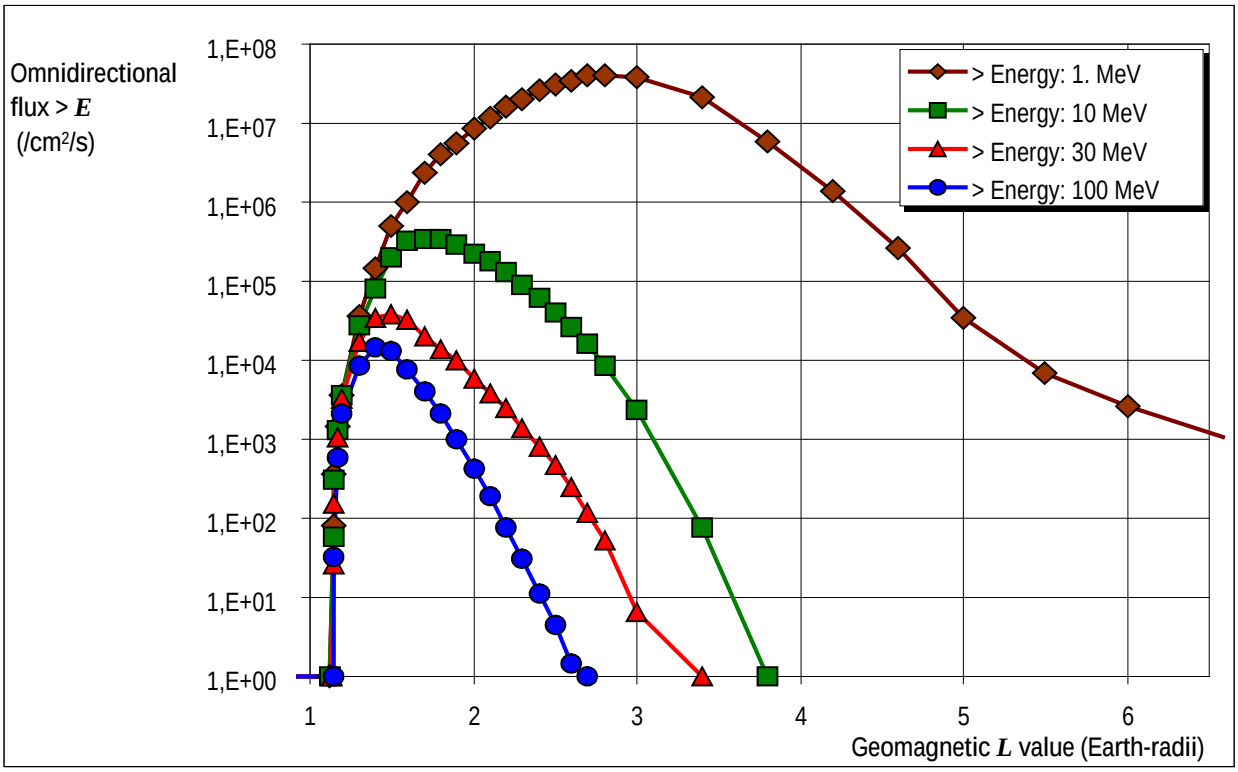

Figure I-2: Electron (a) and proton (b) omnidirectional fluxes, integral in energy, on the geomagnetic equator for various energy thresholds

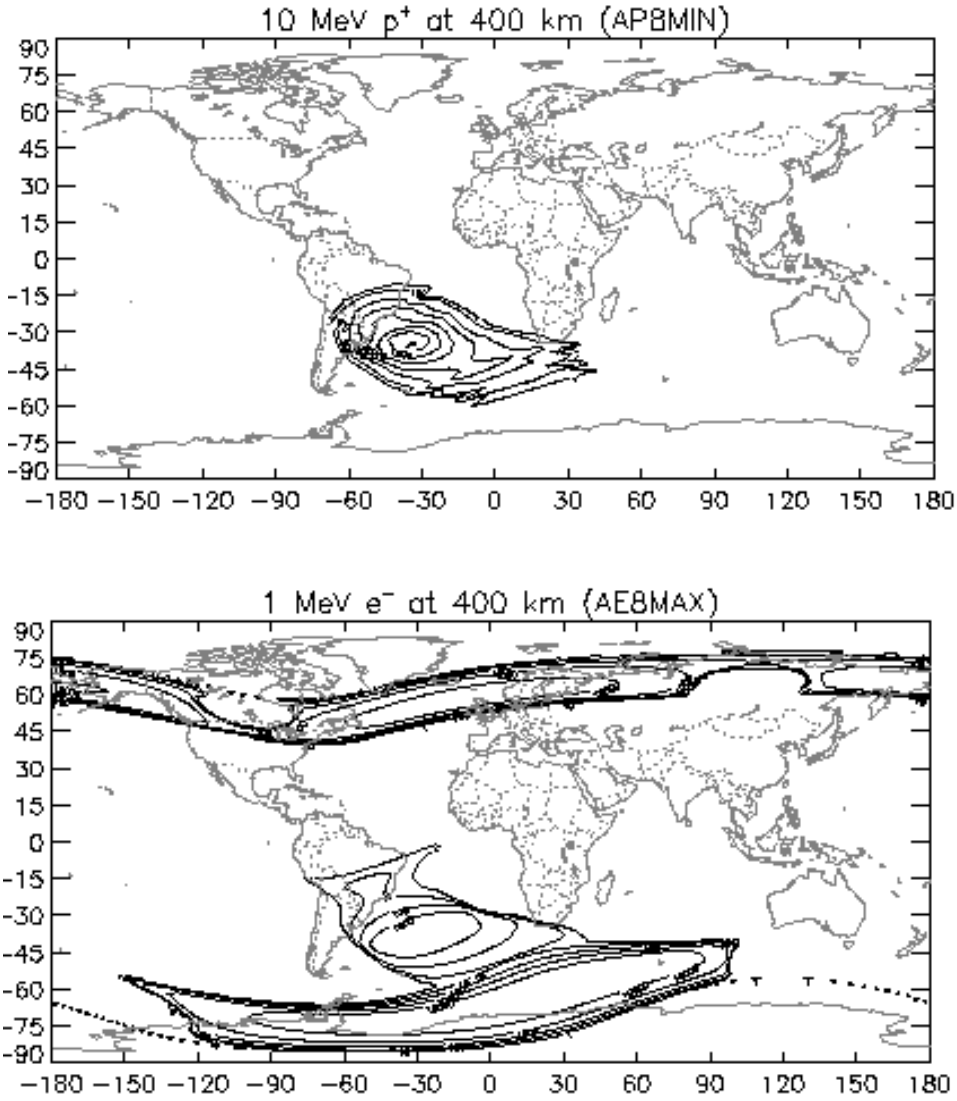

Figure I-3: Integral omnidirectional fluxes of protons (>10 MeV) and electrons (>10 MeV) at 400 km altitude showing the inner radiation belt's "South Atlantic anomaly" and, in the case of electrons, the outer radiation belt encountered at high latitudes

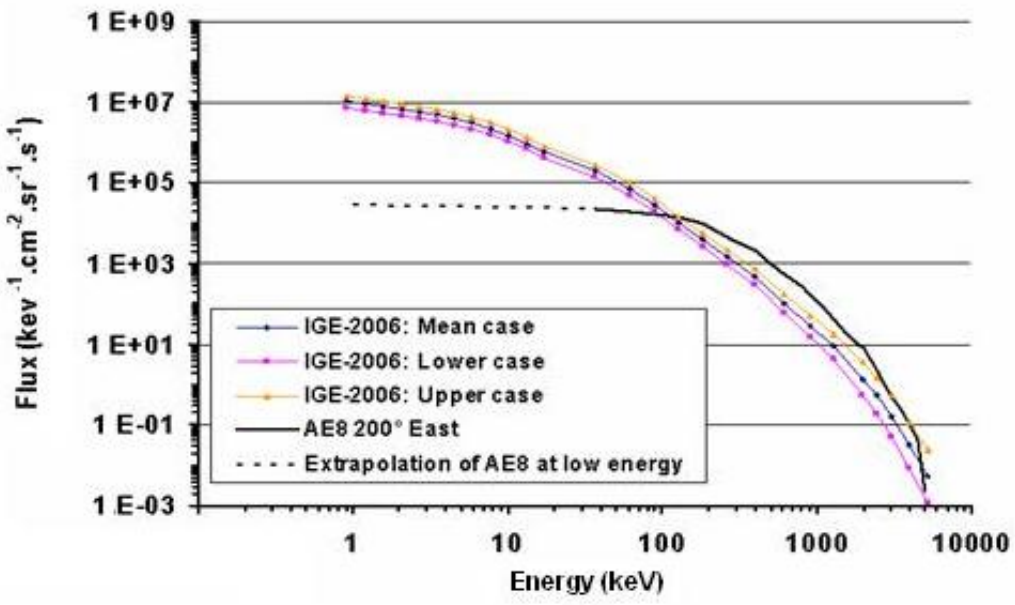

Figure I-4: Comparison of POLE with AE8 (flux vs. Energy) for 15 year mission (with worst case and best case included)

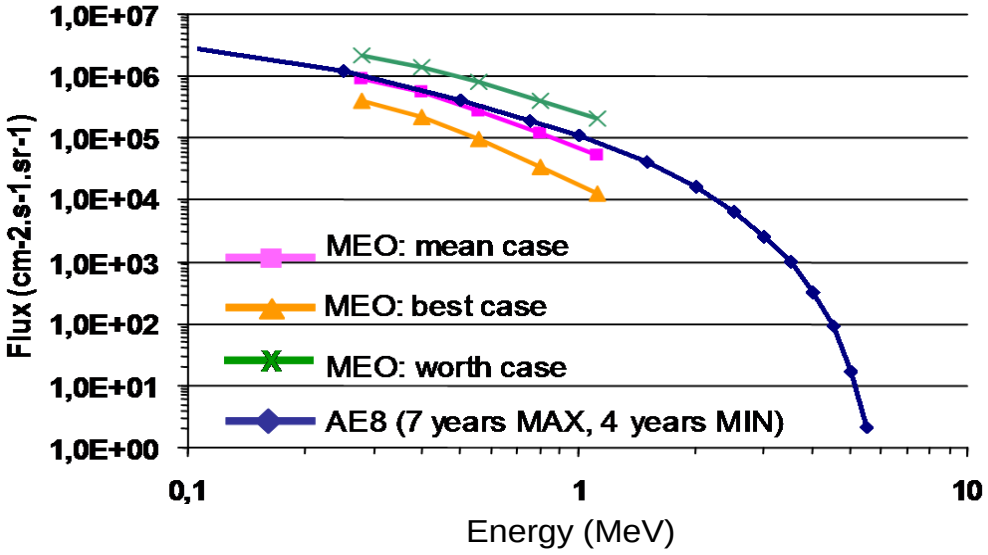

Figure I-5: Comparison of ONERA/GNSS model from 0,28 MeV up to 1,12 MeV (best case, mean case and worst case) with AE8 (flux vs. Energy) for 15 yr mission (with worst case & best case)

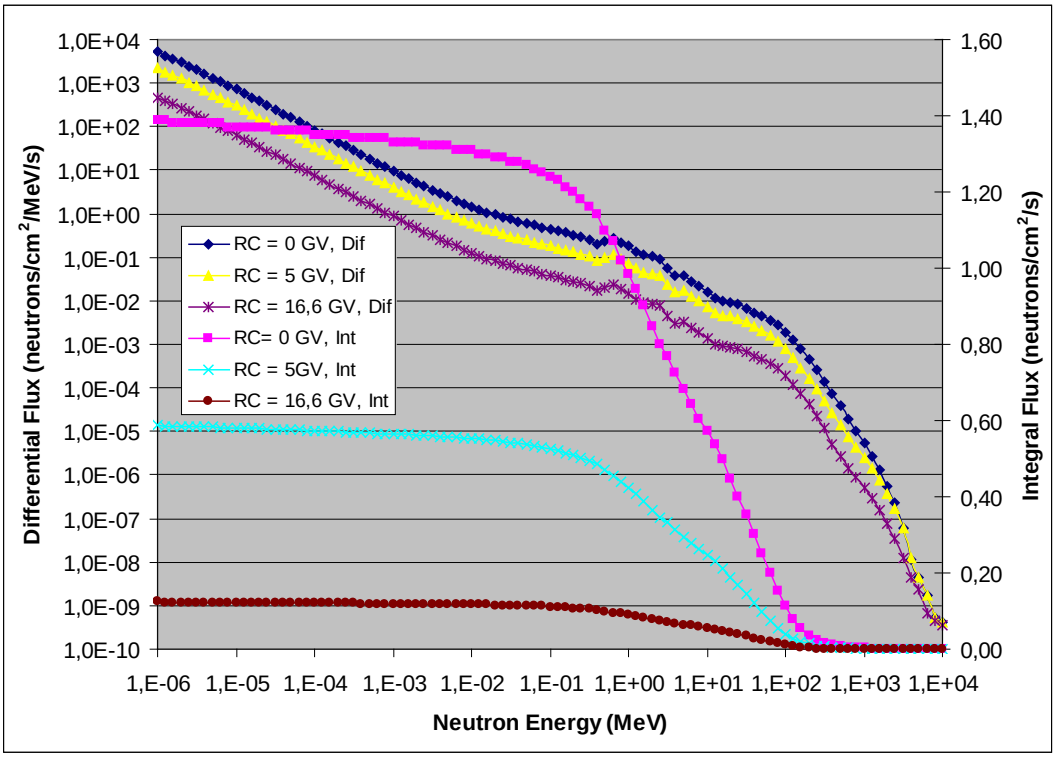

Figure I-6: Albedo neutron spectra at 100 km altitude at solar maximum

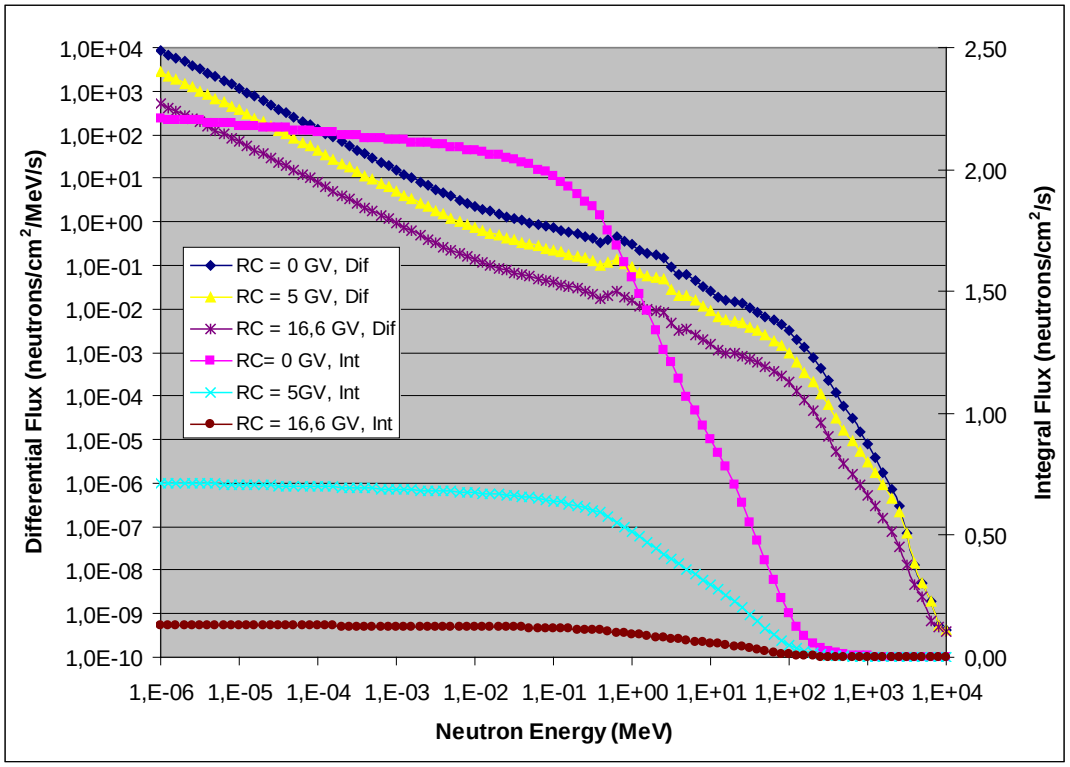

Figure I-7: Albedo neutron spectra at 100 km altitude at solar minimum

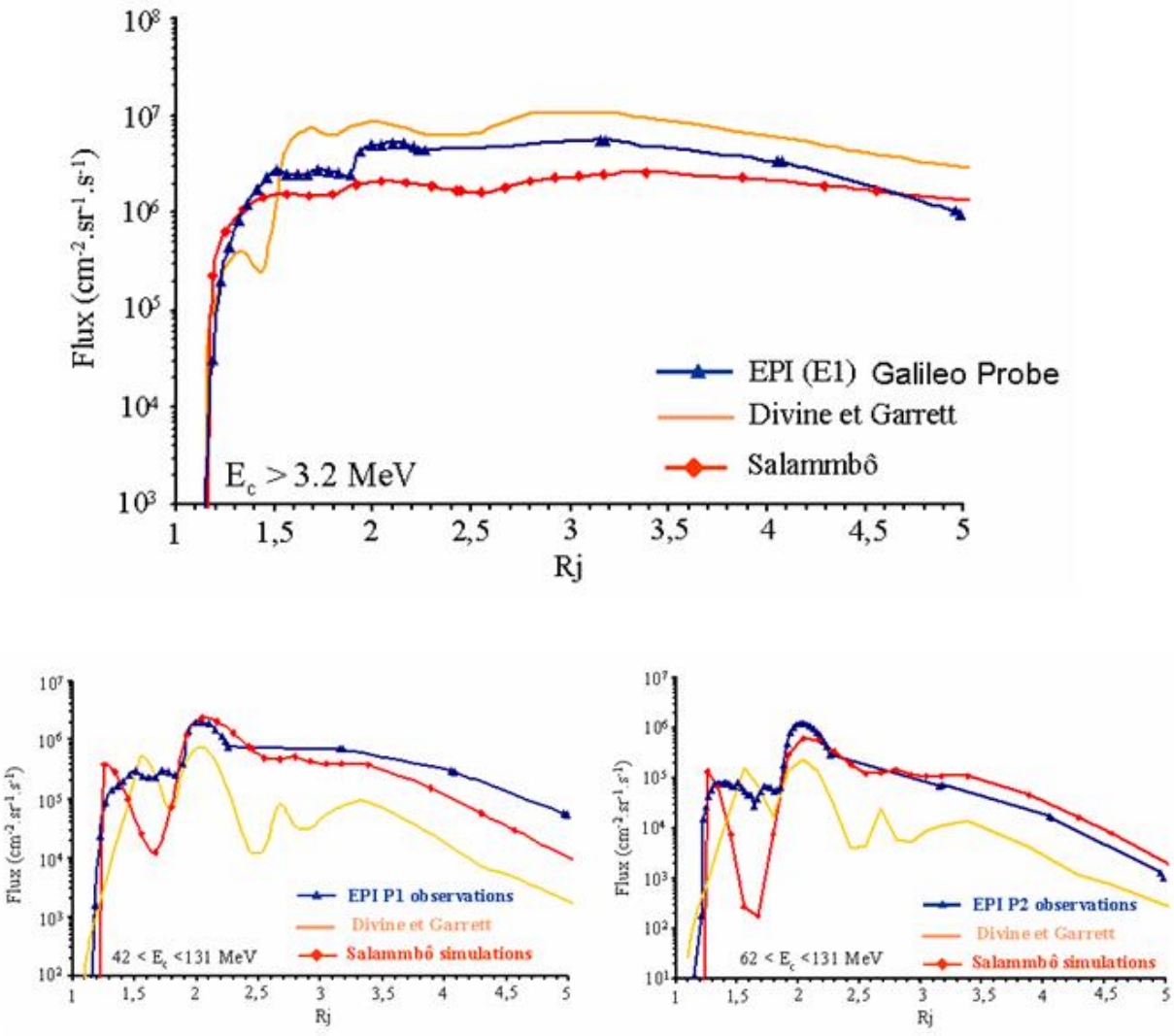

Figure I-8: Jupiter environment model (proton & electron versions)

Annex J (informative)
Space debris and meteoroids

J.1 Reference data

J.1.1 Trackable space debris

The given information on the catalogued space debris population was obtained from the DISCOS [RD.87] database. The figures show the situation in May 2018.

The time evolution of the number of trackable objects in orbit is shown in Figure J-1.

The altitude dependence for the lower altitudes is given in Figure J-2.

The object distribution as function of their inclination is plotted in Figure J-3. A concentration at certain inclinations is clearly visible.

J.1.2 Reference flux data for space debris and meteoroids

Cumulative meteoroid and space debris fluxes (i.e. fluxes of particles of given size or larger) can be obtained directly from the flux models. Figure J-2 to Table J-5 give results from the models specified in the normative part of the document for specific orbits.

Figure J-2 gives the number of impacts m^{-2} yr^{-1} to a randomly tumbling plate for a range of minimum particle sizes. The MASTER-8 model was used for the debris and meteoroid fluxes. The results are for an altitude h = 400 km, inclination i = 51,6°, and the epoch May 1st, 2005. Table J-3 gives the same results for a polar reference orbit (h = 800 km, i = 98°, all other parameters are as for Table J-2).

Table J-4 gives the number of impacts at the geostationary altitude (h = 35 786 km).

Table J-5 gives the number of impacts m^{-2} yr^{-1} to a randomly tumbling plate for a range of minimum particle sizes/masses. The meteoroid model from 10.2.4.1 was used. A position outside the Earth's influence on the meteoroid flux was selected (i.e. no shielding and no gravitational focusing was considered), e.g. the Earth Lagrange points.

Table J-6 gives flux enhancement and shielding factors for sporadic meteoroid fluxes encountered by spacecraft in typical Earth orbits. The procedure described in C.1 was used.

For various distances from Earth, Figure J-4 gives the meteoroid velocity distributions and average velocities as modified by the gravitational attraction of Earth according to the procedure described in C.1.2.

J.2 Additional information on flux models

J.2.1 Meteoroids

J.2.1.1. Meteoroids directionality

The meteoroid flux model given in Annex **Error! Reference source not found.** assumes an isotropic flux with respect to the Earth surface. For an orbiting spacecraft the Earth shielding and the spacecraft motion both introduce a directional dependence.

The directionality caused by the spacecraft motion leads to increased fluxes on forward facing surfaces and to reduced fluxes on trailing surfaces.

Combining the two factors approximate flux ratios for meteoroids are found for 400 km and 800 km altitudes, given in Table J-1.

As resulting effects such as penetration depth or impact plasma generation also depend on parameters such as impact velocity and angle, the directional ratios for these effects can be considerably different from those given in Table J-1.

J.2.1.2. Mass density of meteoroids

The mass density of meteoroids varies widely from about 0,15 g cm^{-3} to 8 g cm^{-3}.

According to reference [RD.21] the average density of micrometeoroids larger than 0,01 g is assumed to be 0,5 g cm^{-3}. Meteoroids smaller than 10^{-6} g are thought to have a higher mean density of 2 g cm^{-3}. The recommended value for masses between 10^{-6} g and 0,01 g is 1 g cm^{-3}.

The reference meteoroid models given in Annex **Error! Reference source not found.** is based on a mass density of 2,5 g cm^{-3}.

However, there is still a considerable uncertainty about these densities.

J.2.1.3. Flux enhancement from gravitational attraction

The method described in Annex **Error! Reference source not found.** to account for a modified velocity distribution and enhanced fluxes due to Earth's gravitational attraction modifies the range and width of each velocity bin given in Table C-1. It is acceptable to account for this re-binning by simply oversampling the original velocity distribution, e.g. using 0,1 km s^{-1} steps in velocity instead of 1 km s^{-1} steps, and ignoring the changes in bin width but simply adding the contribution to the appropriate velocity bin. This gives approximately the same result. For example, the $n(v_\infty)$ velocity distribution at 13,5 km s^{-1} is 4,83E-02 (from Table C-1) where this value represents the contribution from 13 to 14 km s^{-1}. We can oversample $n(v_\infty)$ by a factor of 10 such that we can assign 4,83E-03 to 10 bins between 13 and 14 km s^{-1}. (alternatively, interpolate the $n(v_\infty)$ values to produce a new 0.1 km s^{-1} step distribution, and renormalize it). So for example, a value of $n(v_\infty)$ (or rather, n_k) at 13,95 km s^{-1} (i.e. representing values between 13,90 to 14,00 km s^{-1}) is 4,83E-03. Using expression **Error! Reference source not found.**) a value of v_∞ = 13,95 km s^{-1} becomes v = 17,64 km s^{-1} (assuming v_{esc} = 10,8 km s^{-1} which is true for LEO). Thus our $n(v_\infty)$ value of 4,83E-03 gets added to the 17,6 to 17,7 km s^{-1} bin. Once all values of $n(v_\infty)$ have been considered, the 0,1 step distribution can be converted to the final 1 km s^{-1} step distribution (i.e. this is then n'_k).

J.2.1.4. Meteoroid streams

At peak activity stream fluxes can exceed the sporadic background fluxes by a factor five or more. Occasionally, very high fluxes (meteoroid storms, the visible meteor background flux can be exceeded by a factor 10 000 or more) can be encountered for short periods (1-2 hours). Examples of such storms are the Leonid streams in 1998, 1999 and 2001.

Meteoroid streams consist of relative large particles only (mass > 10^{-8} g) with low density (0,5-1,0 g cm^{-3}).

J.2.1.5. Interplanetary meteoroid model

New interplanetary meteoroid flux models were presented in [RD.106], [RD.110] and [RD.108]. These models are based on different types of meteoroid populations whose relative contributions depend on the particle size range and the distance from the Sun.

The models include directional distributions of the populations.

For Earth orbits the meteoroid models predict similar total fluxes as the reference model in clause 10.2.4. In addition they include directional effects.

The interplanetary meteoroid models are still in the development stage. At present no specific reference model is defined as standard.

J.2.2 Space debris flux models

J.2.2.1. MASTER-8 space debris model

J.2.2.1.1 Overview

MASTER-8 uses a semi-deterministic approach which represents the debris environment by modelling its history from the beginning of spaceflight to present [RD.88]. It considers all known source terms (launch and mission related objects, break-ups, solid rocket motor firings, release of reactor coolant during reactor core ejection by RORSAT satellites as well as leakage observed for two TOPAZ reactors, paint flakes, ejecta and multi-layer insulation fragments) for the debris population and follows the orbital evolutions of the resulting particles. MASTER-8 implements both the Grün and the Divine-Staubach meteoroid model [RD.108] and the seasonal meteoroid stream models from Jenniskens-McBride (see Annex C) and Cour-Palais.

The space debris population at the reference epoch May 1, 2016 is derived from 258 on-orbit break-ups, 16 RORSAT reactor core ejections, 2 TOPAZ reactor leakages and 2438 solid rocket motor firings.

MASTER-8 covers impactor sizes larger than 1µm for Earth-bound target orbits up to lunar altitudes and in Lagrange points at 1 AU. An analysis application allows interrogating the spatial debris distribution to determine collision fluxes for an arbitrary target orbit passing through the control volume. Flux results can be analysed with respect to collision velocity magnitude, its direction (azimuth and elevation), the orbit location, and the 3D position where the flux was encountered.

MASTER-8 is provided via the Space Debris User Portal (J.2.2.1.2) containing the flux database together with the analysis software and runs on Windows, macOS as well as Linux operating systems.

J.2.2.1.2 Access points

The MASTER-8 software, documentation and patches can be obtained online upon registration:

https://sdup.esoc.esa.int.

J.2.2.1.3 Impact velocity for space debris

Impact velocities can range from 0 to about 15,5 km s^{-1} with an average velocity of 10 km s^{-1} for low inclination and of 13 km s^{-1} for high inclination orbits.

J.2.2.1.4 Mass density of space debris objects

The mass density of space debris objects is a function of the object diameter and the space debris sources considered. Different sources release particles of different materials the density of which can vary between 0,01 – 4,7 g cm^{-3}. Since different source terms dominate in different size regimes, the cumulative density averaged over all objects varies significantly with the limiting diameter. For example, objects larger than 1cm are mainly explosion fragments so that the average density of debris is close to that of aluminium (2,7 g cm^{-3}). Objects larger than 1 μm are dominated by solid rocket motor dust (aluminium oxide, 3,5 g cm^{-3}).

J.2.2.2. Other space debris models

J.2.2.2.1 Overview

Several additional space debris models exist for various ranges of applicability and different purpose. Only a subset of these is publicly available and thus of interest for this standard.

For some international space programmes specific models have been defined as applicable. For the International Space Station, additional to the ORDEM3.0 model, also the space debris models NASA-90 [RD.21] or ORDEM-2000 [RD.107] are still applied.

J.2.2.2.2 ORDEM-2000

ORDEM 2000 was developed by the NASA Orbital Debris Program Office at JSC [RD.107]. It uses careful empirical estimates of the orbit populations derived from measurements, incorporating a large set of observational data with the US Space Command Catalog, the Haystack Radar, and the Long Duration Exposure Facility spacecraft returned surfaces being the three primary sources. By this, the model covers an object size range from 10 μm to 10 m and employs a new analytical technique utilizing a maximum likelihood estimator to convert observations into debris population probability distribution functions.

The model describes the orbital debris environment in the low Earth orbit region between 200 and 2,000 km altitude.

J.2.2.2.3 NASA-90 model

From about 1990 until 1996 the NASA space debris engineering model defined in [RD.21] has been most widely used for design applications. This model is given in terms of simple analytical expressions. It is relatively easy to use and widely distributed. However, it has some known shortcomings of which the assumption of spherical orbits for all debris particles is probably the most severe. The user should be aware of its shortcomings.

J.2.3 Model uncertainties

J.2.3.1. General

The meteoroid and space debris environment flux models given in 10 and Annex C contain several known approximations and other uncertainties.

J.2.3.2. Meteoroids

According to [RD.21] uncertainties in the meteoroid models mainly result from uncertainties in particle densities and masses. Fluxes for meteoroids larger than 10^{-6} g are well defined, but the associated masses are quite uncertain. The mass density of meteoroids spans a wide range, from about 0,15 g cm^{-3} to values as large as 8 g cm^{-3}. For meteoroids flux uncertainties at a given mass are estimated to be at least a factor of 0,33 to 3.

J.2.3.3. Space debris

The space debris flux models were developed as a best estimate rather than a conservative one. In [RD.89] the spatial density distributions as predicted by various space debris models are compared. Model predictions are not always consistent, in particular in terms of quantity and for lower debris sizes. Significant modelling related deviations can also occur between model versions.

Fluxes of sub-mm size objects in orbits below 1 000 km have short lifetimes of weeks or months. Their population depends heavily on individual generation events and can vary by an order of magnitude.

Other uncertainties of debris models are the debris density and shape.

A more detailed discussion of model uncertainties is given in [RD.21] and [RD.90].

J.3 Flux uncertainties for space debris are assessed via the model validation in MASTER-8. The large object population (d > 1 cm) is validated against radar and passive optical measurement campaigns whereas the small object population (d < 1 cm) is validated against impact measurements of returned surfaces. The uncertainty quantification is based on statistical evaluation of the validation data where any deviation from measurements is considered. A 1-sigma confidence interval is provided in MASTER-8 for every diameter decade for the total population. Impact risk assessment

J.3.1 Impact risk analysis procedure

For a given surface area and exposure duration the total number of impacts N is obtained from the impact flux by multiplication with the total exposed surface area and exposure duration.

From the number of impacts, N, the probability of exactly n impacts occurring in the corresponding time interval is determined by Poisson statistics:

$$P_n = \left(\frac{N^n}{n!} \right) e^{-N} \tag{J-1}$$

The probability for no impacts, P_0 is given by:

$$P_0 = e^{-N} \tag{J-2}$$

For values of $N << 1$, the probability Q for at least one impact ($Q = 1 - P_0$) is nearly equal to N:

$$Q = 1 - e^{-N} \approx 1 - (1 - N) = N \tag{J-3}$$

J.3.2 <<deleted>>

.

J.3.3 Damage assessment

Here a brief general overview of damage assessment criteria and procedures is given. A more detailed and extensive description can be found in [RD.91]

For each individual project the damage assessment is tailored according to the specific conditions and requirements (e.g. orbit, shielding, damage criteria, and required reliability).

Any damage assessment depends to a large extend on the relevant failure criteria. Possible failure criteria include:

- cratering (sensor degradation, window blinding, surface erosion);
- larger craters (sealing problems, short circuits on solar arrays);
- impact generated plasma (interference, discharge triggering);
- impulse transfer (attitude problems);
- spallation from inner wall (equipment damage, crew injury);
- wall penetration (damage, injury, loss of liquid or air);
- burst, rupture (pressurized parts);
- structural damage.

For a quantitative damage and risk assessment so called damage or design equations for the given shielding configuration are needed. They give critical particle diameters, shielding thresholds or hole sizes for given impact parameters and failure modes. Examples of single and double wall damage equations taken from are provided in J.3.3.1 and J.3.3.2 respectively. Further damage equations can be found in [RD.91]

Sometimes scaled effective thicknesses in combination with known damage equations can be used for a first assessment.

For impact damage and risk assessments secondary ejecta can be important as well. The total mass of the ejected particles can exceed the mass of the primary impactor by orders of magnitude. Secondary particles are typically ejected within a cone around the impact direction. Their velocities are typically below 2 km s^{-1}.

J.3.3.1. Single wall damage equation

The critical diameter for projectiles to cause a failure is given by:

$$D_c = \left(\frac{t_t}{K_f \cdot K_1 \cdot \rho_p^{\beta} \cdot v^{\gamma} \cdot (\cos\alpha)^{\xi} \cdot \rho_t^{\kappa}}\right)^{1/\lambda} \qquad \text{(J-4)}$$

where:

D_c	Critical diameter
t_t	Target thickness
K_f	Failure factor
K_1	Material factor
ρ_p ρ_t	Density of projectile and target
v	Impact velocity
α	Incidence angle (to surface normal)

A typical set for equation parameters is provided by the thick plate model with following parameters:

α	β	γ	ξ	K
1,056	0,519	2/3	2/3	0

The failure factor can vary from 1,8 to 3, where following failures are assumed:

$K_f \geq 3$	Crater generation without spall

$2{,}2 \leq K_f < 3$	Spallation of target
$1{,}8 \leq K_f < 2{,}2$	Spall breaks away
$K_f < 1{,}8$	Perforation

This factor can be interpreted as the fraction of target thickness not affected by the generated crater, i.e. K_f=3 corresponds to one third of the target thickness unaffected by the crater. Note that for pressurized vessels a K_f factor of 4 is typically applied [RD.91]

The K_1 factor reflects the target material properties. Typical values are K_1 = 0.33 for aluminium and K_1 = 0.2 for stainless steel.

J.3.3.2. Double wall damage equation

Double wall damage equations are used to quantify the shielding provided by two wall shielding configurations with an additional protecting layers, the so-called bumber. The critical diameter required to penetrate the shielding structure is given by:

$$D_c = \left(\frac{t_t}{K_1 \cdot \rho_p^{\beta} \cdot v^{\chi} \cdot (\cos\alpha)^{\xi} \cdot \rho_t^{\kappa} \cdot S^{\delta}}\right)^{1/\lambda} \qquad \text{(J-5)}$$

Where:

D_c	Critical diameter
t_t	Target thickness (second impacted wall)
K_f	Failure factor
ρ_p ρ_t	Density of projectile and target (second impacted wall)
v	Impact velocity
α	Incidence angle (to surface normal)
S	Spacing between the two layers

Note that unlike the example provided here, double or multi-wall equations are in general defined in several velocity regimes.

The increased efficiency in shielding is achieved by the fragmentation of the projectile in the bumper and the spread of the fragmentation cloud before impacting the second surface. Thus, for the applicability of the equations it is relevant if the bumber layer can fragment the projectile and if the spacing in between the layers allows for a sufficient spread of fragments. An engineering practice is to assume that the following has to be met in order to be able to apply double wall equations for the considered shielding geometry:

$t_b > D_c/6$

$S > 15\ D_c$

where:

D_c	Critical diameter
t_b	Bumper thickness (first impacted wall)
S	Spacing between the two layers

Note that the applicability of double wall equations for shielding configurations is environment dependent as impact parameters like incidence angle, velocity and projectile density can vary.

J.4 Analysis tools

J.4.1 General

Several numerical tools have been developed to perform impact and impact risk analyses. The following tools are mentioned for information only.

J.4.2 Deterministic analysis

For information and analysis of the deterministic, trackable space objects, the DISCOS database was developed [RD.87]. DISCOS (ESA's Database and Information System Characterising Objects in Space) is a catalogue on Earth orbiting space objects and debris.

DISCOS can be used to extract detailed data on all the tracked objects. DISCOS is implemented at and maintained by ESA/ESOC. It is accessible via https://discosweb.esoc.esa.int for registered users only.

J.4.3 Statistical analysis

J.4.3.1. Overview

Some tools to perform a statistical microparticle risk assessment are listed below. In general, the user specifies the mission, spacecraft geometry, attitude and shielding as well as the particle type, size and velocity range to be analysed. The computed output typically includes:

- the average number of impacts;
- the resulting number of damaging impacts taking into account the spacecraft shielding and damage assessment equations;
- the mean particle impact velocity (amplitude and direction);
- the numbers of craters of specified size;
- the probability of no failure.

J.4.3.2. ESABASE

A statistical tool, ESABASE2/DEBRIS, was developed for a detailed impact risk assessment of smaller, non-trackable particles [RD.30]. ESABASE2/DEBRIS is a fully three dimensional numerical analysis tool including directional and geometrical effects and spacecraft shielding considerations. It is based on environment and particle-wall interaction models and includes several meteoroid and space debris flux models.

ESABASE2/DEBRIS is applicable for earth orbits and allows the optional use of several meteoroid and debris flux models. The tool includes the MASTER-2005 model and the

sporadic and stream meteoroid models given in Annex C.1, including the altitude dependent velocity distribution.

J.4.3.3. Systema Debris

Systema-Debris [RD.171] is a 3D geometrical analysis tool for the computation of space debris and micrometeoroids impacts on spacecraft. This tool computes the probability that a MMOD (micrometeoroids or orbital debris) penetrates a spacecraft surface or equipment. The MMOD environment is defined in a STENVI (Standard Environment Interface) that can be computed by standard environment models like MASTER.

This tool accounts for the 3D geometry, the surface material characteristics (MLI, honeycomb, equipment walls…), computes the number of impacts or penetrations on a meshed surface, the Probability of No-Penetration of the selected elements and the area of craters induced by impacting debris. To compute the impacts, the user can choose among several classical Ballistic Limit Equations: single wall, multiple walls, SRL.

Systema-Debris computation relies on an advanced ray-tracing algorithm, which can handle complex geometry including CAD shapes and shadowing effects. The results (impacting and penetrating flux) can be displayed on the 3D geometry.

J.4.3.4. DRAMA (MIDAS)

The Impact Flux and Damage Assessment Software of DRAMA (MIDAS) is based on the MASTER model. The capabilities of the MIDAS software comprise:

- debris and meteoroid collision flux and damage analysis for any user-defined target orbit and particle size range.
- collision flux and damage analysis for a user-defined time interval, using realistic population snapshots for each time step.
- debris and meteoroid flux analysis for a spherical target or a randomly tumbling plate.
- debris and meteoroid flux and damage analysis for up to ten oriented planar surfaces, where the plate orientation can be selected from three fixed modes (Earth oriented, Sun oriented or inertially fixed).

The user can select different damage equations per surface from four fixed equations and input up to 20 user-defined equations.

J.4.3.5. PIRAT

PIRAT [RD.172] was developed by Fraunhofer EMI. It has been specifically designed for the risk assessment of unmanned missions. It provides an intuitive, reliable, fast, thorough, and resource-effective analysis of a spacecraft for a given set of mission parameters. In particular, it provides improvement on the traditional risk assessment methods by looking beyond structural penetration and additionally investigates impact effects at the level of internal components.

PIRAT provides an interface to ESA's MASTER and NASA's ORDEM space debris models. Geometrical information is directly derived from the 3D satellite model, which can be constructed within PIRAT using geometric primitives.

J.4.3.6. BUMPER

The Bumper code has been developed by NASA and contractors to perform meteoroid and debris risk assessments since 1990. Bumper 3 is a refactored version of Bumper II. The core consists of common code necessary to process the MMOD environment models, assess shadowing and calculate MMOD risk. The library of target response subroutines includes a board range of different types of MMOD shield ballistic limit equations as well as equations describing damage to various spacecraft subsystems or hardware (thermal protection materials, windows, radiators, solar arrays, cables, etc.).

J.5 Tables

Table J-1: Approximate flux ratios for meteoroids for 400 km and 800 km altitudes

	400 km	800 km
Front/random	≈ 2,1	≈ 2,1
Front/rear	≈ 7,7	≈ 7,2
Space face / Earth face	≈ 12,0	≈ 5,5

Table J-2: Cumulative number of impacts, *N*, to a randomly tumbling plate for a range of minimum particle sizes using the MASTER-8 model (version 8.0.0)

Diameter (cm)	N_{deb} ($m^{-2}yr^{-1}$)	N_{met} ($m^{-2}yr^{-1}$)	N_{tot} ($m^{-2}yr^{-1}$)
0,0001	3,13E+01	8,42E+02	8,73E+02
0,0002	3,12E+01	4,23E+02	4,54E+02
0,0003	2,94E+01	2,.62E+02	2,91E+02
0,0005	2,39E+01	1,36E+02	1,60E+02
0,0007	1,45E+01	9,68E+01	1,11E+02
0,001	4,87E+00	7,47E+01	7,96E+01
0,002	1,81E+00	4,02E+01	4,20E+01
0,003	1,71E+00	2,07E+01	2,24E+01
0,005	1,58E+00	6,11E+00	7,69E+00
0,007	1,49E+00	3,08E+00	4,57E+00
0,01	1,32E+00	1,28E+00	2,61E+00
0,02	6,17E-02	1,21E-01	1,83E-01
0,03	1,93E-02	3,33E-02	5,26E-02
0,05	3,66E-03	5,69E-03	9,35E-03
0,07	3,14E-04	1,72E-03	2,03E-03
0,1	1,42E-04	4,54E-04	5,96E-04
0,2	5,30E-05	2,41E-05	7,71E-05
0,3	2,88E-05	5,22E-06	3,40E-05
0,5	1,17E-05	7,01E-07	1,24E-05

Diameter (cm)	N_{deb} ($m^{-2}yr^{-1}$)	N_{met} ($m^{-2}yr^{-1}$)	N_{tot} ($m^{-2}yr^{-1}$)
0,7	6,55E-06	1,85E-07	6,73E-06
1,0	3,54E-06	4,50E-08	3,58E-06
2,0	9,28E-07	2,60E-09-	9,31E-07
3,0	4,80E-07	3,70E-10-	4,81E-07
5,0	3,60E-07	-	3,60E-07
10,0	2,59E-07	-	2,59E-07
NOTE: The results are for an altitude h = 400 km, inclination i = 51.6°, and the epoch November 1st, 2016. For meteoroids the Grün model with constant velocity of 20 km/s was used.			

Table J-3: Cumulative number of impacts, N, to a randomly tumbling plate for a range of minimum particle sizes using the MASTER-8 model (version 8.0.0)

Diameter (cm)	N_{deb} ($m^{-2}yr^{-1}$)	N_{met} ($m^{-2}yr^{-1}$)	N_{tot} ($m^{-2}yr^{-1}$)
0,0001	2,02E+02	9,03E+02	1,10E+03
0,0002	2,02E+02	4,54E+02	6,56E+02
0,0003	1,95E+02	2,81E+02	4,76E+02
0,0005	1,80E+02	1,46E+02	3,26E+02
0,0007	1,52E+02	1,04E+02	2,55E+02
0,001	1,28E+02	8,02E+01	2,08E+02
0,002	5,58E+01	4,31E+01	9,89E+01
0,003	4,45E+01	2,22E+01	6,66E+01
0,005	3,03E+01	6,55E+00	3,68E+01
0,007	2,23E+01	3,30E+00	2,56E+01
0,01	1,68E+01	1,37E+00	1,81E+01
0,02	2,24E+00	1,30E-01	2,37E+00
0,03	6,86E-01	3,57E-02	7,22E-01
0,05	5,05E-02	6,12E-03	5,67E-02
0,07	7,22E-03	1,84E-03	9,06E-03
0,1	2,37E-03	4,85E-04	2,86E-03
0,2	8,28E-04	2,58E-05	8,54E-04
0,3	4,68E-04	5,60E-06	4,74E-04
0,5	2,11E-04	7,52E-07	2,12E-04
0,7	1,37E-04	1,99E-07	1,37E-04
1,0	8,41E-05	4,84E-08	8,42E-05
2,0	2,99E-05	2,88E-09	2,99E-05
3,0	1,79E-05	4,30E-10	1,79E-05
5,0	1,01E-05	-	1,01E-05
10,0	5,07E-06	-	5,07E-06

Diameter (cm)	N_{deb} ($m^{-2}yr^{-1}$)	N_{met} ($m^{-2}yr^{-1}$)	N_{tot} ($m^{-2}yr^{-1}$)
NOTE: The results are for an altitude h = 800 km, inclination i = 98°, and the epoch November 1st, 2016. For meteoroids the Grün model with constant velocity of 20 km/s was used.			

Table J-4: Cumulative number of impacts, N, to a randomly tumbling plate for a range of minimum particle sizes using the MASTER-8 model (version 8.0.0)

Diameter (cm)	N_{deb} ($m^{-2}yr^{-1}$)	N_{met} ($m^{-2}yr^{-1}$)	N_{tot} ($m^{-2}yr^{-1}$)
0,0001	6,80E+01	1,01E+03	1,08E+03
0,0002	6,79E+01	5,07E+02	5,75E+02
0,0003	6,09E+01	3,14E+02	3,75E+02
0,0005	2,,64E+01	1,63E+02	1,89E+02
0,0007	6,,15E+00	1,16E+02	1,22E+02
0,001	1,,30E+00	8,95E+01	9,08E+01
0,002	3,,91E-01	4,81E+01	4,85E+01
0,003	2,,52E-01	2,48E+01	2,50E+01
0,005	2,27E-01	7,32E+00	7,54E+00
0,007	1,91E-01	3,69E+00	3,88E+00
0,01	1,24E-01	1,54E+00	1,66E+00
0,02	2,59E-02	1,45E-01	1,71E-01
0,03	7,29E-03	3,99E-02	4,71E-02
0,05	8,42E-04	6,84E-03	7,68E-03
0,07	1,21E-04	2,05E-03	2,17E-03
0,1	1,17E-05	5,44E-04	5,56E-04
0,2	1,93E-06	2,88E-05	3,08E-05
0,3	7,39E-07	6,25E-06	6,99E-06
0,5	2,00E-07	8,39E-07	1,04E-06
0,7	9,49E-08	2,22E-07	3,17E-07
1,0	4,84E-08	5,39E-08	1,02E-07
2,0	1,32E-08	3,18E-09	1,63E-08
3,0	7,66E-09	4,89E-10	8,15E-09
5,0	4,86E-09	-	4,86E-09
10,0	3,30E-09	-	3,30E-09
NOTE: The results are for an altitude h = 35 786 km, inclination i = 0,5°, and the epoch November 1st, 2016. For meteoroids the Grün model with constant velocity of 20 km/s was used.			

Table J-5: Cumulative number of impacts, N, to a randomly tumbling plate for a range of minimum particle masses

Mass (g)	Diameter (cm)	N_{met} ($m^{-2}yr^{-1}$)
1,00E-12	9,14E-5	1,09E+3
5,00E-12	1,56E-4	6,11E+2
1,00E-11	1,97E-4	4,71E+2
5,00E-11	3,37E-4	2,57E+2
1,00E-10	4,24E-4	2,02E+2
5,00E-10	7,26E-4	1,20E+2
1,00E-9	9,14E-4	9,51E+1
5,00E-9	1,56E-3	5,15E+1
1,00E-8	1,97E-3	3,74E+1
5,00E-8	3,37E-3	1,51E+1
1,00E-7	4,24E-3	9,54E+0
5,00E-7	7,26E-3	2,75E+0
1,00E-6	9,14E-3	1,49E+0
5,00E-6	1,56E-2	3,07E-1
1,00E-5	1,97E-2	1,47E-1
5,00E-5	3,37E-2	2,36E-2
1,00E-4	4,24E-2	1,04E-2
5,00E-4	7,26E-2	1,43E-3
1,00E-3	9,14E-2	5,97E-4
5,00E-3	1,56E-1	7,57E-5
1,00E-2	1,97E-1	3,07E-5
5,00E-2	3,37E-1	3,72E-6
1,00E-1	4,24E-1	1,49E-6
5,00E-1	7,26E-1	1,77E-7
1,00E+0	9,14E-1	7,02E-8
5,00E+0	1,56E+0	8,22E-9
1,00E+1	1,97E+0	3,26E-9
5,00E+1	3,37E+0	3,79E-10
1,00E+2	4,24E+0	1,50E-10
5,00E+2	7,26E+0	1,74E-11

NOTE 1: The meteoroid model specified in 10.2.4.1 was used.

NOTE 2: The results are for an object located outside the Earth's influence (no gravitational focusing and no shielding, e.g. Earth Lagrange Points).

NOTE 3: A density of $\rho = 2,5$ g cm^{-3} was used to convert masses to diameters

Table J-6: Parameters (appearing in Eq.) to account for modified meteoroid fluxes encountered by spacecraft in circular Earth orbits at various altitudes

Altitude [km]	$\overline{G}$	s_f	K
100	2,04	0,50	1,09
200	2,03	0,58	1,09
400	2,00	0,63	1,09
800	1,94	0,70	1,08
1 000	1,92	0,72	1,08
2 000	1,81	0,79	1,08
4 000	1,65	0,87	1,07
10 000	1,41	0,95	1,05
20 000	1,26	0,98	1,04
35 790 (GEO)	1,16	0,99	1,03
100 000	1,06	1,00	1,01
At 1 AU	1,00	1,00	1,00

NOTE: $\overline{G}$ is the weighted mean gravitational enhancement factor for the velocity distribution of Table C-1. The factor s_f accounts for the geometrical shielding of Earth. K gives the flux enhancement for a randomly tumbling plate that result from the spacecraft motion itself.

J.6 Figures

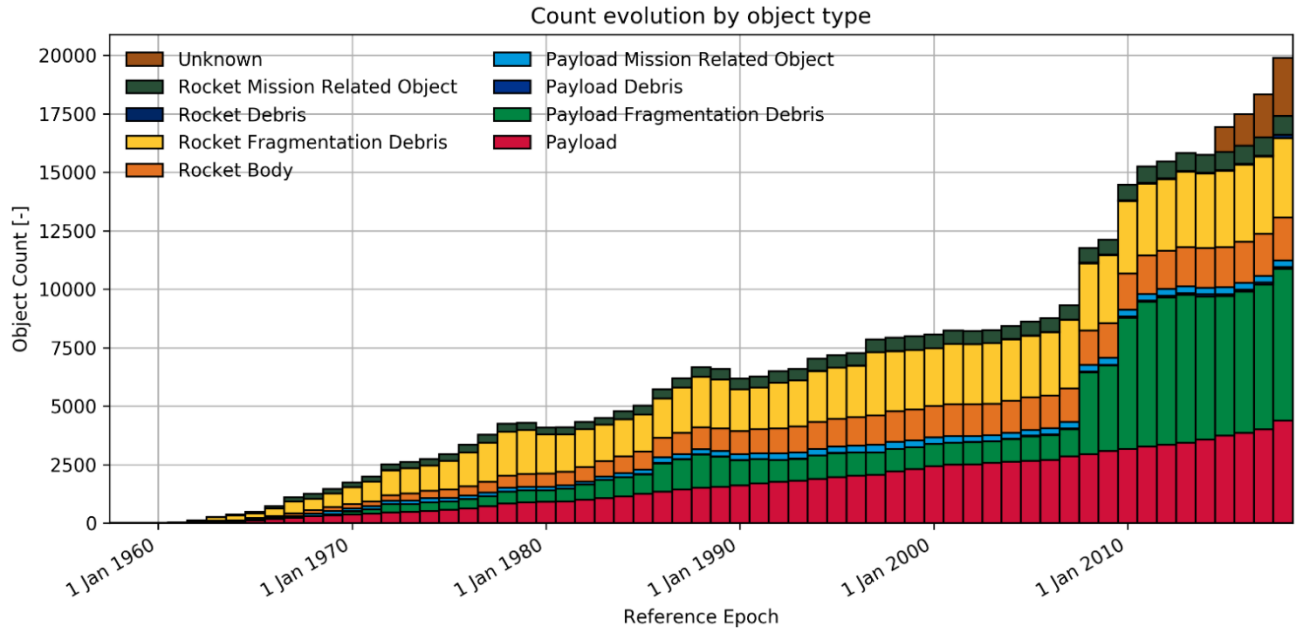

Figure J-1: Time evolution of the number of trackable objects in orbit (as of May 2018). Regular updates available online: https://discosweb.esoc.esa.int/web/guest/statistics

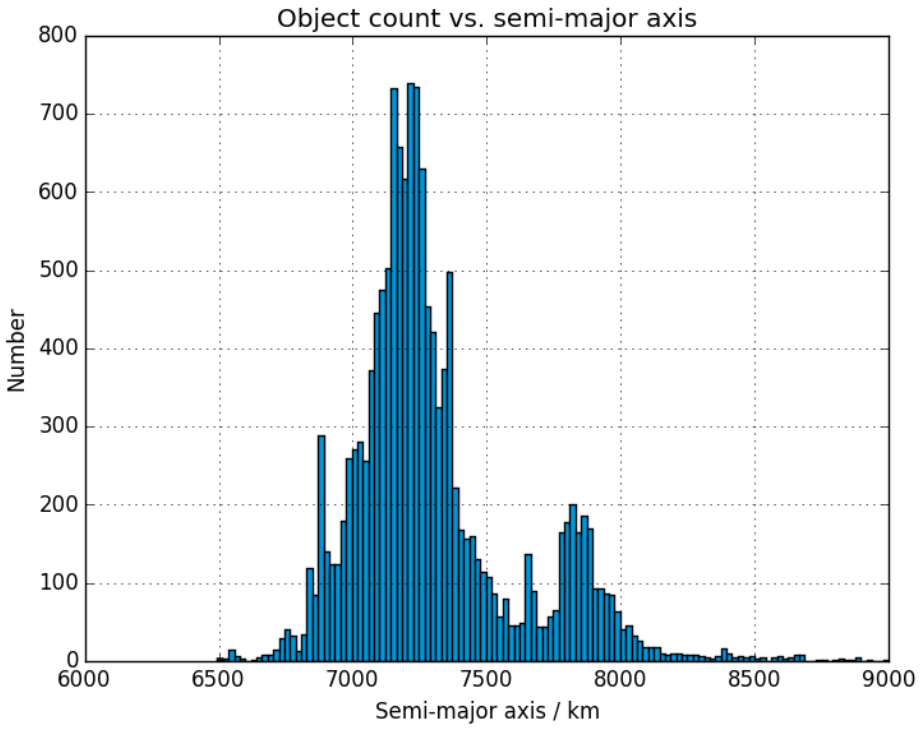

Figure J-2: Semi-major axis distribution of trackable objects in LEO orbits (as of May 2018)

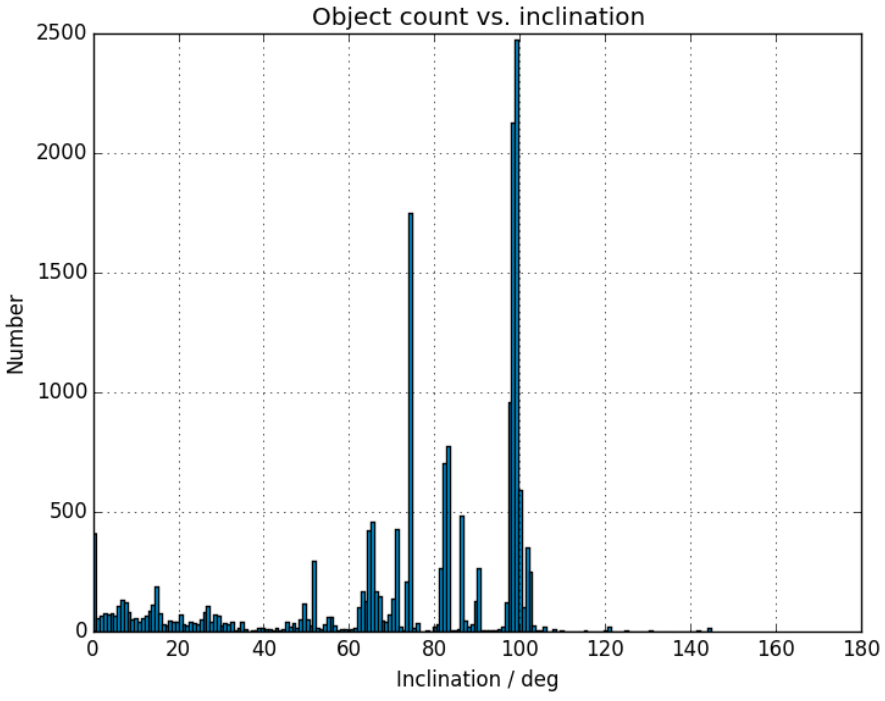

Figure J-3: Distribution of trackable objects as function of their inclination (as of May 2018)

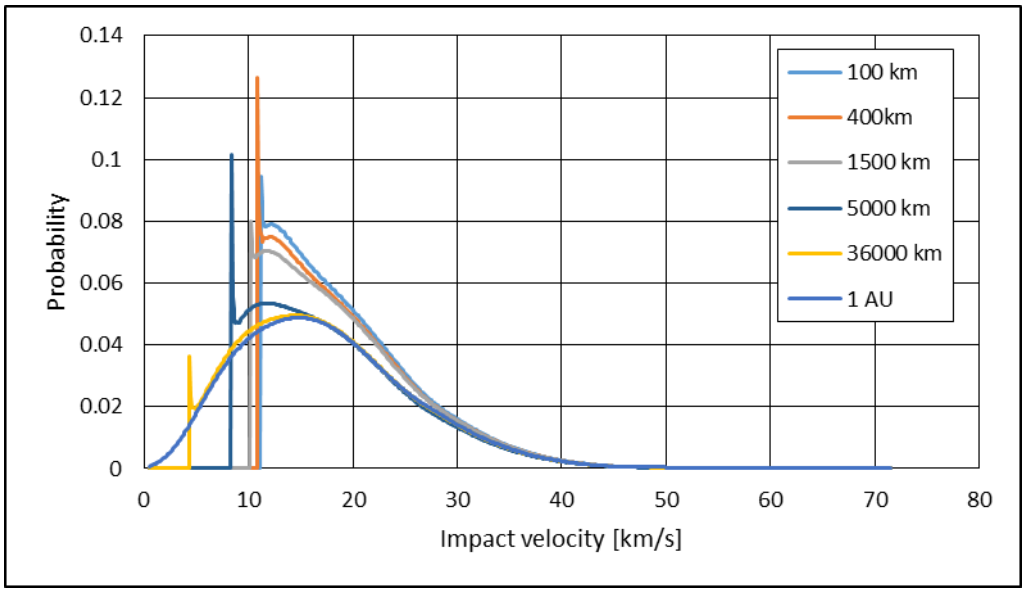

NOTE: The gravitational attraction of Earth shifts the distribution to lower velocities. Average velocities are: 19,7 km/s at 400 km, 19,4 km/s at 1 500 km, 18,6 km/s at 5 000 km, 17,8 km/s at 36 000 km and 17,2 km/s outside of the influence of Earth

Figure J-4: The HRMP velocity distribution for different altitudes from the Earth surface.

Annex K (informative)
<<deleted>>

Bibliography

ECSS-S-ST-00	ECSS system – Description, implementation and general requirements
ECSS-E-ST-10	Space engineering – System engineering general requirements
ECSS-E-ST-10-12	Space engineering – Methods for the calculation of radiation received and its effects and a policy for design margins
ECSS-Q-ST-70-01	Space product assurance – Contamination and cleanliness control
ECSS-E-ST-20-06	Spacecraft engineering – Spacecraft charging
ISO 27852:2016	Space systems - Estimation of orbit lifetime

[RD.1] Montenbruck, O., Gill, E.; Satellite Orbits Models, Methods, Applications; Springer, Berlin-Heidelberg-New York, 2000

[RD.2] ASTM E 490 – 00a, Standard Solar Constant and Zero Air Mass Solar Spectral Irradiance Tables, © ASTM, 100 Barr Harbor Drive, West Conshohocken, PA 19428-2959 (2000).

[RD.3] ISO 21348 “Space System - Space environment – Solar irradiance determinations,” 2007.

[RD.4] Solar Cycle Progression (at NOAA Space Environment Center (SEC) http://www.swpc.noaa.gov/ solar-cycle-progression

[RD.5] K.W. Ogilvie and M.A. Coplan , Solar wind composition, U.S. National Report to IUGG, 1991-1994, Rev. Geophys. Vol. 33 Suppl., AGU, 1995, http://www.agu.org/revgeophys/ogilvi00/ogilvi00.html

[RD.6] S.W.Evans (editor), Natural Environment near the Sun/Earth-Moon L2 libration point, MSFC http://snap.lbl.gov/pub/nj_bscw.cgi/d84104/SNAP-TECH-03009.pdf

[RD.7] “Space Environment for USAF Space Vehicles”, MIL-STD-1809 (USAF), 15 Feb 1991.

[RD.8] Yeh H.-C. and M.S. Gussenhoven, “The statistical Electron Environment for Defense Meteorological Satellite Program Eclipse Charging”, J. Geophys. Res., pp.7705-7715, 1987.

[RD.9] Gussenhoven M.S, D.A. Hardy, F. Rich, W.J. Burke and H.-C. Yeh, “High-Level Spacecraft Charging in the Low-Altitude Polar Auroral Environment”, J. Geophys. Res., pp.11009-11023, 1985.

[RD.10] Solar Wind Radial and Latitudinal Variations From Pole-to-Pole Ulysses Radio measurements, K. Issautier, N. Meyer-Vernet, S. Hoang, M. Moncuquet

[RD.11] H.B. Garrett and A .R. Hoffman , ‘Comparison of Spacecraft Charging Environments at the Earth, Jupiter, and Saturn’, IEEE Trans. Plasma Science, Vol.28, No.6, p.2048, 2000

[RD.12] Hess W.N., “The Radiation Belt and Magnetosphere”, Blaisdell Publ. Co.,1968.

[RD.13] ICRP, “1990 Recommendations of the International Commission on Radiological Protection”, ICRP Publication 60, Annals of the ICRP 21, 1-3 ISBN: 0-08-041144-4, Pergamon Press, NY and Oxford, 1991.

[RD.14] Lemaire J., A.D. Johnstone, D. Heynderickx, D.J. Rodgers, S. Szita and V. Pierrard, "Trapped Radiation Environment Model Development (TREND-2)" Final Report of ESA Contr. 9828, Aeronomica Acta 393-1995, Institut d'Aeronomie Spatiale de Belgique/Belgisch Institut voor Ruimte-Aeornomie, ISSN 0065-3713, 1995.

[RD.15] P. Nieminen, "On the energy spectra and occurrence rate of solar electron events", Proc. of Space Radiation workshop, DERA, Nov. 1999.

[RD.16] J.I. Minow, L. N.Parker, R.L. Altstatt, W.C. Blackwell, Jr, A. Diekmann, "Radiation and internal charging environments for thin dielectrics in interplanetary space", Proc. of 9th Spacecraft Charging Technology Conf., Tsukuba, 2005.

[RD.17] F Lei, S Clucas, C Dyer, P Truscott, An atmospheric radiation model based on response matrices generated by detailed Monte Carlo simulations of cosmic ray interactions, IEEE Transactions in Nuclear Science, Vol 51, No 6, pp 3442-3451, Dec 2004.

[RD.18] F Lei, A Hands, C Dyer, P Truscott, Improvements to and Validations of the QinetiQ Atmospheric Radiation Model (QARM), IEEE Transactions on Nuclear Science Vol. 53, No. 4, pp 1851-1858, Aug. 2006.

[RD.19] Evans R.W, and H.B.Garrett, Modeling Jupiter's Internal Electrostatic Discharge Environment, J.Spacecraft&Rockets, Vol.39, No.6, p.926, 2002

[RD.20] Divine, N. and H. Garrett, Charged particle distribution in Jupiter's magnetosphere. J. Geophys. Res. 88, 6889-6903 (1983)

[RD.21] Anderson B.J., "Natural Orbital Environment Guidelines for Use in Aerospace Vehicle Development", by:, editor and R.E. Smith, compiler; NASA TM 4527, chapter 7, June 1994.

[RD.22] Grün E., H.A. Zook, H. Fechtig and R.H. Giese, "Collisional Balance of the Meteoritic Complex", Icarus, Vol. 62, p.244, 1985.

[RD.23] ECSS-Q-ST-70-02, Space product assurance: Thermal vacuum outgassing test for the screening of space materials.

[RD.24] ASTM E-595, Method for Total Mass Loss and Collected Volatile Condensable Materials from outgassing in a vacuum environment.

[RD.25] S.L. Huston*, Space Environments and Effects: Trapped Proton Model, NASA/CR-2002-211784, 2002

[RD.26] Singley G.W. and I. Vette J.I., "The AE-4 Model of the Outer Radiation Zone Electron Environment", NSSDC/WDC-A-R&S 72-06, NASA-GSFC, 1972.

[RD.27] Taylor, A.D. The Harvard Radio Meteor Project meteor velocity distribution reappraised, Icarus, 116: 154-158, 1995

[RD.28] McBride, N., "The importance of the annual meteoroid streams to spacecraft and their detectors", Adv. In Space Research, Vol. 20, pp 1513 –1516, 1997.

[RD.29] Jenniskens P., "Meteor Stream Activity", Astron. Astrophys. Vol. 287, pp 990-1013, 1994.

[RD.30] Eta_max space, "ESABASE2/DEBRIS, Technical Description", ref. r040_rep025_02_00_01, July 2006.

[RD.31] Kaula, W.M.; 1966 Theory of Satellite Geodesy, Waltham & Blaisdell

[RD.32] Sibeck, D. G., R. E. Lopez, and E. C. Roelof (1991), Solar wind control of the magnetopause shape, location and motion, J. Geophys. Res, 96, 5489.

[RD.33] E 490 – 00a, Standard Solar Constant and Zero Air Mass Solar Spectral Irradiance Tables, © ASTM, 100 Barr Harbor Drive, West Conshohocken, PA 19428-2959 (2000).

[RD.34] Knocke, P.C.; Ries, J.C.; Tapley, B.D., Earth Radiation Pressure Effects on Satellites, AIAA-1988-4292, AIAA/AAS Astrodynamics Conference, Minneapolis/MN, Aug 15-17, 1988

[RD.35] a) Hedin, A. E., Salah, J.E.., Evans, J.V., Reber, C. A., Newton, G. P., Spencer, N. W., Kayser, D.C., Alcayde, D., Bauer, P., Cogger, L., and McClure, J.P., "A Global Thermospheric Model Based on Mass Spectrometer and Incoherent Scatter Data: MSIS 1. N2 density and temperature. ", J. Geophys. Res., Vol. 82, pp. 2139-2147, 1977. b)Hedin, A. E., Reber, C. A., Newton, G. P., Spencer, N. W., Brinton, H. C., Mayr, H. G., and Potter, W. E., "A Global Thermospheric Model Based on Mass Spectrometer and Incoherent Scatter Data: MSIS 2. Composition", J. Geophys. Res., Vol. 82, pp. 2148-2156, 1977.

[RD.36] Hedin, H.E., Reber, C. A., Spencer, N. W., Brinton, H. C. and Kayser, D. C., "Global Model of Longitude/UT Variations in Thermospheric Composition and Temperature Based on Mass Spectrometer Data", J. Geophys. Res., Vol. 84, 1979 p.1.

[RD.37] Hedin, A. E., "A Revised Thermospheric Model Based on Mass Spectrometer and Incoherent Scatter Data: MSIS-83," J. Geophys. Res., Vol. 88, 1983, p., 10170.

[RD.38] Hedin, A. E., "MSIS-86 Thermospheric Model," J. Geophys. Res., Vol. 92, 1987, p. 4649.

[RD.39] Hedin, A. E., "Extension of the MSIS Thermosphere Model into the Middle and Lower Atmosphere," J. Geophys. Res., Vol. 96, 1991, p. 1159.

[RD.40] Bowman, B. R., Marcos, F. A. and Kendra, M. J., "A Method for Computing Accurate Daily Atmospheric Density Values from Satellite Drag Data", AAS-04-173, AAS/AIAA Flight Mechanics Meeting, Maui, HI, 2004.

[RD.41] Angelatsi Coll, M., et al., The first Mars thermospheric general circulation model: The Martian atmosphere from the ground to 240 km, Geophysical Research Letters, Volume 32, Issue 4, CiteID L04201, 2005.

[RD.42] Hedin, A. E., N. W. Spencer, and T. L. Killeen, Empirical Global Model of Upper Thermosphere Winds Based on Atmosphere and Dynamics Explorer Satellite Data, J. Geophys. Res., 93, 9959- 9978, 1988.

[RD.43] Flasar, F.M. et al, An intense stratospheric jet on Jupiter, Nature, 427,132-135, 2004.

[RD.44] Bagenal F., T. Dowling and W. McKinnon Ed., Jupiter, Cambridge University Press, Cambridge, 2004.

[RD.45] Friedson A.J., New observations and modelling of a QBO-like oscillation in Jupiter's stratosphere, Icarus, 137, 34-55, 1999.

[RD.46] Young L., et al., Gravity waves in Jupiter's stratosphere, as measured by the Galileo ASI experiment, Icarus, 173,185-199,2005.

[RD.47] Kliore A.J., V.I Moroz and G.M. Keating Ed., The Venus International Reference atmosphere, Advances in Space Research, 5, 11, 1985.

[RD.48] Mars transportation environment définition document, M. Alexander Ed., NASA/TM-2001-210935.

[RD.49] Justus, C.G., Mars Global Reference Atmospheric Model 2010 Version (Mars-GRAM 2010) Users Guide, NASA/TM-2014-217499, February, 2014..

[RD.50] Justus, C.G., et al. Mars-GRAM 2000: A Mars Atmospheric Model for Engineering Applications, Advances in Space Research, Vol. 29, 193-202, 2002.

[RD.51] Forget, F., F. Hourdin, R. Fournier, C. Hourdin, O. Talagrand, M. Collins, S. R. Lewis, P.L. Read, J-P Huot, Improved General Circulation Models of the Martian Atmosphere from the Surface to Above 80 km, J. Geophys. Res. Vol. 104, No. E10, p. 24,155-24,176, 1999.

[RD.52] Justus, C.G., Duvall, A.L., and Johnson, D.L., Engineering-Level Model Atmospheres for Titan and Neptune, AIAA-2003-4803, 39th AIAA/ASME/ SAE/ASEE Joint Propulsion Conference, Huntsville, Alabama, July 20-23, 2003.

[RD.53] Purvis C.K, H.B. Garrett, A.C. Whittlesey and N.J. Stevens, "Design Guidelines for Assessing and Controlling Spacecraft Charging Effects", NASA TP-2361, 1984.

[RD.54] Burke W.J., D.A. Hardy and R.P. Vancour, "Magnetospheric and High Latitude Ionospheric Electrodynamics", Chapter 8 of "Handbook of Geophysics and the Space Environment", Ed. A. Uram, USAF, 1985.

[RD.55] Scialdone J.J., "An Estimate of the Outgassing of Space Payloads and Its Gaseous Influence on the Environment", J. Spacecraft and Rockets, 23, p.373, 1986.

[RD.56] Huebner W.F. and P.T. Giguere, "A Model of Comet Comae II. Effects of Solar Photodissociative Ionization", Astrophys. J., 238, p.753, 1980.

[RD.57] Huddleston D.E., A.D. Johnstone and A.J. Coates, "Determination of Comet Halley Gas Emission Characteristics from Mass Loading of the Solar Wind", J. Geophys. Res., 95, p.21, 1990.

[RD.58] Belian, R.D., T.E. Cayton, R.A. Christensen, J.C. Ingraham, M.M. Meier, G.D. Reeves and A.J. Lazarus, "Relativistic electrons in the outer-zone: An 11-year cycle; their relation to the solar wind", Proceedings of the Taos Workshop on the Earth's Trapped Particle Environment, Ed, G.D. Reeves, AIP Conference Proceedings 383, 13-18, ISBN 1-56396-540-2, 1986.

[RD.59] SPENVIS: http://www.spenvis.oma.be/spenvis/

[RD.60] OMERE: http://www.trad.fr/

[RD.61] Brautigam, D. H., and J. T. Bell, CRRESELE Documentation, PL-TR-95-2128, Environmental Research Papers, 1178, Phillips Laboratory, 1995.

[RD.62] Meffert, J. D., and M. S. Gussenhoven, CRRESPRO Documentation, PL-TR-94-2218, Environmental Research Papers, 1158, Phillips Laboratory, 1994.

[RD.63] Watts J.W., T.A. Parnell and H.H. Heckman, "Approximate Angular Distribution and Spectra for Geomagnetically Trapped Protons in Low-Earth Orbit", in "High-Energy Radiation Background in Space", AIP Conference Proceedings 186, AIP, NewYork, 1989.

[RD.64] Kruglanski M. and J. Lemaire, "Trapped Proton Anisotropy at Low Altitude", Technical Note 6, ESA/ESTEC/WMA Contr. 10725, Institut d'Aeronomie Spatiale de Belgique, 1996.

[RD.65] Bühler P., A. Zehnder, E. Daly and L. Adams, "REM Measurements on-Board MIR in 1995", Advances in Space Research 21, 1645 (1998)

[RD.66] Tranquille C, "Extension to AE-4 Local Time and Statistical Models for Application to AE-8", ESTEC/WMA Internal Memorandum, 1986.

[RD.67] Evans, H.D.R., D.J Rodgers, E.J. Daly, P. Nieminen, A. Mohammadzadeh, P. Buehler, W. Hajdas, "Energetic electron results from the ESA Monitors and Comparison with Existing Radiation Belt Internal Charging Models", Spacecraft Charging Technology Conference 2007 proceedings.

[RD.68] Feynman J., T. Armstrong, L. Dao- Givner, S. Silverman, "New Interplanetary Proton Fluence Model", J. Spacecraft, Vol 27, No. 4, July-Aug. 1990.

[RD.69] Feynman J., G. Spitale, J. Wang and S. Gabriel, "Interplanetary Proton Fluence Model: JPL 1991", J. Geophys. Res. 98, A8, 13 281-13 294, 1993.

[RD.70] Rosenqvist, L., A. Hilgers, H. Evans, E. Daly, M. Hapgood, R. Stamper, R. Zwickl, S. Bourdarie and D. Bosher, A toolkit for updating interplanetary proton cumulated fluence models, J. Spacecraft and Rockets, Vol. 42, Number 6, Nov-Dec 2005.

[RD.71] Glover, A., A. Hilgers, L. Rosenqvist, S. Bourdarie, Interplanetary Proton Cumulated Fluence Model Update, Advances in Space Research, 2007

[RD.72] King, J.H., “Solar Proton Fluences for 1977-1983 Space Missions”, J. Spacecrafts and Rockets, 11, 401, 1974.

[RD.73] Xapsos, M.A., R J Walters, G P Summers, J L Barth, E G Stassinopoulos, S R Messenger, E A Burke,"Characterizing solar proton energy spectra for radiation effects applications," IEEE Trans. on Nucl. Sci , vol. 47, no. 6, pp 2218-2223, Dec. 2000.

[RD.74] C. S Dyer, F.Lei, S.N. Clucas, D. F. Smart, M.A. Shea, “Solar particle enhancements of single event effect rates at aircraft altitudes,” IEEE Trans. Nucl. Sci. , vol.50, no. 6, pp. 2038-2045, Dec. 2003.

[RD.75] Nymmik, R.A. Probabilistic model for fluences and peak fluxes of solar particles. Ra-diat. Meas. 30, 287-296, 1999

[RD.76] Nymmik R., Initial conditions for radiation analysis : Models of galactic cosmic rays and solar particle events, Advances in Space Research, 38 issue 6, pp 1182-1190, 2006

[RD.77] Adams, J.H., “Cosmic Ray Effects on MicroElectronics, Part IV”, NRL Memorandum Report 5901, Naval Research Laboratory, Washington DC 20375-5000, USA, 1986.

[RD.78] Tylka, A.J., et al., “CREME96: A Revision of the Cosmic Ray Effects on Micro-Electronics Code”, IEEE Trans. Nucl. Sci. NS-44, 2 150-2 160, 1997.

[RD.79] Nymmik, R.A., M.I. Panasyuk, T. I. Pervaja, and A.A. Suslov, “A Model of Galactic Cosmic Ray Fluxes”, by, Nucl. Tracks & Radiat. Meas, 20, 427-429, 1992.

[RD.80] Stassinopoulos E.G. and J.H. King, “Empirical Solar Proton Model For Orbiting Spacecraft Applications”, IEEE Trans. on Aerosp. and Elect. Systems AES-10, 442, 1973.

[RD.81] F Ait-Ouamer, A D Zych, R S White, “Atmospheric neutrons at 8.5 GV Cutoff in the Southern hemisphere,” J. Geophys. Res., Vol. 93, No. A4, pp. 2499-2510, April 1988.

[RD.82] D J Morris, H Aarts, K Bennett, J A Lockwood, M L McConnell, J M Ryan, V sconfelder, H Steinle, X Peng,” Neutron measurements in near-earth orbit with COMPTEL,” J. Geophys. Res., Vol. 100, No. A7, pp. 12243-12249, July 1995.

[RD.83] I. Jun, H.B. Garrett and R. W. Evans, High-energy trapped particle environments at Jupiter: an update IEEE Trans. Nuc. Science, V52, 2281, December 2005

[RD.84] G. De Angelis , M. S. Clowdsley, R. C. Singleterry and J. W. Wilson, A new Mars radiation environment model with visualization, Advances in Space Research, 34 Issue 6, pp 1328-1332, 2004

[RD.85] Keating, A, A. Mohammadzadeh, P. Nieminen, D. Maia, S. Coutinho, H. Evans, M. Pimenta, J-P. Huot, E. Daly, “A Model for Mars Radiation Environment Characterisation”, IEEE Trans. Nucl Sci, Vol 52, No 6. Dec 2005.

[RD.86] Desorgher, L, E. O. Flückiger, M. Gurtner, “The PLANETOCOSMICS Geant4 application”, 36th COSPAR Scientific Assembly. Held 16 - 23 July 2006, in Beijing, China. Meeting abstract from the CDROM, #2361

[RD.87] Hernandez de la Torre C., F. P. Caballero, N. Sanchez Ortiz, H. Sdunnus, H. Klinkrad, “DISCOS Database and Web Interface, Proceedings of the Third European Conference on Space Debris, ESOC, Darmstadt, ESA SP-473, 19-21 March 2001. https://discosweb.esoc.esa.int

[RD.88] Oswald, M., Stabroth, S., Wiedemann, C., Klinkrad, H., Vörsmann, P, MASTER-2005 - The Debris Risk Assessment Tool for the Space Industry,

paper AIAA-2006-7219, AIAA Space 2006 Conference, San Jose, CA, USA, 2006.

[RD.89] Fukushige S., Akahoshi Y., Kitzawa Y., "Comparison of Debris Environment Models; ORDEM2000, MASTER2001 and MASTER2005", IHI Engineering Review, Vol. 40 No.1 February 2007

[RD.90] Kessler D.J., J. Zhang, M.J. Matney, P. Eichler, R.C. Reynolds, P.D. Anz-Meador and E.G. Stansbery, "A Computer Based Orbital Debris Environment Model for Spacecraft Design and Observations in Low Earth Orbit"; NASA TM 104825, November 1996.

[RD.91] Inter-Agency Space Debris Coordination Committee, 'Protection Manual', IADC- -04-03, Version 7.0, Septemberl 2014.

[RD.92] Van Eesbeek M. and A. Zwaal, "Outgassing and contamination model based on residence time", ESA SP232, Proc. of the 3rd European Symp. on spacecraft materials in a space environment, Noordwijk, The Netherlands, 1-4 Oct 1985.

[RD.93] Scialdone J., "Characterisation of the outgassing of spacecraft materials", SPIE Vol. 287 Shuttle Optical Environment, 1981.

[RD.94] Trinks H., "Exhaust Plume Databook Update Version No. 3 / ESA/ESTEC Contract 7590/87/NL/TP".

[RD.95] Simons G.A., "Effect of Nozzle Boundary Layers on Rocket Exhaust Plumes", AIAA Journal, Tech. Notes, vol. 10, No. 11, pp. 1534-1535, 1972.

[RD.96] Trinks H., Exhaust Plume Data Handbook (EPDH IV), Progress Report IV, ESA Contract No 7510/87/NL/PP, Sept. 1991a.

[RD.97] Guernsey C. S., McGregor R. D., Bipropellant rocket exhaust plume analysis on the Galileo spacecraft, AIAA paper No 86-1488, AIAA/ASME/SAE/ASEE 22nd Joint Propulsion Conference, Huntsville, AL, June 16-18, 1986.b.

[RD.98] Tsyganenko, N. A. (2002), A model of the near magnetosphere with a dawn-dusk asymmetry 1. Mathematical structure J. Geophys. Res., v.107(A8), doi:10.1029/2001JA000219

[RD.99] Tsyganenko, N. A., and M. I. Sitnov (2005), Modeling the dynamics of the inner magnetosphere during strong geomagnetic storms, J. Geophys. Res., v. 110 (A3), A03208, doi: 10.1029/2004JA010798.

[RD.100] Menvielle M. and A. Berthelier, "The K-derived Planetary Indices: Description and Availability", Rev. Geophys., 29, 3, pp 415-432, August 1991.

[RD.101] Hess W.N., The Radiation Belt and the Magnetosphere, Blaisdell Publ. Co., New York, 1968.

[RD.102] McIlwain C.E., Co-ordinates for Mapping the Distribution of Geomagnetically Trapped Particles, J. Geophys. Res., 66, 3681, 1961.

[RD.103] Hilton H.H., L Parameter – A New Approximation, J. Geophys. Res., 76, 6952, 1971. (Note that this paper contains a typographical error in its expression for a3 of Eq. 5.3).

[RD.104] Xapsos M.A., Summers G.P., Barth J.L., et al.. Probability model for worst case solar proton event fluences, IEEE Trans. on Nuclear Science, 46 (6), 1481-1485, 1999

[RD.105] Xapsos M.A., Stauffer C., Jordan T., Barth J.L. and Mewaldt A., Model for Cumulative Solar Heavy Ion Energy and Linear Energy Transfer Spectra, IEEE Transactionson Nucl Science, Vol. 54, No. 6, 2007.

[RD.106] Dikarev V., E. Grün, M. Landgraf and R. Jehn, "Update of the ESA Meteoroid Model", Proc. of 4th European Conf. on Space Debris, ESOC, 18-20 April 2005, ESA-SP-587, pp 271—276, 2005.

[RD.107] Liou J.-C., M. J. Matney, P. D. Anz-Meador, D. Kessler, M. Jansen, J. R. Theall “The New NASA Orbital Debris Engineering Model ORDEM2000”, NASA/TP-2002-210780, May 2002.

[RD.108] Staubach P., E. Grün and R. Jehn, “The meteoroid environment of the Earth”, 31th COSPAR Sci. Assembly, Birmingham/UK, July, 1996.

[RD.109] ASTM E-1559, Method for contamination outgassing characteristics of space materials.

[RD.110] Jones J. “Meteoroid Engineering Model – Final Report”, SEE/CR-2004-400, NASA/MSFC, June 2004.

[RD.111] Tsyganenko, N.N., “A Magnetospheric Magnetic Field Model with a Warped Tail Current Sheet”, Planet. Space Sci. 37, 5-20, 1989.

[RD.112] Tsyganenko, N.A. (1995), Modeling the Earth's magnetospheric magnetic field confined within a realistic magnetopause, J.Geophys.Res., v.100, pp.5599-5612

[RD.113] ISO 22009:2009 Space systems - Space environment (natural and artificial) - Model of the earth's magnetospheric magnetic field, http://www.iso.org/iso/catalogue_detail.htm?csnumber=51251

[RD.114] Gussenhoven, M.S. and E.G. Mullen, “Geosynchronuos environment for severe spacecraft charging”, J. Spacecraft and Rockets 20, p. 26, 1988.

[RD.115] Grard R.J.L. and J.K.E. Tunaley, “Photo Electron Sheath Near a planar Probe in Interplanetary Space”, J. Geophys. Res., 76, p.2498, 1971.

[RD.116] Feynman, J., “Solar Wind”, Chapter 3 of “Handbook of Geophysics and the Space Environment”, Ed. A. Juram, USAF, 1985.

[RD.117] Christon, S.P., T.E. Eastman, T. Doke, L.A. Frank, G. Gloeckler, H. Kojima, S. Kokubun, A.T.Y. Lui, H. Matsumoto, R.W. McEntire, T. Mukai, S.R. Nylund, W.R. Paterson, E.C. Roelof, Y. Saito, T. Sotirelis, K. Tsuruda, D.J. Williams, and T. Yamamoto, "Magnetospheric Plasma Regimes Identified Using Geotail Measurements 2. Statistics, Spatial Distribution, and GeomagneticDependence,"J. Geophys. Res., 103, 23521 – 23542, 1998.

[RD.118] Heynderickx, D., J. Lemaire, and E. J. Daly, “Historical Review of the Different Procedures Used to Compute the L-Parameter”, Radiat. Meas. 26, 325-331, 1996

[RD.119] Roederer J.G, “Dynamics of Geomagnetically Trapped Radiation”, Springer, Berlin, 1970

[RD.120] Cabrera and Lemaire, Space Weather, Vol. 5 S04007, doi: 10.1029/2006SW000263, 2007.

[RD.121] Öpik, E.J., “Collision probabilities with the planets and the distribution of interplanetary matter”, Proc. R.I.A., 54, pp. 165-199, 1951.

[RD.122] Tobiska, W.K., S.D. Bouwer, and B.R. Bowman, “The development of new solar indices for use in thermospheric density modelling”, J. Atm. Solar Terr. Phys., 70, pp803-819, 2008

[RD.123] National Aeronautics and Space Administration, U.S. Air Force, and U.S. Weather Bureau, “U.S. Standard Atmosphere 1962”, U.S. Government Printing Office, Washington, DC, 1962.

[RD.124] U.S. Standard Atmosphere Supplements 1966, ESSA, NASA and U.S. Air Force, Dec. 1966.

[RD.125] National Oceanic and Atmospheric Administration, National Aeronautics and Space Administration, U.S. Air Force, “U.S. Standard Atmosphere 1976”, U.S. Government Printing Office, Washington, DC, 1976.

[RD.126] ISO International Standard 2533-1975, “Standard Atmosphere First Edition”, Corrigendum 1 1978, ISO, Geneva, Switzerland.

[RD.127] ISO International Standard 5878-1982, Reference Atmospheres for Aerospace Use, First Edition-1982-04-14, Technical Committee ISO/TC 20, Aircraft and Space Vehicles.

[RD.128] a) Rees, D., Editor, (1988): "COSPAR International Reference Atmosphere 1986, Part l. Thermospheric Models", Advances in Space Research, Vol. 8, No. 5/6Pergamon Press, Oxford and NY. b) Rees, D., J. J. Barnett, and K. Labitzke, editors (1990): "CIRA 1986, COSPAR International Reference Atmosphere, Part II: Middle Atmosphere Models," Advances in Space Research, Vol. 10, No. 12, Pergamon Press, Oxford and NY. c) Keating, G. M., editor (1996): "COSPAR International Reference Atmosphere (CIRA), Part III: Trace Constituent Reference Models," Advances in Space Research, Vol. 18, No. 9/10, Pergamon Press, Oxford and NY.

[RD.129] CIRA 1961, H. Kallmann-Bijl, R.L.F. Boyd, H. Lagow, S.M. Poloskov, and W. Priester (eds.), North-Holland Publishing Company, Amsterdam, 1961.

[RD.130] CIRA 1965, North-Holland Publishing Company, Amsterdam, 1965.

[RD.131] COSPAR International Reference Atmosphere 1972, Compiled by the members of COSPAR Working Group 4, Akademie-Verlag, Berlin, 1972.

[RD.132] Justus C.G., F.N. Alyea, D.M. Cunnold, and D.L. Johnson (1986), GRAM-86, "Improvements in the Global Atmospheric Model", NASA MSFC Report ED-5-15-86.

[RD.133] Justus C.G., F.N. Alyea, D.M. Cunnold, R.S. Blocker, and D.L. Johnson (1988), GRAM-88, "Improvements to the Perturbation Simulation of the Global Reference Atmospheric Model", NASA MSFC Memorandum ES-44-11-9-88.

[RD.134] Justus C.G., F.N. Alyea, D.M. Cunnold, W.R. Jefferies III, and D.L. Johnson (1991), "The NASA/MSFC Global Reference Atmospheric Model – 1990 Version (GRAM-90), Part 1: Technical/Users Manual". NASA TM-4268, Grant NAG8-078.

[RD.135] Justus C.G., W.R. Jefferies III, S.P. Yung, and D.L. Johnson (1995), "The NASA/MSFC Global Reference Atmospheric Model – 1995 Version (GRAM-95)", NASA TM-4715.

[RD.136] Justus C.G., and D.L. Johnson (1999), "The NASA/MSFC Global Reference Atmospheric Model – 1999 Version (GRAM-99)", NASA TM-1999-209630.

[RD.137] Picone, J. M., A. E. Hedin, K. P. Drob, and J. Lean, NRLMSISE-00 Empirical Atmospheric Model: Comparisons to Data and Standard Models. Advances in the Astronautical Sciences, Vol. 109 II//Pages 1385-1387, AAS/AIAA Astrodynamics Conference, July 30-August 2, 2001, Quebec City, Que., ISSN 0065-3438.

[RD.138] Olsen N., H.Lühr,T.J.Sabaka, M.Mandea, M.Rother, L.Tøffner-Clausen and S.Choi , CHAOS—a model of the Earth's magnetic field derived from CHAMP, Ørsted, and SAC-C magnetic satellite data, Geophys. J. Int. 166, 67–75 (2006)

[RD.139] Maus S., H.Lühr2, G.Balasis, M.Rother and M.Mandea, Third generation of the Potsdam Magnetic Model of the Earth (POMME), Geochemistry Geophysics Geosystems, 7, Q07008, 2006

[RD.140] Sabaka T.J., Olsen, N., and M.E. Purucker, Extending comprehensive models of the Earth's magnetic field with Oersted and Champ data, Geophys. J. Int.,159,521-547, (2004)

[RD.141] Mead, G. D. and Fairfield, D. H., A quantitative magnetospheric model derived from spacecraft magnetometer data, J.Geophys. Res., 80, 523-534, (1975)

[RD.142] Olsen, W.P. and Pfitzer, K.A., A dynamic model of the magnetospheric magnetic and electric fields for July 29, 1977, J. Geophys. Res., 87, 5943-5948, (1977)

[RD.143] Hilmer, R. V. (1989), A magnetospheric magnetic field model with flexible internal current systems, PhD thesis, 156pp., Rice Univ., Houston, Texas.

[RD.144] Voight, G.-H. (1981), A mathematical magnetospheric field model with independent physical parameters, Planet. Space Sci., 29(10), 1-20.

[RD.145] Jordan, C. E., Empirical Models of the Magnetospheric Magnetic Field, Rev. Geophys., 32, 2, 139-157, (1994)

[RD.146] Xapsos M. A., J.L. Barth, E.G. Stassinopoulos, E.A. Burke, and G.B. Gee, Space Environment Effects: Model for Emission of Solar Protons (ESP) – Cumulative and Worst-Case Event Fluences, NASA/TP-1999-209763, 1999..

[RD.147] Liu RY, Smith PA and King JW, 'A new solar index which leads to improved foF2 predictions using the CCIR ATLAS',Telecommunication Journal, 1983, Volume 50 (8), pages 408-414.

[RD.148] Kaspi et al., The effect of differential rotation on Jupiter's low-degree even gravity moments", Geophys. Res. Lett., Volume 44, Issue 12, 28 June 2017, https://doi.org/10.1002/2017GL073629

[RD.149] Kopp, G., Lean, J., "A new, lower value of total solar irradiance: Evidence and climate significance", GEOPHYSICAL RESEARCH LETTERS, VOL. 38, L01706, doi:10.1029/2010GL045777, 2011

[RD.150] B. Taylor et al. , "The Interplanetary Electron Model (IEM)", Nuclear Science, IEEE Transactions, Volume 58 Issue 6, 2011, https://doi.org/10.1109/TNS.2011.2171718

[RD.151] Claret A., et al., FLUKA Calculation of the Neutron Albedo Encountered at Low Earth Orbits, IEEE Trans. Nucl. Sci. 61, no. 6, p. 3363, Dec. 2014

[RD.152] Combier N., A. Claret, P. Laurent, V. Maget, D. Boscher, Improvements of FLUKA Calculation of the Neutron Albedo, IEEE Trans. Nucl. Sci. NS-64, 1, 614, January 2017

[RD.153] Structure of the Venus middle atmosphere (VIRA II model), Zasova,Ludmila; Limaye,Sanjay; Ignatiev,Nikolay; Khatuntsev,Igor; Gorinov,Dmitry, 40th COSPAR Scientific Assembly. Held 2-10 August 2014, in Moscow, Russia, Abstract C4.3-1-14.

[RD.154] I.C.F. Muller-Wodarg, M. Mendillo, R.V. Yelle, A.D. Aylward, "A global circulation model of Saturn's thermosphere", Icarus 180 (2006) 147-160.

[RD.155] A. Spiga et al, "High-resolution Global Climate Modelling of Saturn's and Jupiter's tropospheric and stratospheric circulations", EPSC Abstracts, Vol. 11, EPSC2017-195-1, 2017.

[RD.156] P. Rannou, S. Lebonnois, F. Hourdin, D. Luz, "Titan atmosphere database", Advances in Space Research, Vol. 36 Issue 11, 2005, P. 2194-2198.

[RD.157] Huang, X., Reinisch, B., Song, P., Green, J., Gallagher, "Developing an empirical density model of the plasmasphere using IMAGE/RPI observations", doi: 10.1016/j.asr.2003.07.007, 2004.

[RD.158] B.W. Reinisch et al. , "Modeling the F2 topside and plasmasphere for IRI using IMAGE/RPI and ISIS data", Advances in Space Research 39, 2007.

[RD.159] P.A. Webb and E.A. Essex, "A dynamic global model of the plasmasphere", Journal of Atmospheric and Solar-Terrestrial Physics, 66, 2004.

[RD.160] Pierrard, V., and K. Stegen, "A three dimensional dynamic kinetic model of the plasmasphere", J. Geophys. Res. 113, doi:10.1029/2008JA013060, 2008.

[RD.161] A.N. Petrov, O.R. Grigoryan, M.I. Panasyuk, "Energy spectrum of proton flux near geomagnetic equator at low altitudes", Advances in Space Research 41, 1269–1273, 2008.xx

[RD.162] Badhwar, Gautam D.; Konradi, Andrei, "Conversion of omnidirectional proton fluxes into a pitch angle distribution", Journal of Spacecraft and Rockets (ISSN 0022-4650), vol. 27, May-June 1990, p. 350-352.

[RD.163] A.N. Petrov, O.R. Grigoryan, M.I. Panasyuk Energy spectrum of proton flux near geomagnetic equator at low altitudes / Advances in Space Research 41 (2008) 1269–1273.

[RD.164] A. Sicard-Piet et al., “JOSE: A new Jovian Specification Environment model”, IEEE Transactions on Nuclear Science, Vol. 58, No. 3, June 2011.

[RD.165] JUICE team, “JUICE Envirinment Specification”, JS-14-09 v5.5, 24/02/20171, http://space-env.esa.int/Reports/ECSS/JS-14-09_i5.5_JUICE_Environment_spec.pdf

[RD.166] A. Hands, K. Ryden, C. Underwood, D. Rodgers and H. Evans, "A New Model of Outer Belt Electrons for Dielectric Internal Charging (MOBE-DIC)," in IEEE Transactions on Nuclear Science, vol. 62, no. 6, pp. 2767-2775, Dec. 2015

[RD.167] U. Sezen, T. L. Gulyaeva and F. Arikan, "Online international reference ionosphere extended to plasmasphere (IRI-Plas) model," 2017 XXXIInd General Assembly and Scientific Symposium of the International Union of Radio Science (URSI GASS), Montreal, QC, 2017, pp. 1-4.

[RD.168] D. Payan, A. Sicard-Piet, J.C. Mateo-Velez, D.Lazaro, S. Bourdarie, et al.. Worst case of Geostationary charging environment spectrum based on LANL flight data. Spacecraft Charging Technology Conference 2014

[RD.169] Christian Imhof, Holger Mank, Jörg Lange 14th Spacecraft Charging Technology Conference, ESA/ESTEC, Noordwijk, NL, 04-08 APRIL 2016 CHARGING SIMULATIONS FOR A LOW EARTH ORBIT SATELLITE WITH SPIS USING DIFFERENT ENVIRONMENTAL INPUTS

[RD.170] Förste, Christoph; Bruinsma, Sean.L.; Abrikosov, Oleg; Lemoine, Jean-Michel; Marty, Jean Charles; Flechtner, Frank; Balmino, G.; Barthelmes, F.; Biancale, R. (2014): EIGEN-6C4 The latest combined global gravity field model including GOCE data up to degree and order 2190 of GFZ Potsdam and GRGS Toulouse. GFZ Data Services. http://doi.org/10.5880/icgem.2015.1

[RD.171] C. Theroude, G. Chanteperdrix, A. Merle, A new satellite system-level m/od impact risk assessment tool, ISMSE-13, 22-26 June 2015

[RD.172] Max Gulde, Scott Kempf, Frank Schäfer, Fast and Flexible Space Debris Risk Assessment for Satellites, Journal of Space Safety Engineering, Volume 3, Issue 3, December 2016, Pages 111-113